Top-Down Etched Site-Controlled InGaN/GaN Quantum Dots

by

Lei Zhang

A dissertation submitted in partial fulfillment
of the requirements for the degree of
Doctor of Philosophy
(Physics)
in the University of Michigan
2015

Doctoral Committee:

Assistant Professor Hui Deng, Chair
Professor Luming Duan
Associate Professor Pei-Cheng Ku
Professor Roberto D. Merlin
Professor Duncan G. Steel

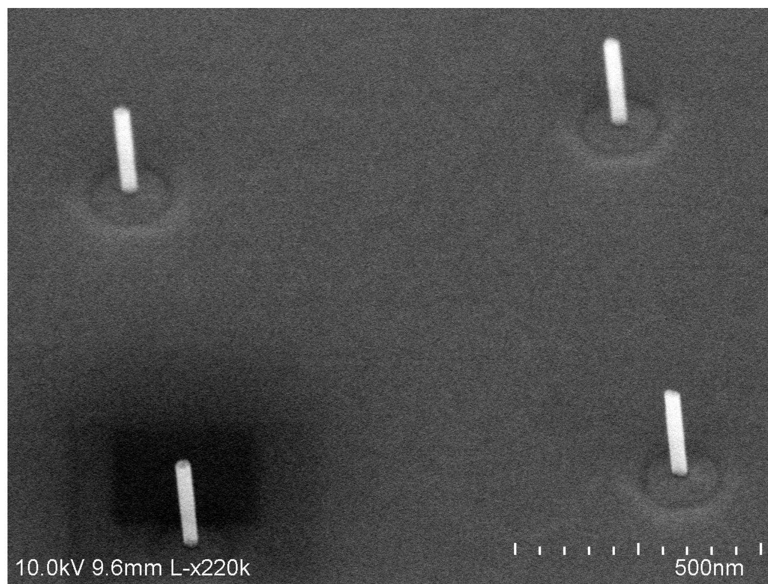
10.0kV 9.6mm L-x220k
500nm

©Lei Zhang

2015

To my parents, Zhengyong Zhang and Ailing Qiu.

Acknowledgments

I would like to first thank my thesis advisor Prof. Hui Deng for her constant support and encouragement. I thank her for providing me great freedom in choosing what I want to do and helping me figuring out ways to achieve them. I thank her for patiently listening to every problem I had and guiding me towards solutions. I thank her for her strong support on every aspect of my research. I thank her for the great understanding and tolerance when my research was going nowhere. I thank her for her encouragement every time I had doubts in the future of our project or my capability of achieving our goals. I thank her for speaking highly of me in many occasions and her generous recommendations whenever I needed them. I thank her for numerous great advices that have influenced my life and career.

I would like to thank other members of my thesis committee Prof. Pei-Cheng Ku, Prof. Duncan Steel, Prof. Roberto Merlin, and Prof. Luming Duan. Prof. Ku is my thesis co-advisor. I thank him for providing me great advices in every stage of my research and sharing his life stories and insights to help me making critical life and career decisions. I thank Prof. Steel for being my mentor when I first came to Michigan and recommending Prof. Hui Deng as my research advisor. I thank Prof. Merlin for all the discussions we had about my data. I thank Prof. Duan for encouraging me to come to Michigan for graduate school, and I am glad that I did.

I would also like to thank my colleagues Tyler, Paul, Bo, Hoon and Glenn, and collaborators Chu-Hsiang, Luke and Brandon. Especially, I thank Paul and Bo who joint Hui's new lab before me and taught me many things; I thank Tyler for spending numerous days and nights with me in the lab; I thank Chu-Hsiang for making most of the samples and helping me during the numerous days and nights in the cleanroom; and I thank Luke for introducing me to the entire site-controlled quantum dot project.

Finally, I thank Amy for her support and companion during the past two yeas and her many evenings and weekends spent in my dark sub-basement lab when I had to run experiments or outside the cleanroom when I had to make samples.

Preface

This thesis is based on three published journal papers [1, 2, 3] and two papers to be submitted for publishing by the author and his colleagues Tyler A. Hill in Prof. Hui Deng's group in the Physic Department, and Dr. Leung-Kway Lee, Chu-Hsiang Teng and Brandon Demory in Prof. Pei-Cheng Ku's group in the Electrical Engineering and Computer Science Department. The author set up all optical and electrical characterization systems in Chap. 3 with guidance from Prof. Hui Deng and assistance from Tyler Hill and measured all data in this thesis unless otherwise mentioned. Dr. Leung-Kway Lee made the very first site-controlled quantum dot (QD) sample that led to the results in Chap. 4. Chu-Hsiang Teng fabricated all samples used in Chap. 5 and 6. The author performed all fabrication processes for the sample used in Chap. 7 except for the electron-beam lithography, which was done by Chu-Hsiang Teng. The entire thesis is done under the guidance of Prof. Hui Deng and Prof. Pei-Cheng Ku.

TABLE OF CONTENTS

Dedication . . . . **ii**

Acknowledgments . . . . **iii**

Preface . . . . **iv**

List of Figures . . . . **viii**

List of Tables . . . . **xiv**

List of Abbreviations . . . . **xv**

Abstract . . . . **xvii**

Chapter

1 Introduction **1**

1.1 Applications of Single Quantum Dots 2
1.1.1 Non-Classical Light Sources 2
1.1.2 Quantum Dot Spin Qubit 5
1.1.3 Quantum Dot Coupled with Microcavity 5
1.2 A Comparison of Existing Quantum Dots 8
1.2.1 Self-Assembled Narrow Bandgap Quantum Dots 9
1.2.2 Site-Controlled Narrow Bandgap Quantum Dots 10
1.2.3 Self-Assembled Wide Bandgap Quantum Dots 11
1.2.4 Site-Controlled Wide Bandgap Quantum Dots 11
1.3 Thesis Overview 12

2 Fundamentals of Quantum Dot Physics and III-Nitride Semiconductors **15**

2.1 Fundamental Physics in Quantum Dots 15
2.1.1 Exciton and Quantum Confinement 15
2.1.2 Narrow Bandgap vs. Wide Bandgap Semiconductors 21
2.2 Material Properties of GaN 23
2.2.1 Band Structure of GaN 23
2.2.2 Band Structure Under Lateral Anisotropy 27
2.2.3 Strain and Stress 29
2.2.4 Deformation Potential 31
2.2.5 Spontaneous Polarization 32
2.2.6 Piezoelectric Polarization 33
2.2.7 Phonons 33

3 Fabrication and Characterization of InGaN/GaN Disk-in-Nanowires **35**

3.1 Device Structure and Fabrication 35

3.1.1 Optically Pumped Disk-in-Nanowires . . . 35
3.1.2 Electrically Pumped Disk-in-Nanowires . . . 36
3.2 Characterization Systems . . . 40
3.2.1 Photoluminescence Characterization . . . 40
3.2.2 Electroluminescence Characterization . . . 42

4 From Quantum Well to Quantum Dot: Effects of Diameter Reduction in InGaN/GaN Nanodisks . . . 44

4.1 Quantum-Well-Nanodisk vs. Quantum-Dot-Nanodisk . . . 44
4.2 Mechanical Properties in a Nanodisk . . . 47
4.3 Electrical Properties in a Nanodisk . . . 49
4.4 Optical Properties in a Nanodisk . . . 51
4.4.1 Absorption Efficiency . . . 52
4.4.2 Local Density of Photon States . . . 52
4.4.3 Collection Efficiency . . . 55
4.4.4 Oscillator Strength . . . 56
4.5 Conclusion . . . 60

5 Carrier Dynamics in InGaN/GaN Quantum Dots . . . 61

5.1 Principles of Carrier Dynamics . . . 61
5.2 The Lateral Potential Barrier Profile . . . 63
5.3 Decay Rates . . . 65
5.3.1 Radiative Decay Rate . . . 67
5.3.2 Tunnelling Decay Rate . . . 69
5.3.3 Thermal Decay Rate . . . 70
5.4 Conclusion . . . 70

6 Optical Properties of Single InGaN/GaN Quantum Dots . . . 72

6.1 Single Quantum Dot Optical Properties . . . 72
6.1.1 Photoluminescence Spectrum . . . 72
6.1.2 Linear Polarization of the Photoluminescence . . . 74
6.1.3 Second Order Correlation Function $g^{(2)}$ . . . 76
6.2 Inhomogeneities in PL properties . . . 81
6.3 Correlations among PL properties . . . 85
6.3.1 The Correlation between I and τ . . . 85
6.3.2 The Correlation between E and τ . . . 85
6.3.3 The Correlation between ΔE and τ . . . 85
6.3.4 The Correlation between $g_0^{(2)}$ and τ . . . 87
6.4 Temperature Dependence of $g_0^{(2)}$ . . . 89
6.5 Conclusion . . . 92

7 Electrically Driving and Controlling InGaN/GaN Quantum Dots . . . 93

7.1 Electrically Driven Single-Photon Emitting Diodes . . . 93
7.1.1 Electroluminescence and Single-Photon Emission . . . 93
7.1.2 Current-Voltage Characteristics . . . 95
7.2 Electrically Controlled Photoluminescence Properties . . . 99
7.2.1 Charge-Tunneling Diode . . . 99
7.2.2 A- and B-Excitons . . . 103
7.2.3 Fine Structures of Neutral and Charged Excitons . . . 103

8 Conclusions and Future Work 106
8.1 Conclusions 106
8.2 Future Work 107
8.2.1 Improve Quantum Dot Scalability 107
8.2.2 Integrated Systems Based on Our Quantum Dots 108
Bibliography 110

LIST OF FIGURES

1.1 (a) Self-assembled InAs/GaAs QDs by Stranski-Krastanov growth. (b) Site-controlled InAs/GaAs QDs grown on lithographically defined nanoholes [4]. 9
1.2 The structures of several site-controlled narrow bandgap QDs. (a) QDs etched from a single quantum well (QW). (b) QDs grown on patterned substrate. (c) QDs form at the apices of micropyramids. (d) QDs grown on oxide stress apertures. . . 10
1.3 Fabrication and structures of three types of site-controlled III-N QDs. (a) InGaN QD on GaN pyramid [5, 6, 7]. (b) GaN QD in GaN-core-AlN-shell nanowire [8]. (c) InGaN QD in GaN nanowire [9, 1]. 13

2.1 Illustration of the strong (a) and weak (b) confinement regimes. 16
2.2 QD oscillator strength f_{os} in the strong and weak confinement regimes. V is the volume of the QD. 20
2.3 Wurtzite and zinc-blende GaN crytal phases. (a) Wurtzite crystal. (b) Zinc-blende crystal. 24
2.4 Wurtzite GaN band structure. (a) Band structure. (b) Crystal field and spin-orbit splitting. Figure adopted from [10]. 25
2.5 Valence band dispersion of strained GaAs and GaN. Taken and modified from [169]. 27
2.6 Wurtzite GaN conduction band (CB) and valence band energy levels and optical transitions. (a) Isotropic shape and strain. The $|Z\rangle$ components in the valence bands are ignored. (b) Lateral anisotropic shape and strain. The $|Z\rangle$ components in the valence bands are ignored. The ellipticals at the bottom illustrate x-direction elongated shape. (c–d) Absorption spectrum for x- (blue, positive) and y- (red, negative) polarizations with isotropic, lateral anisotropic shape and strain, respectively. (e) Absorption spectrum when considering the electron-hole exchange interaction under lateral anisotropic shape and strain. (c–e) are inspired by [189]. . . 28
2.7 (a) Displacement vector. (b) Stress tensor. 30
2.8 Polarity and spontaneous polarization of GaN. (a) Ga-polar. (b) N-polar. 32
2.9 The theoretical phonon dispersion curve of GaN. Figure adopted from [11]. 34

3.1 Structure of optically pumped nanodisks (NDs). (a) The schematic plot of a single GaN nanopillar containing an InGaN nanodisk of diameter $D = 25$ nm. (b) The scanning electron microscope (SEM) image of a part of a dense arrays of QDs of diameter $D = 25$ nm and dot-to-dot separation 300 nm. The viewing angle is 45°. 36
3.2 Fabrication of optically pumped NDs. (a) Planar single $In_{0.15}Ga_{0.85}N$/GaN QW grown on c-plane sapphire. (b) Coat polymethyl methacrylat (PMMA) and electron-beam lithography. (c) Deposit nickel. (d) Nickel liftoff. (e) inductively-coupled plasma (ICP)-reactive-ion etching (RIE) etching. (f) Nickel removal. 37
3.3 The structure of electrically pumped disk-in-nanowires (DINs). (a) A bare DIN without electrical contacts. (b) A DIN with electrical contacts. 37

3.4 Fabrication flow of electrically pumped DINs. (a) Planar single InGaN/GaN QW light-emitting diode (LED) grown on the c-plane of a sapphire substrate by metalorganic chemical vapor deposition (MOCVD). (b) Fabricate cone-shaped DINs following the method in Fig. 3.2. (c) Cleave the slant sidewall using potassium hydroxide (KOH) solution. (d) Spin coat spin-on glass (SOG) and cure. (e) Pattern photoresist etching mask using optical lithography. (f) Wet etch SOG using buffered hydrofluoric acid (HF) to expose part of the GaN for n-contact. (g) Etch back SOG using CF_4-CHF_3 plasma RIE with careful SEM monitoring. (h) Deposit indium-tin-oxide (ITO) using sputtering. (i) Pattern photoresist etching mask using optical lithography. (j) Wet etch ITO using HCl:H2O (1:3). (k) Pattern photoresist etching mask using optical lithography. (l) Deposit Ti/Au contacts and liftoff in acetone. 38
3.5 The SEM images of (a) four DINs after KOH wet-etching, and (b) four DINs after SOG etch-back. All SEM images are 45°-view. 39
3.6 The experimental setup for photoluminescence (PL) characterization. 41
3.7 The experimental setup for direct current (DC) electroluminescence (EL) characterization. 42
3.8 The experimental setup for radio frequency (RF) EL characterization. 43

4.1 (a) The PL spectra from a QW-ND with a diameter of 2 μm (red lines) and a QD-ND with a diameter of 20 nm (blue lines) at excitation intensities $P = 0.4$, 1.4, 4 and 14 W/cm^2. The spectra are normalized to their maxima and vertically shifted to ease the comparison. The spectra of the QW-ND is broadened by optical-phonon replicas as illustrated in dashed green lines. (b) The TRPL decay traces of QW-ND (red) and QD-ND's X peak (blue) measured at $P = 10$ W/cm^2. (c) The mono-exponential decay time of the X peak of the QD-ND τ_X (blue square) and the decay time obtained from mono-exponential fit of the initial 12.5 ns decay trace of the QW-ND τ^*_{QW} (red triangle) at various excitation intensities. (d) The integrated PL intensity of the X (blue square) and XX (green circle) peaks from the QD-ND and the overall integrated PL intensity, including the optical-phonon replicas, from the QW-ND (red triangle). All the intensity values I are normalized by the lateral area of the InGaN layers and hence have a unit of count per second per nanometer square (c/s/nm^2). A linear fit of $log(I)$ vs. $log(P)$ shows that the intensities of the X and XX peaks of the QD-ND, and the spectrally integrated intensity of the QW-ND are proportional to $P^{1.12}$, $P^{2.07}$ and $P^{1.77}$, respectively. . . 45
4.2 Phenomenological strain relaxation model. (a) The schematic plot of the simple 1D theory described in the text. (b) The exciton potential profile at $P = 0.4$ W/cm^2 along the lateral direction in NDs with $D = 15, 20, 30, 50, 100, 400$ nm, plotted using the fitting results of Fig. 2(a), $E_0 = 2.92$ eV, $B_m(P = 0.4) = 303$ meV and $\kappa = 0.055$ nm^{-1}. 47

4.3 PL properties vs. ND diameter. (a) The PL energy E of single NDs vs. the diameter D of the ND at excitation intensity $P = 0.4$ W/cm^2 (blue square) and 14 W/cm^2 (green circle). The single NDs are randomly chosen and isolated using a confocal microscope setup. The ND diameter is the average diameter of the ND's containing array which has a 2 nm standard deviation. The data are fitted using Equ. 4.11 assuming the same E_0 and κ for both low- and high-P data, resulting in $E_0 = 2.92$ eV, $B_{m,low-P} = 303$ meV, $B_{m,high-P} = 19$ meV and $\kappa = 0.055$ nm^{-1}. (b) The time-resolved photoluminescence (TRPL) decay traces of four ensembles of NDs with diameters $D = 2$ μm (blue), 299 nm (green), 107 nm (red) and 18 nm (pink), respectively, at excitation intensity $P = 18$ W/cm^2. Each ensemble contains a 6×6 array of NDs. (c) The total decay rate $\gamma_{tot} = 1/\tau_{tot}$ of ND ensemble vs. ND diameter D at excitation intensities $P = 18$ W/cm^2 (green circle) and $P = 32$ W/cm^2 (red triangle). τ_{tot} is defined as the time taken for the PL intensity to decay from the maximum intensity to half maximum to avoid the complexity of stretched exponential decays. (d) The PL intensity per unit InGaN area of ND ensemble vs. ND diameter D at excitation intensities $P = 0.4$ W/cm^2 (blue square), $P = 18$ W/cm^2 (green circle) and $P = 32$ W/cm^2 (red triangle). 50

4.4 Absorption efficiency finite-difference time-domain (FDTD) simulation. (a) Schematic plot of the incidence of a plane wave to a InGaN ND in a GaN nanopillar. The propagation direction of the incident light is $\theta = 55°$ apart from the normal direction, z-axis. The polarization is along the y-axis. The nanopillar has a height of 120 nm and a sidewall angle of 75°. The center of the ND is 11.5 nm beneath the top cone surface. (b-d) xz-plane 2D cross section maps of $|\boldsymbol{E}(x, y, z)|^2$ for a 390 nm plane wave coupling to NDs of diameters $D = 10$ nm, 160 nm and 1000 nm, respectively. The white lines outline the nanopillar. 53

4.5 local density of photon states (LDPS) and collection efficiency FDTD simulation. (a) Schematic plot of the dipole in the nanopillar and the first-lens collection. (b) The definition of tangential dipole and radial dipole. (c-d) The F_p and η_{col} for tangential (left column) and radial (right column) dipoles at different radial positions r. Different line colors represents different ND diameters. 54

4.6 Conformal dielectric coating on small DINs improves F_p. (a) A schematic plot of conformal coating. (b) The F_p, η_{col} vs. the coating thickness t. 56

4.7 (a) FDTD simulation results: average absorption efficiency $\overline{\eta_{abs}}$ (dotted line), LDPS factor $\overline{F_p}$ (solid line) and collection efficiency $\overline{\eta_{col}}$ (dashed line) vs. ND diameter D. The $\overline{\eta_{abs}}$ curve is normalized to its value at $D = 2$ μm and, hence, only shows the relative trend; while the $\overline{F_p}$ and $\overline{\eta_{col}}$ curves are absolute values. (b-d) Average internal quantum efficiency (IQE) $\overline{\eta_{int}}$, radiative decay rate $\overline{\gamma_r}$ and oscillator strength $\overline{f_{os}}$ vs. D extracted from Fig. 4.1(c) and (d) using Equ. 4.19, 4.20 and 4.21, respectively. The vertical axes of all three figures have arbitrary units (a.u.). . 58

5.1 (a) Exciton decay model. A lateral potential profile is formed mainly due to the reduction in the piezoelectric field at the nanodisk sidewall. An exciton decays mainly through three channels: the radiative decay and the tunnelling and thermal surface nonradiative decay, whose decay rates are denoted as γ_{r}, γ_{tnl} and γ_{thm}, respectively. The latter two processes need to overcome the lateral potential barrier. (b) Biexciton decay model. The presence of another exciton lowers the potential barrier experienced by any of the two excitons due to the screening effect, leading to a lower biexciton QE compared to exciton QE. 62

5.2 QD ensemble PL and TRPL taken at excitation intensity $P = 1\ \mathrm{W/cm^2}$. (a) PL spectra of ensembles of QDs of diameter $D = 21$, 25 and 29 nm and a QW of diameter 5 μm at 10 K. The PL intensity is normalized by the area of the InGaN layer. The spectrum of QW is multiplied by a factor of 8 for better visibility. (b) The TRPL of ensembles of QDs of diameter $D = 21$, 25 and 29 nm at 10 K. (c) and (d) The PL spectra and TRPL of an ensemble of QDs of diameter $D = 29$ nm at temperature $T = 10$, 50 and 80 K. 64
5.3 (a) PL energy E vs. QD diameter D of nine dense arrays of QDs with diameters ranging from 19 nm to 33 nm and a 5 μm diameter QW taken at excitation intensity $P = 1\ \mathrm{W/cm^2}$. The inset is a zoomed-in version of the nine dense QD arrays. The solid line is a fitting curve based on Eq. (4.11). (b) The exciton potential profiles of QDs of diameter $D = 19$, 22, 25, 29, 33 and 600 nm calculated using Eq. (4.10). The inset is a zoomed-in version of the five smaller diameters. 65
5.4 (a) The total decay time τ (square, left axis) and PL intensity I (triangle, right axis) vs. QD diameter D dense arrays at 10 K. The $\tau(D)$ data is fitted using Eq. (5.4), yielding $\gamma_{\mathrm{r0}} = 59$ MHz and $c_1 = 15$ m/s. (b) The $I(T)$ data of four dense arrays with QD diameter $D = 22$ nm (blue square), 25 nm (red circle), 29 nm (green triangle), 33 nm (cyan star) nm, respectively. (c) The $\tau(T)$ data of the same four arrays described in (b), which are simultaneously fitted using Eq. (5.3), yielding $c_2 = 2 \times 10^{-3}$ and $c_3 = 0.33$, as shown by blue solid, red dash, green thick dash and cyan thick solid curves. The fitting took into account the instrument time-resolution of 0.2 ns (Sec. 3.2). 67
5.5 (a) The relative $\tau_{\mathrm{r}}(D)$ extracted from the $I(D)$ and $\tau(D)$ data in Fig. 5.4(a) using Eq. (5.5). $\tau_{\mathrm{r}}(D)$ is normalized to the average value (dashed line). (b) The $\tau_{\mathrm{r}}(T)$ relation of dense arrays with $D = 22$ nm (blue square), 25 nm (red circle), 29 nm (green triangle), 33 nm (cyan star) nm. Each τ_{r} data point is proportional to the ratio of the corresponding τ and I values in Figs. 5.4(c) and (b), respectively. All four sets of data are then fitted together using Eq. (5.6) with γ_{r0} and Δ being the fitting parameters, resulting in $\Delta = 8.6$ meV and an arbitrary γ_{r0} value. All data and the fitted curve (solid line) are scaled in the way that $\gamma_{\mathrm{r0}} = 59$ MHz, as obtained in Fig. 5.4(a). 68

6.1 10 K optical properties of a QD of $D = 29$ nm in diameter. (a) The PL spectra at excitation intensity $P = 6.37$ W/cm^2. The inset is a semi-logarithm plot of the same spectrum to emphasize the OP replicas. The two black vertical lines represent the spectral window for the $g^{(2)}$ measurement in Fig. **??**(a). (b) The PL intensity I vs. the excitation intensity P. A fit (solid line) of $\log(I)$ vs. $\log(P)$ shows that I has a linear dependence on P. (c) The time-resolved PL decay curve of the ZPL. A mono-exponential fit (white line) shows a 3.40 ns decay time. (d) Exciton emission intensity I vs. angular orientation (θ) of the linear polarizer. The data are fitted with the equation $acos^2(\theta + b) + c$ (solid line). The fitting results are $a = 0.832, b = 0°, c = 0.08$. The absolute value of the polarizer angle has no physical meaning and is offset so that $b = 0°$. 73
6.2 The origin of the linearly polarized exciton emission. (a) Wurzite GaN crystal structure. The z-axis is defined as the crystal growth direction (0001) or c-axis. The x- and y-axes are perpendicular to the z-axis. (b) and (c) Energy eigenstates without and with asymmetric lateral strains, respectively. 75

6.3 Single photon emission up to 90 K. All data are without any background subtraction. (a) 10 K $g^{(2)}$ data of the QD described in in Fig. 6.1. (b) 90 K $g^{(2)}$ data measured from another QD of $D = 29$ nm in diameter. The solid curves are the fitted $g^{(2)}$ function[24] showing $g^{(2)}(0) = 0.18$ for (a) and $g^{(2)}(0) = 0.38$ for (b), respectively. 76

6.4 Pulsed $g^{(2)}$ fitting theory. (a) Illustration of the pulse injection after which the QD has w_j probability to be in the $|j\rangle$ state and the following free evolution of all states given that the QD is initialized in the $|j\rangle$ state. In the pulse injection stage, the QD is initialized at state $|j\rangle$ with probability w_j governed by the Poisson distribution (dashed profile). The free evolution stage, in which the excitation is off, then starts with state $|j\rangle$ at $t = 0$. The probability of the QD being at $|i\rangle$ at time t is described by the $p_{ij}(t)$ in Equ. 6.4. Eventually at $t = \infty$ the QD will be in the $|0\rangle$ ground state if no excitation comes to reset the QD. Otherwise, the QD will go back to the pulse injection stage. (b) Illustration of the four $g^{(2)}$ integrands f_1, f_2, f_3, f_4 and how they make up the $g^{(2)}$ curve. Each integrand on the right-hand-side panel is obtained from the corresponding correlation of the two shaded areas in the left-hand-side panel except for $f_1(t)$ whose formation is described in Equ. 6.5. The $g^{(2)}(t)$ curve at the bottom is obtained by the summation of the four integrands and the replication using $g^{(2)}(t)|_{t=[k\Lambda,(k+1)\Lambda]} = g^{(2)}(t)|_{t=[\Lambda,2\Lambda]}, k = 1, 2, ...$, and $g^{(2)}(t) = g^{(2)}(-t)$. 78

6.5 (a) The PL spectra of D1 and D2 with peak energies at 2.96 eV and 2.88 eV, integrated intensities of 3.7 kcps and 5.8 kcps, and ZPB FWHM of 15 meV and 35 meV, respectively. (b) The TRPL decay curves of D1 and D2 with decay times of 3.4 ns and 16.2 ns, respectively. (c) and (d) are the $g^{(2)}$ functions of D1 and D2 measured with the excitation intensity $P = 204$ W/cm^2 (0.4 photons per pulse) and $P = 76$ W/cm^2 (0.14 photons per pulse), respectively. The spectral filter window used in our second-order correlation measurements in this work are always adjusted to include the entire ZPB. 82

6.6 The statistical distributions of (a) the PL energy E, (b) the PL intensity I, (c) the FWHM ΔE of the ZPB and (d) the PL decay time τ of 30 QDs randomly chosen from the same array of diameter $D = 29$ nm. All data were taken at 10 K. The PL intensity unit kcps stands for kilo-count per second recorded by the end detector. . 83

6.7 Statistical correlations among PL energy E, intensity I, decay time τ and the FWHM ΔE of the ZPB taken from 30 QDs randomly chosen from the same array of dot diameter $D = 29$ nm. All data are taken at 10 K. (a) The I-τ correlation. Each data point represents the data from one QD. The solid line is a linear fit showing an excellent linearity between I and τ. (b) The E-τ correlation. The solid line is the theoretical curve obtained by sweeping the ϕ_B value as described in Sec. 6.3.1. (c) The ΔE-τ correlation. The solid line is a fitting using Equ. 6.6. . 86

6.8 (a) The $g_0^{(2)}$ vs. decay time τ data of 16 randomly chosen QDs of diameter $D = 29$ nm. The solid line is obtained by sweeping the value of ϕ_B as explained in Sec. 6.3.4. (b) An illustration of the different physics in the three regions described in Sec. 6.3.4. The solid arrows represent dominant decay channels, whereas the dashed arrows represent less dominant channels. 89

6.9 (a) The PL spectra of a QD of $D = 29$ nm at $P = 100$ W/cm^2, $T = 10$ K (blue); $P = 100$ W/cm^2, $T = 80$ K (red); and $P = 25$ W/cm^2, $T = 10$ K (green). (b-d) The scattered data points form the measured $g^{(2)}(t)$ of the QD at 10, 50 and 80 K, respectively, at $P = 100$ W/cm^2. All data are without background subtraction. The solid lines are the fitting curves obtained from the method developed in [**?**] (also briefly described in Sec. **??**). Each fitting returns the biexciton-to-exciton QE ratio $\eta_{\mathrm{XX}}/\eta_{\mathrm{X}}$, exciton total decay time τ_{X} and $g_0^{(2)}$. The fitted $g_0^{(2)}$ values are shown next to the central $g^{(2)}$ peaks (dips). 90
6.10 The blue squares in (a) and (b) are the $g_0^{(2)}$ and τ_{X} extracted from the $g^{(2)}(t)$ data of the QD at 10, 30, 50, 80 and 90 K, three of which are shown in Fig. 6.9(b-d). The red lines are the theoretical curves based on the ϕ_B and B_{XX} values extracted from Fig. 6.9(a) as described in the text. The inset in (a) is an extension of the theoretical $g_0^{(2)}(T)$ curve to 300 K. 91

7.1 EL properties at 10 K. (a) The integrated EL intensities of the DIN vs. applied bias. (b) The EL spectra of the QD at various bias voltages. All spectra are normalized to their maximum intensity and shifted vertically for comparison. (c) The EL intensity vs. angle of the polarization selection at 5.7 V forward bias. The solid line is a fitting curve. (d) The $g^{(2)}(t)$ of the DIN EL at 5.7 V forward bias without background subtraction. The solid line is a fitting curve. 94
7.2 The current-voltage (I-V) characteristic of the DIN at 10 K. The upper-left inset is the semi-log of the I-V curve. The lower-right inset illustrates the effective circuit in which the pin-junction and the ITO/p-GaN Schottky contact are connected in series. 95
7.3 PL properties at 10 K. (a) The PL spectra of the DIN at several applied voltages. (b) The PL peak energy vs. the applied voltage. 97
7.4 Schematic band diagrams of the DIN at $V_{bias} = 0$ V (upper panel), $0 < V_{bias} < 2$ V (middle panel) and $V_{bias} > 2$ V (lower panel). 98
7.5 Sample structure and band profiles. (a) 45°-angle SEM image of four nanowire diodes without SOG and contacts. (b) Schematic cross-section view of a single InGaN/GaN DIN diode, including the ITO/Ti/Au p-contact, SOG insulating layer and Ti/Au n-contact. (c) Working principle of the charge-tunneling diode. (d) The conduction band (CB) and valence band (VB) profile along the growth direction (z). (e) The intrinsic (i) section of (d). 100
7.6 Voltage-dependent μ-PL spectra form two QDs, QD1 (a-c) and QD2 (d-f). (a) and (d) show spectra at voltages indicated by the dashed lines in (b) and (e), respectively. (c) and (f) shows the PL energy of various neutral and excitons as functions of voltage extracted from (b) and (e), respectively. Voltages are corrected from the laser induced photo-voltage. 102
7.7 A-B exciton splitting in QD1. (a) PL spectra of -0.04 V corrected voltage at 90° (solid line) and 0°, respectively. (b) Intensity of X_{A}^{0} and X_{B}^{0} at -0.04 V corrected voltage and at various excitation densities. 104
7.8 Fine-structures of X_{A}^{0} and X_{A}^{1-} in QD2. (a) Illustration of the optical transitions of X_{A}^{0}, X_{A}^{1-}, X_{B}^{0} and X_{B}^{1-} and their fine-structures. (b) X_{A}^{0} (0 V) and X_{A}^{1-} (0.5 V) spectra at 90° (solid lines) and 0° (dashed lines). The inset contains the same spectra but normalized to their respective maximum in order to show the fine-structure splitting of X_{A}^{0}. (c) and (d) show the polarization-dependent emission energy (dot) and intensity (square) of X_{A}^{1-} and X_{A}^{0}, respectively. 105

LIST OF TABLES

2.1 Comparison between the lattice constants and the bandgap of common semiconductors. 21
2.2 The bandgap E_g, electron effective mass m_e, exciton binding energy E_B and exciton Bohr radius a_B of several semiconductors. 22
2.3 Elasticity, spontaneous polarization and piezoelectric polarization constants for nitride semiconductors. All values are for Ga/Al/In-polar crystals. Data taken from [12]. 31

5.1 Summary of parameters of the exciton dynamics model extracted from the QD-array data in Secs. 5.2 and 5.3. The uncertainty of each value represents the 95 % confidence interval of the corresponding fitting. 71

6.1 The contributions of the thickness l, indium fraction x and diameter D fluctuations to the total PL energy E inhomogeneity ΔE for a circular $\mathrm{In}_{x=0.15}\mathrm{Ga}_{0.85}\mathrm{N}$ nanodisk with $l = 3$ nm and $D = 29$ nm. ΔE is calculated from each contribution as $\Delta E = \sqrt{\Delta E_l^2 + \Delta E_x^2 + \Delta E_D^2}$. 82

LIST OF ABBREVIATIONS

QD quantum dot

QW quantum well

LED light-emitting diode

ND nanodisk

DIN disk-in-nanowire

PL photoluminescence

TRPL time-resolved photoluminescence

TIPL time-integrated photoluminescence

TREL time-resolved electroluminescence

TIEL time-integrated electroluminescence

EL electroluminescence

OP optical phonon

AP acoustic phonon

SEM scanning electron microscope

HBT Hanbury Brown-Twiss

TCSPC time-correlated single-photon counting

FDTD finite-difference time-domain

TC time correlator

APD avalanche photodiode

PIN p-i-n photodiode

CCD charge-coupled device

NA numerical aperture

QE quantum efficiency

IQE internal quantum efficiency

PMMA polymethyl methacrylat

ICP inductively-coupled plasma

RIE reactive-ion etching

ML monolayer

uid-GaN unintentionally doped GaN

RPM round per minutes

MIBK methyl isobutyl ketone

IPA isopropyl alcohol

KOH potassium hydroxide

FWHM full width at half maximum

ITO indium-tin-oxide

SOG spin-on glass

MOCVD metalorganic chemical vapor deposition

HF hydrofluoric acid

DC direct current

RF radio frequency

SMU source measurement unit

DIP dual in-line package

IV current-voltage

QCSE quantum-confined Stark effect

LDPS local density of photon states

ZPL zero-phonon line

ZPB zero-phonon band

EHP electron-hole pair

ABSTRACT

Quantum technologies such as quantum communication and computation may one day revolutionize the landscape of communication and computing industry, which so far has been largely based on the classical manipulation of the flow of many photons and electrons. Many important quantum technologies have been demonstrated on single atoms which have discrete energy levels and can interact strongly with light, both functionalities are key to quantum technologies. However, single atoms are difficult to integrate with other photonic and electronic components, which are equally crucial to most of the applications.

Semiconductor quantum dots are considered as the key building block to scalable quantum technologies due to their atom-like functionality and solid-state integrability. To date, many proof-of-principle integrated quantum devices have been demonstrated based on single quantum dots. However, most of the devices were not suitable for large-scale practical applications mainly due to the adoption of self-assembled III-As quantum dots, which form at random sites and operate only at liquid-helium temperatures. These drawbacks may be resolved by using III-N quantum dots with controlled forming site and optical properties, and high operating temperatures.

This thesis studies site-controlled InGaN/GaN quantum dots fabricated by top-down etching a planar single quantum well. Compared to other existing site-controlled III-N quantum dots, ours have the following advantages: 1) the fabrication approach allows flexible control of the emission energy, oscillator strength and polarization of each quantum dot; 2) their emission is free from wetting layer contamination leading to purer single-photon emission; 3) they can be efficiently driven by electrical current.

We demonstrate in this thesis that these quantum dots have all the essential properties required for most quantum technologies. They are efficient light emitters due

to the strain relaxation that enhances the radiative recombination and limits the non-radiative surface recombination. They have discrete energy levels due to the strong exciton-exciton interaction by the small lateral size, manifested by both optically and electrically driven single-photon sources using our quantum dots. Finally, the net charges in each quantum dot can be controlled electrically via Coulomb blockade, which enables the understanding of exciton charging and fine structures crucial to many quantum technologies.

CHAPTER 1

Introduction

Semiconductor QDs are nanostructures whose sizes are about the De Broglie wavelengths of the electrons and holes in the system. A QD typically contains a QD region made of narrower bandgap materials and surrounding barrier regions made of wider bandgap materials or air. Because of the band offset between the QD and barrier, carriers are three-dimensionally confined, leading to localized electron and hole wavefunctions as well as discrete energy levels. These features closely resemble those of a single atom. Therefore, QDs are often also referred as artificial atoms, despite that they typically contain hundreds and thousands of atoms.

QDs are key to the scalable realization of many quantum technologies such as quantum communication and computation. This is because they possess atom-like functionalities, such as discrete energy levels and strong light-coupling strength, and can be integrated with other solid-state photonic and electronic components, such as photonic-crystal microcavities and pn-junctions.

To date, many milestone applications have been demonstrated using self-assembled III-As QDs, such as single-photon source, entangled-photon source, and single-electron spin qubit. In some cases, even the integration of these QDs with other solid-state components have been realized. However, this type of integrations cannot be applied to large-scale practical applications due to QDs' random forming sites, typically come with large property inhomogeneity, and extremely low operating temperatures, typically require liquid-helium cooling.

To overcome these issues, site-controlled III-N QDs are actively pursued. Their controlled forming sites allow scalable integration with other solid-state components. III-N QDs have demonstrated high operating temperatures due to their wide bandgaps. Materials with wide bandgaps typically have large exciton binding energies and allows greater bandgap offset between QD and barrier, both contributing to their high operating temperatures. III-N semiconductors are particular of interest because of their wide applications in blue LEDs and lasers and mature p-type doping technology which is unpaired by other wide bandgap materials. The electrical driving capability is always desired for ultimate scalability.

This thesis focuses on the properties and applications of site-controlled InGaN/GaN QD. As the introduction chapter, we will first list several important applications of single QDs in general and explain why site-controlled wide bandgap QDs are particularly important for realizing

scalable devices. We will then compare four major categories of existing QDs based on their operating temperature and integrability to show the significance of our QDs.

1.1 Applications of Single Quantum Dots

To date, many of the atom-like quantum functionalities have been demonstrated on single epitaxial QDs, such as bright and efficient single-photon sources [13, 14, 15], polarization-entangled single-photon-pair sources [16, 17, 18], QD spin qubit [19], and coupling between single QDs and photonic microcavity [20, 21, 22, 23]. These seminal works have demonstrated the great potentials of QDs and inspired tremendous amount of research on epitaxial QD-based quantum devices. In this section, we will briefly introduce some of the most important applications of single QDs and show how many of these applications require or will benefit from site-controlled wide bandgap QDs

1.1.1 Non-Classical Light Sources

1.1.1.1 Single Photon Generation

An ideal single-photon source is a light source that generates one and only one photon with desired properties (wavelength, polarization, etc.) after each trigger event. Single-photon sources have a wide range of applications, including quantum communication [24], quantum information processing [25, 26], precision measurement [27, 28], and random number generation [29]. Among these applications, quantum communication have been one of the strongest motivations for the development of single-photon sources.

The idea of using single-photons as information carrier for secure communication stems from the seminal work of Charles Bennett and Gilles Brassard in 1984 [24]. The BB84 quantum key distribution protocol utilizes the quantum non-clone theorem [30] of a single photon. To illustrate this, let us assume Alice and Bob communicate a stream of binary code (0, 1, 1, 0, 1, ...) using linearly polarized single-photons whose polarization directions are vertical (0°), horizontal (90°) or $\pm 45^\circ$. Alice randomly chooses 0° or 90° to represent 1, and randomly chooses $+45^\circ$ or -45° to represent 0. To eavesdrop Alice and Bob's communication without being detected, Eve needs to somehow steal a photon from the communication channel and measure the state of this photon and send an identical copy back into the channel. However, the uncertainty principle of quantum mechanics dictates that Eve can neither deterministically measure the polarization direction of a photon without any pre-knowledge about the polarization nor make a copy of the photon. Therefore, any eavesdropping attempts will be detected by Alice and Bob.

However, to date, due to the lack of efficient and low cost single-photon sources, most quantum key distribution systems are based on attenuated classical light sources such as lasers. Classical light sources are fundamentally different from single-photon sources in their photon

number statistics, i.e. the number of photons after each trigger event obeys Poisson statistics. To reduce the probability of multi-photon generation, lasers have to be attenuated to a degree that most of the time no photons are generated at all. This severely limits the communication bit rates. Therefore, efficient and practical single-photon sources are still widely sought-after for realizing high performance quantum communication systems.

Like several other quantum emitters, such as single atoms [31], organic molecules [32], solid-state defects [33, 34, 35] and colloidal QDs [36], epitaxial QDs can also be used as single-photon source [37]. The operation principle of these quantum-emitter-based single-photon source lies in their discrete atom-like energy levels. In an epitaxial QD, the energy level discretization is typically due to two reasons. For a QD in the strong confinement regime, electron and hole levels are discretized separately by the small QD volume and transitions occur among certain levels. For a QD in the weak confinement regime, discrete energy levels are due to interaction among excitons in the QD [37, 1]. After each trigger pulse, multiple excitons may be generated in a QD, but the transition energy from biexciton to exciton is different from the transition energy from exciton to ground state due to exciton-exciton interaction. This allows the spectral isolation of only one photon after each trigger pulse. The QD spatial confinement only has indirect contribution to the discrete energy levels through enhancing the exciton-exciton interaction.

To date, despite numerous progresses, practical single-photon sources are still unavailable due to at least one of the following problems: low generation efficiency, low collection efficiencies, low operating temperature and low scalability. The first and third problems are related: high temperatures tends reduce the quantum efficiency by enhancing nonradiative carrier recombination or suppressing radiative recombination. The second and fourth problems are related: high collection efficiency requires controlling the photon emission direction and pattern which is usually realized by integrating quantum emitters with other photonic components such as waveguides [13] and cavities [38, 14, 15]. Taking all these requirements into consideration, epitaxial QDs are the most promising candidates for practical single-photon sources. High operating temperature can be achieved using wide-bandgap, such as III-nitride [39, 40] and II-VI [41], semiconductors. High scalability with other photonic components can be achieved using site-controlled QDs [42, 43, 4, 44, 45, 46, 47, 48, 49, 50, 51, 5, 6, 7, 8, 9, 1].

1.1.1.2 Entangled Photon Generation

Entanglement is a non-local quantum correlation between two or more particles. A famous example of entanglement is a pair of photons, photon 1 and 2, in one of the so-called Bell states:

$$|\psi^{\pm}_{\text{Bell}}\rangle = \frac{1}{\sqrt{2}}\left(|H\rangle_1|H\rangle_2 \pm |V\rangle_1|V\rangle_2\right), \tag{1.1}$$

$$|\phi^{\pm}_{\text{Bell}}\rangle = \frac{1}{\sqrt{2}}\left(|H\rangle_1|V\rangle_2 \pm |V\rangle_1|H\rangle_2\right), \tag{1.2}$$

in which $|H\rangle$ and $|V\rangle$ represent horizontal and vertical polarization, respectively. Entangled-photon-pair states cannot be separated into the direct product of two photons' states. Like single-photon sources, entangled-photon sources are also the key element for many quantum communication and computation applications. To date, entangled-photon sources have been demonstrated on atoms, non-linear crystals and epitaxial QDs. Again, epitaxial QDs have the unique advantage of being compatible with existing semiconductor technology.

There are two major methods of obtaining entangled-photons from a QD, indirect generation through indistinguishable single-photons and direct generation from biexciton and exciton transitions. The indirect method [52, 53] uses two sequentially triggered polarized single-photons from a QD. For simplicity of discussion, let us assume that these two photons are indistinguishable, that is, they have exactly the same wavelength, polarization and temporal profile. One photon's polarization is rotated by 90°. This photon $|H\rangle$ is delayed by the triggering period and then sent to one port of a non-polarizing beamsplitter together with the other photon $|V\rangle$ being sent to the second port. The output of the beamsplitter can be written as the direct product of two photon states:

$$\begin{aligned} |\psi\rangle_{\text{out}} &= \frac{1}{\sqrt{2}}(|H\rangle_1 + i|H\rangle_2) \otimes \frac{1}{\sqrt{2}}(-i|V\rangle_1 + |V\rangle_2) \\ &= \frac{1}{2}(|H\rangle_1|V\rangle_2 + |H\rangle_2|V\rangle_1 + i|H\rangle_2|V\rangle_2 - i|H\rangle_1|V\rangle_1), \end{aligned} \tag{1.3}$$

where 1 and 3 denotes the two output ports. The entangled-photon pair $|\phi^+_{\text{Bell}}\rangle$ can be post-selected by simultaneously detecting a photon at both output ports. This method however can at most generate entangled-photons 50% of the time.

The direct generation method utilizes the two-fold degeneracy of QD bright excitons and the difference in exciton and biexciton transition energies. When one (two) electron-hole pair(s) occupy an QD, the QD is in the exciton $|\text{X}\rangle$ (biexciton $|\text{XX}\rangle$) state. The biexciton transition energy E_{XX} is different from the exciton transition energy E_{X} due to the Coulomb and exchange interactions between two excitons. The angular momentum for $|\text{XX}\rangle$ is 0, for bright excitons are -1 or 1, and for the ground state is 0. Selection rule dictates that there are only two possible paths for the $|\text{XX}\rangle \rightarrow |\text{X}\rangle \rightarrow |0\rangle$ cascade transition and the resulting photon pair is in the following entangled state:

$$\frac{1}{\sqrt{2}}(|\sigma^-_{\text{XX}}\rangle|\sigma^+_{\text{X}}\rangle + |\sigma^+_{\text{XX}}\rangle|\sigma^-_{\text{X}}\rangle), \tag{1.4}$$

in which $|\sigma^+\rangle$ and $|\sigma^-\rangle$ are left and right circularly polarized states, respectively. The challenge of this approach is to eliminate the fine-structure splitting between the two bright exciton states, which commonly exists in epitaxial QDs due to shape or strain anisotropy. This can be achieved by tuning the fine-structure splitting using external fields [16, 54] or grow QDs along certain highly symmetrical crystal orientation [55, 18].

Similar to single-photon sources, entangled-photon sources with high operating temperature and device scalability are not available but highly desired.

1.1.2 Quantum Dot Spin Qubit

Quantum computer has the capability of performing certain important tasks much faster than classical computers, such as factoring, searching and quantum simulation. The fundamental building block of quantum computer is qubit. A qubit is a bit of information that contains the arbitrary quantum superposition of orthogonal states $|1\rangle$ and $|0\rangle$. Qubit is to quantum computer as classical bit to classical computer. Many physical systems have been proposed for universal quantum computing including semiconductor QDs [56, 57]. A single exciton [19] or eletron (hole) in a QD can be used as a qubit. The latter has an advantage that their coherence lifetime of milliseconds [58, 59] is much longer than the nanosecond lifetime of typical QD exciton.

The realization of a universal quantum computer requires not only the initialization, manipulation and readout of a single qubit, but also the entanglement operations (closely related to C-NOT gate [26]) of multiple qubits. The electron spin qubits is described by the superposition of the two Pauli eigenstates $|\uparrow\rangle$ and $|\downarrow\rangle$. To date, the initialization [60, 61, 62], manipulation [63, 64, 65] and readout [66, 67] of a single QD spin qubit have been demonstrated. However, the coherent coupling between multiple qubits remains challenging. To realize multi-qubit gates, two major approaches are being taken, coupling two qubits through photonic microcavity [68, 69, 70] and coupling through tunneling between two neighboring QDs [71]. Clearly, both approaches can benefit greatly from site- and property-controlled QDs.

1.1.3 Quantum Dot Coupled with Microcavity

When a QD is coupled to a microcavity, photons are passed back and forth between the QD and the microcavity. Depending on how fast the energy feedback, characterized by the coupling strength g, is compared to the energy loss in the system, characterized by the loss rate γ and κ, the coupling can be roughly divided into two regimes. When $g \gg \gamma, \kappa$, the system is in the strong coupling regime; when $g \ll \gamma, \kappa$, the system is in the weak coupling regime. Both regimes have interesting physics and bear many potential applications.

1.1.3.1 Semiconductor Microcavity

Microcavities confines photons in a finite space by reflecting photon back when the photon reaches cavity boundaries. The microcavities deployed for coupling with QDs provide reflective confinement through mainly photonic bandgap or internal refraction or both. Photonic bandgap can be created by periodic modulation of the material dielectric constant to form the so-called photonic crystals [72]. This is similar to the electronic bandgap created in semiconductor due to the periodic lattice potential [73]. Photons with energy in this bandgap cannot propagate through the photonic crystal.

An example of 1D photonic crystal is distributed Bragg reflector which contains alternating high and low dielectric layers each with quarter-wavelength optical thickness. A distributed Bragg reflector has a broad high reflectivity band, corresponding to the bandgap of photonic

crystal. Using two distributed reflectors as the top and bottom mirrors, a vertical direction 1D cavity is realized. If one etch down this vertical cavity into pillars of diameters comparable to the wavelength, a 3D microcavity is formed whose sidewalls confine photon through internal refraction. Other widely used photonic microcavities include microdisk, microtoroid, microsphere all completely relying on internal refraction, 3D photonic crystal microcavities completely relying on photonic bandgap, and 2D membrane photonic crystal cavities that utilize both photonic bandgap and internal refraction.

The performance of a microcavity is characterized by its quality factor, or Q-factor, defined as the ratio of the total energy stored in the cavity and the energy loss per optical cycle λ/c (mainly through the mirror loss). Obviously, when all other parameters are fixed, Q-factor increases as the volume V of the cavity increase as it stores more energy while dissipates the same amount at the mirror per optical cycle. Therefore, the quality of a cavity is also often characterized by an alternative quantity, finesse, defined as $f = Q/V$.

1.1.3.2 Weak Coupling

In the weak coupling regime, the decay of the QD is irreversible, the microcavity mainly alters the radiative lifetime of the QD. If the spatial and spectral matching between the QD and the cavity are perfect, the radiative decay rate will be enhanced by a Purcell factor:

$$F_{\mathrm{p}} = \frac{3}{4\pi^2}\frac{\lambda^3}{n^3}\frac{Q}{V}, \tag{1.5}$$

in which λ is the QD emission wavelength, n is the refractive index of the QD surrounding medium, Q is the cavity Q-factor, and V is the cavity volume. Purcell factor is the ratio between the cavity density of state $d_{\mathrm{cav}} = 1/(\Delta\nu V)$ and the free space density of state $d_0 = 8\pi n^3\nu^3/c^3$, considering that $Q = \nu/\Delta\nu$. In practice, however, the matching between the QD and the cavity is imperfect, leading to the corrected enhancement factor [74]

$$F = F_{\mathrm{p}}\left(\frac{\boldsymbol{E}(\boldsymbol{r}_{\mathrm{QD}})\cdot\boldsymbol{\mu}}{|\boldsymbol{E}_{\mathrm{max}}||\boldsymbol{\mu}|}\right)^2 \frac{1}{1+4Q^2\left(\frac{\lambda}{\lambda_{\mathrm{cav}}}-1\right)^2}, \tag{1.6}$$

in which $\boldsymbol{E}(\boldsymbol{r})$ is the electrical field spatial profile in the cavity, $\boldsymbol{r}_{\mathrm{QD}}$ is the position of the QD, $\boldsymbol{\mu}$ is the QD dipole moment, λ_{cav} is the cavity mode wavelength. This equation shows that in order to reach the maximum enhancement, the QD needs to be placed where the electrical field intensity is maximal, the QD emission polarization and energy need to match with the cavity as well. On the other hand, severe mismatch can leads to suppression or even prohibition of QD radiation.

Purcell enhancement of the radiative lifetime is a powerful tool for producing fast, bright and indistinguishable single-photons. The shortened radiative lifetime allows higher photon generation rate, or bit rate. The enhanced radiative decay also reduces the probability for non-

radiative decay and, hence, increases the quantum efficiency. In addition, Purcell enhancement allows the photon to have a temporal width less than the decoherence time of the QD[75, 14], making them indistinguishable from each other. Indistinguishable single-photon sources are useful not only in generating entangled photons [52, 53] as we mentioned earlier, but also in quantum teleportation [30] and linear optics quantum computation [76].

1.1.3.3 Strong Coupling

In the strong coupling regime, the energy transfer between the QD and microcavity is reversible, that is, photons are passed between the QD and microcavity many times before they dissipate away. The system Hamiltonian is written as [77]:

$$H = \frac{\hbar\omega_{\text{ab}}}{2}\sigma_z + \hbar\omega_{\text{cav}}a^+a + \hbar g(\sigma_+ a + a^+\sigma_-) \tag{1.7}$$

in which $\hbar\omega_{\text{ab}}$ is the QD transition energy from excited state $|a\rangle$ to ground state $|b\rangle$, σ_z and $\sigma_\pm$ are Pauli z and ladder matrices, $a^\pm$ are the creation and annihilation operators for photon. If we restrict ourselves to the basis $\{|a,n\rangle, |b,n+1\rangle\}$ that contains $n+1$ excitations, we can write the Hamiltonian as:

$$H_n = \hbar\omega\left(n+\frac{1}{2}\right)\begin{pmatrix}1 & 0\\ 0 & 1\end{pmatrix} + \frac{\hbar}{2}\begin{pmatrix}\delta & 2g\sqrt{n+1}\\ 2g\sqrt{n+1} & -\delta\end{pmatrix}, \tag{1.8}$$

where $\delta = \omega_{\text{ab}} - \omega$ is the QD-cavity detuning. Obviously, $|a,n\rangle$ and $|b,n+1\rangle$ are no longer good eigenstates for such coupled system. Instead, the Hamiltonian needs to be re-diagonalized resulting in two QD-photon dressed states with energies

$$E_{n+} = \hbar\omega\left(n+\frac{1}{2}\right) + \frac{\hbar}{2}R_n, \tag{1.9}$$

$$E_{n-} = \hbar\omega\left(n+\frac{1}{2}\right) - \frac{\hbar}{2}R_n, \tag{1.10}$$

where $R_n = \sqrt{\delta^2 + 4g^2(n+1)}$ is the Rabi splitting. Similar to the Prucell factor F_{p} in weak coupling regime, the coupling coefficient g also depends on the dipole moment $\boldsymbol{\mu}$ of the QD, spatial alignment between QD and cavity mode maximum, and polarization alignment between $\boldsymbol{\mu}$ and $\boldsymbol{E}$.

Note that strong coupling induced Rabi splitting is not unique in single-atom-cavity or single-QD-cavity systems. In fact, similar physics has been observed in mesoscopic systems such as atomic-ensemble-cavity and quantum-well-cavity systems, which has yielded rich polariton physics. What makes single-atom/QD-cavity system unique is that they bring optical non-linearity to single-photon or few-photon level as shown by the n-dependent Rabi splitting R_n expression. For example, it has been shown that a few photons can drastically alter the transmission spectrum of a cavity [78, 79, 80]. This giant non-linearity at single-photon level is

important for numerous applications, including ultra-low power optical switch [81], quantum logic gate [82], single-photon detection [83], coherent transfer of QD state to photon state [84].

To date, nearly all strong-coupled QD-cavity systems [85, 22, 23] are based on low bandgap III-As QDs which usually have very small dipole moment. To enable the observation of strong coupling, large QDs are typically used. As we have shown earlier, for QDs in the weak confinement regime, their oscillator strength f_{os} scale linearly with QD size. Even so, the Rabi splitting remains small (~ 0.1 nm). This imposes very high requirements on the quality of the cavity as well as the operating temperature of these devices, as the spectral linewidths of the cavity and the QD must not exceed the Rabi splitting.

An alternative way is to use QDs made of wide-bandgap semiconductors which naturally possess large exciton oscillator strength due to the small exciton Bohr radius, as we explained in Sec. 2.1.1.2. Also the high operating temperature of these QDs could enable more practical devices. Indeed, using wide-bandgap semiconductor such as GaN as the active medium for strong coupling phenomena has shown great success in mesoscopic structures and has enabled ultralow threshold room temperature polariton laser [86, 87], etc. We have many reasons to believe that using wide bandgap QD will also have great successes in smaller devices. Of course, once more, wide bandgap site-controlled QDs will be a very good candidate that can offer both high performance and high scalability.

1.2 A Comparison of Existing Quantum Dots

Many applications shown in the previous section requires or will benefit greatly from the integration of single QD with other electronic or photonic components. However, most of the demonstrations so far are based on self-assembled QDs whose spatial and spectral properties are mostly random. Therefore, the spatial and spectral matching between the QD and the photonic structures, have been largely hit-and-miss processes, severely hindering the scalability.

Another obstacle that hinders scalable applications of the demonstrated devices is the low operating temperatures of the III-As/P QDs. QDs made of narrow bandgap materials, such as III-As and III-P semiconductors, typically have small QD-barrier bandgap offsets and small exciton binding energies as explained in Sec. 2.1.2. As a result, they require cryogenic operating temperatures to maintain the three-dimensional confinement and the exciton phenomenon.

In light of the above challenges in scalability, QDs with controlled spatial and spectral properties and high operating temperatures are desired. To improve the spatial and spectral control, various methods have been developed to achieve site- and property-controlled QDs using traditional narrow bandgap semiconductors. To improve the operating temperature, QDs based on wide bandgap II-VI and III-N semiconductors have been developed. Very recently, as the technology in the growth and nano-processing of wide bandgap materials becomes mature, we start to see fast development in QDs that have both high operating temperatures and high spatial and spectral controllability. In the following we provide a brief comparison among these

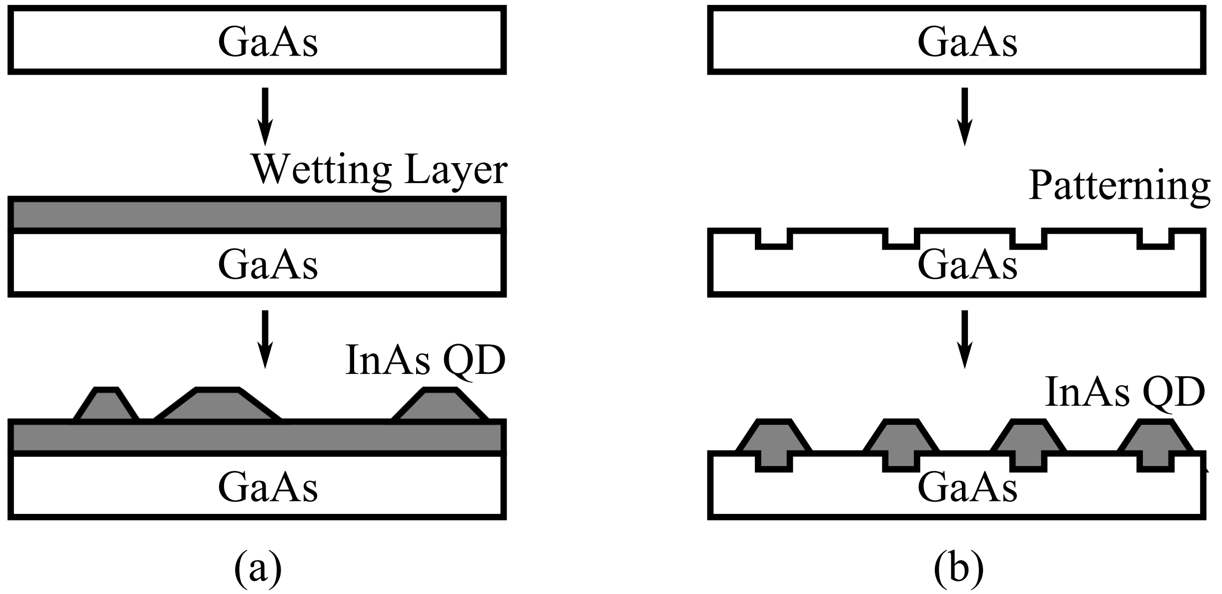

Figure 1.1: (a) Self-assembled InAs/GaAs QDs by Stranski-Krastanov growth. (b) Site-controlled InAs/GaAs QDs grown on lithographically defined nanoholes [4].

four categories of QDs.

1.2.1 Self-Assembled Narrow Bandgap Quantum Dots

Self-assembled QDs based on narrow bandgap semiconductors such as III-As and III-P are probably the most studied epitaxial QDs. The past three decades of research and development have accumulated an in-depth understanding of their growth mechanisms and physical properties as well as a series of mature nano-processing techniques. These combined with the highly matured III-As and III-P photonic device technology has led to the demonstration of numerous quantum photonic applications.

The formation of self-assembled QDs typically utilizes so-called Stranski-Krastanov epitaxial growth (Fig. 1.1(a)), during which 3D islands of nanometer sizes forms on top of a thin 2D wetting layer. Taking the InAs/GaAs QDs for example, the growth of InAs epitaxial layer starts in a 2D mode until about 1.7 monolayers (MLs) [88], after which 3D InAs islands of a few nanometers in height and tens of nanometers in diameter form on the surface. If the growth stops before the islands reach a size that leads to strain relaxation and dislocation formation, the islands are coherently formed and dislocation-free [89]. The islands are then covered by GaAs to terminate the exposed surfaces.

Coherently self-assembled QDs have superior optical properties compared to those with interfacial or surface defects [90]. Narrow sub-meV linewidths have been observed as the charge-trapping defects are eliminated, which would otherwise cause linewidth broadening through the Stark effect. QDs free from nonradiative processes are also demonstrated which is important for high efficiency light sources.

Despite the high optical quality of self-assembled QDs, they suffer from random forming

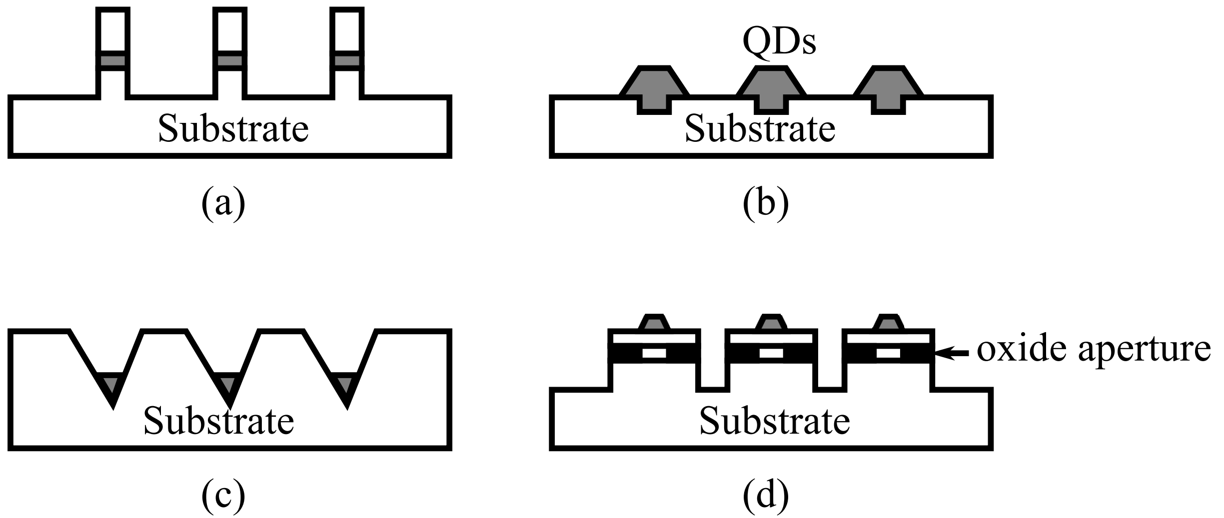

Figure 1.2: The structures of several site-controlled narrow bandgap QDs. (a) QDs etched from a single QW. (b) QDs grown on patterned substrate. (c) QDs form at the apices of micropyramids. (d) QDs grown on oxide stress apertures.

location and large dispersion in QD properties. This severely limits scalable integration of these QDs with other photonic components which is the key advantage of epitaxial QDs compared to other light-emitters such as single atom, single molecule, colloidal QD, and solid-state defects.

1.2.2 Site-Controlled Narrow Bandgap Quantum Dots

In order to improve the scalability, various methods have been developed to fabricate site-controlled QDs based on narrow bandgap semiconductors. One of the earliest attempts is to pattern the surface of a single QW using electron-beam lithography and then deeply etch the sample using wet chemical to form site-controlled QDs [42, 43] (Fig. 1.2(a)). After the etching, additional confinement barriers and cap layers may be regrown [43] to reduce the surface defects.

Another way of controlling the forming site is to use patterned substrates (Fig. 1.1(b) and Fig. 1.2(b)). Patterning can be done using electron-beam lithography [4] and atomic-form microscope local oxidation lithography[44, 45] followed by wet chemical etching. During subsequent epitaxial growth, QDs tend to form at the etched nanoholes. Typically, multiple layers of QD-buffer layers were grown before the growth of the final functional QD layer. This is to reduce the threading and dislocation defects in the functional QDs.

A similar approach is to grow QDs in inverted pyramids as shown in Fig. 1.2(c) [46, 47]. The inverted pyramids are formed on (111)B-GaAs substrate using optical lithography followed by anisotropic wet chemical etching. During the subsequent growth, QDs tend to form at the apices of the micropyramids. To improve the light extraction efficiency, the samples are typically up-side-down bonded on another substrate followed by selective removal of the original substrate. This leads to upright-standing pyramids. An advantage of using the (111)B GaAs substrate is the capability of forming highly symmetric QDs ideal for generating entangled

single-photon pairs [48, 49]. A disadvantage of this type of QDs is the large size of the pyramids, limiting the integration of these QDs with other photonic components which typically have the same as or even smaller size than the pyramids.

Site-controlled narrow bandgap QDs can also form on top of buried oxide stressor layers as illustrated in Fig. 1.2(d) [50]. First, mesas containing AlGaAs layer are formed using optical lithography and etching. AlGaAs can be oxidized to form Al_2O_3 ring surround the central AlGaAs aperture. This oxide aperture creates local strain potential leading to the preferential formation of QDs on top of the aperture. Highly efficient current injection can be realized in this type of QDs due to the natural constrain of the current pathway by the oxide aperture [91], the same principle used in vertical cavity surface emitting lasers (VCSELs). However, in this method, it is difficult to control the number of QDs grown on each oxide aperture.

In addition to the above methods, there are other ways of making site-controlled narrow bandgap QDs, such as using a scanning tunneling microscope tip during growth [51].

1.2.3 Self-Assembled Wide Bandgap Quantum Dots

Despite of the great success in self-assembled and site-controlled narrow bandgap QDs, these QDs can hardly be used in practical settings. The main limitation is their low operating temperatures, which are typically cryogenic. To make truly practical QD-based devices, QDs with high operating temperatures are necessary. The most promising candidates are QDs based on wide bandgap semiconductors. As we mentioned earlier, wide bandgap III-N and II-V materials can have operating temperature close to or higher than the room temperature due to their large exciton binding energy.

Similar to narrow bandgap QDs, the development of wide bandgap QDs also first starts with the study on self-assembled ones. In 2006, a single-photon source based on Stranski-Krastanov self-assembled GaN QDs was demonstrated to operate at 200 K [39], much higher than all previous single-photon sources based on narrow bandgap QDs. It was important, because 200 K is reachable by established thermo-electric cooling technology. This sparkled great interest in developing wide bandgap QDs. Since then, many devices based on self-assembled III-N and II-V QDs have been reported to operate at higher than 200 K temperatures, including InGaN QDs in self-grown AlGaN nanowires [92] and CdSe QDs in self-grown ZnSe nanowires[41].

It is worth pointing out that other materials have also been used to achieve the quantum functionalities at high operating temperatures, such as defects in SiC [93] and diamond [94, 95], organic molecules [32], colloidal QDs [36]. However, they can hardly match the scalability promised by epitaxial QDs.

1.2.4 Site-Controlled Wide Bandgap Quantum Dots

To ultimately solve both operating temperature and scalability issues, site-controlled wide bandgap QDs are one of the most promising candidates. In this domain, III-N semiconduc-

tors have been the main material playground. This is not only because they are relatively better understood materials with wide industrial applications, such as blue LED and laser, but also because their mature p-type doping [96, 97, 98] and contacting [99, 100, 101, 102] technologies, which are important for making electrically driven devices to further enhance the device scalability. Despite progresses, high quality p-type doping and contacting technologies remain difficult to achieve in other wide bandgap materials, such as ZnO.

So far, several types of site-controlled wide bandgap QDs have emerged, including InGaN QDs at the apex of site-controlled GaN micro-pyramids [5, 6, 7], GaN QDs inserted in GaN/AlN nanowires [8] as well as our lithographically etched InGaN QD in GaN nanowires [9, 1]. Their fabrication and structure are illustrated in Fig. 1.3. The first two methods use selective area growth method, in which a mask is patterned by either optical lithography or electron beam lithography. This allows selective growth of GaN at eh mask openings. In the first method, InGaN QDs form at the apex of micropyramid. In the second method, AlN/GaN/AlN double heterostructure is grown on top of the GaN nanowire, leading to the formation of GaN QDs at the top. Recently, room temperature single-photon emission has been observed from QDs grown by the second approach [40].

The site-controlled InGaN/GaN QDs studied in this thesis are etched from single InGaN/GaN QWs as shown in Fig. 1.3(c). Using these QDs we have demonstrated optically pumped single-photon sources at up to 90 K [1] and electrically driven single-photon sources at 10 K. We have carried out systematic studies on the carrier dynamics [**?**] in these QDs and gained good understanding in the exciton radiative and nonradiative dynamics for QDs of various diameters [2] and at broad range of temperatures.

1.3 Thesis Overview

This thesis is about the understanding of the optoelectronic properties of our site-controlled InGaN/GaN QDs and the demonstration of several quantum photonic devices based on these QDs. It is organized as following. Chapter 1 introduces the applications of semiconductor QDs, reviews the past efforts towards making scalable and practical QDs, and provides the motivation for the study in this thesis. Chapter 2 introduces the fundamental physics needed to understand semiconductor QDs and the fundamental properties of wurtzite nitride semiconductors. Chapter 3 describes the fabrication of the samples used in this thesis and the experimental setups used for characterizing their optoelectronic properties. Chapter 4 shows the changes in the lateral strain profile and optical properties of InGaN-disk-in-GaN-nanowires as they transition from QWs to QDs accompanying the reduction of their diameters. Chapter 5 shows the exciton radiative and nonradiative decay dynamics in our QDs and how they are impacted by the exciton potential profile induced by the lateral strain profile. Chapter 6 shows the optical properties of individual QDs, and the origin of the inhomogeneity from dot to dot and the statistical correlations among various optical properties. Chapter 7 demonstrates an electrically

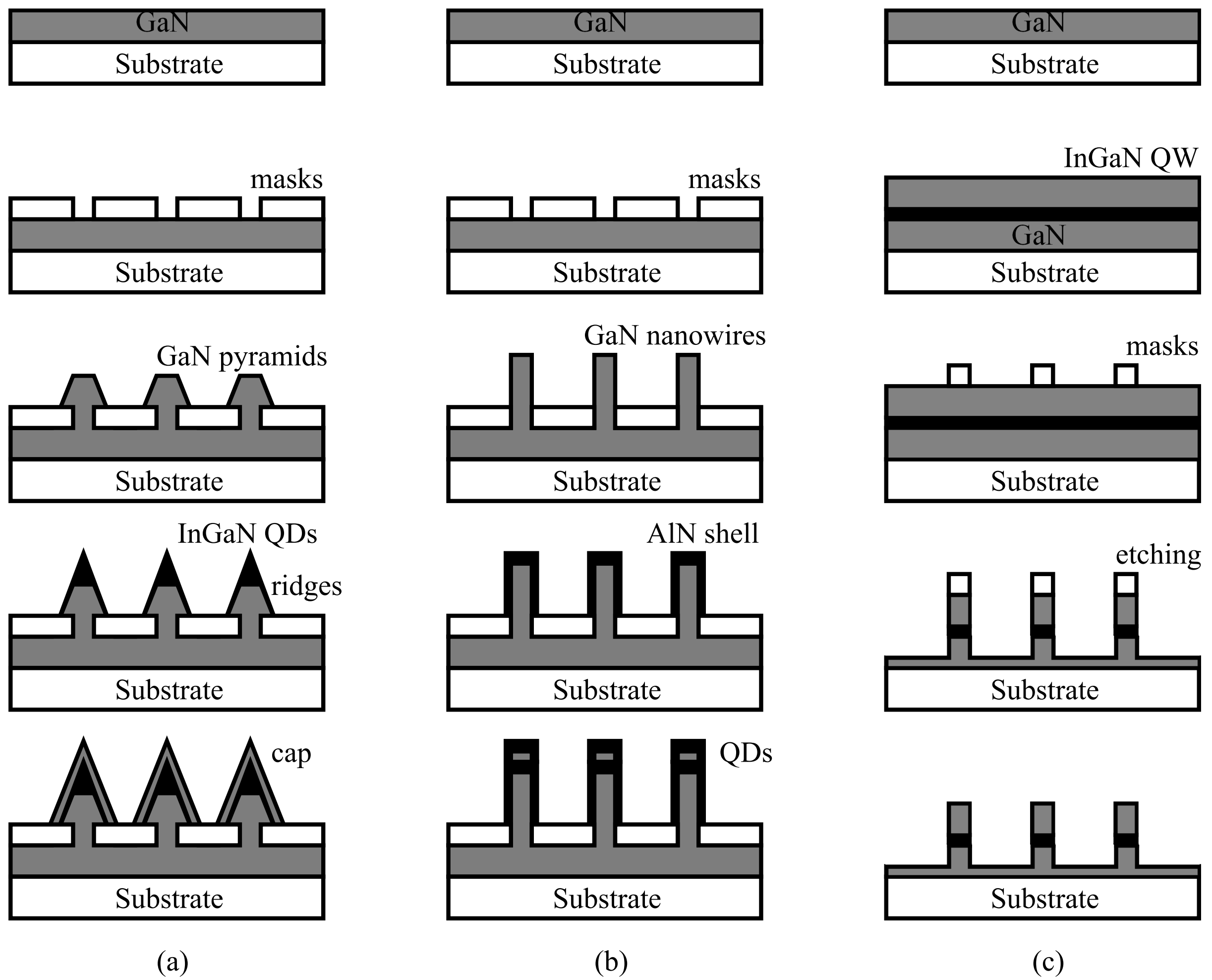

Figure 1.3: Fabrication and structures of three types of site-controlled III-N QDs. (a) InGaN QD on GaN pyramid [5, 6, 7]. (b) GaN QD in GaN-core-AlN-shell nanowire [8]. (c) InGaN QD in GaN nanowire [9, 1].

driven single-photon emitter based on our QDs and show that the same device can also be used to control the number of charged in a QD to study the neutral and charged excitons. Chapter 8 concludes the thesis and point out future work based on this thesis.

CHAPTER 2

Fundamentals of Quantum Dot Physics and III-Nitride Semiconductors

This chapter will first introduce the fundamental physics in a semiconductors QD with emphasis on how exciton oscillator strength depends on the size of the QD and the bandgap of the semiconductor. Then the material properties of GaN (gallium nitride) and InGaN (indium gallium nitride) are introduces.

2.1 Fundamental Physics in Quantum Dots

In this section, we show that the exciton binding energy and oscillator strength increase with the size and bandgap of an unstrained QD.

2.1.1 Exciton and Quantum Confinement

Many important applications of QDs rely on their interaction with photons. QDs interact with photons through the formation and recombination of excitons. The emission energy and carrier dynamics in a QD are determined by the exciton. Therefore, it is important to understand the properties of QD exciton.

The exciton wavefunction can be written as [103, 104]

$$\Psi(\boldsymbol{r}_e, \boldsymbol{r}_h) = \sum_{\boldsymbol{R}_e, \boldsymbol{R}_h} \Phi(\boldsymbol{R}_e, \boldsymbol{R}_h) a_{\boldsymbol{R}_e}(\boldsymbol{r}_e) a_{\boldsymbol{R}_h}(\boldsymbol{r}_h). \tag{2.1}$$

Here, $\boldsymbol{R}_e$ and $\boldsymbol{R}_h$ are the locations of unit cells. There are N number of unit cells in the system. $a_{\boldsymbol{R}_e}(\boldsymbol{r}_e)$ and $a_{\boldsymbol{R}_h}(\boldsymbol{r}_h)$ are the Wannier functions for electron and hole, respectively. $\Phi(\boldsymbol{R}_e, \boldsymbol{R}_h)$ is the electron-hole pair envelope wavefunction. It can be shown that the Schrödinger equation for $\Phi(\boldsymbol{R}_e, \boldsymbol{R}_h)$ can be written as

$$\left[-\frac{\hbar^2}{2m_e} \boldsymbol{\nabla}^2_{\boldsymbol{R}_e} - \frac{\hbar^2}{2m_h} \boldsymbol{\nabla}^2_{\boldsymbol{R}_h} - \frac{e^2}{4\pi\varepsilon_0\varepsilon |\boldsymbol{R}_e - \boldsymbol{R}_h|} + V_e(\boldsymbol{R}_e) + V_h(\boldsymbol{R}_h) \right] \Phi(\boldsymbol{R}_e, \boldsymbol{R}_h) = E\Phi(\boldsymbol{R}_e, \boldsymbol{R}_h). \tag{2.2}$$

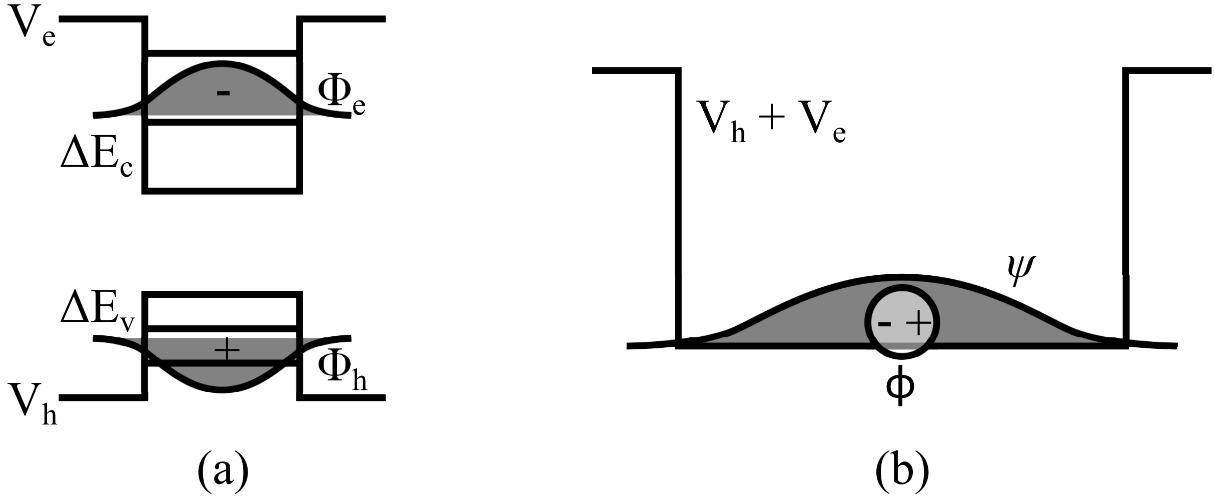

Figure 2.1: Illustration of the strong (a) and weak (b) confinement regimes.

Here, m_e and m_h are the effective masses of electron and hole, respectively. ε_0 is the vacuum permittivity and ε is the relative permittivity of the semiconductor. $\frac{e^2}{4\pi\varepsilon_0\varepsilon|\boldsymbol{R}_e-\boldsymbol{R}_h|}$ describes the Coulomb interaction between the electron and hole. $V_e(\boldsymbol{R}_e)$ and $V_h(\boldsymbol{R}_h)$ are the confinement potential for electron and hole, respectively, as shown in Fig. 2.1(a).

The confinement potential $V_e(\boldsymbol{R}_e)$ and $V_h(\boldsymbol{R}_h)$ lead to characteristic energy level separations ΔE_e and ΔE_h for electron and hole, respectively. For instance, in an infinite potential box with $L \times L \times L$ spatial dimensions, $\Delta E_e \sim \frac{\hbar^2}{m_e L^2}$ and $\Delta E_h \sim \frac{\hbar^2}{m_h L^2}$. The Coulomb interaction leads to hydrogen-atom-like binding between electron and hole with a binding energy $E_\mathrm{B} = \frac{e^2}{4\pi\varepsilon_0\varepsilon a_\mathrm{B}}$. Here, a_B is the Bohr radius. Both E_B and a_B will be derived later.

If $\Delta E_e, \Delta E_h \gg E_\mathrm{B}$, or equivalently $L \gg a_\mathrm{B}$ [105], the QD is in the strong confinement regime. If $\Delta E_e, \Delta E_h \ll E_\mathrm{B}$, or equivalently $L \ll a_\mathrm{B}$, the QD is in the weak confinement regime. Figure 2.1 illustrates these two regimes. In the following we will show the different physics in these two confinement regimes.

2.1.1.1 Strong Confinement Regime

In the strong confinement regime, $\Phi(\boldsymbol{R}_e, \boldsymbol{R}_h)$ is mainly determined by $V(\boldsymbol{R}_e)$ and $V(\boldsymbol{R}_h)$. We can therefore treat the Coulomb interaction $-\frac{e^2}{4\pi\varepsilon_0\varepsilon|\boldsymbol{R}_e-\boldsymbol{R}_h|}$ as perturbation after we solve the approximated form of Equ. 2.2:

$$\left[-\frac{\hbar^2}{2m_e}\boldsymbol{\nabla}^2_{\boldsymbol{R}_e} - \frac{\hbar^2}{2m_h}\boldsymbol{\nabla}^2_{\boldsymbol{R}_h} + V_e(\boldsymbol{R}_e) + V_h(\boldsymbol{R}_h)\right]\Phi(\boldsymbol{R}_e, \boldsymbol{R}_h) = E\Phi(\boldsymbol{R}_e, \boldsymbol{R}_h). \tag{2.3}$$

This wave equation can be written as two decoupled ones

$$\left[-\frac{\hbar^2}{2m_e}\boldsymbol{\nabla}^2_{\boldsymbol{R}_e} + V_e(\boldsymbol{R}_e)\right]\Phi_e(\boldsymbol{R}_e) = E_e\Phi_e(\boldsymbol{R}_e), \tag{2.4}$$

$$\left[-\frac{\hbar^2}{2m_h}\boldsymbol{\nabla}^2_{\boldsymbol{R}_h} + V_h(\boldsymbol{R}_h)\right]\Phi_h(\boldsymbol{R}_h) = E_h\Phi_h(\boldsymbol{R}_h). \tag{2.5}$$

And the electron-hole pair wavefunction can be rewritten as

$$\Psi(\boldsymbol{r}_e, \boldsymbol{r}_h) = \sum_{\boldsymbol{R}_e,\boldsymbol{R}_h} \Phi_e(\boldsymbol{R}_e)\Phi_h(\boldsymbol{R}_h)a_{\boldsymbol{R}_e}(\boldsymbol{r}_e)a_{\boldsymbol{R}_h}(\boldsymbol{r}_h). \tag{2.6}$$

The Wannier functions can be expressed using the Bloch wavefunctions $\psi_{n\boldsymbol{k}}$ as

$$\begin{aligned}
a_{\boldsymbol{R}_e}(\boldsymbol{r}_e) &= \frac{1}{\sqrt{N}}\sum_{\boldsymbol{k}_e} \mathrm{e}^{-i\boldsymbol{k}_e\cdot\boldsymbol{R}_e}\psi_{c\boldsymbol{k}_e}(\boldsymbol{r}_e),\\
a_{\boldsymbol{R}_h}(\boldsymbol{r}_h) &= \frac{1}{\sqrt{N}}\sum_{\boldsymbol{k}_h} \mathrm{e}^{-i\boldsymbol{k}_h\cdot\boldsymbol{R}_h}\psi_{v\boldsymbol{k}_h}(\boldsymbol{r}_h),
\end{aligned} \tag{2.7}$$

where the subscript c and v represent conduction band and valance band, respectively. Using these two expressions, $\Psi(\boldsymbol{r}_e, \boldsymbol{r}_h)$ can be rewritten as

$$\Psi(\boldsymbol{r}_e, \boldsymbol{r}_h) = \sum_{\boldsymbol{R}_e,\boldsymbol{R}_h} \Phi_e(\boldsymbol{R}_e)\Phi_h(\boldsymbol{R}_h)\frac{1}{N}\sum_{\boldsymbol{k}_e,\boldsymbol{k}_h} \mathrm{e}^{-i\boldsymbol{k}_e\cdot\boldsymbol{R}_e - i\boldsymbol{k}_h\cdot\boldsymbol{R}_h}\psi_{c\boldsymbol{k}_e}(\boldsymbol{r}_e)\psi_{v\boldsymbol{k}_h}(\boldsymbol{r}_h). \tag{2.8}$$

The oscillator strength of the exciton transition to the ground state $|0\rangle$ is [106, 103]

$$f_{os} = \frac{2}{m_e\hbar\omega}\left|\langle\Psi(\boldsymbol{r}_e, \boldsymbol{r}_h)|\hat{\mathrm{e}}\cdot\boldsymbol{p}|0\rangle\right|^2, \tag{2.9}$$

where ω is the transition angular frequency, $\hat{\mathrm{e}}$ is the polarization direction and $\boldsymbol{p}$ is the momentum operator. To evaluate the transition matrix element $\langle\Psi(\boldsymbol{r}_e, \boldsymbol{r}_h)|\hat{\mathrm{e}}\cdot\boldsymbol{p}|0\rangle$, we only need to consider terms in $\Psi(\boldsymbol{r}_e, \boldsymbol{r}_h)$ that satisfy $\boldsymbol{K} = \boldsymbol{k}_e + \boldsymbol{k}_h = 0$ [103]. This is because photon has much steeper dispersion compared to exciton's. Therefore, they intersect at $\boldsymbol{K} \sim 0$. Using this condition the transition matrix element can be written as

$$\begin{aligned}
&\langle\Psi(\boldsymbol{r}_e, \boldsymbol{r}_h)|\hat{\mathrm{e}}\cdot\boldsymbol{p}|0\rangle\\
&= \sum_{\boldsymbol{R}_e,\boldsymbol{R}_h} \Phi_e(\boldsymbol{R}_e)\Phi_h(\boldsymbol{R}_h)\frac{1}{N}\sum_{\boldsymbol{k}_e,\boldsymbol{k}_h} \mathrm{e}^{-i\boldsymbol{k}_e\cdot\boldsymbol{R}_e - i\boldsymbol{k}_h\cdot\boldsymbol{R}_h}\langle\psi_{c\boldsymbol{k}_e}(\boldsymbol{r}_e)\psi_{v\boldsymbol{k}_h}(\boldsymbol{r}_h)|\hat{\mathrm{e}}\cdot\boldsymbol{p}|0\rangle\\
&= \sum_{\boldsymbol{R}} \Phi_e(\boldsymbol{R})\Phi_h(\boldsymbol{R})\langle\psi_{c\boldsymbol{k}}(\boldsymbol{r}_e)\psi_{v-\boldsymbol{k}}(\boldsymbol{r}_h)|\hat{\mathrm{e}}\cdot\boldsymbol{p}|0\rangle\\
&= p_{cv}\sum_{\boldsymbol{R}} \Phi_e(\boldsymbol{R})\Phi_h(\boldsymbol{R}).
\end{aligned} \tag{2.10}$$

Here, we used $\sum_{\boldsymbol{k}} \mathrm{e}^{i\boldsymbol{k}\cdot\boldsymbol{r}} = N\delta(\boldsymbol{r})$, and assumed that $p_{cv} = \langle \psi_{c\boldsymbol{k}}(\boldsymbol{r}_e)\psi_{v-\boldsymbol{k}}(\boldsymbol{r}_h)|\hat{\mathrm{e}}\cdot\boldsymbol{p}|0\rangle$ is independent of $\boldsymbol{k}$. Hence, the oscillator strength

$$f_{os} = \frac{2}{m_e\hbar\omega}\left|\sum_{\boldsymbol{R}} \Phi_e(\boldsymbol{R})\Phi_h(\boldsymbol{R})\right|^2 |p_{cv}|^2 . \tag{2.11}$$

This result shows several features for f_{os} in the strong confinement regime. First, f_{os} has a maximum value

$$f_{os} < \frac{2}{m_e\hbar\omega} |p_{cv}|^2 , \tag{2.12}$$

as $\left|\sum_{\boldsymbol{R}} \Phi_e(\boldsymbol{R})\Phi_h(\boldsymbol{R})\right|^2 < 1$. Second, f_{os}'s magnitude is mainly determined by the electron-hole envelope function overlap integral $\left|\sum_{\boldsymbol{R}} \Phi_e(\boldsymbol{R})\Phi_h(\boldsymbol{R})\right|^2$. Third, f_{os} is largely independent on N. The last feature can be understood as following. As the number of unit cells N increases, the amplitudes of $\Phi_e(\boldsymbol{R})$ and $\Phi_h(\boldsymbol{R})$ decrease as $1/\sqrt{N}$. Hence, $\Phi_e(\boldsymbol{R})\Phi_h(\boldsymbol{R})$ decreases as $1/N$. On the other hand, the summation over $\boldsymbol{R}$ has N summands, which cancels the N-dependence of $\Phi_e(\boldsymbol{R})\Phi_h(\boldsymbol{R})$. However, the change in N typically leads to small changes in $\Phi_e(\boldsymbol{R})$ and $\Phi_h(\boldsymbol{R})$, resulting a weak N-dependence of f_{os} [107]. As we will see next, this weak N-dependence of f_{os} in the strong confinement regime is in sharp contrast with the strong N-dependence of f_{os} in the weak confinement regime.

2.1.1.2 Weak Confinement Regime

In the weak confinement regime, $\Phi(\boldsymbol{R}_e, \boldsymbol{R}_h)$ is mainly determined by the Coulomb interaction $-\frac{e^2}{4\pi\varepsilon_0\varepsilon|\boldsymbol{R}_e-\boldsymbol{R}_h|}$. We can therefore treat $V_e(\boldsymbol{R}_e)$ and $V_h(\boldsymbol{R}_h)$ as perturbation after we solve

$$\left[-\frac{\hbar^2}{2m_e}\boldsymbol{\nabla}^2_{\boldsymbol{R}_e} - \frac{\hbar^2}{2m_h}\boldsymbol{\nabla}^2_{\boldsymbol{R}_h} - \frac{e^2}{4\pi\varepsilon_0\varepsilon|\boldsymbol{R}_e - \boldsymbol{R}_h|}\right]\Phi(\boldsymbol{R}_e, \boldsymbol{R}_h) = E\Phi(\boldsymbol{R}_e, \boldsymbol{R}_h). \tag{2.13}$$

To solve this equation, we transform $\boldsymbol{R}_e$ and $\boldsymbol{R}_h$ into two new coordinates: the center-of-mass coordinate $\boldsymbol{R}$ and the relative motion coordinate $\boldsymbol{r}$ as following

$$\boldsymbol{R} = \frac{m_e\boldsymbol{R}_e + m_h\boldsymbol{R}_h}{m_e + m_h}, \tag{2.14}$$

$$\boldsymbol{r} = \boldsymbol{R}_e - \boldsymbol{R}_h. \tag{2.15}$$

This leads to the decoupling of the Schrödinger equation into a center-of-mass equation

$$-\frac{\hbar^2}{2M}\nabla^2_{\boldsymbol{R}}\psi(\boldsymbol{R}) = E_R\psi(\boldsymbol{R}) \tag{2.16}$$

and a relative motion equation

$$\left(-\frac{\hbar^2}{2\mu}\nabla_{\boldsymbol{r}}^2 - \frac{e^2}{4\pi\varepsilon_0\varepsilon r}\right)\phi(\boldsymbol{r}) = E_r\phi(\boldsymbol{r}), \tag{2.17}$$

in which $M = m_e + m_h$ is the total exciton mass and $\mu = \frac{m_e m_h}{m_e + m_h}$ is the reduce mass.

The relative motion equation is similar to that in the hydrogen atom theory, from which the wavefunction ϕ in spherical coordinates (r, θ, ϕ) is

$$\phi_{nlm}(\boldsymbol{r}) = R_{nl}(r)Y_{lm}(\theta, \phi) \tag{2.18}$$

in which R_{nl} is associated to the generalized Laguerre polynomial of degree $n-l-1$ and Y_{lm} is spherical harmonic function of degree l and order m. The ϕ_{100} or 1S state exciton wavefunction is:

$$\phi_{100}(\boldsymbol{r}) = \frac{1}{\sqrt{\pi a_{\mathrm{B}}^3}}\mathrm{e}^{-r/a_{\mathrm{B}}}, \tag{2.19}$$

in which the Bohr radius

$$a_{\mathrm{B}} = \frac{4\pi\varepsilon_0\varepsilon\hbar^2}{\mu e^2}. \tag{2.20}$$

The binding energy of the 1S state exciton is

$$E_{\mathrm{B}} = \frac{\mu e^4}{2\hbar^2(4\pi\varepsilon_0\varepsilon)^2}. \tag{2.21}$$

The total wavefunction can now be written as

$$\Psi(\boldsymbol{r}_e, \boldsymbol{r}_h) = \sum_{\boldsymbol{R}_e, \boldsymbol{R}_h} \psi(\boldsymbol{R})\phi_{nlm}(\boldsymbol{r})a_{\boldsymbol{R}_e}(\boldsymbol{r}_e)a_{\boldsymbol{R}_h}(\boldsymbol{r}_h). \tag{2.22}$$

Using Equs. 2.7, $\Psi(\boldsymbol{r}_e, \boldsymbol{r}_h)$ can be rewritten as

$$\Psi(\boldsymbol{r}_e, \boldsymbol{r}_h) = \sum_{\boldsymbol{R}_e, \boldsymbol{R}_h} \psi(\boldsymbol{R})\phi_{nlm}(\boldsymbol{r})\frac{1}{N}\sum_{\boldsymbol{k}_e, \boldsymbol{k}_h} \mathrm{e}^{-i\boldsymbol{k}_e\cdot\boldsymbol{R}_e}\mathrm{e}^{-i\boldsymbol{k}_h\cdot\boldsymbol{R}_h}\psi_{c\boldsymbol{k}_e}(\boldsymbol{r}_e)\psi_{v\boldsymbol{k}_h}(\boldsymbol{r}_h). \tag{2.23}$$

Similar to Equ. 2.10 the transition matrix element can be written as

$$\begin{aligned}\langle\Psi(\boldsymbol{r}_e, \boldsymbol{r}_h)|\hat{\mathrm{e}}\cdot\boldsymbol{p}|0\rangle &= \sum_{\boldsymbol{R}_e, \boldsymbol{R}_h} \psi(\boldsymbol{R})\phi_{nlm}(\boldsymbol{r})\frac{1}{N}\sum_{\boldsymbol{k}} \mathrm{e}^{-i\boldsymbol{k}\cdot\boldsymbol{r}}\langle\psi_{c\boldsymbol{k}}(\boldsymbol{r}_e)\psi_{v-\boldsymbol{k}}(\boldsymbol{r}_h)|\hat{\mathrm{e}}\cdot\boldsymbol{p}|0\rangle \\ &= p_{cv}\sum_{\boldsymbol{R}} \psi(\boldsymbol{R})\phi_{nlm}(0).\end{aligned} \tag{2.24}$$

Again, we used $\sum_{\boldsymbol{k}} \mathrm{e}^{i\boldsymbol{k}\cdot\boldsymbol{r}} = N\delta(\boldsymbol{r})$, and assumed that $p_{cv} = \langle\psi_{c\boldsymbol{k}}(\boldsymbol{r}_e)\psi_{v-\boldsymbol{k}}(\boldsymbol{r}_h)|\hat{\mathrm{e}}\cdot\boldsymbol{p}|0\rangle$ is inde-

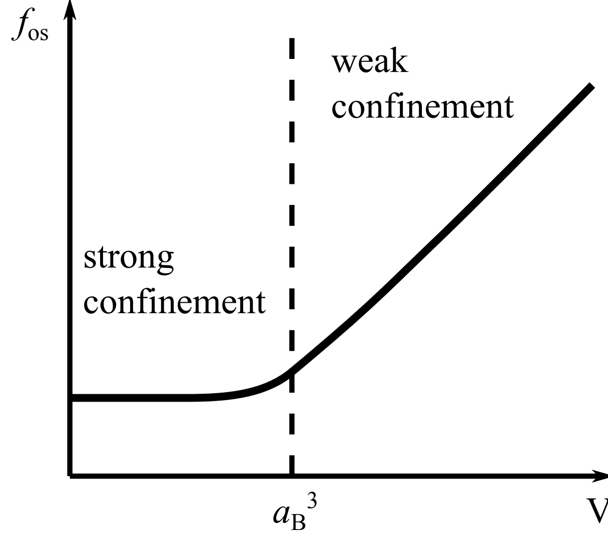

Figure 2.2: QD oscillator strength f_{os} in the strong and weak confinement regimes. V is the volume of the QD.

pendent of $\boldsymbol{k}$. Hence, the oscillator strength

$$f_{os} = \frac{2}{m_e \hbar\omega} \left| \sum_{\boldsymbol{R}} \psi(\boldsymbol{R}) \phi_{nlm}(0) \right|^2 |p_{cv}|^2 . \tag{2.25}$$

This result shows several important properties of QD oscillator strength in the weak confinement regime. First, only the 1S or ϕ_{100} exciton has allowed optical transition, since higher order states have $\phi_{nlm}(0) = 0$. Second, f_{os} is proportional to the electron-hole wavefunction overlap $|\phi_{100}(0)|^2$ and inversely proportional to the volume of the exciton, as $|\phi_{100}(0)|^2 = \frac{1}{\pi a_{\text{B}}^3}$. Third, f_{os} is proportional to the number of unit cells N in the system, i.e.

$$f_{os} \sim \frac{2}{m_e \hbar\omega} N \, |\phi_{nlm}(0)|^2 \, |p_{cv}|^2 . \tag{2.26}$$

This can be seen by assigning $\psi(\boldsymbol{R}) \sim 1/\sqrt{N}$. The N-dependence of f_{os} is illustrated in Fig. 2.2. The different f_{os}-N behaviors in the weak and strong confinement regimes can be understood as following. When Coulomb interaction is less significant, as in the strong confinement regime, the locations of electron and hole are uncorrelated. Hence, the amplitude of the wavefuntion $\Psi(\boldsymbol{R}, \boldsymbol{R})$ of having both electron and hole within a unit cell $\boldsymbol{R}$ decreases as $\Psi_e(\boldsymbol{R})\Psi_h(\boldsymbol{R}) \sim 1/N$. When Coulomb interaction is dominant, as in the weak confinement regime, electrons and holes are no longer uncorrelated; instead, they are binded together to form excitons and the amplitude of the wavefuntion $\Psi(\boldsymbol{R}, \boldsymbol{R})$ decreases slower as $\psi(\boldsymbol{R})\phi_{nlm}(0) \sim \phi_{nlm}(0)/\sqrt{N}$.

Table 2.1: Comparison between the lattice constants and the bandgap of common semiconductors.

Properties	IV			III-N (wurtzite)			III-As		
	C	Si	Ge	AlN	GaN	InN	AlAs	GaAs	InAs
c (Å)	3.57	5.43	5.66	3.1* 5.0**	3.2* 5.2**	3.5* 5.7**	5.66	5.65	6.05
E_g (eV)	5.47	1.12	0.67	6.28	3.44	0.7	2.16	1.43	0.36

* Lattice constant perpendicular to the c-axis.
** Lattice constant along the c-axis.

2.1.2 Narrow Bandgap vs. Wide Bandgap Semiconductors

The bandgap of a semiconductor largely depends on its lattice constant. Smaller lattice constants generally leads to wider bandgaps. In the free-electron band structure theory, the opening of the band gap is proportional to the Fourier component of the periodic ion potential $V(\boldsymbol{r})$ [73](p167). This suggests that semiconductors with smaller lattice constants have larger bandgap as shown in Tab. 2.1. For example, the lattice constant c of Ge, Si and C (diamond) have $c_{\mathrm{C}} < c_{\mathrm{Si}} < c_{\mathrm{Ge}}$. Therefore their bandgaps satisfy $E_{\mathrm{C}} > E_{\mathrm{Si}} > E_{\mathrm{Ge}}$. Similarly, we have $E_{\mathrm{g,AlN}} > E_{\mathrm{g,GaN}} > E_{\mathrm{g,InN}}$. However, it is worth mentioning that an important exception is between AlAs and GaAs for which $E_{\mathrm{g,AlAs}} < E_{\mathrm{g,GaAs}}$ even though c_{GaAs} is greater than c_{InAs} by a very small amount.

Wider bandgap typically leads to greater effective masses of electron and hole. This can be seen from Tab. 2.2, which shows the electron effective mass of several common semiconductors. It can be understood using a simple 1D free-electron band structure model. In this model, electrons with momentum p have energy $E = \frac{p^2}{2m}$. The bandgap is formed due to the interaction between $|p_1\rangle$ and $|p_2 = -p_1\rangle$ states at the edge of the Brillouin zone, i.e. $p_1 - p_2 = 2\hbar\frac{2\pi}{\Lambda}$, where Λ is the lattice constant. The Hamiltonian at the vicinity of the Brillouin zone edge can be expressed on the basis $\{|p_1\rangle, |p_2\rangle\}$ as:

$$H = \begin{pmatrix} E_1 & E_{\mathrm{g}}/2 \\ E_{\mathrm{g}}/2 & E_2 \end{pmatrix}. \tag{2.27}$$

Therefore, the degeneracy between $|p_1\rangle$ and $|p_2\rangle$ is lifted into two bands of energies

$$E_+ = \frac{E_1 + E_2}{2} + \sqrt{\left(\frac{E_1 - E_2}{2}\right)^2 + \left(\frac{E_{\mathrm{g}}}{2}\right)^2} \tag{2.28}$$

$$E_- = \frac{E_1 + E_2}{2} - \sqrt{\left(\frac{E_1 - E_2}{2}\right)^2 + \left(\frac{E_{\mathrm{g}}}{2}\right)^2}. \tag{2.29}$$

From this expression, $E_+ - E_- = E_{\mathrm{g}}$ when $p_1 = -p_2$. At the vicinity of $p_1 = \hbar\frac{2\pi}{\Lambda}$, we have

Table 2.2: The bandgap E_g, electron effective mass m_e, exciton binding energy E_B and exciton Bohr radius a_B of several semiconductors.

Materials	E_g (eV)	m_e/m_0*	E_B (meV)	a_B (Å)
InSb	0.237	0.014	0.5	860
InAs	0.354	0.023	1.0	340
Ge	0.89	0.038	1.4	360
GaAs	1.519	0.066	4.1	150
InP	1.423	0.078	5.0	140
CdTe	1.606	0.089	10.6	80
ZnSe	2.82	0.13	20.4	60
ZnO	3.3	0.29	60	18
InN**	0.65	0.11	6.1	71
GaN**	3.51	0.13	27	24
AlN**	6.2	0.4	48	12

* m_0 is the free electron mass.
** A-exciton of Wurtzite crystal.

$E_1 - E_2 \ll E_g$, $p_1 - p_2 \sim 2\hbar\frac{2\pi}{\Lambda}$, and

$$E_+ = \frac{E_1 + E_2}{2} + \frac{E_g}{2}\left[1 + \frac{(E_1 - E_2)^2}{2E_g^2}\right] \tag{2.30}$$

$$= \frac{E_1 + E_2}{2} + \frac{E_g}{2} + \frac{p^2}{2m^\star}, \tag{2.31}$$

in which $p = p_1 + p_2$, and the effective mass $m^\star = \frac{1}{2}\left(\frac{\Lambda m}{\pi\hbar}\right)^2 E_g$. Hence, we can see that the effective mass, or the flatness of the bandedge dispersion, is proportional to the bandgap E_g.

Wider bandgap semiconductors generally have smaller exciton Bohr radii a_B and larger exciton binding energies E_B. This can be easily seen from the $a_B(\mu)$ and $E_B(\mu)$ expressions in Equs. 2.20 and 2.21, respectively. Therefore, wide bandgap materials such as GaN, AlN and ZnO have larger exciton binding energies compared to other III-V materials as shown in Tab. 2.2. The magnitude of E_B is important for bulk semiconductors and QDs in the weak confinement regime as it determines the upper limit of the temperatures in which they are optically active. If temperature exceeds E_B the exciton dissociates so that $|\phi(0)|^2$ in the exciton oscillator strength Equ. 2.26 becomes very small. For GaN, AlN and ZnO, their E_B's are close to or greater than the room temperature thermal energy $k_B T = 26$ meV, which make them excellent optical materials at room temperature.

Finally, wider bandgap semiconductors typically have greater exciton oscillator strengths. This is a direct result of their smaller a_B resulting in larger probably $|\phi(0)|^2$ of finding electron and hole at the same location. For example, the oscillator strength per unit volume of the A- and B-exciton transitions in bulk GaN can be extracted from the A values [108] via the following expression derived from [103]:

$$f_{os} = \frac{\epsilon_0 m_e}{\hbar^2 e^2} A. \tag{2.32}$$

The results are $f_{os,A} = 2.5 \times 10^{-5}$ and $f_{os,B} = 1.8 \times 10^{-5}$ Å^{-3} for A- and B-exciton transitions respectively. This is an order of magnitude higher than the typical values of 10^{-6} Å^{-3} in III-As or III-P materials [109, 110]. It is worth mentioning that another wide bandgap material ZnO has an even higher oscillator strength of 10^{-4} Å^{-3} [111]. Large oscillator strength enhances the light-matter interaction, lowing the requirements for achieving some of the strong coupling phenomena, as we shall see in the next section.

2.2 Material Properties of GaN

Bulk GaN and InN crystals have two major phases, wurtzite and zinc-blende, as shown in Fig. 2.3. The zinc-blende phase has cubic lattice as shown in Fig. 2.3(b). Several symmetry directions (001), (100) and (111) are illustrated. Wurtzite GaN have hexagonal lattices as shown in Fig. 2.3(a). Three major symmetry directions (0001), (1000) and ($0\bar{1}10$) are illustrated. The lattice constant c along the (0001) direction is different from the lattice constant a in the plane perpendicular to the (0001) direction.

The phase of the crystal is largely determined by the material and orientation of the substrate. Cubic (zinc-blende) GaN has been grown on (001) GaAs and (001) Si substrates, etc. Wurtzite GaN has been grown on sapphire, (111) Si and (111) GaAs, etc. Cubic crystals are common for III-As and III-P semiconductors. However, for III-N semiconductors the most available crystals are wurtzite.

Depending on the growth plane, wurtzite GaN can be polar, semi-polar and non-polar. Figure 2.3(a) lower panel shows the most popular substrate planes including polar c-plane, semi-polar r-plane, and non-polar α- and m-planes. In this dissertation, we use the most commonly available form, wurtzite polar GaN grown on c-plane sapphire. From now on, we only discuss about this form of GaN unless otherwise specified.

2.2.1 Band Structure of GaN

The Block equation for the periodic part of the Bloch function $u_{n\boldsymbol{k}}(\boldsymbol{r})$ is [112]:

$$\begin{aligned} Hu_{n\boldsymbol{k}}(\boldsymbol{r}) &= \left(H_0 + \frac{\hbar^2 k^2}{2m_0} + \frac{\hbar}{m_0}\boldsymbol{k}\cdot\boldsymbol{p} + H_{so} \right) u_{n\boldsymbol{k}}(\boldsymbol{r}) \\ &= E_n(\boldsymbol{k}) u_{n\boldsymbol{k}}(\boldsymbol{r}), \end{aligned} \tag{2.33}$$

in which

$$H_0 = \frac{p^2}{2m_0} + V(\boldsymbol{r}), \tag{2.34}$$

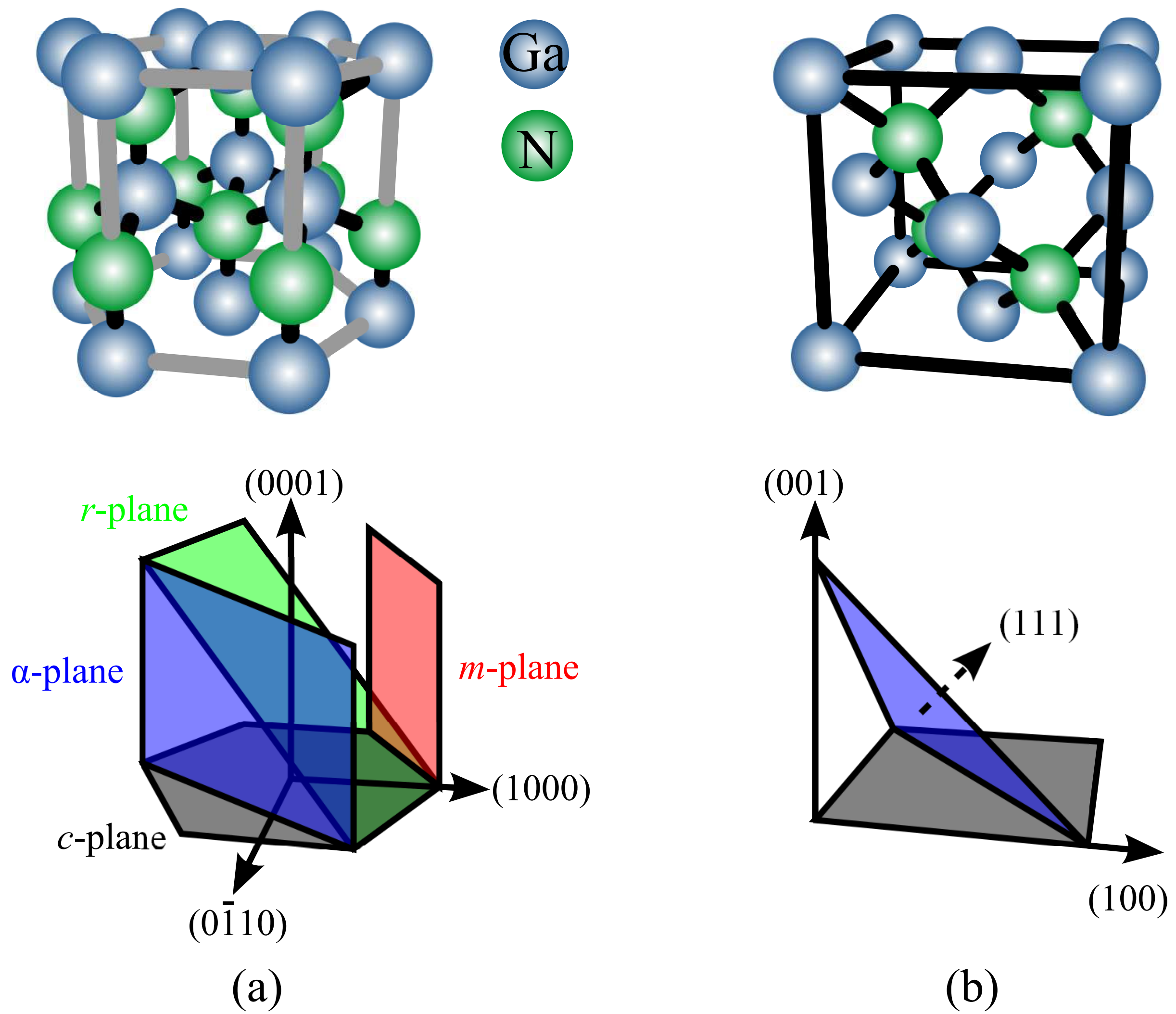

Figure 2.3: Wurtzite and zinc-blende GaN crytal phases. (a) Wurtzite crystal. (b) Zinc-blende crystal.

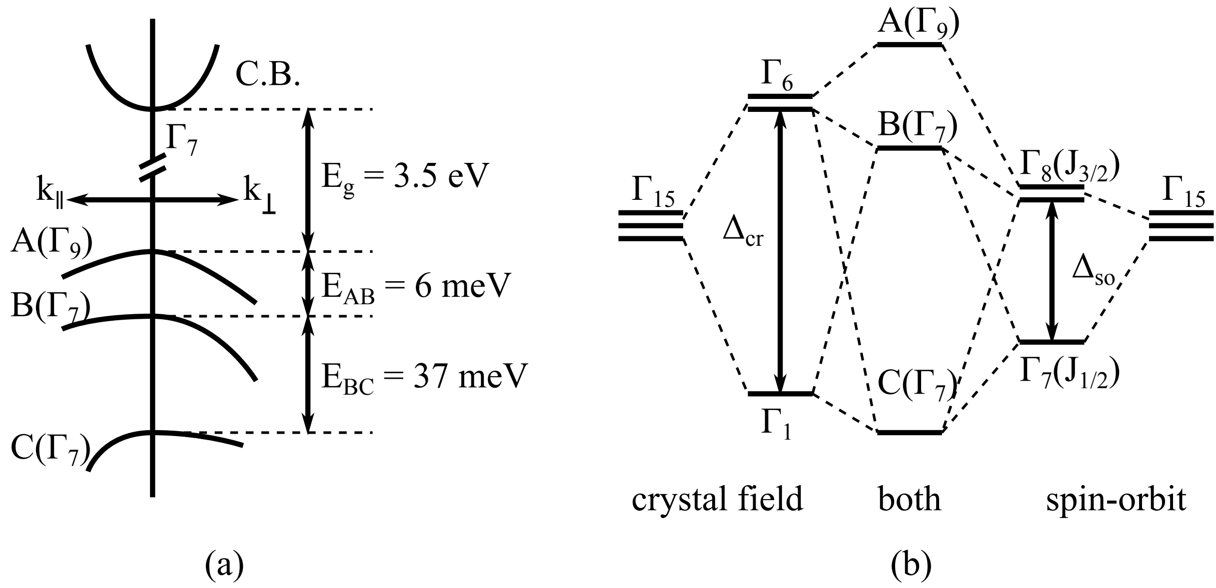

Figure 2.4: Wurtzite GaN band structure. (a) Band structure. (b) Crystal field and spin-orbit splitting. Figure adopted from [10].

$V(\boldsymbol{r})$ is the periodic potential;

$$\begin{aligned} H_{so} &= \frac{\hbar}{4m_0^2c^2}\nabla V \times \boldsymbol{p}\cdot\boldsymbol{\sigma} \\ &= H_{sx}\sigma_x + H_{sy}\sigma_y + H_{sz}\sigma_z \end{aligned} \tag{2.35}$$

is the spin-orbital coupling Hamiltonian; and σ_x, σ_y and σ_z are the Pauli matrices.

The band structure of GaN is shown in Fig. 2.4(a). It has a direct band gap of $E_g = 3.5$ eV at the Γ point. The conduction band is in the atomic s state. The valence bands are composed of three sub bands A, B and C corresponding to heavy hole, light hole and split-off hole states respectively based on how flat the band edge is. The splitting between A and B valence band is $E_{AB} = 6$ meV and that between B and C is $E_{BC} = 37$ meV. The splitting results from crystal anisotropy and spin-orbit coupling.

Without considering any of the splitting mechanism, the valence band is in the atomic p state leading to a six-fold degeneracy, considering the two-fold spin degeneracy. They have Γ_{15} symmetry. Γ_{15} is a Bouckaert, Smoluchowski and Wigner (BSW) notation for a set of wavefunctions that forms a irreducible representation for the wurtzite crystal symmetry group [103]. In Koster notation they may also be labeled as Γ_4 or Γ_5. One set of such wavefunctions are

$$|p_x\rangle = \frac{1}{\sqrt{2}}(|j=1,m=1\rangle - |j=1,m=-1\rangle), \tag{2.36}$$

$$|p_y\rangle = \frac{i}{\sqrt{2}}(|j=1,m=1\rangle + |j=1,m=-1\rangle), \tag{2.37}$$

$$|p_z\rangle = |j=1,m=0\rangle, \tag{2.38}$$

in which $|j=1,m=0,\pm1\rangle$ are the eigenfunction of angular momentum operators L^2 and L_z with j and m being their respective quantum numbers. In spherical coordinates, $|j=1,m=0,\pm1\rangle$ can be written as

$$\langle\theta,\phi|j=1,m=\pm1\rangle = Y_{1,\pm1}(\theta,\phi) = \mp\sqrt{\frac{3}{8\pi}}\sin\theta e^{\pm i\phi}, \tag{2.39}$$

$$\langle\theta,\phi|j=1,m=0\rangle = Y_{1,0}(\theta,\phi) = \sqrt{\frac{3}{4\pi}}\cos\theta. \tag{2.40}$$

$|p_x\rangle$, $|p_y\rangle$ and $|p_z\rangle$ together with the two spin eigenstates $|\uparrow\rangle$ and $|\downarrow\rangle$ of the spin angular momentum S form a six-fold degeneracy.

When only the spin-orbit coupling is considered, the six-fold degeneracy is broken into $J=3/2$ states with four-fold degeneracy and $J=1/2$ states with two-fold degeneracy as shown in Fig. 2.4(b), in which J is the quantum number of the total angular moment $J^2=(L+S)^2$. States that satisfy $J=3/2$ are

$$|J=3/2,J_z=3/2\rangle = \frac{-1}{\sqrt{2}}(|p_x\rangle + i|p_y\rangle)|\uparrow\rangle, \tag{2.41}$$

$$|J=3/2,J_z=-3/2\rangle = \frac{1}{\sqrt{2}}(|p_x\rangle - i|p_y\rangle)|\downarrow\rangle, \tag{2.42}$$

$$|J=3/2,J_z=1/2\rangle = \frac{-1}{\sqrt{6}}[(|p_x\rangle + i|p_y\rangle)|\downarrow\rangle - 2|p_z\rangle|\uparrow\rangle], \tag{2.43}$$

$$|J=3/2,J_z=-1/2\rangle = \frac{1}{\sqrt{6}}[(|p_x\rangle - i|p_y\rangle)|\uparrow\rangle + 2|p_z\rangle|\downarrow\rangle]. \tag{2.44}$$

Those satisfy $J=1/2$ are

$$|J=1/2,J_z=1/2\rangle = \frac{-1}{\sqrt{3}}[(|p_x\rangle + i|p_y\rangle)|\downarrow\rangle + |p_z\rangle|\uparrow\rangle], \tag{2.45}$$

$$|J=1/2,J_z=-1/2\rangle = \frac{1}{\sqrt{3}}[(|p_x\rangle - i|p_y\rangle)|\uparrow\rangle - |p_z\rangle|\downarrow\rangle]. \tag{2.46}$$

The $J=3/2$ states has an energy Δ_{so} higher than the $J=1/2$ states.

When only the crystal field anisotropy is considered, the splitting occurs between $|p_{x,y}\rangle$ and $|p_z\rangle$ due to the difference between $V(z)$ and $V(x,y)$. It turns out that $|p_z\rangle$ has lower energy compared to $|p_x\rangle$ and $|p_y\rangle$ resulting in the crystal field splitting of Δ_{cr} between $|p_z\rangle$ and $|p_{x,y}\rangle$ [112].

When both effects are combined, the A, B and C valence bands are formed with A containing the $J=3/2$ states made of only $|p_x\rangle$ and $|p_y\rangle$ (Equ. 2.41 and 2.42), and B and C containing significant portion of $|p_z\rangle$. The splitting among the three valence bands are related to Δ_{cr} and

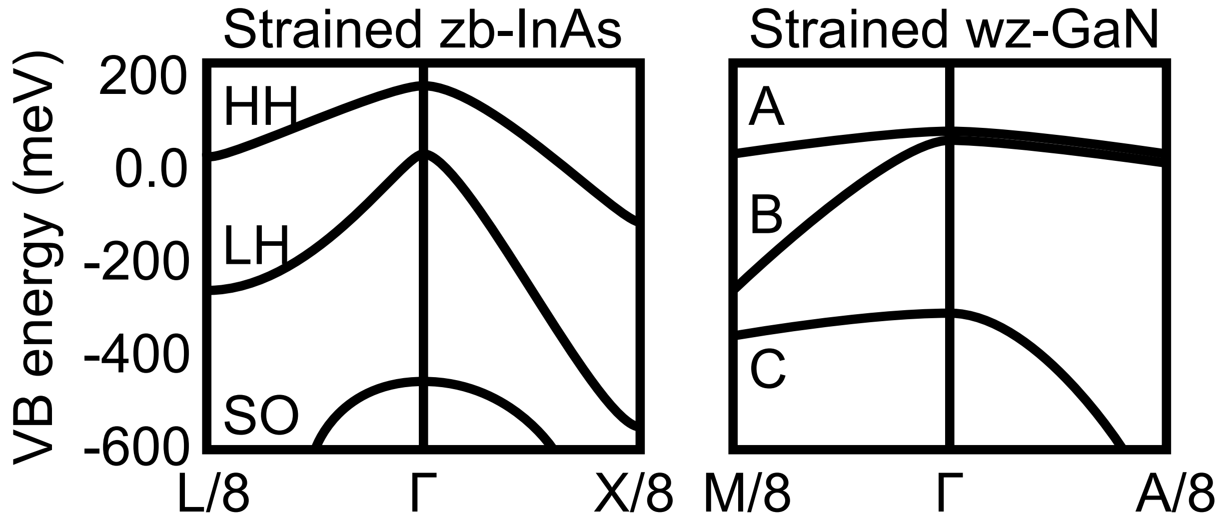

Figure 2.5: Valence band dispersion of strained GaAs and GaN. Taken and modified from [169].

Δ_{so} as [112]:

$$E_{AB} = \frac{1}{2}\left(\Delta_{cr} + \Delta_{so} - \sqrt{(\Delta_{cr} + \Delta_{so})^2 - \frac{8}{3}\Delta_{cr}\Delta_{so}}\right), \tag{2.47}$$

$$E_{BC} = \sqrt{(\Delta_{cr} + \Delta_{so})^2 - \frac{8}{3}\Delta_{cr}\Delta_{so}}. \tag{2.48}$$

2.2.2 Band Structure Under Lateral Anisotropy

The band structure of III-N and III-As materials are both influenced by the size and the strain distribution. However, the change in the valence band are very different between them when a biaxial strain exists as shown in Fig. 2.5. Biaxial lateral strain is commonly present in QDs made of both type of materials. The heave-hole (HH) and light-hole (LH) valence bands in zinc-blend GaAs are separated by almost 200 meV, whereas the corresponding A and B valence bands are separated by only a few meV to about ten meV. The large HH-LH splitting in III-As QDs greatly simplifies the analysis of their optical transition spectrum, since in most cases, only HH related transitions are observed. However, in III-N QDs, both A and B valence bands can have significant contribution to the spectrum.

Without anisotropy in the lateral strain and shape, the energy levels of a GaN QD are shown in Fig. 2.6(a) (the $|Z\rangle$ component of B valence bands are ignored). The allowed optical transitions are marked by the arrows, all of which representing circularly polarized light with σ^+ and σ^- representing clockwise and counter-clockwise rotation. The absorption spectrum in this case is illustrated in Fig. 2.6(c), where peaks with blue and red colors represent x- and y-polarized absorption spectra, respectively.

When there is a lateral anisotropy in the QD's strain and shape, mixing occurs between $|(X - iY)\downarrow\rangle$ and $|(X + iY)\downarrow\rangle$, and $|(X + iY)\uparrow\rangle$ and $|(X - iY)\uparrow\rangle$. Assuming the anisotropy

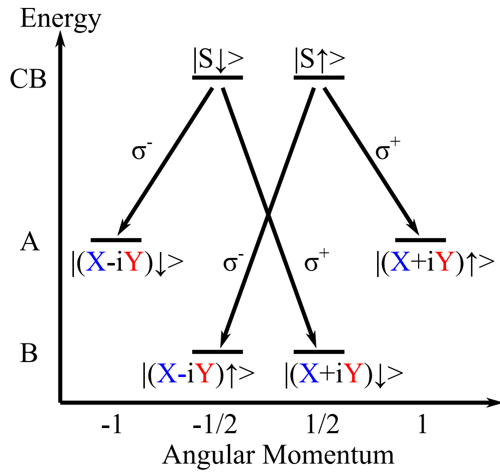

(a)

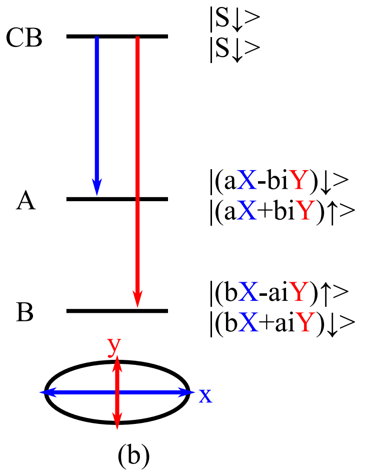

(b)

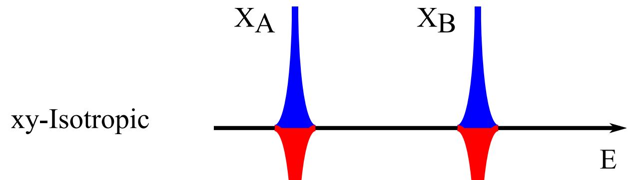

(c)

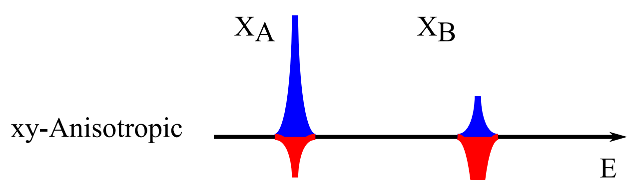

(d)

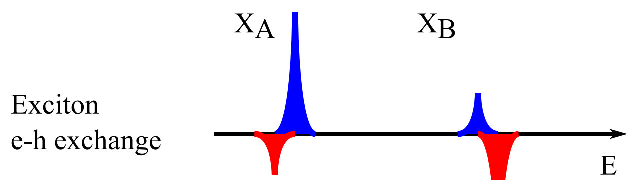

(e)

Figure 2.6: Wurtzite GaN conduction band (CB) and valence band energy levels and optical transitions. (a) Isotropic shape and strain. The $|Z\rangle$ components in the valence bands are ignored. (b) Lateral anisotropic shape and strain. The $|Z\rangle$ components in the valence bands are ignored. The ellipticals at the bottom illustrate x-direction elongated shape. (c–d) Absorption spectrum for x- (blue, positive) and y- (red, negative) polarizations with isotropic, lateral anisotropic shape and strain, respectively. (e) Absorption spectrum when considering the electron-hole exchange interaction under lateral anisotropic shape and strain. (c–e) are inspired by [189].

is due to an x-direction elongation in the QD's shape, then the mixing can be described by a rediagonalization of the following Hamiltonian:

$$\begin{pmatrix} \Delta_{AB}/2 & \Xi \\ \Xi & -\Delta_{AB}/2 \end{pmatrix}, \tag{2.49}$$

which uses $\{|(X-iY)\downarrow\rangle, |(X+iY)\downarrow\rangle\}$ or $\{|(X+iY)\uparrow\rangle, |(X-iY)\uparrow\rangle\}$ basis. This resulting in two elliptical A valence band states $|(aX-biY)\downarrow\rangle$ and $|(aX+biY)\downarrow\rangle$, and B valence band states $|(bX+aiY)\uparrow\rangle$ and $|(bX-aiY)\uparrow\rangle$, respectively. Here a and b are functions of Δ_{AB} and Ξ, as illustrated in Fig. 2.6(b). The resulting absorption spectrum in this case is illustrated in Fig. 2.6(d).

So far, we have not considered the exchange interaction between electron and hole. If the exchange interaction is considered, a fine structure splitting will occure in both A and B excitons as show in Fig. 2.6(e).

2.2.3 Strain and Stress

Strain plays an important role in the properties of GaN based devices. This is especially true in those made of heterostructures, where lack of lattice matching between GaN and its alloys leads to more complicated electric and optical properties compared to other materials such as GaAs. Therefore, it is worthwhile to have a basic understanding of the mechanical characteristics of GaN. We start with a brief introduction of elasticity theory in solid.

Let us consider a solid body S which deforms into S' under external force as shown in Fig. 2.7(a). The deformation can be described by the displacement $\boldsymbol{u}(\boldsymbol{r})$ of each point (atom) $\boldsymbol{r}$ in S to a corresponding point (same atom) $\boldsymbol{r'}$ in S'. To describe strain we use a set of the derivative of $\boldsymbol{u}(\boldsymbol{r}) = (u_x(\boldsymbol{r}), u_y(\boldsymbol{r}), u_z(\boldsymbol{r}))$:

$$\begin{pmatrix} \frac{\partial \boldsymbol{u}(\boldsymbol{r})}{\partial x} \\ \frac{\partial \boldsymbol{u}(\boldsymbol{r})}{\partial y} \\ \frac{\partial \boldsymbol{u}(\boldsymbol{r})}{\partial z} \end{pmatrix} = \begin{pmatrix} u_{xx} & u_{yx} & u_{zx} \\ u_{xy} & u_{yy} & u_{zy} \\ u_{xz} & u_{yz} & u_{zz} \end{pmatrix}. \tag{2.50}$$

where u_{ij} denotes $\frac{\partial u_i(\boldsymbol{r})}{\partial j}$, $i, j = x, y, z$.

We can reduce the number of variables needed to describe strain by using the following strain tensor elements

$$\epsilon_{ij} = \frac{1}{2}(u_{ij} + u_{ji}), \tag{2.51}$$

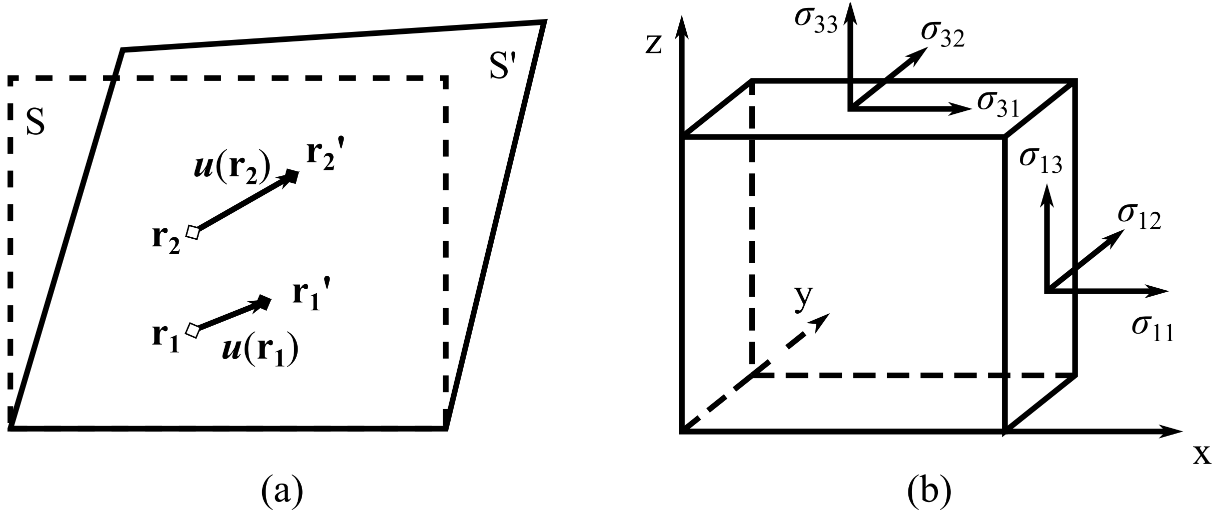

Figure 2.7: (a) Displacement vector. (b) Stress tensor.

or in an expanded form:

$$\begin{pmatrix} \epsilon_1 \\ \epsilon_2 \\ \epsilon_3 \\ \epsilon_4 \\ \epsilon_5 \\ \epsilon_6 \end{pmatrix} = \begin{pmatrix} \epsilon_{xx} \\ \epsilon_{yy} \\ \epsilon_{zz} \\ \epsilon_{yz} \\ \epsilon_{xz} \\ \epsilon_{xy} \end{pmatrix} = \begin{pmatrix} u_{xx} \\ u_{yy} \\ u_{zz} \\ \frac{u_{yz}+u_{zy}}{2} \\ \frac{u_{xz}+u_{zx}}{2} \\ \frac{u_{xy}+u_{yx}}{2} \end{pmatrix}. \tag{2.52}$$

This is because, elements like $u_{ij} - u_{ji}$ represents a rigid rotation. For example, $u_{yz} - u_{zy}$ represents a rotation along x-axis which does not stretch, compress or twist the solid.

The stress tensor describe the force applied to a unit area of the surface of a solid body as shown in Fig. 2.7(b). We define the surface norm direction $\boldsymbol{n_1}$, $\boldsymbol{n_2}$ and $\boldsymbol{n_3}$ pointing along the x-, y- and z-axes respectively. The stress tensor element σ_{ij} denotes the force with a direction of j applied on the surface with a norm of $\boldsymbol{n_i}$. It can be proven that in order for the solid to be in equilibrium, i.e. no translational and rotational acceleration, the stress tensor elements have to be symmetric, i.e. $\sigma_{ij} = \sigma_{ji}$. For example, in Fig. 2.7(b) if σ_{13} and σ_{31} are the only non-zero elements, they have to be equal, otherwise the rigid body will rotate along the y-axis. Similar to strain tensors, we denote stress tensor elements as:

$$\begin{pmatrix} \sigma_1 \\ \sigma_2 \\ \sigma_3 \\ \sigma_4 \\ \sigma_5 \\ \sigma_6 \end{pmatrix} = \begin{pmatrix} \sigma_{xx} \\ \sigma_{yy} \\ \sigma_{zz} \\ \sigma_{yz} \\ \sigma_{xz} \\ \sigma_{xy} \end{pmatrix}. \tag{2.53}$$

Table 2.3: Elasticity, spontaneous polarization and piezoelectric polarization constants for nitride semiconductors. All values are for Ga/Al/In-polar crystals. Data taken from [12].

Materials	GaN	AlN	InN
C_{11} (GPa)	390	396	223
C_{12} (GPa)	145	137	115
C_{13} (GPa)	106	108	92
C_{33} (GPa)	398	373	224
C_{44} (GPa)	105	116	48
P_{sp} (C/cm^2)	-0.034*	-0.090*	-0.042*
d_{13} (pm/V)	-1.6	-2.1	-3.5
d_{33} (pm/V)	3.1	5.4	7.6
d_{15} (pm/V)	3.1	3.6	5.5

* Negative sign means opposite to the growth direction.

The stress and strain tensors are connected by the stiffness tensor C_{ij} as:

$$\sigma_i = \sum_j C_{ij}\epsilon_j, \tag{2.54}$$

where $i, j = 1, 2, ..., 6$. However, not all C_{ij} are non-zero. The crystal symmetry of wurtzite crystal leads to a reduction of $[C_{ij}]$ into [113]:

$$(C_{ij}) = \begin{pmatrix} C_{11} & C_{12} & C_{13} & 0 & 0 & 0 \\ C_{12} & C_{11} & C_{13} & 0 & 0 & 0 \\ C_{13} & C_{13} & C_{33} & 0 & 0 & 0 \\ 0 & 0 & 0 & C_{44} & 0 & 0 \\ 0 & 0 & 0 & 0 & C_{44} & 0 \\ 0 & 0 & 0 & 0 & 0 & \frac{C_{11}-C_{12}}{2} \end{pmatrix}. \tag{2.55}$$

The values of C_{ij} are shown in Tab. 2.3.

2.2.4 Deformation Potential

As we mentioned earlier that the bandgap of a semiconductor increases as its lattice constant increases. Therefore, when GaN or any other semiconductor is compressed or stretched, the bandgap as well as the energetic position of the conduction and valence bands will increase or decrease. This is particularly important in InGaN/GaN quantum wells as will be presented in details later.

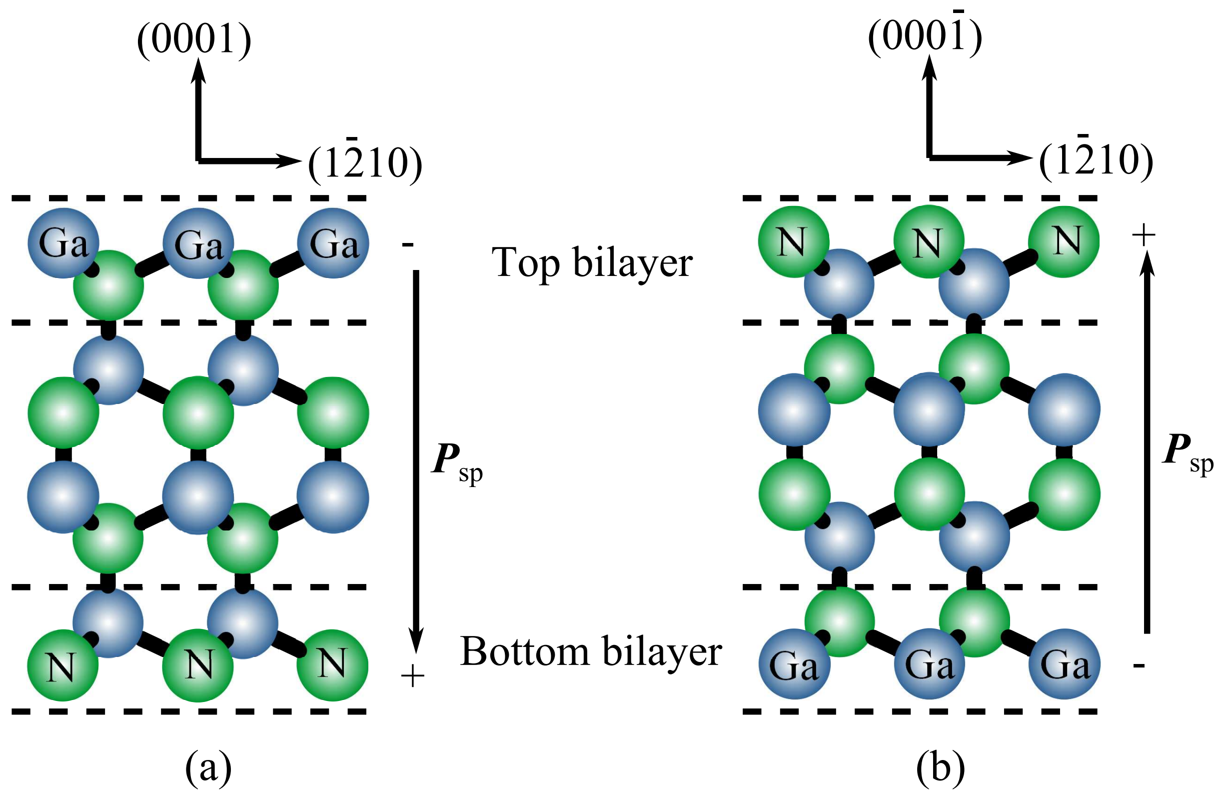

Figure 2.8: Polarity and spontaneous polarization of GaN. (a) Ga-polar. (b) N-polar.

2.2.5 Spontaneous Polarization

In c-plane GaN, the Ga^+ layer and N^- layer alternate along the growth direction as shown in Fig. 2.8. If the top surface is terminated by Ga-monolayer the crystal is called Ga-polar, otherwise, it is called N-polar. Equivalently, the polarity is also defined by the relative position of the Ga and N atoms in the Ga-N bilayer. Typically, GaN grown by MOCVD on c-sapphire are Ga-polar [114]. N-polar GaN surface can be obtained from the interface between the GaN and the substrate by removing the substrate. In molecular beam epitaxy (MBE) growth, N-polar GaN can also be obtained by inserting a AlN buffer layer.

The polarity gives rise to spontaneous polarization. In Ga-polar GaN (Fig. 2.8(a)), the top bilayer has negative charge, because the N-atoms in the top bilayer attract electrons from the Ga-atoms in the top second bilayer. This leads to negative charge at the top surface. Similarly, the bottom surface exhibit positive charge in Ga-polar GaN. The surface charge density is about 2×10^{17} e/cm^2, leading to a spontaneous polarization of 0.034 C/cm^2 pointing to the bottom surface. The opposite occurs for N-polar GaN as shown in Fig. 2.8(b). Table 2.3 summaries the spontaneous polarization for GaN, AlN and InN [12]. The spontaneous polarization in III-N semiconductors are much greater than other III-V semiconductors.

Under normal environment, however, bulk GaN does not display a net dipole moment expected from the spontaneous polarization. This is because the dipole moment is neutralized by external charges accumulated at the surfaces. Only when the crystal is perturbed, for example by heating, the electric dipole moment starts to display. The phenomenon of heating-induced

polarization is called pyroelectricity.

2.2.6 Piezoelectric Polarization

Polar crystals can also display polarization under mechanical stress. This phenomenon is called piezoelectricity. The piezoelectric polarization $\boldsymbol{P}_{\mathrm{pz}} = (P_{\mathrm{pz,x}}, P_{\mathrm{pz,y}}, P_{\mathrm{pz,z}})^T$ is connected with the stress tensor $[\sigma]$ as:

$$\begin{pmatrix} P_{\mathrm{pz,x}} \\ P_{\mathrm{pz,y}} \\ P_{\mathrm{pz,z}} \end{pmatrix} = \begin{pmatrix} 0 & 0 & 0 & 0 & d_{15} & 0 \\ 0 & 0 & 0 & d_{15} & 0 & 0 \\ d_{13} & d_{13} & d_{33} & 0 & 0 & 0 \end{pmatrix} \begin{pmatrix} \sigma_1 \\ \sigma_2 \\ \sigma_3 \\ \sigma_4 \\ \sigma_5 \\ \sigma_6 \end{pmatrix}. \tag{2.56}$$

From this equation we can see that when tensile or compressive stress is applied to GaN, it will generate a piezoelectric polarization along the c-axis. The values of the piezoelectricity constants are shown in Tab. 2.3.

2.2.7 Phonons

GaN, as well as all III-V semiconductors, have two atoms in each unit cell. Therefore, there are six vibrational degree of freedoms, corresponding to six phonon bands. Three of them are acoustic phonon bands whereas the other three are optical phonon bands. Acoustic phonon modes are due to the center of mass vibration of the unit cell. Optical phonon modes are due to the relative motion between the Ga and N atoms. Both acoustic and optical phonons can be longitudinal or transversal depending on the whether the vibration direction is aligned with the phonon propagation direction (wave-vector).

Acoustic phonons energy is linearly dependent on the wave vector k when $k \ll \frac{2\pi}{\Lambda}$, as expected for acoustic waves. Optical phonons, on the other hand, have finite value at $k = 0$ and have nearly flat dispersion curves. This is because optical phonons originate from the relative motion of the two atoms within a unit cell. Among the two types optical phonons, longitudinal optical (LO) phonons have higher energy than the transversal optical (TO) phonons. This is because the LO phonon vibration is coupled with the Coulomb interaction between Ga and N atoms [103]. This also leads to the coupling between exciton and LO phonon.

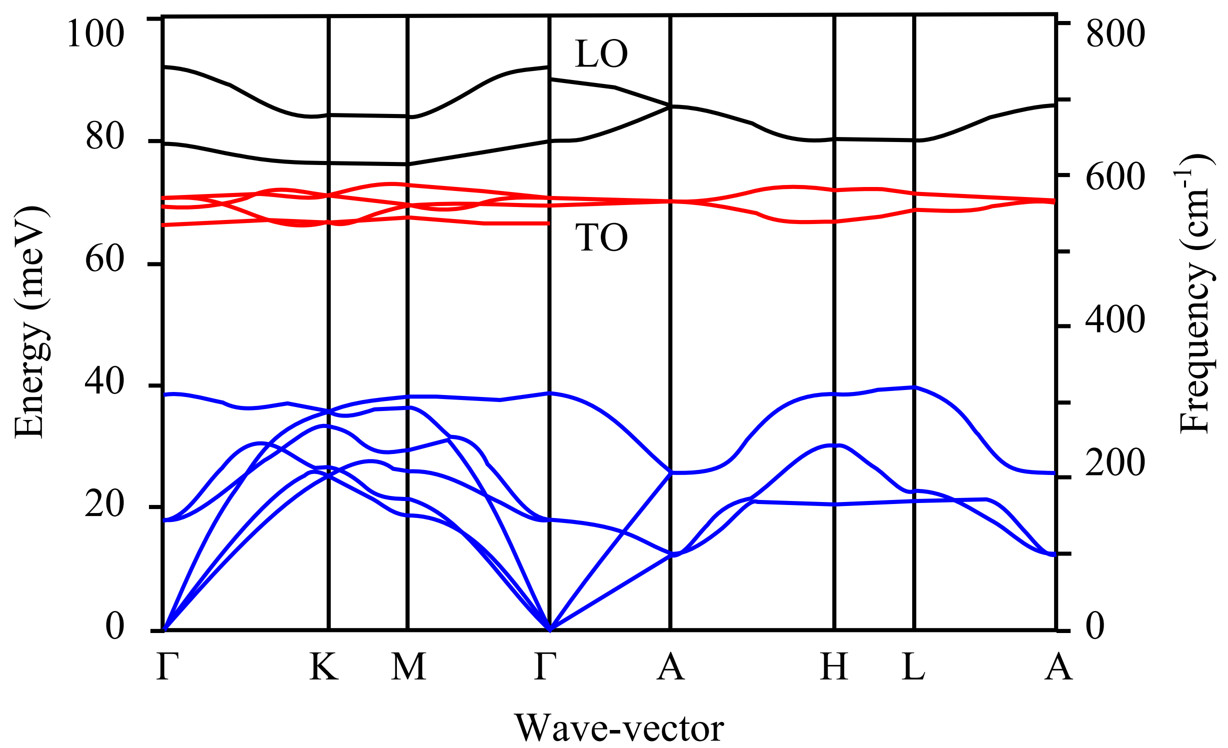

Figure 2.9: The theoretical phonon dispersion curve of GaN. Figure adopted from [11].

CHAPTER 3

Fabrication and Characterization of InGaN/GaN Disk-in-Nanowires

In this chapter, we first show the device structure and fabrication flow for both optically and electrically pumped site-controlled InGaN/GaN DINs in Sec. 3.1. The experimental setups used to characterize the PL and EL properties are shown in Sec. 3.2.

3.1 Device Structure and Fabrication

3.1.1 Optically Pumped Disk-in-Nanowires

The structure of an optically pumped DIN is shown in Fig. 3.1(a). Each DIN is made of a 3 nm thick $In_{0.15}Ga_{0.85}N$ ND in a 120 nm tall cone-shaped GaN pillar. The ND has a 10 nm thick GaN at the top and has sidewalls exposed in air. The GaN pillar has a sidewall slope of 75 °. The diameter of each ND can be controlled down to 15 nm with $\sim$ 2 nm standard deviation. The location of each DIN can be controlled with a few nanometer precision.

In all our samples, we have dense arrays of DINs with 300 nm inter-dot separation and sparse arrays of DINs with 5 μm inter-dot separation. Fig. 3.1(b) shows the SEM image of four DINs with 25 nm diameter in a dense array.

The fabrication flow of the optically pumped DINs is shown in Fig. 3.2 [9, **?**]. It starts with a planar single $In_{0.15}Ga_{0.85}N$/GaN QW grown on (0001) c-plane sapphire substrate by MOCVD. The thickness of the InGaN layer is 3 nm with 2 MLs of fluctuation. It is sandwiched by a 10 nm thick unintentionally doped GaN (uid-GaN) on the top and a 5 μm thick uid-GaN buffer layer at the bottom. The planar sample is first coated with PMMA at 6000 round per minutes (RPM) for 30 seconds which is followed by a baking at 180 °C for 180 seconds. The sample is then loaded into a Jeol JBX-6300FS electron-beam lithography system with the following writing configuration: current 500 pA, voltage 100 kV, spot size 2 nm, dose 1600 $\mu C/cm^2$. After the electron-beam writing, the sample is developed in methyl isobutyl ketone (MIBK):isopropyl alcohol (IPA) (1:3) solution for 1 minute and then IPA for 30 seconds. After drying the sample with a nitrogen gun, it is loaded into an electron-beam evaporator to deposit a layer of Ni with 60 nm in thickness. The base pressure for the deposition is 2×10^{-6} mbar. After electron-beam

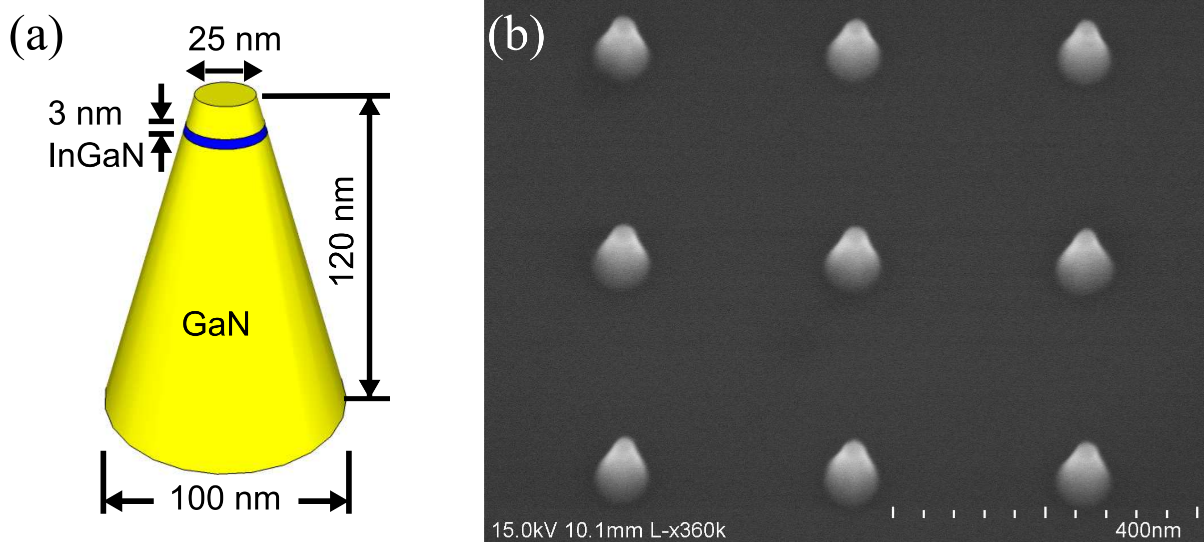

Figure 3.1: Structure of optically pumped NDs. (a) The schematic plot of a single GaN nanopillar containing an InGaN nanodisk of diameter $D = 25$ nm. (b) The SEM image of a part of a dense arrays of QDs of diameter $D = 25$ nm and dot-to-dot separation 300 nm. The viewing angle is 45°.

evaporation, unwanted Ni and PMMA are liftoff by immersing the sample in acetone, leaving Ni islands as the etching mask for the next step. The diameter of the Ni island determine the diameter of ND. The NDs are formed by etching the sample in a LAM 9400 plasma etcher for 45 seconds using the following ICP-RIE recipe: TCP RF 200 W, bias RF 150 W, Cl_2 15 sccm, Ar 20 sccm. Finally, the Ni islands are removed using HNO_3:H_2O (1:2) solution for 60 seconds.

3.1.2 Electrically Pumped Disk-in-Nanowires

The structure of an DIN for electrical pumping is similar to that of an optically pumped one. Each DIN, as shown in Fig. 3.3(a), contains a 3 nm thick $In_{0.15}$GaN QD sandwiched between a 120 nm thick Mg-doped GaN (p-GaN) and 12 nm thick uid-GaN layers at the top, and a 12 nm thick uid-GaN and 83 nm thick Si-doped GaN (n-GaN) layers at the bottom. The doping densities of the p-GaN and n-GaN are 3×10^{17} cm^{-3} and 1×10^{18} cm^{-3}, respectively.

The structure of an electrically driven device based on such a DIN is illustrated in Fig. 3.3(b). The top 30 nm portion of the p-GaN layer is in contact with a 200 nm thick semi-transparent ITO conductive film, which is electrically insulated from the n-GaN by a layer of 200 nm thick SOG. The p- and n-contacts are both metalized by Ti/Au (25 nm/500 nm) pads.

The fabrication flow of electrically pumped DINs is summarized in Fig. 3.4. It starts with a planar single InGaN QW LED grown on the (0001) plane (c-plane) of a sapphire substrate by MOCVD. We first fabricate cone-shaped DINs by patterning Ni etching-masks using electron-beam lithography and then etching the GaN using Ar-Cl_2 RIE, as explained in Fig. 3.2. The only difference is that here the Ar-Cl_2 RIE lasts for 75 second in order to achieve 230 nm pillar height.

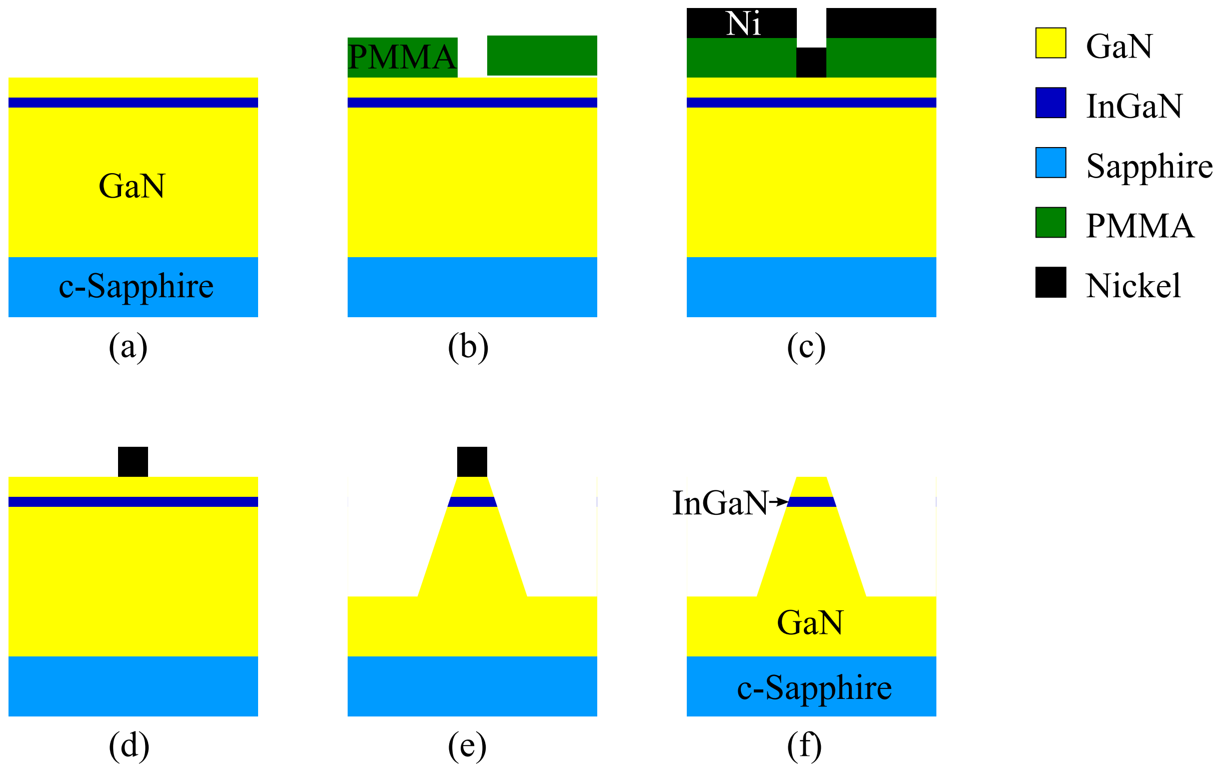

Figure 3.2: Fabrication of optically pumped NDs. (a) Planar single $In_{0.15}Ga_{0.85}N$/GaN QW grown on c-plane sapphire. (b) Coat PMMA and electron-beam lithography. (c) Deposit nickel. (d) Nickel liftoff. (e) ICP-RIE etching. (f) Nickel removal.

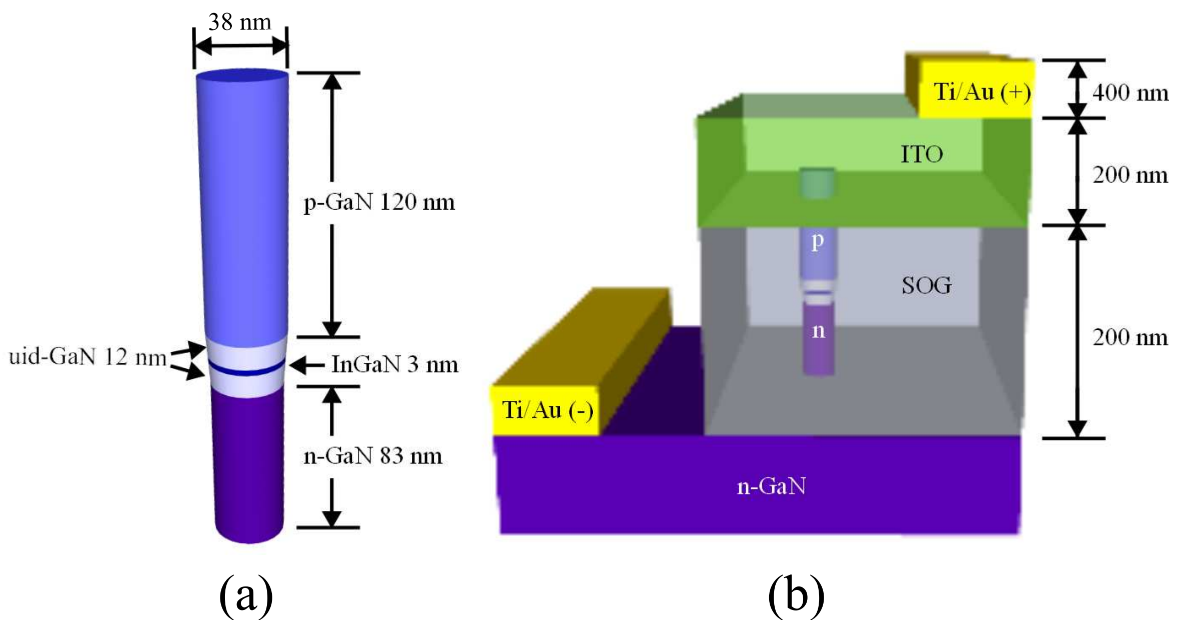

Figure 3.3: The structure of electrically pumped DINs. (a) A bare DIN without electrical contacts. (b) A DIN with electrical contacts.

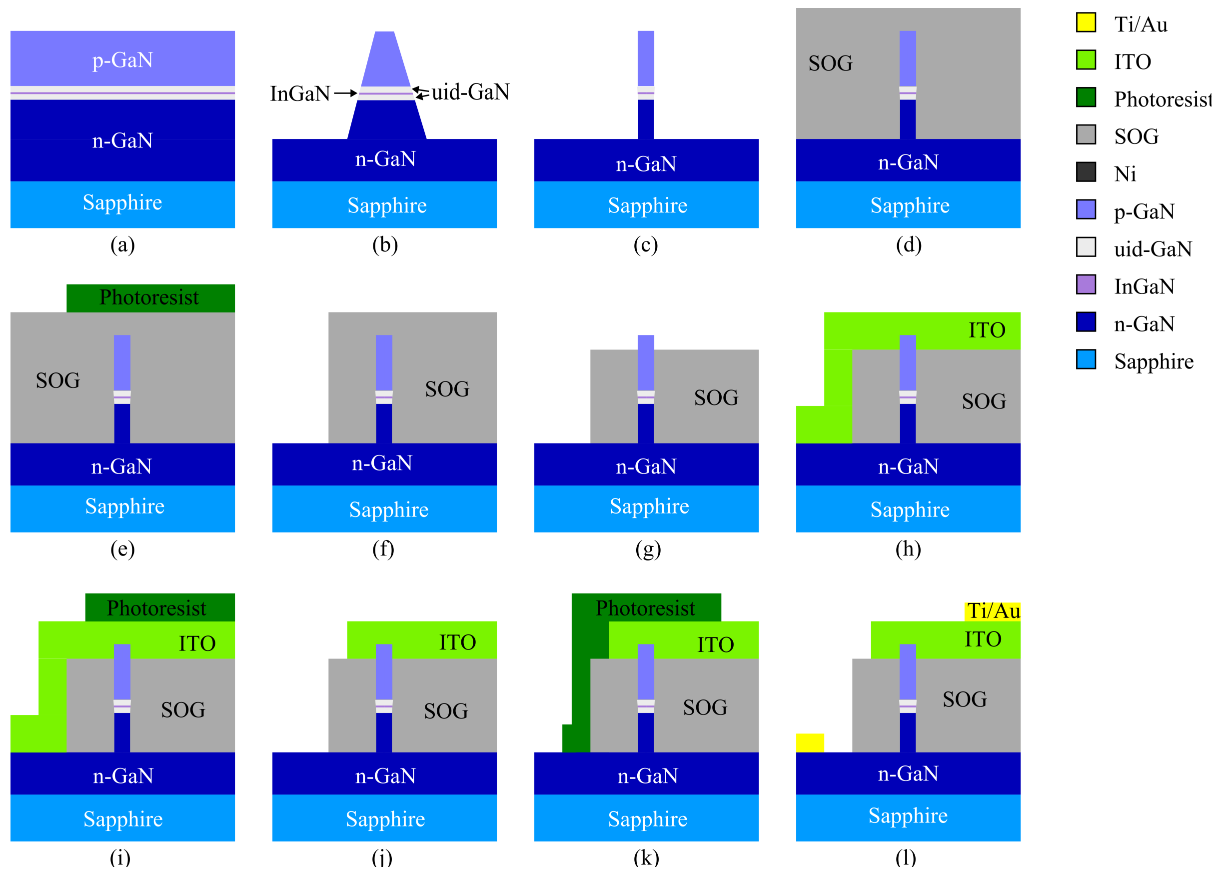

Figure 3.4: Fabrication flow of electrically pumped DINs. (a) Planar single InGaN/GaN QW LED grown on the c-plane of a sapphire substrate by MOCVD. (b) Fabricate cone-shaped DINs following the method in Fig. 3.2. (c) Cleave the slant sidewall using KOH solution. (d) Spin coat SOG and cure. (e) Pattern photoresist etching mask using optical lithography. (f) Wet etch SOG using buffered HF to expose part of the GaN for n-contact. (g) Etch back SOG using CF_4-CHF_3 plasma RIE with careful SEM monitoring. (h) Deposit ITO using sputtering. (i) Pattern photoresist etching mask using optical lithography. (j) Wet etch ITO using HCl:H2O (1:3). (k) Pattern photoresist etching mask using optical lithography. (l) Deposit Ti/Au contacts and liftoff in acetone.

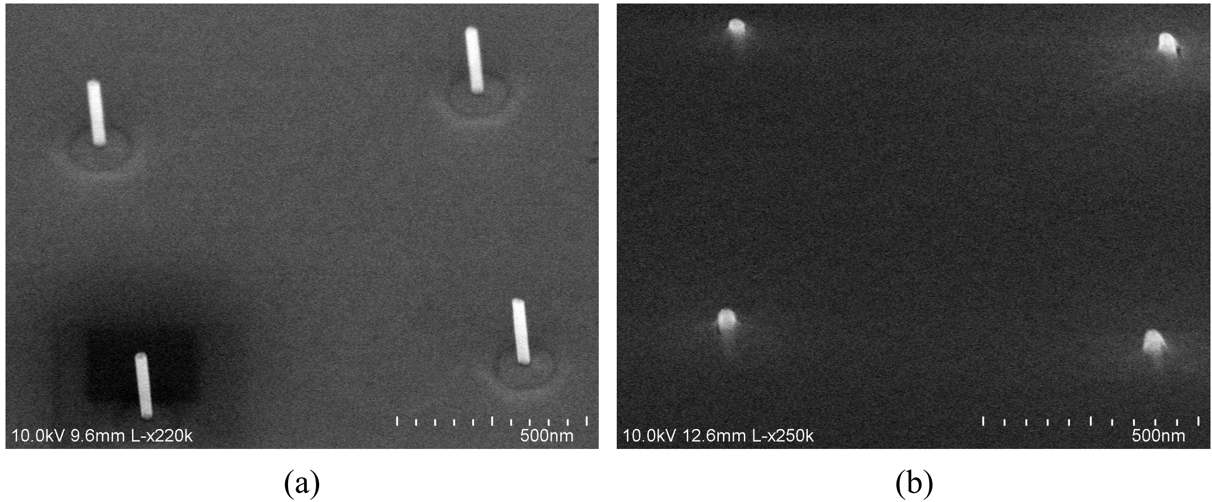

(a) (b)

Figure 3.5: The SEM images of (a) four DINs after KOH wet-etching, and (b) four DINs after SOG etch-back. All SEM images are 45°-view.

The slanted sidewall of these cone-shaped DINs are then cleaved by selective wet-etching in a KOH-based solution AZ400K developer [115] for 220 minutes. The KOH solution etches the DIN's sidewall $(10\bar{1}0)$ m-plane and has negligible impacts on the DIN's top diameter and height. The SEM image of four DINs after KOH wet-etching is shown in Fig. 3.5(a). This technique removes the plasma damaged sidewall material and reduces the surface defect states [115], which may have improved the current-injection efficiency in our DINs. Most importantly, it allows us to fabricate cylindrical DINs that have simultaneously thick p-GaN for applying electrical contact and small InGaN ND diameter for quantum confinement [2], which could not be easily achieved on cone-shaped DINs.

To apply electrical contacts to the DINs, we first planarize the sample by spin-coating Filmtronics 500F SOG at 3000 RPM for 30 seconds. This is followed by a three-step pre-baking at 80, 130, 250 °C. Then the sample is transfered to a nitrogen purged hotplate which ramps the temperature from 20 °C to 400 °Cat 450 °C/hour ramp rate. The sample stays in 400 °C for an hour and naturally cool down to 20 °C. The thickness of the SOG is measured to be ∼580 nm. The quality of the planarization depends on the DIN diameter as well as the inter-dot separation. We have made sure that the sample is planarized within 10 nm for DINs with diameter as large as 100 nm and DIN arrays with inter-dot separation as small as 500 nm.

After the planarization, the SOG is patterned using optical lithography and buffered HF to expose a part of the n-GaN substrate for applying the n-contact. The SOG is then etched back using CF_4-CHF_3 plasma to expose 30 nm p-GaN layer for applying the p-contact. This etch-back step needs to be carefully monitors as over-etching will cause short circuit and under-etching will cause open circuit. We used multiple etching steps each followed by an SEM check. The SEM image of an array of DINs after SOG etch-back is presented in Fig. 3.5(b), showing DINs embedded in the SOG except for their top 30 nm portion of p-GaN layer.

The ITO contact is deposited using a Kurt J. Lesker Lab-18 magnetron sputter. An ITO layer

of 200 nm in thickness is deposited by DC sputtering an ITO target (10% SnO_2 by weight) in Ar-O_2 (2.5% O_2 by volume) atmosphere. The deposition rate is $\sim$2 Å/s. Afterward, a layer of photoresist (SPR220 3.0) is spin coated on the sample and patterned using optical lithography to form the ITO etching mask. The ITO is patterned by wet etching in HCl:H_2O (1:3) solution for 50 seconds. As-deposited ITO exhibits poor transparency and high ITO/p-GaN contact resistivity. To improve the ITO film quality, the sample is annealed in a Jetfirst annealer in forming gas at 400 °C for 5 minutes. The annealed ITO is more transparent and conductive. Most importantly, we have seen significant reduction in the ITO/p-GaN contact resistivity.

The p- and n-contacts are metalized by patterning photoresist, electron-beam evaporating Ti/Au (25 nm/500 nm) film and acetone liftoff. The Ti layer is used to improve the adhesion between the Au film and the underlying ITO layer. This is very important for the wire-bonding process in the next step.

Finally, in the packaging step, the sample is diced into 5 mm$\times$8 mm dies using an ADT 7100 dicing saw and Au-Au wire-bonded to a Spectrum-Semiconductor CSB01660 ceramic dual in-line package (DIP) chip carrier using a K&S 4123 wire bonder. The die is fixed in the cavity of the chip carrier by Emerson and Cuming Stycast epoxy containing 2850 FT resin and catalyst 9. The DIP chip is plugged onto a customized cold finger in our Janis ST-500 cryostat for electrical and optical characterizations. A thin layer of Apiezon N vacuum grease is applied between the DIP and the copper cold finger to ensure good thermal contact.

3.2 Characterization Systems

3.2.1 Photoluminescence Characterization

The setup used to characterized the PL of NDs is illustrated in Fig. 3.6. The sample is mounted on the copper cold finger of a Janis ST-500 He-flow cryostat with Ted Pella 16062 conductive silver paint. The cold finger temperature is controlled and stabilized by a Lakeshore 335 temperature controller together with the temperature sensor and heater installed in the cryostat. The sample is excited from an angle 55° from the normal direction with a 390 nm laser. The 390 nm laser is obtained by frequency doubling a 780 nm wavelength Spectra-Physics Tsunami Ti:Sapphire laser which has a 150 fs pulse duration and an 80 MHz repetition rate. The Ti:Sapphire laser is pumped by a 530 nm Spectra-Physics Millennia diode pumped solid state (DPSS) laser capable of providing up to 15 W power. The laser spot on the sample surface was elliptical with a 20 μm short axis and a 35 μm long axis.

We study the PL and TRPL properties of NDs using a confocal microscope setup. This setup consists an objective lens L1 with a focal length $f = 5$ mm and a numerical aperture (NA) 0.6 and a pair of confocal lenses L2 and L3 with a focal length $f = 75$ mm. The setup is switchable between ensemble and single ND measurements by removing or placing a 25 μm pinhole at the confocal plane. The pinhole is capable of isolating the emission of a single ND as long as the

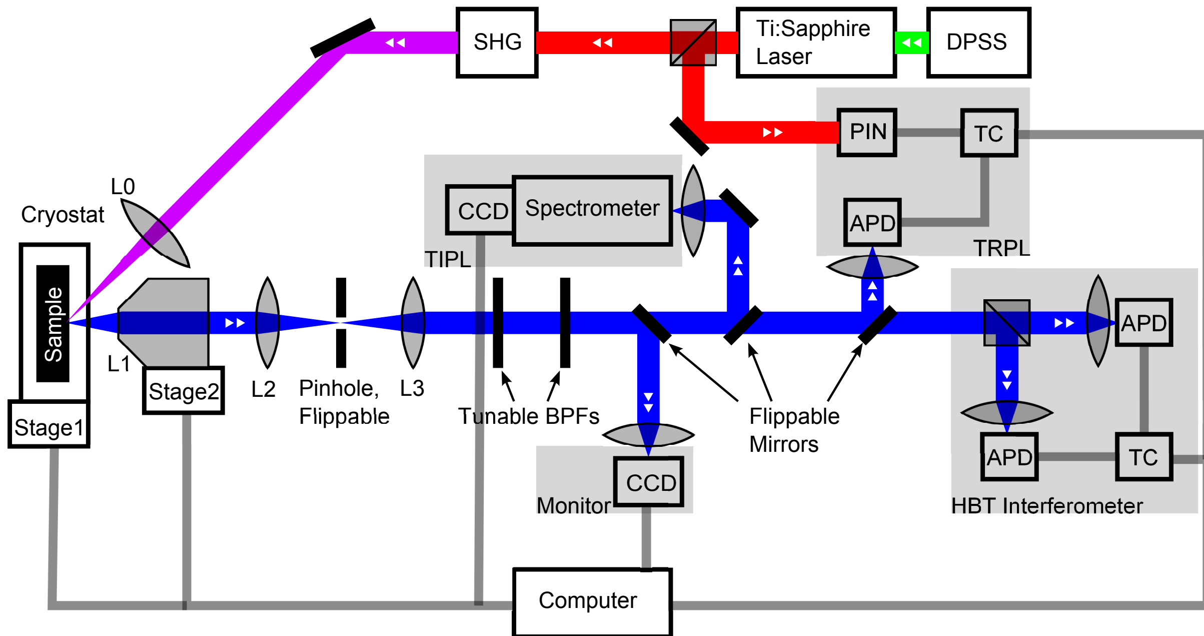

Figure 3.6: The experimental setup for PL characterization.

neighboring NDs are over 1 μm away.

A Semrock FF02-409/LP longpass filter (not shown) is used to remove the scattered laser and only allow wavelengths longer than 400 nm through. For TRPL measurements, an additional pair of Semrock TBP01-449/15 tunable bandpass filters (BPFs) are used to further select a spectral window with tunable position from 400 nm to 440 nm and tunable bandwidth from 2 nm to 10 nm.

A charge-coupled device (CCD) camera is used to monitor the position of NDs through their PL by applying the longpass filter. The CCD image is recorded by a computer which also controls the motion of the cryostat and the objective lens L1. The cryostat is mounted on a high-load XYZ-stage driven by stepper motors with $\sim$1 μm positioning accuracy and 1 inch travel range. The objective lens is mounted on a XYZ-stage driven by piezo-actuators which allows fast (due to the low weight of the objective lens compared to the cryostat) and accurate (nanometer resolution) positioning. The XYZ-stage of the objective lens and the CCD monitoring camera form a fast-response feedback loop to allow real-time compensation of the mechanical drift of the cryostat. This is necessary for measurements requiring hour-long data collection time.

The time-integrated photoluminescence (TIPL) spectrum is measured using a Princeton Instrument Acton SP2500i spectrometer with 0.5 m focal length, 6.5 f-ratio, and a 600 g/mm grating. This provides a 0.6 meV (0.08 nm) spectral resolution at $\sim$ 3 eV (400 nm). The spectrometer is equipped with a nitrogen-cooled Princeton Instrument Spec-10 CCD camera which contains a 1024$\times$256 array of pixels of 26 μm in size. Each pixel has over 50% quantum efficiency (QE) at $\sim$400 nm wavelength and a negligible dark count due to the nitrogen cooling. The CCD chip is typically cooled down to -90 °C.

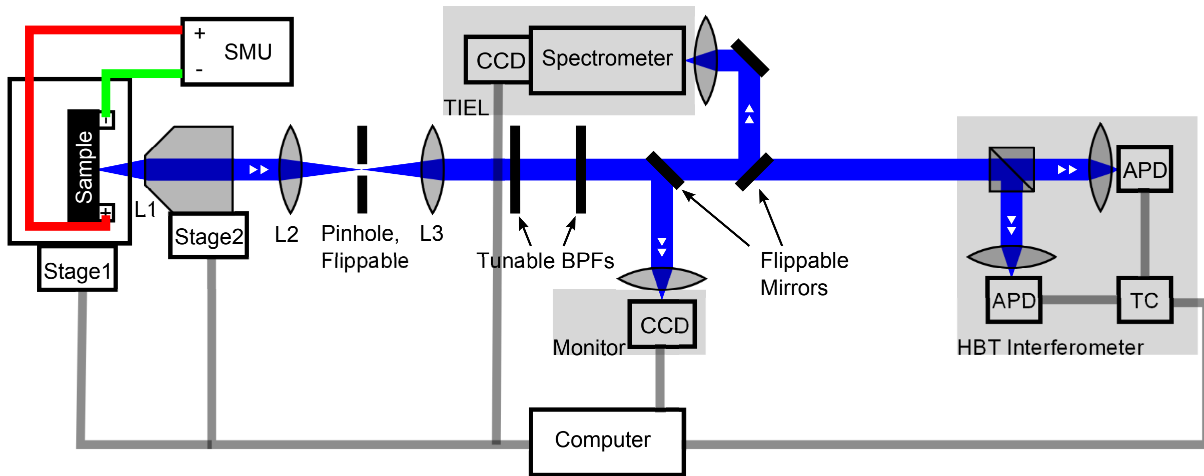

Figure 3.7: The experimental setup for DC EL characterization.

The TRPL measurement is done by a time-correlated single-photon counting (TCSPC) setup composed of an avalanche photodiode (APD), a p-i-n photodiode (PIN) and a time correlator (TC). The APD has a QE of 40% at 400 nm, a dark count rate of 70 cps and a 200 ps full width at half maximum (FWHM) in its instrument response function (IRF) at 400 nm. The PIN converts laser pulses from the Ti:Sapphire laser into TTL signals. After each laser pulse, the TTL signal generatd by the PIN starts a timer in the TC. The timer record the time until a photon is received by the APD which triggers the end of the timer. The TC records the number of start-stop signal pairs as a function of the time delay between them. This forms the TRPL traces.

The second-order correlation ($g^{(2)}$) function of single DINs is measured using a Hanbury Brown-Twiss (HBT) interferometer [116] composed of a 50:50 unpolarized beamsplitter, two APDs and a TC. The operation principle is very similar to that of the TRPL measurement, except that in an HBT interferometer the PIN is replaced by an APD. Obviously, if the DIN only emits one photon at a time, it is impossible for the TC to record start-stop signal pairs separated by zero time delay, i.e. one photon cannot be detected by the two APDs simultaneously. Hence, we can use the HBT interferometer to verify if a photon source is a single-photon source or not.

3.2.2 Electroluminescence Characterization

The experimental setup used to characterize the EL is similar to the one used for PL characterization, except for the way the sample is pumped. We perform both DC and RF characterizations for our samples.

The DC setup, illustrated in Fig. 3.7, uses a source measurement unit (SMU) to provide voltage (current) source and measuring the resulting current (voltage) across the sample. This setup allows us to perform current-voltage (IV), time-integrated electroluminescence (TIEL) and $g^{(2)}$ measurements.

The RF setup, illustrated in Fig. 3.8, used a DC biased RF source to pump the sample. A

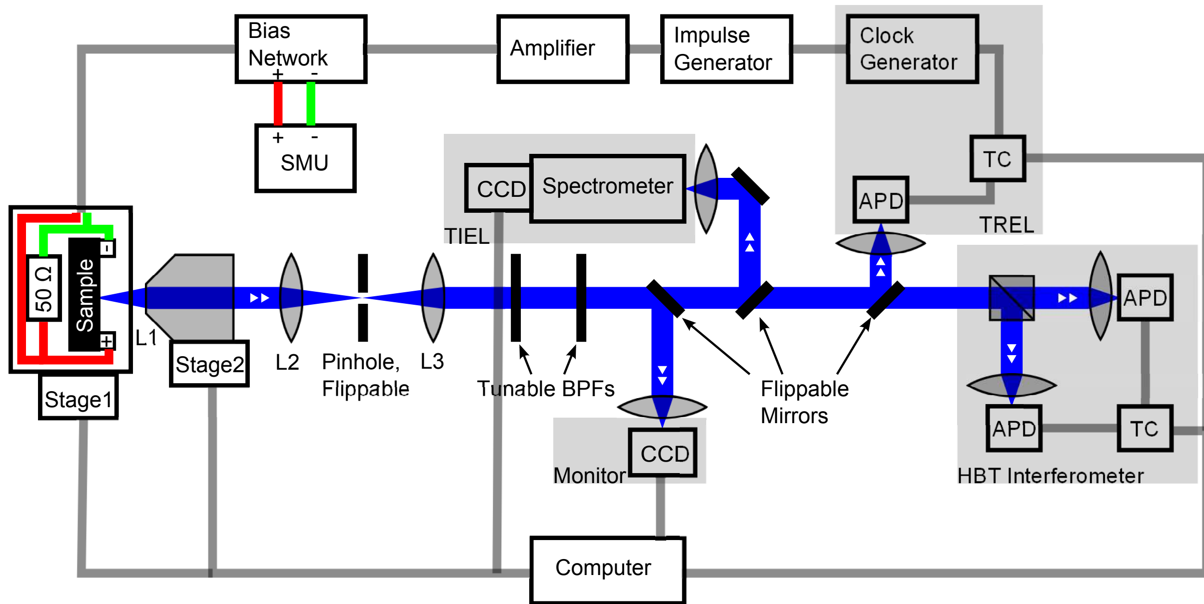

Figure 3.8: The experimental setup for RF EL characterization.

Stanford Research System CG635 clock generator capable of generating up to 2 GHz square waves is used to trigger an Alnair Labs EPG-200 impulse generator capable of generating electrical impulses with positive polarization, 500 mV V_{pp} and 80 ps FWHM at up to 2 GHz repetition rate. The impulses are amplified by a tunable RF amplifier to obtain up to 4.5 V V_{pp}. A DC bias from the SMU is added to the RF impulses via an Aeroflex 8810SFF1-26 bias tee. All RF components described above require 50 Ω impedance matching. In order to match the impedance, a 50 Ω TEH100M50R0JE-ND non-inductive resistor is connected in parallel to the sample and placed in the cryostat close to the sample.

This setup allows us to perform time-resolved electroluminescence (TREL) and pulsed-$g^{(2)}$ measurements. The TREL measurement uses the clock generator and an APD to send start and stop triggers to the TC, which is similar to the TRPL measurement explained in Fig. 3.6.

CHAPTER 4

From Quantum Well to Quantum Dot: Effects of Diameter Reduction in InGaN/GaN Nanodisks

As explained in the previous chapters, the DINs studied in this dissertation are etched from a planar InGaN/GaN QW, and hence have finite diameters. In this chapter, we study the diameter dependence of the mechanical, electrical and optical properties of the InGaN ND in a DIN. In Sec. 4.1, we show the drastic difference in the optical properties of a ND with very large diameter and a ND with very small diameter, which is ultimately due to the strain relaxation at the ND sidewall. In Sec. 4.2, we show that the lateral strain distribution in a ND can be understood by a simple analytical model. In Sec. 4.3, we show that the strain relaxation leads to a strong blueshift in ND's PL energy as a result of the quantum-confined Stark effect (QCSE). In Sec. 4.4, we show that the strain relaxation also leads to a drastic enhancement in the oscillator strength of the ND. Section 4.4 concludes this chapter.

4.1 Quantum-Well-Nanodisk vs. Quantum-Dot-Nanodisk

To highlight the drastic effects of the diameter of a ND, we first compare the optical properties of a very large and a very small NDs. The large ND is 2 μm in diameter and fully strained; it corresponds to the QW-regime and we call it QW-ND. The small ND is 15 nm in diameter and should have the least amount of strain. It is found to be QD-like and will be called QD-ND.

The emission from the QW-ND is strongly influenced by the strain in the InGaN layer, common to III-N QWs grown on c-plane[117, 118], as explained in Chap. 2. At low excitation intensities, as shown in Fig. 4.1(a), the PL spectra are hundreds of meV broad with pronounced optical-phonon replicas due to the strain-enhanced wavefunction overlapping between electrons, holes and the longitudinal interface optical-phonon modes[119, 120]. The TRPL measurement shows that carriers decay very slowly in the QW-ND (Fig. 4.1(b)). In order to quantify the decay time of the QW-ND, we used a mono-exponential function to fit the initial 12.5 ns decay curve and got a $1/e$ initial decay time of $\tau_{QW}^{*} = 152$ ns. Such a slow PL decay indicates a weak oscillator strength f_{os} due to large strain-induced electric fields. Note, however, that it is expected that a strained InGaN QW has a stretched exponential decay trace

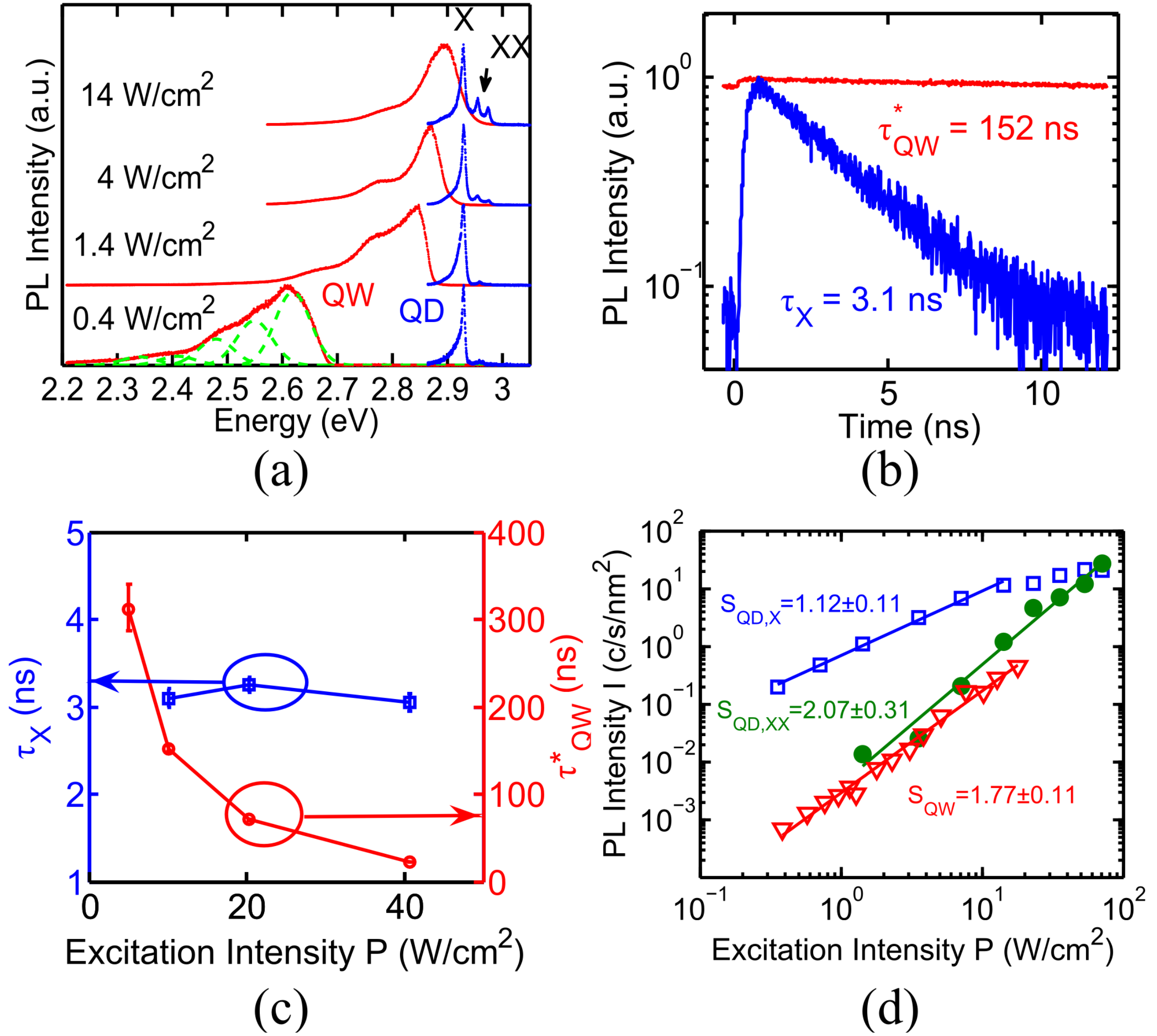

Figure 4.1: (a) The PL spectra from a QW-ND with a diameter of 2 μm (red lines) and a QD-ND with a diameter of 20 nm (blue lines) at excitation intensities $P = 0.4$, 1.4, 4 and 14 W/cm^2. The spectra are normalized to their maxima and vertically shifted to ease the comparison. The spectra of the QW-ND is broadened by optical-phonon replicas as illustrated in dashed green lines. (b) The TRPL decay traces of QW-ND (red) and QD-ND's X peak (blue) measured at $P = 10$ W/cm^2. (c) The mono-exponential decay time of the X peak of the QD-ND τ_X (blue square) and the decay time obtained from mono-exponential fit of the initial 12.5 ns decay trace of the QW-ND τ^*_{QW} (red triangle) at various excitation intensities. (d) The integrated PL intensity of the X (blue square) and XX (green circle) peaks from the QD-ND and the overall integrated PL intensity, including the optical-phonon replicas, from the QW-ND (red triangle). All the intensity values I are normalized by the lateral area of the InGaN layers and hence have a unit of count per second per nanometer square (c/s/nm^2). A linear fit of $log(I)$ vs. $log(P)$ shows that the intensities of the X and XX peaks of the QD-ND, and the spectrally integrated intensity of the QW-ND are proportional to $P^{1.12}$, $P^{2.07}$ and $P^{1.77}$, respectively.

due to the reduction of the carrier density and, thus, the increase of the piezo-electric field over time, which is not obvious in Fig. 4.1(b) due to the short time window.

With increasing excitation intensity P, optical-phonon replicas are reduced, the PL peak energy E blueshifts by more than 300 meV (Fig. 4.1(a)), and the decay time of the emission shortens (Fig. 4.1(c)) by orders of magnitude. These can all be qualitatively explained by the screening of the built-in field with increased photo-carrier density.

The integrated PL intensity I, including optical-phonon replicas, increases super-linearly with the excitation intensity P as $I \propto P^{1.77}$ (Fig. 4.1(d)). This is because non-radiative recombination processes either have little dependence on carrier density, such as for the Shockley-Hall-Read process[121], or have negligible contributions over the range of excitation intensities investigated here, such as for the Auger recombination[122]. Therefore, at higher excitation intensities, an enhanced radiative decay results in an improved IQE, manifested as the super-linear increase of the PL intensity. Assuming that the photo-carrier generation rate is proportional to P, it immediately follows that the IQE η_{int} increases with P as $\eta_{int} \propto I/P \propto P^{0.77}$.

In contrast to the QW-ND, the emission from the QD-ND show distinct properties. As shown in Fig. 4.1(a), at low excitation intensities of $P < 10$ W/cm^2 the PL of the QD-ND is dominated by a single peak labeled as X at 2.925 eV. The mono-exponential decay time of the X emission $\tau_X = 3.1$ ns is much shorter than τ^*_{QW}, suggesting that the built-in electric field is weaker in the QD-ND than in the QW-ND. At high excitation intensities of $P > 10$ W/cm^2, two additional peaks at higher-energies 2.955 eV (XX) and 2.970 eV (possibly charged XX) appear (Fig. 4.1(a)). The integrated intensity of the X-peak increases linearly with P up to the saturation intensity of ~ 15 W/cm^2, while the intensity of the XX-peak increases quadratically with P (Fig. 4.1(d)). Hence we assign peak X to the single exciton emission, and peak XX to the biexciton-to-exciton transition.[123, 124] The large negative binding energies of XX (> 10 meV) are commonly observed in III-N QDs[125, 126, 127, 128, 129, 130, 131, 132]. It is due to the residual strain, even in dots with such small sizes, which enhances the repulsive exciton-exciton Coulomb interaction[127]. Despite the residual strain, both the PL energy (Fig. 4.1(a)) and decay time (Fig. 4.1(d)) of the X-peak remain nearly constant as the excitation intensity increases significantly. These again supports that the X-peak comes from the discrete ground state in a zero-dimensional dot, and is thus un-affected by carrier screening. The carrier density only changes the relative occupation among different energy levels, leading to changes in the relative intensities of corresponding spectral lines.

The above study shows that the optical properties of the QW-ND, including PL energy, decay time and IQE, depend strongly on the excitation intensity as a result of strain and screening. On the other hand, in the QD regime, the effect of strain and screening on the exciton emission from the QD-ND becomes obscure due to the energy-level quantization.

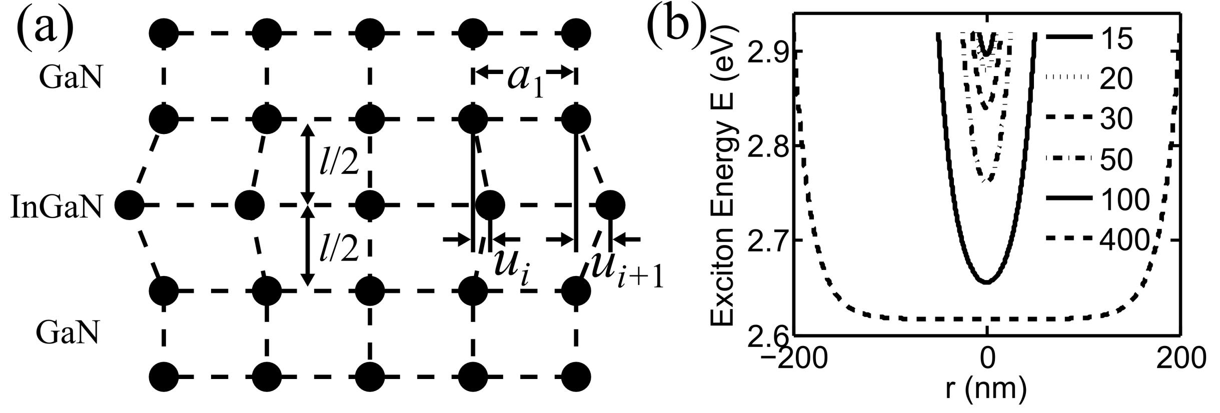

Figure 4.2: Phenomenological strain relaxation model. (a) The schematic plot of the simple 1D theory described in the text. (b) The exciton potential profile at $P = 0.4$ W/cm^2 along the lateral direction in NDs with $D = 15, 20, 30, 50, 100, 400$ nm, plotted using the fitting results of Fig. 2(a), $E_0 = 2.92$ eV, $B_m(P = 0.4) = 303$ meV and $\kappa = 0.055$ nm^{-1}.

4.2 Mechanical Properties in a Nanodisk

The previous section used strain relaxation at the sidewall of ND to qualitatively explain the sharp difference in the optical properties of QD-NDs and QW-NDs. In this section, we provide a simple phenomenological model of 2D coupled-springs to understand the strain relaxation and derive an analytical expression for the strain distribution in the ND.

We illustrate our model in Fig. 4.2(a). The InGaN QW of thickness l is simplified to a single layer of 1D lattice, $l/2$ away from the upper and lower GaN barriers. Black dots represent the lattice sites. The upper and lower lattices represent the GaN barriers. The lattice constants of GaN and InGaN perpendicular to the c-axis are a_1 and a_2, respectively. If the InGaN layer is fully stressed, the InGaN lattice lines up with the GaN lattices and has lattice constance a_1. This represents the limit of infinite lateral size, which we call the pre-relaxation configuration. Due to the finite lateral size of our ND the strain is partially relaxed to minimize the mechanical elastic energy E_m of the entire system, which we call the post-relaxation configuration. We assume that the GaN lattices are fixed for simplicity. Note that this will lead to an overestimation of the change in the piezo-electric polarization fields, since tensile-strained GaN will produce opposite polarization charges at the InGaN/GaN interfaces. But this only contributes to a proportionality factor to the piezoelectric field. The displacement of the ith lattice site in the post-relaxation configuration in respect to the pre-relaxation configuration is denoted as u_i.

The equilibrium value of u_i is determined by both minimization of the total elastic energy E_m and the balance between forces at each site i. At each site, the atom is subject to a shear stress F_{si} between InGaN and GaN layers and a hydrostatic stress F_{hi} within the InGaN layer. The two forces are given by the displacement u_i as:

$$F_{si} = -k_1 u_i, F_{hi} = k_2(u_{i-1} + u_{i+1} - 2u_i). \tag{4.1}$$

The coefficients k_1 and k_2 can be understood as related to the Shear modulus at the InGaN/GaN interface and the Young's modulus in InGaN QW layer, respectively. Local force balance requires that:

$$F_{si} + F_{hi} = 0. \tag{4.2}$$

Substituting Equ. 4.1 into Equ. 4.2, and translating into the continuous form yields:

$$k_1 u = k_2 a_1^2 \frac{\mathrm{d}^2 u}{\mathrm{d}r^2}, \tag{4.3}$$

in which r is the radial distance from the center of the InGaN disk. This equation can be readily solved considering that $u(r = 0) = 0$ at the center of the disk and that $u(r)$ is an odd function of r, resulting in:

$$u(r) = C\left(e^{\kappa r} - e^{-\kappa r}\right), \kappa = \frac{1}{a_1}\sqrt{\frac{k_1}{k_2}}. \tag{4.4}$$

Here C is a constant to be determined.

The total elastic energy E_m of the InGaN lattice, ignoring the coupling energy between the InGaN lattice and the barrier layers, can be written as:

$$E_m = \sum_i \frac{1}{2}k_1 u_i^2 + \frac{1}{2}k_2[(a_2 - a_1) - (u_i - u_{i-1})]^2. \tag{4.5}$$

Re-writing E_m in the continuous form gives:

$$\begin{aligned} E_m &= 2\int_0^{D/2} \frac{1}{2a_1}[k_1 u^2 + k_2 a_1^2 \left(\frac{a_2 - a_1}{a_1} - \frac{\mathrm{d}u}{\mathrm{d}r}\right)^2]\mathrm{d}r \\ &= 2\sqrt{k_1 k_2}\sinh\left(2\kappa D/2\right)C^2 + 4k_2(a_1 - a_2)\sinh\left(\kappa D/2\right)C + \frac{(a_1 - a_2)^2}{a_1}k_2 D/2. \end{aligned} \tag{4.6}$$

Minimizing E_m above gives C and thus $u(r)$ as:

$$C = \frac{a_2 - a_1}{2}\sqrt{\frac{k_2}{k_1}}\mathrm{sech}\left(\kappa D/2\right), \tag{4.7}$$

$$u(r) = (a_2 - a_1)\sqrt{\frac{k_2}{k_1}}\mathrm{sech}\left(\kappa D/2\right)\sinh\left(\kappa r\right). \tag{4.8}$$

With $u(r)$, we obtain the hydrostatic compression strain along the radius direction defined as:

$$\varepsilon(r) = -\frac{a_2 - a_1}{a_1} + \frac{du}{dr} = \varepsilon_0\left[1 - \mathrm{sech}\left(\kappa D/2\right)\cosh\left(\kappa r\right)\right], \tag{4.9}$$

in which $\varepsilon_0 = -(a_2 - a_1)/a_1$ denotes the maximum strain in a fully stressed InGaN layer.

This expression is by no mean a full description of the strain in a real InGaN/GaN QW, since there are several more strain components that need to be considered. However, it provide a simple analytical expression backed by an easy to understand physical picture. Most importantly, as will be shown in the rest of this dissertation, it allows us to establish phenomenological

models that match well with our experimental results.

4.3 Electrical Properties in a Nanodisk

As we have explained in Sec. 4.1, strain relaxation will lead to changes in the electrical properties of an ND, which in turn will affect their optical properties. To obtain a quantitative picture of the effect of strain relaxation on the electrical properties of NDs, we performed a controlled systematic study of how PL energy changes with the diameter. We measured NDs of 21 different diameters, varying from D =15 nm – 2 μm, fabricated on the same single-QW wafer of fixed thickness ($<$ 2 mono-layer fluctuation) and fixed indium fraction ($<$ 2% fluctuation). For each diameter, we measured one randomly chosen ND from a 6×6 array, the results of which are presented in Fig. 4.3(a).

Figs. 4.3(a) shows that the peak energy of zero-phonon band (ZPB) blueshifts as the diameter of the ND reduces from 2 μm to 19 nm, consistent with previous studies [117, 133, 134, 135, 136, 137, 138]. The large amount of blueshift ($\sim$ 300 meV) from QW to ND shows that the piezoelectric polarization gives the dominant contribution to the electrical properties in our NDs. The piezoelectric polarization lowers the exciton energy due to the QCSE [139]. Therefore, reducing the diameter decreases the overall strain and piezoelectric polarization, leading to an increase in the exciton energy. In contrast, the deformation potential increases the bandgap [140] and would lead to a redshift of the exciton energy with decreasing the nanodisk diameter. The spontaneous polarization also cannot explain the blueshift, since it is largely independent of the strain and, therefore, the nanodisk diameter.

The predominance of the piezoelectric polarization in shaping the potential profile suggests a lower exciton potential at the center of the nanodisk. This is because the higher residue strain at the center of the nanodisk leads to stronger piezoelectric field and Stark redshift compared to at the sidewall.

Since the amount of piezoelectric field, and hence the amount of Stark redshift, is proportional to the amount of residue strain, the lateral potential profile at radial position r can be expressed as:

$$\phi'(r) = -B_m[1 - \mathrm{sech}(\kappa D/2)\cosh(\kappa r)]. \tag{4.10}$$

This can be quickly derived from Equ. 4.9. Here, B_m represents the amount of exciton energy shift from an unstrained QW to an fully-strained QW, $1/\kappa$ is the characteristic length of the region from the InGaN nanodisk sidewall where the compressive strain of the InGaN layer is relaxed as explained in the previous section. Due to the predominance of the piezoelectric polarization over the deformation potential, B_m is always positive, i.e. $\phi'(0) < \phi'(D/2)$.

At low excitation intensities, the diameter-dependent PL energy $E(D)$, corresponding to the exciton energy at $r = 0$, can be written as:

$$E = E_0 - B_m[1 - \mathrm{sech}(\kappa D/2)]. \tag{4.11}$$

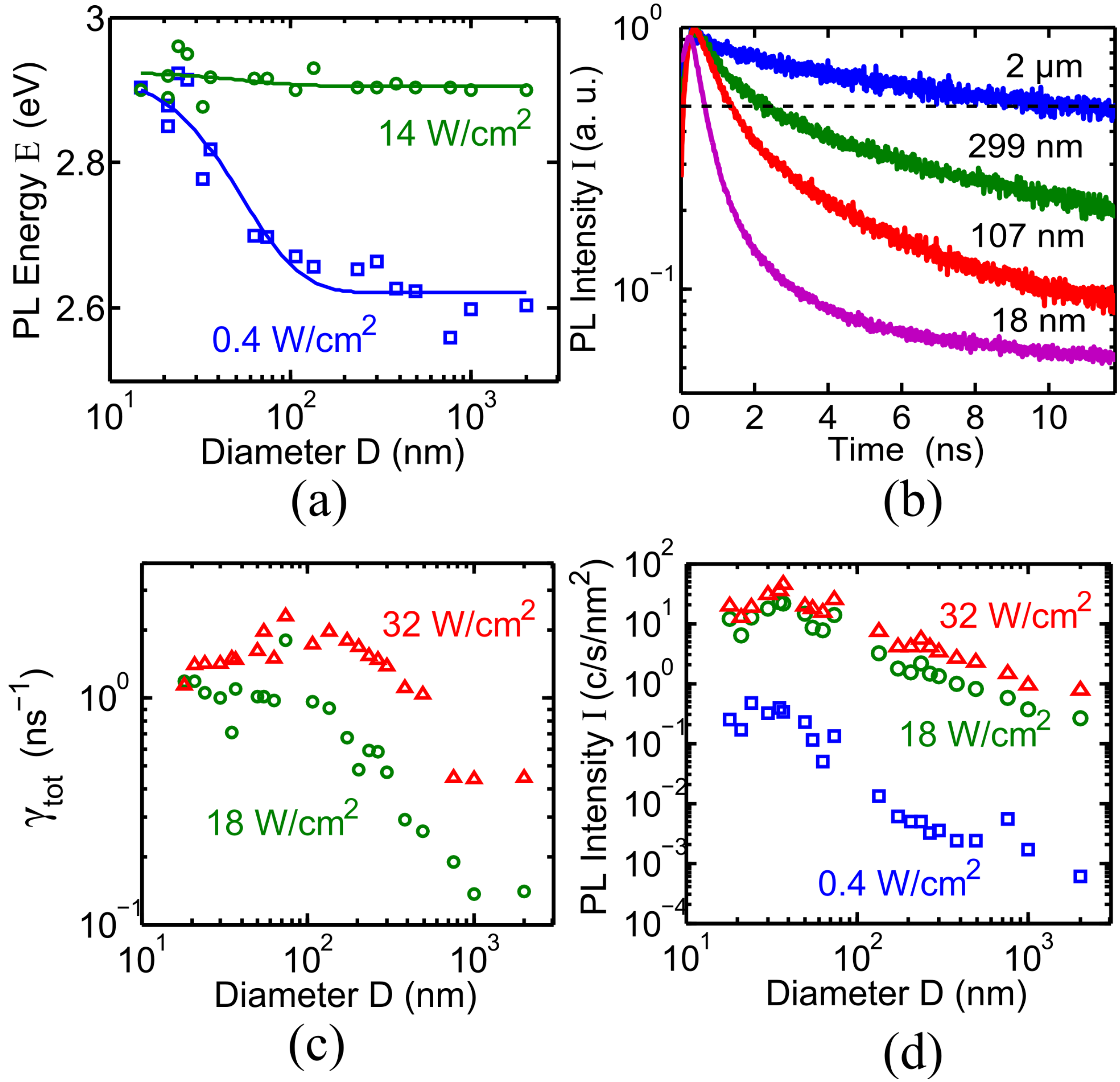

Figure 4.3: PL properties vs. ND diameter. (a) The PL energy E of single NDs vs. the diameter D of the ND at excitation intensity $P = 0.4$ W/cm^2 (blue square) and 14 W/cm^2 (green circle). The single NDs are randomly chosen and isolated using a confocal microscope setup. The ND diameter is the average diameter of the ND's containing array which has a 2 nm standard deviation. The data are fitted using Equ. 4.11 assuming the same E_0 and κ for both low- and high-P data, resulting in $E_0 = 2.92$ eV, $B_{m,low-P} = 303$ meV, $B_{m,high-P} = 19$ meV and $\kappa = 0.055$ nm^{-1}. (b) The TRPL decay traces of four ensembles of NDs with diameters $D = 2$ μm (blue), 299 nm (green), 107 nm (red) and 18 nm (pink), respectively, at excitation intensity $P = 18$ W/cm^2. Each ensemble contains a 6×6 array of NDs. (c) The total decay rate $\gamma_{tot} = 1/\tau_{tot}$ of ND ensemble vs. ND diameter D at excitation intensities $P = 18$ W/cm^2 (green circle) and $P = 32$ W/cm^2 (red triangle). τ_{tot} is defined as the time taken for the PL intensity to decay from the maximum intensity to half maximum to avoid the complexity of stretched exponential decays. (d) The PL intensity per unit InGaN area of ND ensemble vs. ND diameter D at excitation intensities $P = 0.4$ W/cm^2 (blue square), $P = 18$ W/cm^2 (green circle) and $P = 32$ W/cm^2 (red triangle).

Here, E_0 is the exciton energy at $r = D/2$ where the strain is considered as being fully relaxed. Therefore, it represents the bandgap of an unstrained QW or a nanodisk of $D \to 0$.

The characteristic strain relaxation parameters B_m and κ as well as E_0 are obtained by using Eq. (4.11) to fit the measured $E(D)$ data, as shown in Fig. 4.3(a). We obtain, for this particular sample, $E_0 = 2.92$ eV, $B_m = 303$ meV, and $\kappa = 0.055$ nm^{-1} (or $1/\kappa = 18$ nm, consistent with earlier numerical predictions[136]). With B_m and κ, we use Eq. (4.10) to calculate the exciton potential profile for QDs with different diameters as shown in Fig. 4.2(b).

4.4 Optical Properties in a Nanodisk

This section shows that the reduction of strain in smaller NDs leads to a drastic enhancement in the oscillator strength f_{os}. However, this does not lead to a drastic enhancement in the radiative decay rate nor the IQE, because of the suppression of the LDPS as the diameter of the NDs reduces. The basic method used to obtain this finding is explained as following.

First, f_{os} together with LDPS ρ determines the radiative decay rate γ_r as $\gamma_r \propto f_{os}\rho$. The effects of ρ can be taken into account by a factor $F_p = \rho/\rho_0$, where ρ_0 is the LDPS when the ND is in a infinite GaN universe. So f_{os} can be written as:

$$f_{os} \propto \gamma_r / F_p. \tag{4.12}$$

Hence, to know $f_{os}(D)$ relation we only need to know $F_p(D)$ and $\gamma_r(D)$.

The effect of $F_p(D)$ relation, can be calculated theoretically using widely available optical simulation techniques such as FDTD method. The γ_r can be obtained using

$$\gamma_r = \eta_{int}\gamma_{tot}, \tag{4.13}$$

in which η_{int} is the IQE and γ_{tot} is the total decay rate. The $\gamma_{tot}(D)$ relation can be measured directly from the TRPL of NDs with different D. The $\eta_{int}(D)$ is related to the PL intensity $I(D)$ at a given excitation laser intensity P. However, $\eta_{int}(D)$ is not directly proportional to $I(D)$ since the laser absorption efficiency η_{abs} and collection efficiency η_{col} also change with D. Taking this into consideration, η_{int} can be expressed as:

$$\eta_{int}(D) \propto I(D)/(\eta_{abs}(D)\eta_{col}(D)). \tag{4.14}$$

Among the three parameters on the right-hand side, $I(D)$ can be measured experimentally, $\eta_{abs}(D)$ and $\eta_{col}(D)$ can be calculated numerically.

In this section, we first calculate the $\eta_{abs}(D)$, $F_p(D)$ and $\eta_{col}(D)$ using FDTD method. Then we extract the diameter D dependence of η_{int}, γ_r and f_{os} from the measured $I(D)$ and $\gamma_{tot}(D)$ data using Equ. 4.14, 4.13 and 4.12, respectively.

4.4.1 Absorption Efficiency

In our experiment, we use a 390 nm (3.18 eV) pulsed laser to excite the sample at $\theta = 55^\circ$ from the normal direction as described in Sec. 3.2 and illustrated in Fig. 3.6 and 4.4(a). We neglect the absorption of the incident light by GaN, due to its large bandgap of ~ 3.5 eV. To calculate the absorption in the InGaN layer, we first calculated the spatial distribution of the optical field $\boldsymbol{E}(x, y, z)$ produced by an incident plane wave. The average absorption efficiency $\overline{\eta_{abs}}$ can then be calculated via:

$$\overline{\eta_{abs}} = \frac{4}{\pi D^2 l} \int\limits_{ND} -\frac{1}{2}\omega\epsilon_0 |\boldsymbol{E}|^2 \mathrm{Im}(\epsilon_r)\mathrm{d}V, \tag{4.15}$$

in which $\omega = 2\pi/\lambda$ is the angular frequency of the excitation laser, ϵ_0 is the vacuum permittivity, Im(ϵ_r) is the imaginary part of the dielectric constant ϵ_r, D and l are the diameter and thickness of the InGaN ND, respectively. The integration only covers the ND region. Since ϵ_r is constant in the InGaN ND, we have:

$$\overline{\eta_{abs}} \propto \frac{1}{D^2} \int\limits_{ND} |\boldsymbol{E}|^2 \mathrm{d}V. \tag{4.16}$$

The exact value of ϵ_r for $In_{0.15}Ga_{0.85}N$ is unknown. Hence we approximate it using the ϵ_r of bulk GaN. This is approximately valid, since our InGaN NDs have a small thickness (3 nm) and a low indium composition ($\sim 15\%$), which should not disturb the $\boldsymbol{E}(x, y, z)$ of a pure GaN nanopillar significantly.

As shown in Fig. 4.7(a), the absorption efficiency $\overline{\eta_{abs}}$ is almost the same for very small ($D < 40$ nm) and very large ($D > 1000$ nm) NDs. However, it is enhanced by up to five times for NDs of diameter 100–200 nm. Fig. 4.4(b-d) compared the 2D cross sections of $|\boldsymbol{E}(x, y, z)|^2$ for NDs of diameters $D = 10$ nm, 160 nm and 1000 nm, respectively. At $D = 160$ nm, the nanopillar effectively forms a low-quality cavity; while at $D = 10$ nm and 1000 nm, coupling of the incident light into the nanopillar is poor.

4.4.2 Local Density of Photon States

The LDPS factor F_p can be numerically calculated using the ratio of the radiation power of a dipole in a ND and that of a dipole in a GaN universe[141]. In the simulation, we used a wavelength $\lambda = 420$ nm, corresponding to the PL energy of NDs. The $F_p(\boldsymbol{p}, r; D)$ depends on the diameter D of the ND, radial position $\boldsymbol{r}$ of the dipole and polarization $\boldsymbol{p}$ of the dipole. We define tangential polarization $\boldsymbol{p} \perp \boldsymbol{r}$ as $\boldsymbol{p}_\perp$ and radial polarization $\boldsymbol{p} \parallel \boldsymbol{r}$ as $\boldsymbol{p}_\parallel$ (Fig. 4.5(b)). The electromagnetic field generated by a randomly oriented dipole can be obtained from the fields generated by a tangential and a radial dipole, due to the vectorial nature of the electromagnetic field.

Fig. 4.5(c) shows that the F_p generally increases with D for dipoles of both polarizations. In small NDs of $D < 40$ nm, from $r = 0$ to $D/2$, the F_p only increase slightly. In large NDs

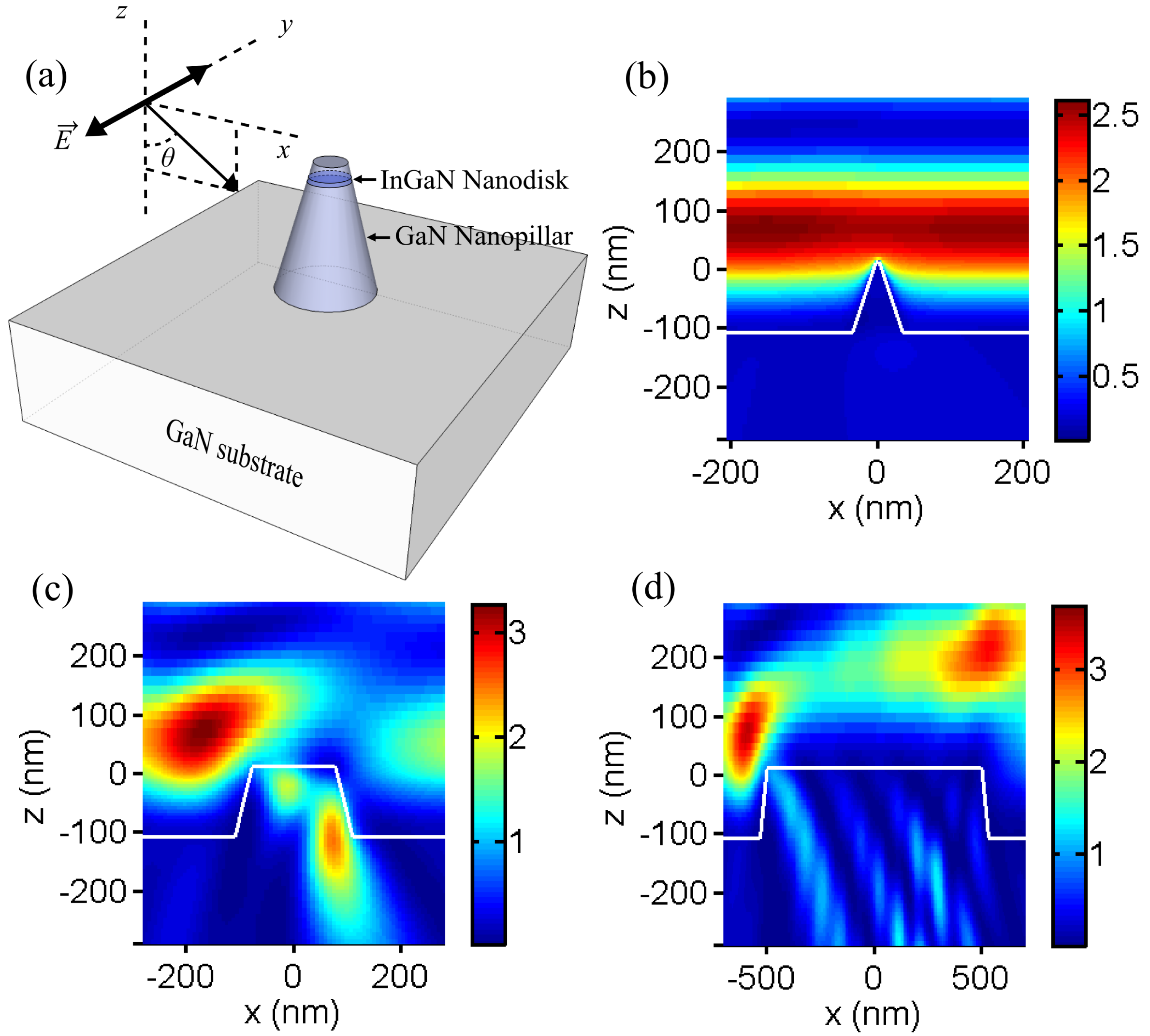

Figure 4.4: Absorption efficiency FDTD simulation. (a) Schematic plot of the incidence of a plane wave to a InGaN ND in a GaN nanopillar. The propagation direction of the incident light is $\theta = 55°$ apart from the normal direction, z-axis. The polarization is along the y-axis. The nanopillar has a height of 120 nm and a sidewall angle of 75°. The center of the ND is 11.5 nm beneath the top cone surface. (b-d) xz-plane 2D cross section maps of $|\boldsymbol{E}(x, y, z)|^2$ for a 390 nm plane wave coupling to NDs of diameters $D = 10$ nm, 160 nm and 1000 nm, respectively. The white lines outline the nanopillar.

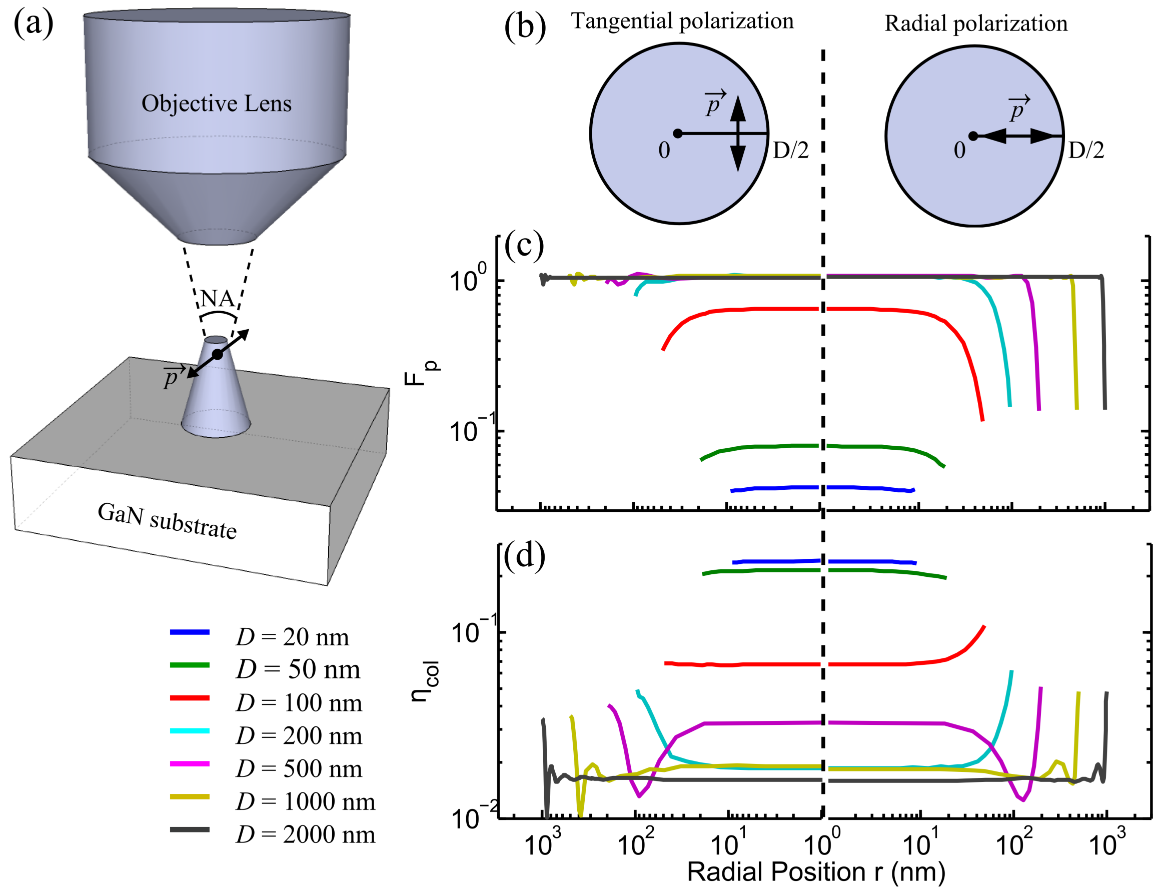

Figure 4.5: LDPS and collection efficiency FDTD simulation. (a) Schematic plot of the dipole in the nanopillar and the first-lens collection. (b) The definition of tangential dipole and radial dipole. (c-d) The F_p and η_{col} for tangential (left column) and radial (right column) dipoles at different radial positions r. Different line colors represents different ND diameters.

of $D > 100$ nm, from $r = 0$ to $D/2$, the F_p is nearly constant until r is within ~ 50 nm from $D/2$. Close to $r = D/2$, $F_p(\boldsymbol{p}_\perp)$ fluctuates by $< 20\%$ and $F_p(\boldsymbol{p}_\parallel)$ decreases by ~ 8 folds. In NDs of 40 nm $< D < 100$ nm, both $F_p(\boldsymbol{p}_\perp)$ and $F_p(\boldsymbol{p}_\parallel)$ drops significantly as r approaches $D/2$, but the decrease is not as drastic as that of $F_p(\boldsymbol{p}_\parallel)$ in larger NDs.

The F_p behavior can be understood using the results of earlier studies on the spontaneous emission of a dipole placed closely to the interface of two infinite dielectric materials with refractive indices $n = n_1$ and n_2, respectively[142, 143]. Considering the case in which $n_1 > n_2$, as the dipole approaches the interface to within half of the wavelength from the side of $n = n_1$, if its polarization is parallel to the interface, the F_p will oscillate mildly; if its polarization is perpendicular to the interface, the F_p will decrease quickly toward a finite value. This explains well the F_p behavior for dipoles in NDs of $D > 100$ nm. In smaller NDs, the dipole is always close to the sidewall air-dielectic interface, so its F_p is always a small but finite value.

Once we have the $F_p(\boldsymbol{p}, r)$ values for all r from 0 to $D/2$, and for both tangential dipole $\boldsymbol{p}_\perp$ and radial dipole $\boldsymbol{p}_\parallel$, the averaged F_p can be calculated as:

$$\overline{F_p(D)} = \frac{4}{D^2} \int_0^{D/2} (F_p(\boldsymbol{p}_\perp, r) + F_p(\boldsymbol{p}_\parallel, r)) r \mathrm{d}r. \tag{4.17}$$

The resulting $\overline{F_p}(D)$ is shown Fig. 4.7(a).

We note that the strong suppression in F_p with the reduction of D, as shown in Fig. 4.7(a), is detrimental to the IQE of our NDs. However, this can be engineered using many methods, one of which will be presented at the end of the next discussion about the η_{col}.

4.4.3 Collection Efficiency

The first-lens collection efficiency η_{col} is defined by the ratio of the far-field radiation power within a collection cone of NA$= 0.55$ (Fig. 4.5(a)) vs. the total radiation power. Just like $F_p(\boldsymbol{p}, r; D)$ the $\eta_{col}(\boldsymbol{p}, r; D)$ also depends on the diameter D of the ND, radial position $\boldsymbol{r}$ of the dipole and polarization $\boldsymbol{p}$ of the dipole. We use FDTD simulation to obtain $\eta_{col}(\boldsymbol{p}, r; D)$ as shown in Fig. 4.5(d).

The simulation shows that the η_{col} generally decreases with D for dipoles of both polarizations. Unlike F_p, the behavior of η_{col} is largely insensitive to the dipole's polarization. In small NDs of $D < 40$ nm, η_{col} is nearly constant with $\eta_{col}(r = 0)$ slightly greater than $\eta_{col}(r = D/2)$. In large NDs of $D > 500$ nm, the η_{col} in the region $D/2 - 100$ nm $< r < D/2$ is two to three times of that in the rest of the ND. This is because at the center of large NDs, the radiation of a dipole into the objective lens is hindered by the strong internal reflection at the top GaN/air interface, whereas, at the edge of NDs the sidewall scatters light into the objective lens collection cone.

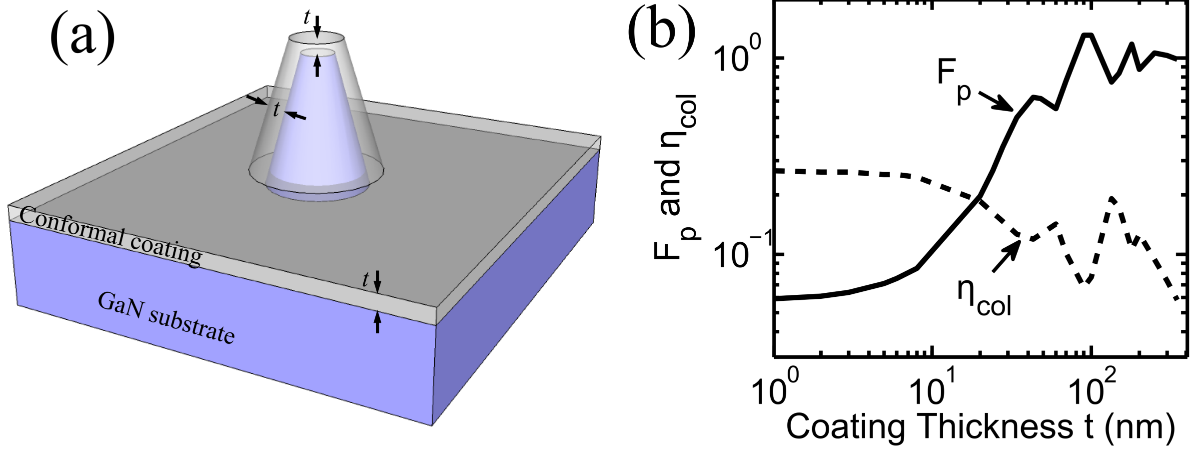

Figure 4.6: Conformal dielectric coating on small DINs improves F_p. (a) A schematic plot of conformal coating. (b) The F_p, η_{col} vs. the coating thickness t.

Similar to $\overline{F_p}$, we can calculate $\overline{\eta_{col}}$ using the following expression:

$$\overline{\eta_{col}(D)} = \frac{4}{D^2} \int_0^{D/2} (\eta_{col}(\boldsymbol{p}_\perp, r) + \eta_{col}(\boldsymbol{p}_\parallel, r)) r \mathrm{d}r. \tag{4.18}$$

The resulting $\overline{\eta_{col}(D)}$ is shown in Fig. 4.7(a). As expected from the previous discussion, the η_{col} in small DINs is much higher than that in large DINs as a result of interface scattering.

We noted earlier that the F_p is strongly suppressed at small D, as shown in Fig. 4.7(a). This is detrimental to the IQE of our NDs. A simple way to improve the F_p in NDs in the QD limit, while maintaining the relatively high collection efficiency ($\eta_{col} \sim 15\%$), is conformally coating the sample with GaN, as illustrate in Fig. 4.6(a). Fig. 4.6(b) shows the F_p and η_{col} of a $D = 30$ nm ND vs. the thickness t of the GaN coating. As t increases, the F_p is improved by 10 folds to about unity when $t > 70$ nm; the η_{col} generally decreases, but has a local maximum at around 150 nm. Therefore, by depositing a 150 nm thick GaN conformally, one can achieve $\sim$ 10-fold F_p enhancement without degrading η_{col}. More sophisticated methods such as those incorporating tapered nanowires[144] and micro-cavities[14] may improve η_{col} and F_p much more.

4.4.4 Oscillator Strength

Now that we have a good understanding of the external optical efficiencies, we are ready to extract the change in f_{os} with D using the total decay time rate $\gamma_{tot}(D)$ and PL intensity $I(D)$ that can be measured from the TRPL and PL of ND ensembles with different D's. Fig. 4.1(b) shows TRPL traces of four ensembles. The decay accelerates as the diameter decreases consistent with what we have seen in Sec. 4.1. All TRPL curves are stretched exponential, as expected for QW-NDs as well as for QD-ND ensembles with inhomogeneous ND properties. We characterized their decay using the half-life-time τ_{tot}, the time it takes to go to half of the initial

PL amplitudes (dashed line in Fig. 4.1(b)). Fig. 4.1(c) shows the total decay rate $\gamma_{tot} = 1/\tau_{tot}$ vs. ND diameter D. At both $P = 18$ and 32 W/cm^2, the total decay rate γ_{tot} (including both radiative and nonradiative decays) increases drastically with the reduction of D from 2 μm to 100 nm as expected, but plateaus or even slightly decreases with further reduction of D. Corresponding to the enhancement in the total decay rate, we measured a drastic increase in I at a fixed P (Fig. 4.1(d)).

As we have discussed at the beginning of this chapter, the measured I is determined by the excitation intensity P, absorption efficiency η_{abs}, IQE η_{int} and collection efficiency η_{col}. Therefore, η_{int} can be calcualted by:

$$\overline{\eta_{int}} \propto I/(P\overline{\eta_{abs}}\,\overline{\eta_{col}}), \tag{4.19}$$

in which $\overline{\eta_{int}}$, $\overline{\eta_{abs}}$ and $\overline{\eta_{col}}$ are averaged η_{int}, η_{abs} and η_{col} values over the entire ND and all dipole polarizations. The same definition is used for $\overline{\gamma_r}$, $\overline{\gamma_{tot}}$, $\overline{F_p}$ and $\overline{f_{os}}$ in the rest of this work.

We evaluate η_{abs} and η_{col} using the FDTD method[145]. The results are summarized in Fig. 4.7(a). The $\overline{\eta_{abs}}$ are nearly the same in the QW and QD limits. The highest $\overline{\eta_{abs}}$ appears at $D \sim 150$ nm when the GaN nanopillar effectively forms a low-quality cavity in the lateral direction for light at 390 nm wavelength. The first-lens collection efficiency $\overline{\eta_{col}}$ increases from merely 2% in the QW limit to about 30% in the QD limit; and the most drastic increase occurs in the region 40 nm $< D < 100$ nm. A similar trend in η_{col} has been predicted for a dipole emitter embedded near the end of a semi-infinite dielectric nanowire[146, 147]. It was shown that[146], for a large nanopillar, most light is coupled into two guided HE_{11} modes, one propagating upwards and the other downwards into the substrate. However, the upwards-propagating guided mode is mostly reflected back into the substrate by the top facet of the nanopillar. For a small nanopillar[147], the coupling to the guided mode is strongly suppressed while the dissipation into free-space modes is relatively enhanced, leading to an increased collection efficiency.

Using Equ. 4.19 and the calculated $\overline{\eta_{abs}}$ and $\overline{\eta_{col}}$, we extracted $\overline{\eta_{int}}$ as shown in Fig. 4.7(b). Note that we cannot obtain the absolute value of $\overline{\eta_{int}}$ from Equ. 4.19, so $\overline{\eta_{int}}$ is a relative value with an arbitrary unit (a.u.). Nonetheless, Fig. 4.7(b) suggests that the $\overline{\eta_{int}}$ in the QD limit is enhanced compared to that in the QW limit; and the enhancement saturates or even slightly decreases when D reduces further. The enhancement is ~ 10 folds at $P = 0.4$ W/cm^2, but only $\sim$ 50% at $P = 18$ and 32 W/cm^2. This is because at high P the oscillator strength f_{os} in large NDs is already enhanced due to screening. The saturation of $\overline{\eta_{int}}$ at $D < 40$ nm in Fig. 4.7(b) could be due to two factors: the radiative decay rate $\overline{\gamma_r}$ enhancement is saturated, and at $D = 40$ nm the $\overline{\eta_{int}}$ is already close to 100%.

The variation of $\overline{\gamma_r}$ with D can be obtained from $\overline{\eta_{int}} = \overline{\gamma_r}/\overline{\gamma_{tot}}$ as follows:

$$\overline{\gamma_r} \propto I\,\overline{\gamma_{tot}}/(\overline{\eta_{abs}}\,\overline{\eta_{col}}P), \tag{4.20}$$

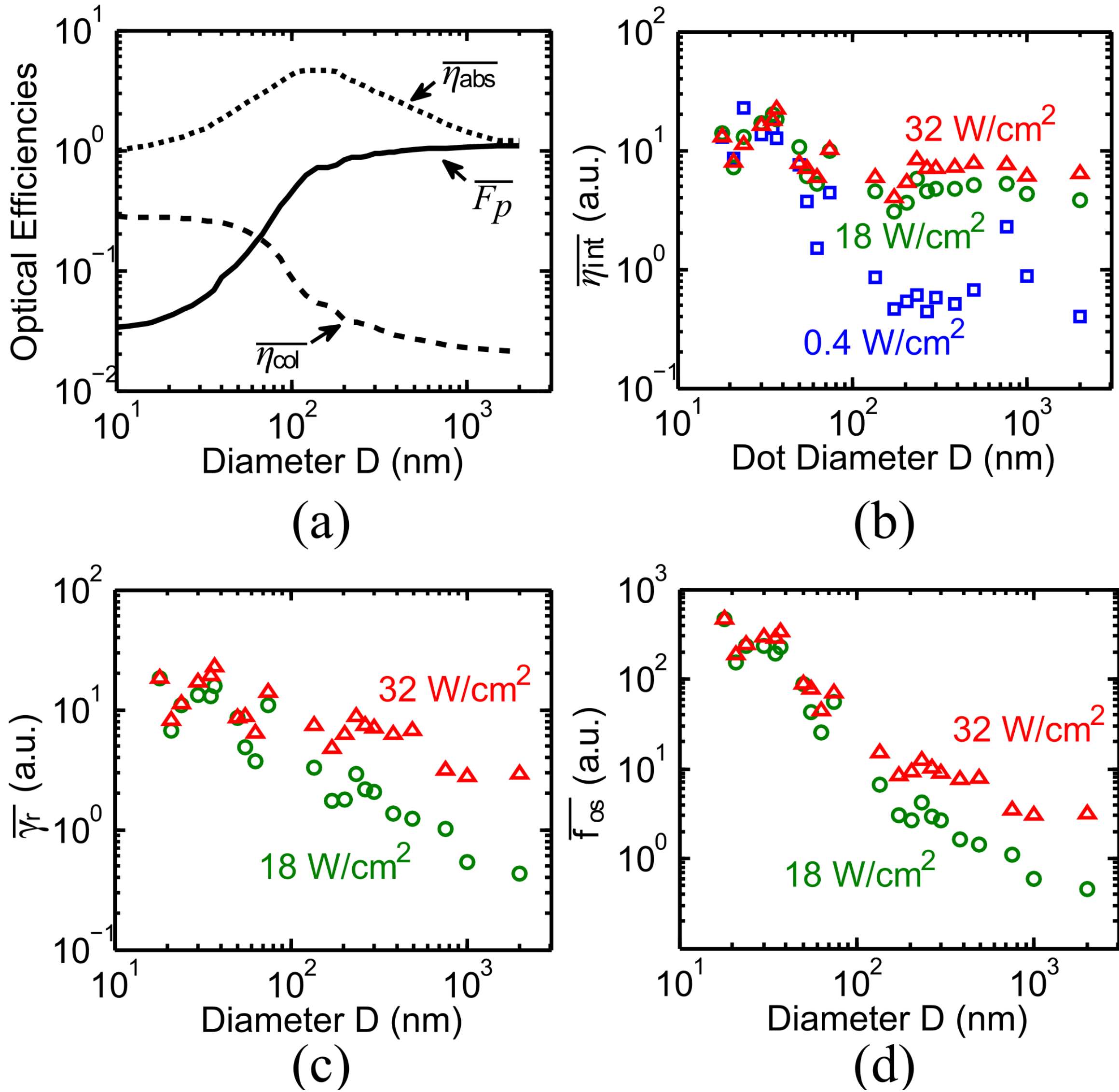

Figure 4.7: (a) FDTD simulation results: average absorption efficiency $\overline{\eta_{abs}}$ (dotted line), LDPS factor $\overline{F_p}$ (solid line) and collection efficiency $\overline{\eta_{col}}$ (dashed line) vs. ND diameter D. The $\overline{\eta_{abs}}$ curve is normalized to its value at $D = 2\ \mu$m and, hence, only shows the relative trend; while the $\overline{F_p}$ and $\overline{\eta_{col}}$ curves are absolute values. (b-d) Average IQE $\overline{\eta_{int}}$, radiative decay rate $\overline{\gamma_r}$ and oscillator strength $\overline{f_{os}}$ vs. D extracted from Fig. 4.1(c) and (d) using Equ. 4.19, 4.20 and 4.21, respectively. The vertical axes of all three figures have arbitrary units (a.u.).

in which $\overline{\gamma_{tot}}$ is measured in Fig. 4.1(c). Fig. 4.7(c)shows that the $\overline{\gamma_r}$ improves by only ~ 10 folds as D decreases from $2\ \mu$m to 40 nm and saturates at $D < 40$ nm. However, the 10-fold improvement is not the true potential of $\overline{\gamma_r}$ improvement in our NDs. According to Fermi's Golden Rule[148, 141], γ_r is determined by both the oscillator strength f_{os} and LDPS ρ:

$$\overline{\gamma_r} \propto \overline{f_{os}}\,\overline{F_p}, \tag{4.21}$$

in which, $F_p = \rho/\rho_0$ is the ratio of the LDPS ρ of a dipole in a nanopillar to the LDPS ρ_0 of the same dipole in bulk GaN. Note that the oscillator strength f_{os}, defined as the ratio between the radiative decay rate of the ND in bulk GaN and that of a classical electron oscillator in bulk GaN[149], is proportional to the square of the radiative transition matrix element[103]. As we shall show below, the $\overline{\gamma_r}$ in the QD limit is mainly limited by the LDPS factor F_p.

The F_p changes with the change of local dielectric environment. As shown in Fig. 4.7(a), in the QD limit, the average LDPS factor $\overline{F_p}$ is strongly suppressed, with $\overline{F_p} < 1/10$. Such a strong suppression in the LDPS should be universal for all nano-emitters closely surrounded by air-dielectric interfaces, such as colloidal QDs[150], QDs in nanowires[92, 41, 151, 152] and QDs at the apices of micro-pyramids[46]. Experimentally, it has been demonstrated for nano-emitters in nano-spheres[153] and nanowires[147]. The radiative decay rate γ_r in our NDs in the QD limit can be further enhanced by increasing the LDPS. For example, simply by conformal-coating the sample with 150 nm GaN, we can recover the $\overline{F_p}$ to unity while maintaining the relatively high $\overline{\eta_{col}} = 15\%$ in QD-NDs[**?**]. Larger $\overline{F_p}$ and $\overline{\eta_{col}}$ enhancements may be achieved with more sophisticated structures, such as by enclosing a ND in a micro-cavity[14] and in a tapered nanowire[144].

With the results of $\overline{\gamma_r}$ and $\overline{F_p}$ we can calculate the oscillator strength $\overline{f_{os}}$ using Equ. 4.21. As shown in Fig. 4.7(d), $\overline{f_{os}}$ is enhanced by over 100 folds in the QD limit compared to the QW limit at $P = 18$ and 32 W/cm^2. The $\overline{f_{os}}$ enhancement is a direct result of the strain-relaxation-induced reduction in the piezo-electric polarization fields, which leads to a better overlap between the electron and hole wavefunctions.

We would like to point out that to extract $\overline{\gamma_r}$, $\overline{\eta_{int}}$ and $\overline{f_{os}}$, we had to deal with the average-of-product. For example,

$$I \propto P\overline{\eta_{abs}}\,\overline{\eta_{col} f_{os} F_p/\gamma_{tot}}, \tag{4.22}$$

in which, γ_{tot} includes both γ_r ($\propto f_{os}F_p$) and γ_{nr}. The $P\overline{\eta_{abs}}$ in Equ. 4.22 is decoupled from the rest of parameters, which reflects that the carrier generation and decay are two independent processes. All parameters in the second average vary with both radial position r and dipole polarization $\boldsymbol{p}$. This average-of-product is approximated by the product-of-average: $\overline{\eta_{col}}\,\overline{f_{os}}\,\overline{F_p}\,\overline{1/\gamma_{tot}}$. Due to this approximation, our results on f_{os}, γ_r and η_{int} should be regarded as order-of-magnitude estimations.

4.5 Conclusion

In conclusion, we have systematically investigated the optical properties of individual and ensembles of InGaN/GaN nanodisks with precisely controlled diameters varying from the QD limit of D less than 40 nm, to the QW limit of D up to 2 μm. We found significant strain relaxation in nanodisks with diameters less than 100 nm, leading to a 100-fold enhancement in the oscillator strength in the QD limit compared to in the QW limit. Together with the 10-fold suppression in the local density of photon states, this leads to a 10-fold enhancement in the radiative decay rate, which can be further enhanced by increasing the local density of photon states.

CHAPTER 5

Carrier Dynamics in InGaN/GaN Quantum Dots

In this chapter, we show that the carrier dynamics in an InGaN/GaN DIN is governed by two competing mechanisms: 1) excitons are protected from surface recombination by a potential barrier formed due to strain-relaxation at the sidewall surface; 2) excitons can overcome the potential barrier by tunnelling and thermal activation. This is revealed by the PL energy and decay time of NDs with diameters from 20 nm to 2 μm at temperatures from 10 K to 120 K.

5.1 Principles of Carrier Dynamics

In this section, we summarize the principles of the carrier dynamics and how they were identified by using our site- and structure-controlled NDs. The detailed deduction of the model based on the experimental data will be presented in later sections. In our NDs the nonradiative decay is determined by two competing processes: on one hand, the strain-relaxation at the sidewall forms a confinement potential protecting excitons from recombining with the nonradiative surface states; on the other hand, excitons can overcome the potential barrier through tunnelling and thermal activation.

In an etched InGaN/GaN nanodisk, the lateral confinement potential for the exciton is formed due to strain-relaxation at the sidewall [154, 155, 156], as explained in Sec. 4.3 and illustrated in Fig. 5.1(a). This is manifested as a continuous blueshift of ND PL energy with the reduction of the diameter (Fig. 5.3), which shows the piezoelectric field is the determining factor of the potential profile, as explained in [157]. The larger strain-relaxation at the sidewall compared to the center of the nanodisk leads to a weaker piezoelectric field and, thus, higher exciton energy. The resulting confinement potential protects excitons from reaching the detrimental sidewall surface, and thus plays a critical role in exciton dynamics. The potential profile will be obtained in Sec. 5.2.

The exciton dynamics is governed by its radiative and nonradiative mechanisms. We will examine them in Sec. 5.3 by the diameter and temperature dependence of the PL intensity and decay time of QD ensembles. Here we first present main principles of radiative and nonradiative decay.

The radiative decay rate γ_{r} of an exciton in an InGaN/GaN nanodisk is determined by its

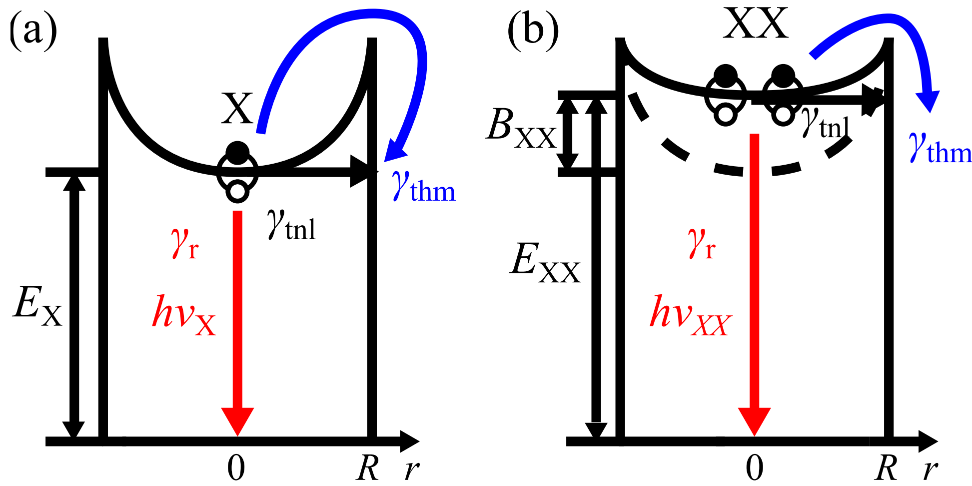

Figure 5.1: (a) Exciton decay model. A lateral potential profile is formed mainly due to the reduction in the piezoelectric field at the nanodisk sidewall. An exciton decays mainly through three channels: the radiative decay and the tunnelling and thermal surface nonradiative decay, whose decay rates are denoted as γ_{r}, γ_{tnl} and γ_{thm}, respectively. The latter two processes need to overcome the lateral potential barrier. (b) Biexciton decay model. The presence of another exciton lowers the potential barrier experienced by any of the two excitons due to the screening effect, leading to a lower biexciton QE compared to exciton QE.

oscillator strength, the local density of photon states (LDPS) and the temperature. The oscillator strength increases due to strain relaxation, whereas the LDPS decreases as the nanodisk diameter is reduced [157]. Meanwhile, since an exciton can be thermally scattered out of the radiation zone in the momentum space, the averaged γ_{r} is expected to decrease as temperature increases [158, 159]. The relative γ_{r} is reflected by the ratio of the PL intensity and the decay time, as will be explained in Sec. 5.3.1.

The nonradiative decay of an exciton can occur at the surface and in the volume of a QD. The volume recombination includes the Shockley-Read-Hall [121, 160] and Auger [161] processes. In our QDs, the volume recombination was negligible, because at any given temperature the planar QW on the same sample had a measured total decay time over ten times longer than that observed from the QDs investigated in this work [157].

The surface nonradiative recombination is of major concern for nanosturctures with large surface-to-volume ratios. There are two types of surface nonradiative decay processes based on the way excitons overcome the potential barrier and reach the sidewall surface: the tunneling decay and thermal decay, as illustrated in Fig. 5.1(a), which is analogous to the field emission and thermionic emission in the standard Schottky barrier theory [162, 163].

The tunnelling decay is the dominant nonradiative decay mechanism at low temperatures in our QDs. It is due to the tunnelling of the exciton through the potential barrier to the surface, and is determined by the wavefunction overlap of the exciton and surface states. Hence, the tunnelling decay rate γ_{tnl} is finite even at zero temperature as shown in Sec. 5.3.2. It strongly depends on the potential barrier profile and only has a weak temperature dependence, similar to the thermionic-field-emission component in the Schottky barrier theory [162].

The thermal decay becomes the dominant nonradiative decay mechanism as the temperature increases. It is due to the thermal activation of the exciton over the potential barrier to the surface. Therefore, the thermal decay rate γ_{thm} depends strongly on the temperature as well as the potential barrier profile as shown in Sec. 5.3.3.

Experimentally characterizing the radiative, tunnelling and thermal decay independently is, however, far from straightforward, since only the total decay rate and PL intensity can be directly measured. Each of these decay rates varies differently with the potential profile, while the potential profile is determined by multiple structural parameters of the QD, such as the diameter, thickness and indium mole fraction. Therefore, to obtain the dependence of each decay mechanism on each structural parameter, one would have to measure the change of the optical properties while varying each structural parameter separately. This cannot be done with QDs self-assembled at random sites, whose structural parameters are often correlated with each other and suffer from large inhomogeneity.

On the other hand, using the site- and structure-controlled QDs described in Sec. 3.1, we can measure the dependence of the optical properties on one of the structure parameters while keeping the fluctuations in others minimal. This enables us to extract the decay rates and their dependence on various structural parameters, as we discuss in Sec. 5.3.

5.2 The Lateral Potential Barrier Profile

As explained in the preceding section, the carrier dynamics in an InGaN/GaN nanodisk strongly depends on the exciton potential profile in the nanodisk. Therefore, the first step towards modeling the carrier dynamics is to determine the potential profile.

This is done by following the same procedure as in Sec. 4.3. We measure the PL spectra of nine dense arrays of QD-nanodisks with diameters varying from 19 nm to 33 nm as well as a QW-nanodisk with 5 μm diameter on the same sample at 10 K temperature. We use a very low excitation intensity $P = 1\ \mathrm{W/cm^2}$ to avoid significant screening of the electric field. Fig. 5.2(a) shows the PL spectra of the QW-nanodisk and several QD-nanodisks. Each spectrum is composed of a dominant ZPBand a serials of optical phonon (OP) replicas at the lower energy side of the ZPB. The OP replicas of the QW-nanodisk are more pronounced compared to those of QD-nanodisks due to the strain-enhanced wavefunction overlap between carriers and the longitudinal interface OP modes [119, 120]. The PL intensity of the QW-nanodisk is weaker compared to those of QD-nanodisks due to the suppression of the exciton oscillator strength in the QW-nanodisk (Sec. 4.4). Note that PL intensity in this study is normalized to the area of the InGaN layer and corrected by the collection and absorption efficiencies calculated by FDTD simulation (Sec. 4.4).

Figs. 5.2(a) and 5.3(a) show that the peak energy of ZPB blueshifts as the diameter of the QD reduces from 5 μm to 19 nm, consistent with what we observed in another sample in Sec. 4.3 and with previous studies [117, 133, 134, 135, 136, 137, 138]. The $E(D)$ data in

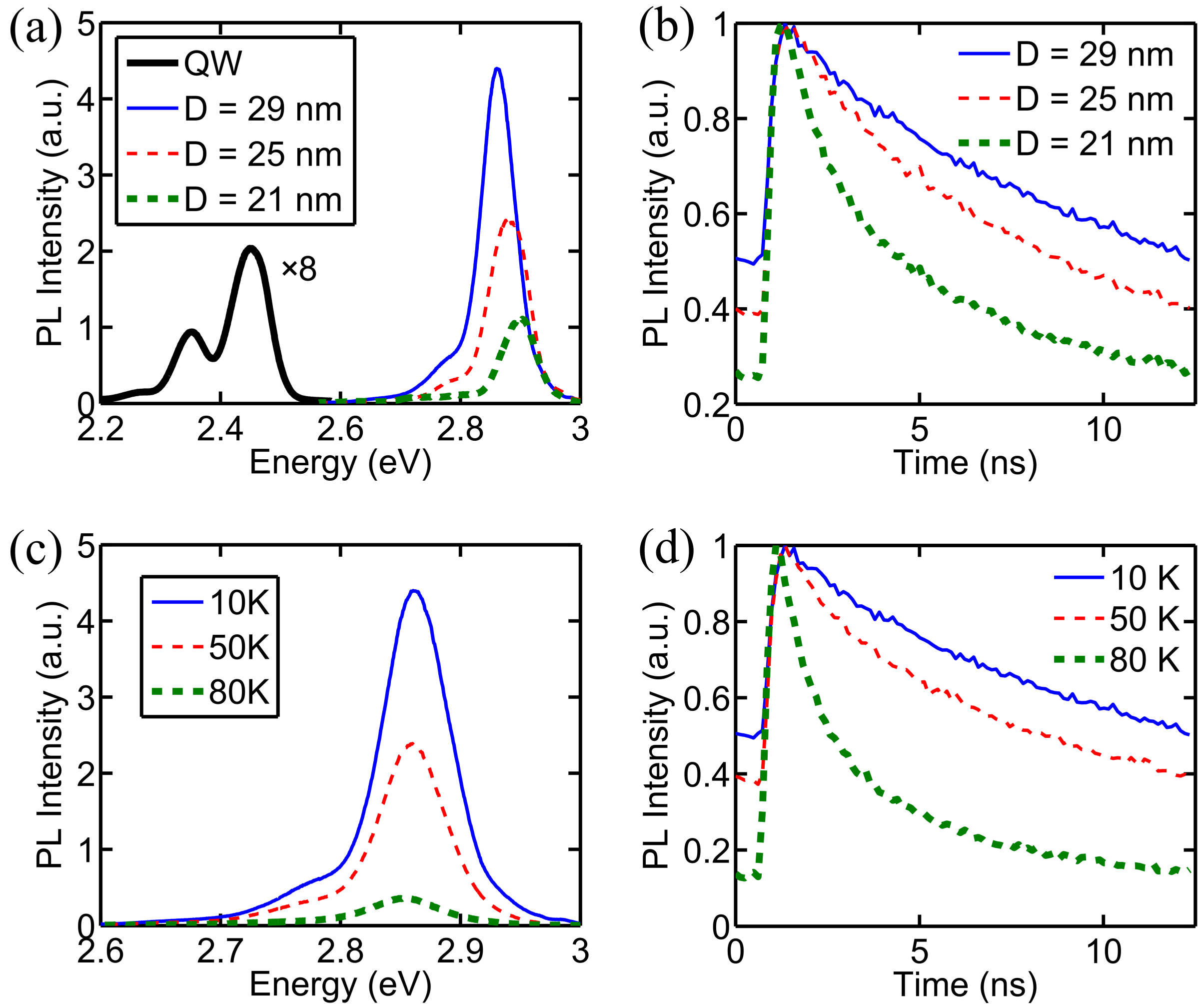

Figure 5.2: QD ensemble PL and TRPL taken at excitation intensity $P = 1\ \mathrm{W/cm^2}$. (a) PL spectra of ensembles of QDs of diameter $D = 21$, 25 and 29 nm and a QW of diameter 5 μm at 10 K. The PL intensity is normalized by the area of the InGaN layer. The spectrum of QW is multiplied by a factor of 8 for better visibility. (b) The TRPL of ensembles of QDs of diameter $D = 21$, 25 and 29 nm at 10 K. (c) and (d) The PL spectra and TRPL of an ensemble of QDs of diameter $D = 29$ nm at temperature $T = 10$, 50 and 80 K.

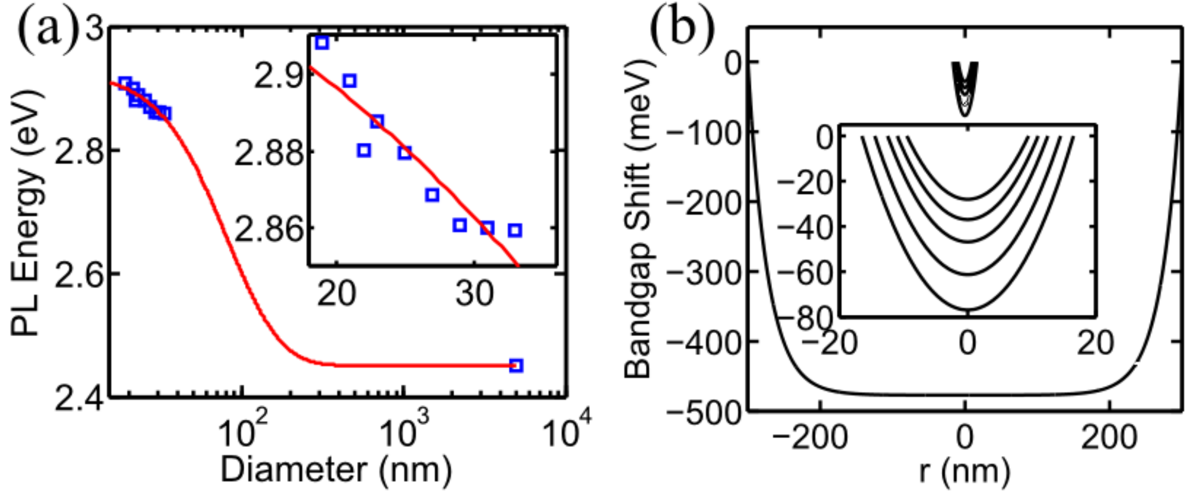

Figure 5.3: (a) PL energy E vs. QD diameter D of nine dense arrays of QDs with diameters ranging from 19 nm to 33 nm and a 5 μm diameter QW taken at excitation intensity $P = 1\ \mathrm{W/cm^2}$. The inset is a zoomed-in version of the nine dense QD arrays. The solid line is a fitting curve based on Eq. (4.11). (b) The exciton potential profiles of QDs of diameter $D = 19$, 22, 25, 29, 33 and 600 nm calculated using Eq. (4.10). The inset is a zoomed-in version of the five smaller diameters.

Fig. 5.3(a) can be used to extract the characteristic strain relaxation parameters B_m, κ and E_0 by a fitting using Eq. (4.11. We obtain, for this particular sample, $E_0 = 2.93$ eV, $B_m = 477$ meV, and $1/\kappa = 27$ nm. With B_m and κ, we use Eq. 4.10) to calculate the exciton potential profile for QDs with different diameters as shown in Fig. 5.3(b).

For describing the carrier dynamics, only the shape of the potential profile matters. For convenience in later discussions, we shift the $\phi'(r)$ in Eq. (4.10) by an r-independent constant to obtain $\phi(r)$ so that $\phi(r = 0) = 0$:

$$\phi(r) = B_m \mathrm{sech}(\kappa D/2)[\cosh(\kappa r) - 1]. \tag{5.1}$$

For a QD of diameter D, $\phi(r)$ reaches the maximum and minimum at $r = D/2$ and $r = 0$, respectively, i.e. the potential barrier height is:

$$\phi_B = \phi(D/2) - \phi(0) = B_m[1 - \mathrm{sech}(\kappa D/2)]. \tag{5.2}$$

5.3 Decay Rates

As explained in Sec. 5.1, an exciton in an QD mainly undergoes three decay processes: the radiative, tunnelling and thermal decay (Fig. 5.1(a)). In this section, we show that to consistently explain all measured diameter and temperature dependence of the total decay time and

PL intensity in this study, the total decay rate $\gamma = \gamma_{\mathrm{r}} + \gamma_{\mathrm{tnl}} + \gamma_{\mathrm{thm}}$ has to be expressed as:

$$\gamma = \gamma_{\mathrm{r0}}(1 - \mathrm{e}^{-\Delta/k_B T}) + \frac{c_1}{D}\mathrm{e}^{-\frac{2\sqrt{2m}}{\hbar}\int_0^{D/2}\sqrt{\phi(r)}\mathrm{d}r} + \frac{c_2 v_B}{D}\mathrm{e}^{-c_3\phi_B/k_B T}. \tag{5.3}$$

The three terms on the right-hand-side correspond to γ_{r}, γ_{tnl} and γ_{thm}, respectively.

We show in Sec. 5.3.1, in the γ_{r} term, γ_{r0} is the radiative decay rate at temperature $T \to 0$, it is independent of the QD diameter D for 21 nm $< D <$ 33 nm; k_B is the Boltzmann constant; and Δ is the exciton homogeneous linewidth limited mainly by impurity and interface scattering. γ_{r} decreases as T increases, due to the thermal scattering of excitons out of the radiation zone [158]. We show in Sec. 5.3.2, in the γ_{tnl} term, c_1 is a unit conversion factor reflecting the probability of the surface recombination; m is the exciton effective mass; and $\hbar$ is the reduced Planck constant. The exponential factor $\mathrm{e}^{-\frac{2\sqrt{2m}}{\hbar}\int_0^{D/2}\sqrt{\phi(r)}\mathrm{d}r}$ is proportional to the probability for a ground state exciton to tunnel through the potential profile $\phi(r)$ to the sidewall surface; the $1/D$ factor takes into account the surface-to-volume ratio. We show in Sec. 5.3.3, in the γ_{thm} term, c_2 is a scaling factor similar to c_1 but with a different unit; c_3 is a factor that adjust the potential barrier height to account for the temperature-dependent part of the tunneling decay; the exponential factor $\mathrm{e}^{-c_3\phi_B/k_B T}$ is the thermal population of excitons with kinetic energy higher than $c_3\phi_B$; v_B is defined as $v_B = \sqrt{2(c_3\phi_B + k_B T)/m}$, the average velocity of excitons with kinetic energies higher than $c_3\phi_B$.

The parameters $\phi(r)$ and ϕ_B in Eq. (5.3) have been obtained in Sec. 5.2. The remaining five unknown parameters in Eq. (5.3), γ_{r0}, Δ, c_1, c_2 and c_3, can be obtained from carefully designed control experiments. These include measuring the diameter and temperature dependence of the PL intensity I and the total decay time $\tau = 1/\gamma$ of QD arrays with tightly controlled structural parameters, as shown in Figs. 5.2 and 5.4. Fig. 5.2 shows examples of raw data from which Fig. 5.4 is extracted.

The diameter and temperature dependence of γ_{r} can be obtained from the ratio of the PL intensity and the total decay time I/τ. At low temperatures, τ_{r} is approximately τ_{r0}, and we found it to be independent of QD diameter D as shown in Fig. 5.5(a). Since at $T \to 0$, γ_{thm} is negligible, the total decay rate in Eq. (5.3) can be simplified into:

$$\gamma(D, T \to 0) = \gamma_{\mathrm{r0}} + \gamma_{\mathrm{tnl}} = \gamma_{\mathrm{r0}} + \frac{c_1}{D}\mathrm{e}^{-\frac{2\sqrt{2m}}{\hbar}\int_0^{D/2}\sqrt{\phi(r)}\mathrm{d}r}. \tag{5.4}$$

From the $\tau(D, T \to 0)$ data in Fig. 5.4(a) we obtained γ_{r0} and c_1. Δ is obtained from the $\tau_{\mathrm{r}}(T)$ data in Fig. 5.5(b), which is generated from Figs. 5.4(b) and (c) using Eq. (5.5). Finally, after obtaining all the parameters related to γ_{r} and γ_{tnl}, we obtain the γ_{thm} parameters, c_2 and c_3, by fitting the $\tau(T)$ data in Fig. 5.4(c) using Eq. (5.3).

In the rest of this section, we will provide further explanations for the expression of each decay channel in Eq. (5.3) and the procedures for extracting the five parameters from Figs. 5.4

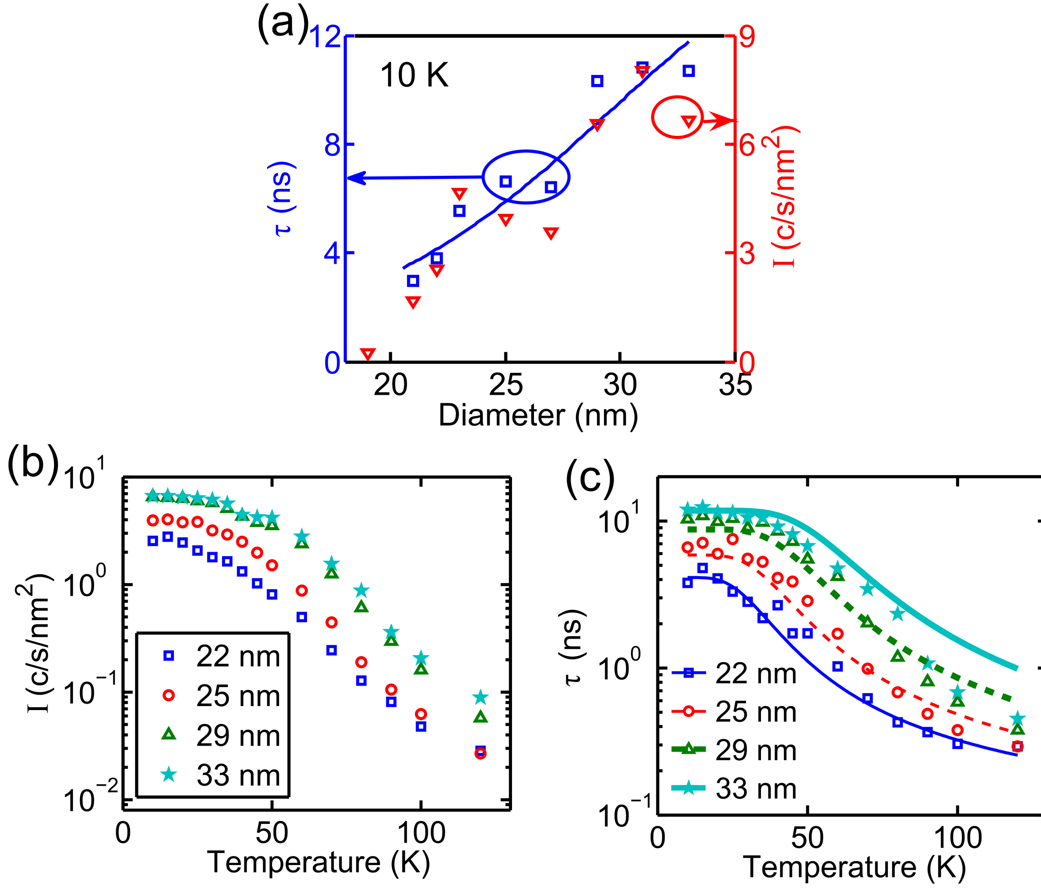

Figure 5.4: (a) The total decay time τ (square, left axis) and PL intensity I (triangle, right axis) vs. QD diameter D dense arrays at 10 K. The $\tau(D)$ data is fitted using Eq. (5.4), yielding $\gamma_{\mathrm{r0}} = 59$ MHz and $c_1 = 15$ m/s. (b) The $I(T)$ data of four dense arrays with QD diameter $D = 22$ nm (blue square), 25 nm (red circle), 29 nm (green triangle), 33 nm (cyan star) nm, respectively. (c) The $\tau(T)$ data of the same four arrays described in (b), which are simultaneously fitted using Eq. (5.3), yielding $c_2 = 2 \times 10^{-3}$ and $c_3 = 0.33$, as shown by blue solid, red dash, green thick dash and cyan thick solid curves. The fitting took into account the instrument time-resolution of 0.2 ns (Sec. 3.2).

and 5.5.

5.3.1 Radiative Decay Rate

First, we show that the radiative decay rate γ_{r} of our QDs is mostly independent of the QD diameter D at 21 nm $< D < 33$ nm. γ_{r} can be calculated from the total decay rate γ and the PL intensity I [164] using the following equation:

$$\gamma_{\mathrm{r}} \propto \gamma I. \tag{5.5}$$

This is because, on one hand, γ_{r} of an exciton is related to the total decay rate γ and QE η via $\eta = \gamma_{\mathrm{r}}/\gamma = \gamma_{\mathrm{r}}/(\gamma_{\mathrm{r}} + \gamma_{\mathrm{nr}})$, in which γ_{nr} is the nonradiative decay rate; on the other hand, η is proportional to I, for QDs of diameter 10 nm $< D < 40$ nm excited by the same laser intensity

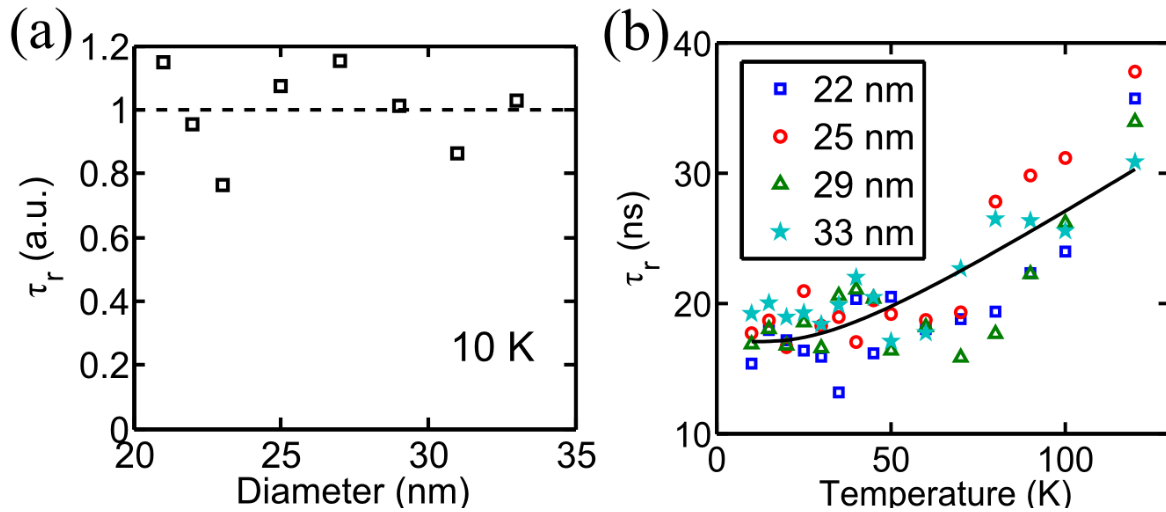

Figure 5.5: (a) The relative $\tau_{\mathrm{r}}(D)$ extracted from the $I(D)$ and $\tau(D)$ data in Fig. 5.4(a) using Eq. (5.5). $\tau_{\mathrm{r}}(D)$ is normalized to the average value (dashed line). (b) The $\tau_{\mathrm{r}}(T)$ relation of dense arrays with $D = 22$ nm (blue square), 25 nm (red circle), 29 nm (green triangle), 33 nm (cyan star) nm. Each τ_{r} data point is proportional to the ratio of the corresponding τ and I values in Figs. 5.4(c) and (b), respectively. All four sets of data are then fitted together using Eq. (5.6) with γ_{r0} and Δ being the fitting parameters, resulting in $\Delta = 8.6$ meV and an arbitrary γ_{r0} value. All data and the fitted curve (solid line) are scaled in the way that $\gamma_{\mathrm{r0}} = 59$ MHz, as obtained in Fig. 5.4(a).

[157]. Applying Eq. (5.5) to the $\tau(D)$ ($\tau = 1/\gamma$) and $I(D)$ data in Fig. 5.4(a), we obtain the relative radiative decay time τ_{r} ($\propto \tau/I$) for QD arrays of various D's at 10 K, as shown in Fig. 5.5(a). This figure suggests that for QDs of 21 nm $< D <$ 33 nm, τ_{r} is almost constant for different D's with $< 24\%$ fluctuations. Henceforth, we use γ_{r0} to denote γ_{r} of all QDs of 21 nm $< D <$ 33 nm at 10 K. The value of γ_{r0} is extracted to be 59 MHz from the $\tau(D)$ data in Fig. 5.4(a).

The above D-independence of γ_{r} at 21 nm $< D <$ 33 nm is not inconsistent with the drastic increase of γ_{r} as D decreased from 2 μm to 40 nm in Sec. 4.4. In Sec. 4.4, the increase of γ_{r} was due to the strain relaxation at the nanodisk sidewall [136], which led to the reduction in the overall polarization fields in the nanodisk and, consequently, the improvement in the exciton oscillator strength [117, 133]. In this work, the strain is already greatly relaxed in QD of $D < 40$ nm, so that further reduction in D does not significantly improve the oscillator strength any more.

Second, we show that the radiative decay rate γ_{r} decreases slightly with increasing temperature due to the scattering and thermalization processes [158], as shown by the increase of τ_{r} in Fig. 5.5(b). In an ideal 2D system, free of impurity-, phonon- and interface-scatterings, an exciton only radiatively recombines if its in-plane momentum $k = 0$, or equivalently, kinetic energy $E_k = 0$. In the presence of various scatterings, characterized by a homogeneously broadened linewidth Δ, an exciton with $k = 0$ may be scattered away from $k = 0$, leading to a reduced recombination probability $\propto 1/\Delta$, whereas an exciton with $E_k < \Delta$ can be scattered

into $k = 0$. According to Boltzmann distribution, the probability for an exciton to have $E_k < \Delta$ is $(1 - \mathrm{e}^{-\Delta/k_B T})$. Therefore, the T-dependence of γ_r follows $\gamma_\mathrm{r} \propto (1 - \mathrm{e}^{-\Delta/k_B T})/\Delta$ [158]. The linewidth Δ depends on T as $\Delta = \alpha + \beta T$ in the temperature range studied here, with α due to the impurity- and interface-scatterings, and βT due to the acoustic-phonon-scattering. The $\tau_\mathrm{r}(T)$ data in Fig. 5.5(b) shows a non-linear T-dependence of τ_r, suggesting that Δ is NOT much less than $k_B T$. On the other hand, $\beta T \ll k_B T$, since $\beta \sim 1.7$ μeV/K for InGaN QDs [165, 166, 123, 167]. Therefore, we have $\beta T \ll \alpha$, i.e. impurity- and interface-scatterings are the dominant scattering mechanisms in our QDs. Henceforth, we treat Δ as T-independent, which leads to a simplified γ_r expression:

$$\gamma_\mathrm{r} = \gamma_{\mathrm{r}0}(1 - \mathrm{e}^{-\Delta/k_B T}). \tag{5.6}$$

Using this equation to fit the $\tau_\mathrm{r}(T)$ data in Fig. 5.5(b), we obtained $\Delta = 8.6$ meV.

The above discussion on the T-dependence of γ_r assumed that the PL of our QDs is dominated by the free-exciton emission as opposed to localized- or bound-exciton emissions. This is supported by the sharp cutoff of the $I(D)$ data at $D \approx 20$ nm, as shown in Fig. 5.4(a). In our sample, $> 90\%$ of QDs with $D > 25$ nm are optically active, while hardly any QDs with $D < 19$ nm are. Such high sensitivity of I to D suggests that the surface nonradiative channels on the nanodisk sidewall dictate the exciton decay process, and that excitons are not confined by a-few-nanometer-scale localization centers or impurities, but by the entire nanodisk.

5.3.2 Tunnelling Decay Rate

At temperature $T \to 0$, the dominant surface nonradiative recombination is due to the tunnelling of excitons through the potential barrier to the sidewall surface. The rate of the tunnelling decay is determined by the coupling of the exciton and the sidewall surface states. A rigorous calculation of this recombination rate requires the full knowledge of the wave-functions of the exciton and surface states as well as the coupling Hamiltonian, which are difficult to obtain. Alternatively we evaluate such a pure quantum-mechanical nonradiative decay by a phenomenological semi-classical model. We calculate the probability for an exciton with zero kinetic energy to tunnel to the sidewall through the potential barrier $\phi(r)$ using the Wentzel-Kramers-Brillouin (WKB) approximation along the nanodisk radius and write the tunnelling decay rate γ_tnl as:

$$\gamma_\mathrm{tnl} = \frac{c_1}{D} \mathrm{e}^{-\frac{2\sqrt{2m}}{\hbar} \int_0^{D/2} \sqrt{\phi(r)} \mathrm{d}r}. \tag{5.7}$$

Here, the scaling constant c_1 is proportional to the probability of an exciton at the surface to recombine with surface states, for which we neglected its temperature dependence. The $1/D$ factor is the sidewall surface-to-volume-ratio taking into account that the tunnelling happens along the entire nanodisk circumference πD and that the exciton is distributed over the entire area $\pi D^2/4$. The potential barrier $\phi(r)$ was obtained in Sec. 5.2.

Neglecting γ_{thm} at low T, we can obtain the parameter c_1 together with γ_{r0} from the $\tau(D, T \to 0)$ data in Fig. 5.4(a), using Eq. (5.4), as mentioned earlier. The fitting yields $c_1 = 15$ m/s and $\gamma_{\text{r0}} = 59$ MHz.

As T increases, γ_{tnl} increases due to the occupation of states with higher kinetic energies. Excitons in higher kinetic energy states see effectively lower potential barriers and thus tunnel faster. However, to simplify the discussion, we only retain the T-independent part of the tunnelling decay rate in γ_{tnl} and include the T-dependent part into the thermal decay rate γ_{thm} by lowering the effective barrier height for thermal decay, as discussed next.

5.3.3 Thermal Decay Rate

At a given temperature T, an exciton has a probability $\mathrm{e}^{-\phi_B/k_BT}$ to gain a kinetic energy greater than the potential barrier height ϕ_B defined in Sec. 5.2. Such an exciton can overcome the potential barrier without tunnelling and travel with thermal velocity v_B towards the sidewall surface to recombine nonradiatively. Therefore, the thermal decay rate γ_{thm} can be written as:

$$\gamma_{\text{thm}} = \frac{c_2 v_B}{D} \mathrm{e}^{-c_3\phi_B/k_BT}, \tag{5.8}$$

in which, c_2 is a proportionality factor, and $1/D$ is again the sidewall surface-to-volume-ratio explained in Eq. (5.7), $v_B = \sqrt{2(c_3\phi_B + k_BT)/m}$ is the average thermal velocity derived using the Boltzmann distribution. Note that we lowered the effective barrier height by multiplying a factor c_3 (< 1) with the ϕ_B in Eq. (5.8) to include the T-dependent part of the tunnelling decay rate, as discussed in Sec. 5.3.2. Combining Eqs. (5.6), (5.7) and (5.8), we obtain the total decay rate γ as Eq. (5.3).

Equation (5.3) fits the $\tau(D, T)$ data very well as shown in Fig. 5.4(c). The fitting gives $c_2 = 2 \times 10^{-3}$ and $c_3 = 0.33$, whereas all other parameters in Eq. (5.3) have been obtained in previous sections.

5.4 Conclusion

In conclusion, we have established a quantitative model to describe the single-exciton potential profile (Eq. (5.1), Sec. 5.2) and the single-exciton decay processes (Eq. (5.3), Sec. 5.3) in an InGaN/GaN QD. All parameters needed in the model were obtained from the measured optical properties of QD arrays, each containing QDs with very similar structures. These parameters are summarized in Table 5.1.

However, there is always unavoidable structural variations from QD to QD within the same array, which result in variations in the optical properties of individual QDs, including their PL energy, intensity, decay time and photon-antibunching properties. We will address these issues in the next two chapters.

Table 5.1: Summary of parameters of the exciton dynamics model extracted from the QD-array data in Secs. 5.2 and 5.3. The uncertainty of each value represents the 95 % confidence interval of the corresponding fitting.

	Value	Unit	Equation	Physical meaning
E_0	2.93 ± 0.02	eV	(4.11)	Exciton energy in unstrained QW
B_m	477 ± 26	meV	(5.1)	Strain-induced redshift in a planar QW
κ	0.037 ± 0.007	nm^{-1}	(5.1)	$1/\kappa$: strain-relaxed region width
γ_{r0}	59 ± 24	MHz	(5.3), (5.6)	Radiative decay rate at $T \to 0$
Δ	8.6 ± 1.4	meV	(5.3), (5.6)	Scattering-induced linewidth
c_1	15 ± 7	m/s	(5.3), (5.7)	Surface recombination factor
c_2	0.0020 ± 0.0008	none	(5.3), (5.8)	Surface recombination factor
c_3	0.33 ± 0.06	none	(5.3), (5.8)	Potential-height factor for γ_{thm}

CHAPTER 6

Optical Properties of Single InGaN/GaN Quantum Dots

In this chapter, we will first present in Sec. 6.1 that the PL properties of a single InGaN/GaN QD and show that it can serve as single-photon source at temperatures up to 90 K. In Sec. 6.2 we show that despite good control of the site and structure of a QD, there is inhomogeneity in the QD's optical properties. However, the fluctuations in different optical properties can be modeled using the fluctuation of a single phenomenological parameter, the lateral potential barrier height, as will be explained in Sec. 6.3. Finally, in Sec. **??**, we show that this model successfully explains the unusual temperature dependence of the photon-antibunching of a QD.

6.1 Single Quantum Dot Optical Properties

The state of a QD is described by the number of electron-hole pairs (EHPs) it contains. A QD with N EHPs is said to be in the Nth-excitonic state, denoted as $|N\rangle$. The decay of the QD follows a cascade process in which the number of EHPs reduces one by one until the QD is in the ground state $|0\rangle$, i.e. the decay follows $|N\rangle \rightarrow |N-1\rangle \rightarrow |N-2\rangle \rightarrow ... \rightarrow |0\rangle$. Due to the exciton-exciton interaction and electronic state filling, the amount of energy released during $|N\rangle \rightarrow |N-1\rangle$ is usually different from that released in $|N-1\rangle \rightarrow |N-2\rangle$. If the energy released in every cascade step is in the form of a photon, the QD will exhibit a luminescence spectrum containing multiple discrete spectral lines, each corresponding to one of the cascade steps. In this work, we denote the exciton $|1\rangle$ and biexciton $|2\rangle$ states as $|\mathrm{X}\rangle$ and $|\mathrm{XX}\rangle$, respectively. The spectral lines corresponding to $|\mathrm{XX}\rangle \rightarrow |\mathrm{X}\rangle$ and $|\mathrm{X}\rangle \rightarrow |0\rangle$ are called the biexciton and exciton emission, respectively.

6.1.1 Photoluminescence Spectrum

The PL spectrum of a single QD of $\sim$ 29 nm in diameter is shown in Fig. 6.1(a), taken at 10 K with an excitation intensity of $P = 6.4$ W/cm^2. It consists of a dominant zero-phonon line (ZPL) and a series of weak replicas at the lower energy side of the ZPL (Fig. 6.1(a), inset).

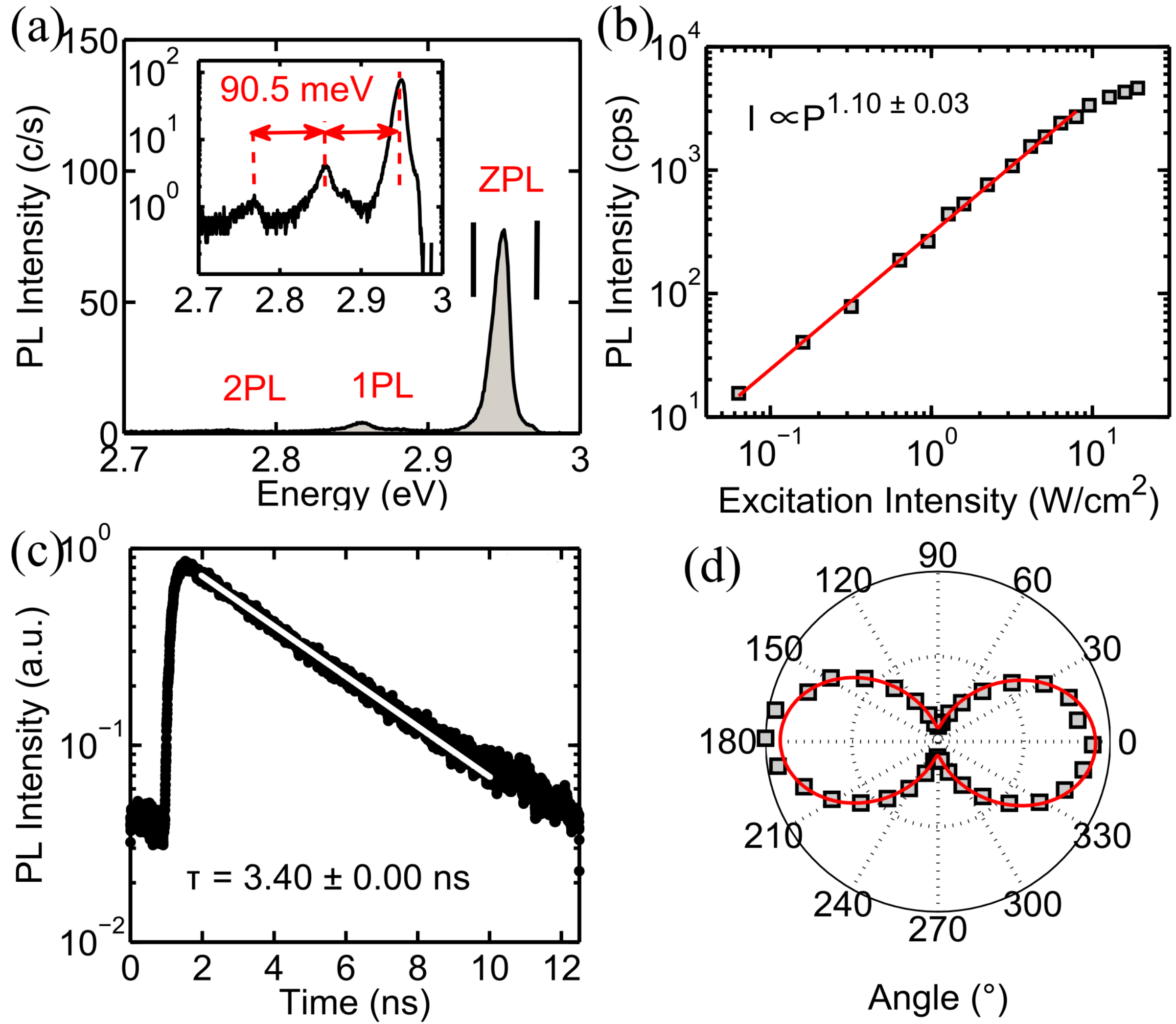

Figure 6.1: 10 K optical properties of a QD of $D = 29$ nm in diameter. (a) The PL spectra at excitation intensity $P = 6.37$ W/cm^2. The inset is a semi-logarithm plot of the same spectrum to emphasize the OP replicas. The two black vertical lines represent the spectral window for the $g^{(2)}$ measurement in Fig. **??**(a). (b) The PL intensity I vs. the excitation intensity P. A fit (solid line) of $\log(I)$ vs. $\log(P)$ shows that I has a linear dependence on P. (c) The time-resolved PL decay curve of the ZPL. A mono-exponential fit (white line) shows a 3.40 ns decay time. (d) Exciton emission intensity I vs. angular orientation (θ) of the linear polarizer. The data are fitted with the equation $acos^2(\theta + b) + c$ (solid line). The fitting results are $a = 0.832, b = 0°, c = 0.08$. The absolute value of the polarizer angle has no physical meaning and is offset so that $b = 0°$.

The integrated intensity of the ZPL increases linearly as the excitation intensity increases as shown in Fig. 6.1(b). Most frequently, this is attributed to the single exciton emission. However, this attribution assumes that ZPL contains only one excitonic state. Under this assumption, it cannot be biexciton or tri-exciton emission, which would lead to quadratic or cubic dependence, respectively. This assumption is verified by the strong antibunching in the second order correlation function of the ZPL, which will be discussed later. Therefore, we conclude that the ZPL is indeed due to the single exciton emission.

The ZPL has a broad FWHM of 14 meV which can be due to the finite radiative decay time, the impurity scattering as discussed in Sec. 5.3.1, and the spectral diffusion. To evaluate the contribution from the finite radiative decay time, we measured the TRPL of the ZPL as shown in Fig. 6.1(c). The decay trace is mono-exponential, consistent with the conclusion that the ZPL is due to a single discrete QD state. The total decay time $\tau = 3.4$ ns, corresponding to a homogeneous linewidth of < 6 μeV, much narrower than the PL linewidth of $\sim$14 meV for the ZPL. Therefore, the linewidth of the ZPL is mainly due to impurity scattering and spectral diffusion. The spectral diffusion[168] is caused by the charge trapping and releasing processes on the free surfaces nearby, such as the QD sidewall and the top of the capping layer. Therefore the spectral diffusion could be reduced by GaN regrowth after surface treatment. The impurity scattering has been discussed in Sec. 5.3.1 which causes a decrease of radiative decay rate with increasing temperature.

The series of replicas at the lower energy side of the ZPL has an energy interval of $\sim$90 meV (Fig. 6.1(a), inset). This value corresponds to the OP energy in GaN (Chap. 2). Hence, we attribute the replicas to the exciton-OP coupling. Unlike acoustic phonons (APs), OPs has a flat dispersion curve. The 1PL and 2PL emission occur when the exciton also emits one and two OPs, respectively. In this process, the energy and momentum conservations are guaranteed because OPs have flat dispersion curve, i.e. they can have finite energy at zero momentum.

6.1.2 Linear Polarization of the Photoluminescence

The ZPL is linearly polarized as depicted in Fig. **??**(d). Linearly polarized exciton emission has been observed by several groups in InGaN QDs of different forms.[7, 169] This has been attributed to the anisotropy of the QD strain profile, possibly caused by the anisotropy in QD geometry.[169] Without additional control measures, the plasma etching process attacks the sidewall randomly and introduces anisotropy in the lateral geometry, leading to the linear polarization with random orientations.

To understand how anisotropy causes linearly polarized exciton emission, we need to consider the electron band structure discussed in Chap. 2. Without external strain, the energy eigenstates of electrons and holes are shown in Fig. 6.2(b). The conduction band states are S orbital angular momentum states with spin up ($|\uparrow\rangle$) and down ($|\downarrow\rangle$) options. The valence band is in the P orbit and, hence, has three orbital angular momentum eigenstates $|P_{-1}\rangle = |X - iY\rangle$,

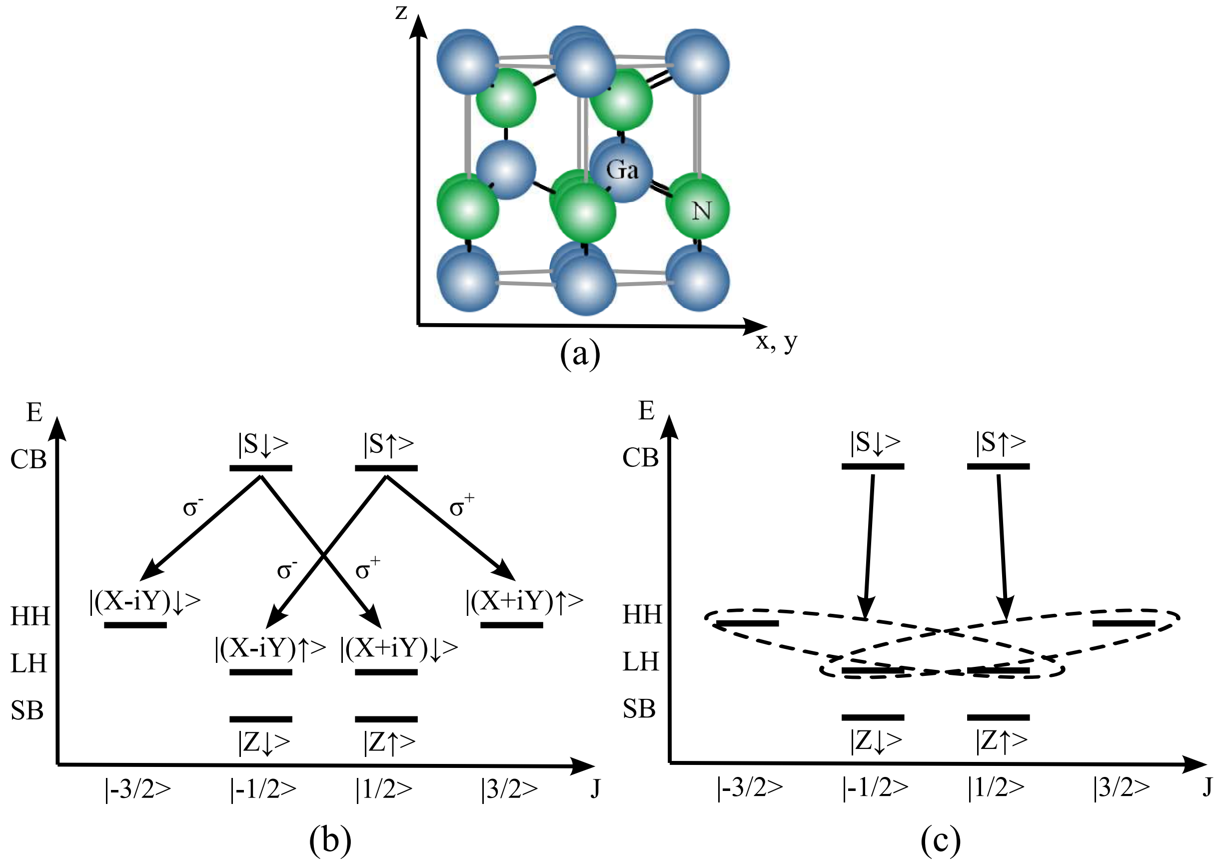

Figure 6.2: The origin of the linearly polarized exciton emission. (a) Wurzite GaN crystal structure. The z-axis is defined as the crystal growth direction (0001) or c-axis. The x- and y-axes are perpendicular to the z-axis. (b) and (c) Energy eigenstates without and with asymmetric lateral strains, respectively.

$|P_{+1}\rangle = |X + iY\rangle$ and $|P_0\rangle = |Z\rangle$, in which $|X\rangle$, $|Y\rangle$ and $|Z\rangle$ are along the x-, y- and z-axes defined in Fig. 6.2(a). For convenience, we neglected the normalization of the wave-functions. The valence band can be divided into the heavy-hole band, the light-hole band and the split-off band. The split-off band is mainly composed of $|Z\rangle$ and have very different energy from $|X\rangle$ and $|Y\rangle$ due to the asymmetry between the c-axis and the lateral plane. Therefore, we ignore the contribution from the split-off band in the following discussion. The heavy-hole and light-hole bands have different energy due to the spin-orbital coupling. The total angular momenta J of the four hole states are labeled in the J-axis in Fig. 6.2(b). The allowed optical transitions have to obey the angular momentum selection rule as well as the conservation of the spin. With these limitations, there are only four allowed optical transitions and they are all circularly polarized ($\sigma^{\pm}$) if observed along the a-axis.

When an asymmetrical strain is applied in the lateral plane, the energy eigenstates mix with each other as illustrated in Fig. 6.2(c). It turns out that this mixture is very sensitive to the amount of strain, i.e. a very tiny amount of asymmetry in the strain will cause very high degree of mixture, leading to highly linearly polarized emission. The 50:50 mixture $|(X - iY) \downarrow\rangle + |(X + iY) \downarrow\rangle$ results in $|X \downarrow\rangle$ with 100% polarization along the x-axis.

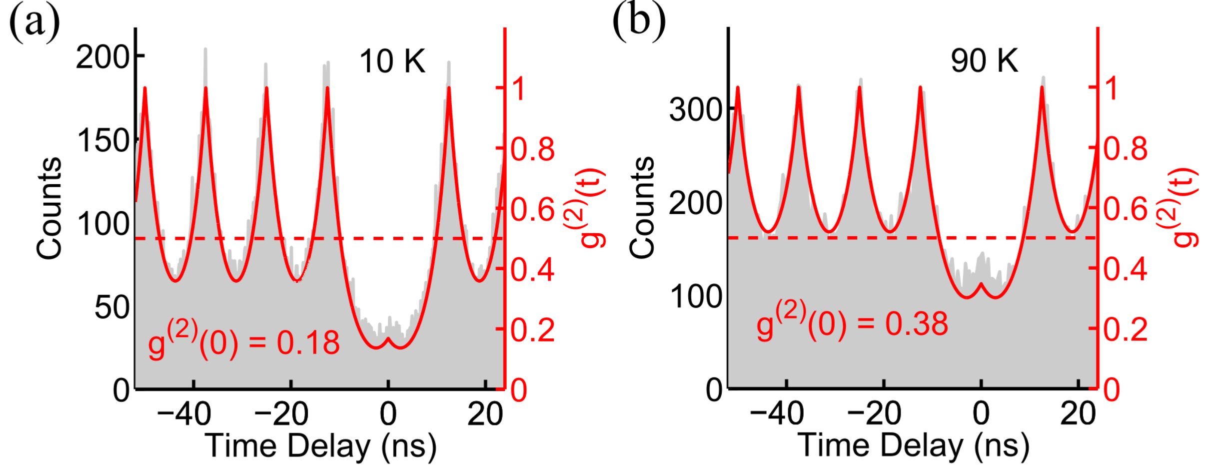

Figure 6.3: Single photon emission up to 90 K. All data are without any background subtraction. (a) 10 K $g^{(2)}$ data of the QD described in in Fig. 6.1. (b) 90 K $g^{(2)}$ data measured from another QD of $D = 29$ nm in diameter. The solid curves are the fitted $g^{(2)}$ function[24] showing $g^{(2)}(0) = 0.18$ for (a) and $g^{(2)}(0) = 0.38$ for (b), respectively.

6.1.3 Second Order Correlation Function $g^{(2)}$

As mentioned earlier, to verify that the ZPL in the PL spectrum in Fig. 6.1(a) is from a single discrete state, we need to perform the second-order correlation ($g^{(2)}$) measurement. We do this by applying a spectral bandpass filter with a bandwidth of 30 meV as marked by the pair of vertical lines in Fig. 6.1(a). Using the HBT setup in Fig. 3.6, without saturating the exciton state, at $P = 4.77$ W/cm^2 excitation intensity, we obtained the $g^{(2)}$ function of the ZPL as shown in Fig. 6.3(a).

The $g^{(2)}(t)$ function is defined as:

$$g^{(2)}(t) = \frac{\langle I_1(t')I_2(t'+t)\rangle}{\langle I_1(t')\rangle\langle I_2(t')\rangle}, \tag{6.1}$$

in which $I_1(t')$ and $I_2(t')$ are the photon flux intensities at time t' detected by the two arms of the HBT interferometer, and $\langle\rangle$ stands for the average over t'. For an ideal single-photon source, it is impossible for the two arms to detect photons simultaneously, therefore, we have $I_1(t')I_2(t') = 0$ and $g^{(2)}(0) = 0$.

In our experiment, we use pulsed laser to trigger the QD. To characterize the number of photons emitted after each pulse, we define the quantity $g_0^{(2)}$ as:

$$g_0^{(2)} = \frac{\int_{0^{th}\ peak} g^{(2)}(t)\mathrm{d}t}{\int_{i^{th}\ peak,\ i>1} g^{(2)}(t)\mathrm{d}t}. \tag{6.2}$$

In most experimental systems, due to the low photon extraction and detection efficiencies ($\ll 1$), this expression can be simplified as [170]: $g_0^{(2)} = \langle n(n-1)\rangle/\langle n\rangle^2$, where n is the number

of photons emitted after each pulse.

Obviously, Equ. 6.2 is only applicable when the laser pulse period is much longer than the decay time of the QD so that the $g^{(2)}$ peaks do not overlap. In many of our QDs, however, the decay time is comparable with the 12.5 ns laser pulse period so that the $g^{(2)}$ peaks overlap considerably with each other, rendering Equ. 6.2 inapplicable.

In this case, in order to extract the equivalent $g_0^{(2)}$, we first need to fit the data by a model taking into account the dynamics of the emitter. Using the fitting results, we can reconstruct the $g^{(2)}$ function assuming a pulse period Λ much longer than the PL pulse duration, so that the central $g^{(2)}$ peak is well separated from the side peaks and $g_0^{(2)}$ can then be calculated using Equ. 6.2.

Following Dekel's work[171], we assume that the spectral window includes the emission from N excitonic states $|1\rangle$, ..., $|i\rangle$, ..., and $|N\rangle$. We use $|0\rangle$ to represent the ground state. To simplify the formalism, we assume that the laser excitation pulse duration is infinitely short and that it is followed by the free evolution of QD states until the arrival of the next pulse which resets the QD as illustrated in Fig. 6.4(a). The assumption is reasonable given that our laser pulse duration is only $\sim$150 fs, much shorter than the nanosecond time scale of the QD carrier dynamics. For excitation lasers with long pulse durations, our theory can be readily generalized by convolution. The use of laser excitation, a coherent light source, implies that the initial photo-injected number of EHPs obeys the Poisson distribution, i.e. the probability for the QD to be in $|i\rangle$ is $w_i = \frac{I^i e^I}{i!}$, where I is the average number of injected EHPs. We denote the radiative, nonradiative and total decay times (rates) of $|i\rangle$ as $\tau_{r,i}$ ($\gamma_{r,i}$), $\tau_{nr,i}$ ($\gamma_{nr,i}$) and τ_i (γ_i), respectively. They satisfy $\gamma_i = \gamma_{r,i} + \gamma_{nr,i} = 1/\tau_i = 1/\tau_{r,i} + 1/\tau_{nr,i}$. Also we defined the QE of $|i\rangle$ as $\eta_i = \gamma_{r,i}/\gamma_i$. For a given initial QD state $|j\rangle$ the probability for the QD being at the $|i\rangle$ state at time t is $p_{ij}(t)$ ($0 \le p_{ij} \le 1$). The corresponding rate equation can be written as $\frac{\mathrm{d}\mathbf{p_j}}{\mathrm{d}t} = \mathbf{\Gamma p_j}$, in which

$$\mathbf{\Gamma} = \begin{pmatrix} 0 & \gamma_1 & & & & & & \\ & -\gamma_1 & \gamma_2 & & & & & \\ & & \cdots & & & & & \\ & & & -\gamma_i & \gamma_{i+1} & & & \\ & & & & \cdots & & & \\ & & & & & -\gamma_{N-1} & \gamma_N \\ & & & & & & -\gamma_N \end{pmatrix}, \tag{6.3}$$

and $\mathbf{p_j} = (p_{0j}, \ldots, p_{ij}, \ldots, p_{Nj})^T$. With the initial conditions $p_{jj} = 1$ and $p_{i \neq j,j} = 0$, $\mathbf{p_j}$ can be

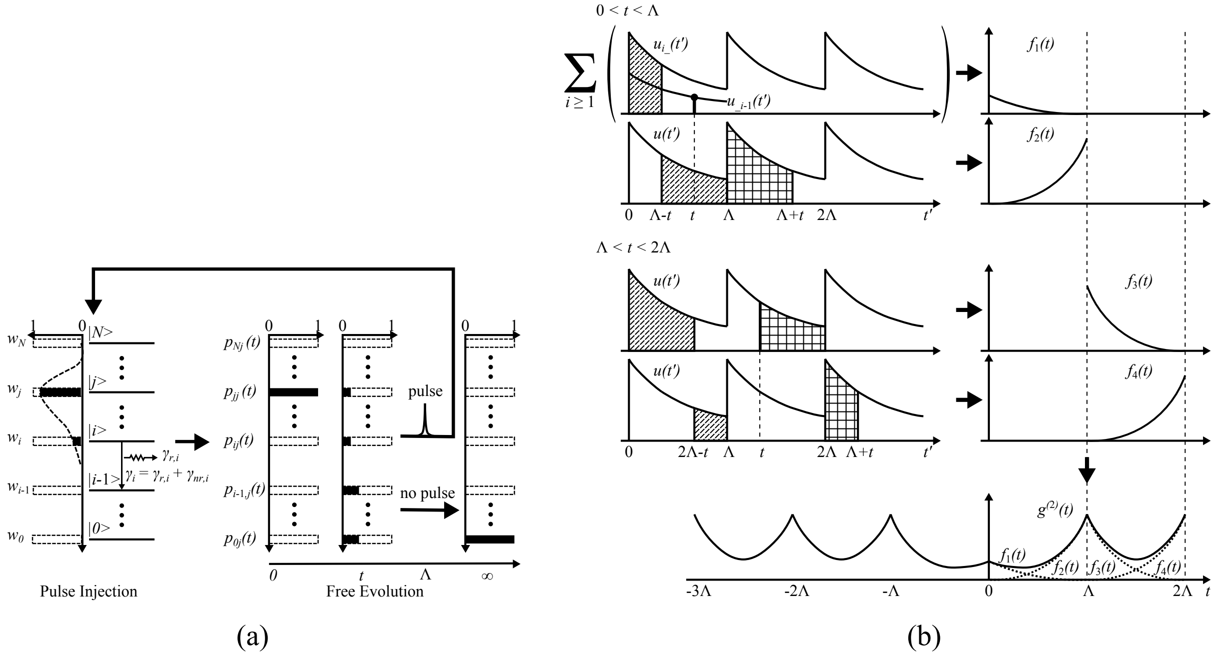

Figure 6.4: Pulsed $g^{(2)}$ fitting theory. (a) Illustration of the pulse injection after which the QD has w_j probability to be in the $|j\rangle$ state and the following free evolution of all states given that the QD is initialized in the $|j\rangle$ state. In the pulse injection stage, the QD is initialized at state $|j\rangle$ with probability w_j governed by the Poisson distribution (dashed profile). The free evolution stage, in which the excitation is off, then starts with state $|j\rangle$ at $t = 0$. The probability of the QD being at $|i\rangle$ at time t is described by the $p_{ij}(t)$ in Equ. 6.4. Eventually at $t = \infty$ the QD will be in the $|0\rangle$ ground state if no excitation comes to reset the QD. Otherwise, the QD will go back to the pulse injection stage. (b) Illustration of the four $g^{(2)}$ integrands f_1, f_2, f_3, f_4 and how they make up the $g^{(2)}$ curve. Each integrand on the right-hand-side panel is obtained from the corresponding correlation of the two shaded areas in the left-hand-side panel except for $f_1(t)$ whose formation is described in Equ. 6.5. The $g^{(2)}(t)$ curve at the bottom is obtained by the summation of the four integrands and the replication using $g^{(2)}(t)|_{t=[k\Lambda,(k+1)\Lambda]} = g^{(2)}(t)|_{t=[\Lambda,2\Lambda]}, k = 1, 2, ...,$ and $g^{(2)}(t) = g^{(2)}(-t)$.

solved analytically [171],

$$p_{ij}(t) = \begin{cases} \sum_{l=1}^{j} \frac{\tau_l^{j-1}}{\prod_{m=1,m\neq l}^{j} (\tau_l - \tau_m)} \left(1 - e^{-t/\tau_l}\right), & i = 0 \\ \sum_{l=i}^{j} \frac{\tau_l^{j-i-1}}{\prod_{m=1,m\neq l}^{j} (\tau_l - \tau_m)} e^{-t/\tau_l}, & 0 < i \leq j \\ 0, & i > j. \end{cases} \tag{6.4}$$

To get the $g^{(2)}$ function, we need to consider all different initial states $|j\rangle$ and average their effects. To simplify the derivation we first define the following quantities: $u_{ij}(t) = \gamma_{r,i} p_{ij}(t)$, the emission intensity of $|i\rangle$ at t following the initial state $|j\rangle$; $u_{i_}(t) = \sum_{i \leq j \leq N} w_j u_{ij}(t)$, the averaged emission intensity of $|i\rangle$ at t considering the fluctuation of j; $u_{_j}(t) = \sum_{0 \leq i \leq j} u_{ij}(t)$,

the total emission intensity of the QD at t after the initial state $|j\rangle$; and $u(t) = \sum_{0\le i\le N} u_{i_}(t)$, the total emission intensity. It turns out that to get the $g^{(2)}(t)$ curve over the entire time delay range $t = [-\infty, +\infty]$ we only need to calculate two sections $g^{(2)}(t)|_{t=[0,\Lambda]}$ and $g^{(2)}(t)|_{t=[\Lambda,2\Lambda]}$, where Λ is the period of the excitation pulse. These two sections can be written as following:

$$
\begin{aligned}
g^{(2)}(t)|_{t=[0,\Lambda]} &= f_1(t) + f_2(t) \\
&= \frac{1}{A}\sum_{i\ge 1} u_{_i-1}(t)\int_0^{\Lambda-t} u_{i_}(t')\mathrm{d}t' + \frac{1}{A}\int_{\Lambda-t}^{\Lambda} u(t')u(t'+t-\Lambda)\mathrm{d}t', \\
g^{(2)}(t)|_{t=[\Lambda,2\Lambda]} &= f_3(t) + f_4(t) \\
&= \frac{1}{A}\int_0^{2\Lambda-t} u(t')u(t'+t-\Lambda)\mathrm{d}t' + \frac{1}{A}\int_{2\Lambda-t}^{\Lambda} u(t')u(t'+t-2\Lambda)\mathrm{d}t',
\end{aligned}
\tag{6.5}
$$

where the first integral $f_1(t)$ corresponds to the correlation occurs within the same pulse period considering that once an ith-exciton photon is detected the QD is known to be in the state $|i-1\rangle$; $f_2(t)$corresponds to the correlation between two sequential pulses; $f_3(t)$ ($f_4(t)$) is the correlation between the first pulse and the second (third) pulse; and $A = \int_0^{\Lambda} u^2(t')\mathrm{d}t'$ is the normalization factor. Figure 6.4(b) illustrates the four integrands as well as how they compose the entire $g^{(2)}$ curve. The rest of the $g^{(2)}(t)$ curve can be assembled using $g^{(2)}(t)|_{t=[k\Lambda,(k+1)\Lambda]} = g^{(2)}(t)|_{t=[\Lambda,2\Lambda]}, k = 1, 2, ...$, if there is no longer-time-scale blinking effects; and $g^{(2)}(t) = g^{(2)}(-t)$, if we only consider self-correlation measurement, i.e. the two photo-detectors detects the same photon flux.

It is not hard to see that $g^{(2)}(k\Lambda) = 1, k = \pm 1, \pm 2, ...$ which is due to the normalization factor A in Equ. 6.5. According to Equ. 6.5, if $u(t)$ has a characteristic decay time τ_u much shorter than $\Lambda/2$ so that $u(t \ge \Lambda/2) \sim 0$, we get $g^{(2)}(\frac{k+1}{2}\Lambda) \sim 0$, i.e. all peaks are clearly separated, and that $g^{(2)}(t)$ only has significant values at the vicinities $[k\Lambda - \tau_u, k\Lambda + \tau_u]$, k is an arbitrary integer. This is the only situation where Equ. 6.2 is applicable. In addition, from Fig. 6.4(b) and Equ. 6.5, we can readily tell that $f_2(t)$ and $f_3(t)$ are mirror symmetric about $t = \Lambda$, and that $f_4(t)$ is a translation of $f_3(t)$ with $t \to t - \Lambda$. Hence, $g^{(2)}(t)|_{t=[\Lambda,2\Lambda]}$ is an even function with respect to $t = \frac{3}{2}\Lambda$ but $g^{(2)}(t)|_{t=[0,\Lambda]}$ is not, which means the shape of all $g^{(2)}$ peaks, defined on $t = [(k - \frac{1}{2})\Lambda, (k + \frac{1}{2})\Lambda]$ for arbitrary k, are symmetric except for the $\pm 1^{st}$ peaks. The $\pm 1^{st}$ peaks has approximately the same shape as other side peaks only when $\Lambda \gg \tau_X$. The integrand f_1 is the only term in Fig. 6.5 that reflects the quantum nature of the QD emission. If only one state $|i\rangle$ is selected to perform the $g^{(2)}$ measurement, which effectively sets the QEs of all other states zero by not collecting them, $u_{_i-1}(t)$ is always zero so $g^{(2)}(0) = 0$. Interestingly, if one selects multiple states, none of which is adjacent to another state, simultaneously (for instance, $|1\rangle$, $|3\rangle$ and $|6\rangle$) to perform the $g^{(2)}$ measurement, $g^{(2)}(0)$ is still zero.

The above model for $g^{(2)}$ requires the following input parameters to fit the experimental data: the average number of photo-injected EHPs by each laser pulse P_N, the total decay times

and the QEs of all QD states τ_i and η_i, respectively, and the normalization factor A.

The parameter P_N can be calculated from the laser excitation intensity P and the absorption cross section σ_{abs} of the QD. It is not straightforward to calculate σ_{abs} since it is related to the QD's geometry, orientation in respect to the laser propagation and polarization direction, dielectric environment, and InGaN complex refractive index. Using FDTD software we calculated the absorption cross section for our QD as $\sigma_{abs} \sim 10\ nm^2$ from which we get $P_N = 0.15$ and $P_N = 0.6$ for Fig. 6.3(a) and (b), respectively.

We can further reduce the number of fitting parameters to only include the normalization factor A, the exciton total decay time τ_1 and the relative QE of XX $\tilde{\eta}_{XX/X} = \eta_2/\eta_1$ by making the following assumptions. First, we assume that the radiative decay time of all states are connected with exciton radiative decay time $\tau_{r,1}$ by $\tau_{r,i} = i/\tau_{r,1}$ which is, to the first order approximation, correct for most QDs. In addition, we define the relative QEs of higher order multi-excitonic states in respect to exciton as $\tilde{\eta}_i = \eta_i/\eta_1$ and assume that all higher order multi-excitonic states than biexciton has negligible QEs, i.e. $\tilde{\eta}_i = 0$ for $i > 2$. Note that we only need to know the relative QE $\tilde{\eta}_{XX/X}$ but not η_1, since η_1 only appears as a constant in the u_{ij} expression as $u_{ij}(t) = i\eta_1\gamma_1 p_{ij}(t)$ which will be cancelled by the same component in the normalization factor A in the $g^{(2)}$ expression Equ. 6.5. Once we get the three parameters, the Equ. 6.2 can then be applied by reconstructing the $g^{(2)}$ curve using a pulse period $\Lambda \gg \tau_1$.

The $g^{(2)}$ data fitting using three parameters τ_1, $\tilde{\eta}_{XX/X}$ and A is valid, since τ_1 mainly affects the width of the $g^{(2)}$ peaks, $\tilde{\eta}_{XX/X}$ mainly affects the amplitude of the 0th peak ($\tilde{\eta}_{XX/X} = 0$ means $g_0^{(2)} = 0$ i.e. single photon emission), and A is the amplitude of the $g^{(2)}$ side peaks. To minimize the artificial cutoff due to the finite N, in our calculations we use $N = 20$. For the data in Fig. 6.3(a) the fitting gives $\tilde{\eta}_{XX/X} = 0.16 \pm 0.01$, $\tau_1 = 3.74 \pm 0.03\ ns$ and $A = 181 \pm 1.94$ from which we get $g_0^{(2)} = 0.18$ well below 0.5. Fitting the data in Fig. 6.3(c) leads to $\tilde{\eta}_{XX/X} = 0.36 \pm 0.03$, $\tau_1 = 5.2 \pm 0.11\ ns$ and $A = 323 \pm 4.06$ which yields $g_0^{(2)} = 0.38$.

The non-zero $g^{(2)}(0)$ value comes from emission by multi-exciton states within our spectral window. Single photon sources based on QDs typically require a narrow spectra filter to separate the exciton emission from multi-exciton emissions. Due to the large built-in electric field, the emission lines in III-N QDs, including in our QDs, are often severely broadened by spectral diffusion and are difficult to separate, which typically would forbid anti-bunching in the emission. The good anti-bunching in the $g^{(2)}$ data, despite the inclusion of multi-exciton emissions, indicates that excitons have much higher quantum efficiencies (QEs) than multi-exciton states.

The difference in QEs results from the lateral potential profile derived in Sec. 5.2, which serves as a barrier to protect EHPs from reaching the sidewall surface where they recombine nonradiatively.[172] Therefore, higher potential barriers result in higher EHP QEs. As will be discussed in more detail, due to the exciton-exciton interaction, biexciton experiences a shallower potential profile compared to that experienced by exciton, leading to a relatively lower QE for the biexciton. At low excitation intensities, $g^{(2)}(0)$ is approximately the biexciton-to-exciton QE ratio.[170]

6.2 Inhomogeneities in PL properties

Compared to self-assembled InGaN QDs, our QDs have significantly improved control over all key structural parameters: the nanodisk thickness l, the indium mole fraction x and the disk diameter D. Therefore, they have significantly reduced inhomogeneities in optical properties compared to self-assembled ones made of the same material.

However, inhomogeneities cannot be completely eliminated. There still exist finite fluctuations in all three parameters: $\delta l = 2$ MLs limited by MOCVD growth, $\delta D = 2$ nm limited by the electron-beam lithography and plasma etching processes, and $\delta x = 0.2$ % limited by the Poisson distribution of the number of indium atoms, as we have analyzed in [**?**].

To study the influence of the structural fluctuations to the inhomogeneities in optical properties, we measured the PL energy, intensity, decay time, spectral linewidth and photon-antibunching of 30 QDs with the same nominal diameter of 29 nm. We find that all these properties are strongly correlated despite large inhomogeneities in each of them. We can successfully explain these correlations and account for the inhomogeneities of the QDs by varying only the potential barrier height ϕ_B defined in Eq. (5.2).

To illustrate the inhomogeneities, we intentionally choose two QDs, namely D1 and D2, with the same nominal diameter $D = 29$ nm but with very different optical properties at 10 K. As shown in Fig. 6.5(a), these two dots share some common spectral features, such as a prominent ZPB and weak but discernible OP replicas with an OP energy of ~ 91 meV [**?**]. However, the PL peak energy of D1 is higher than that of D2 by ~ 80 meV; the integrated PL intensity of D1 is only 74% of that of D2; and the ZPB full-width-at-half-maximum (FWHM) of D1 is 15 meV, only 42% of D2's FWHM. Moreover, Fig. 6.5(b-d) shows that their decay times and $g^{(2)}$ functions differ significantly. D1 has a decay time of 3.4 ns, 79% less than that of D2, and a $g_0^{(2)}$ value of 0.18 in comparison to D2's 0.76. The $g_0^{(2)}$ value is a measure of the degree of photon-antibunching, as will be defined and discussed later in Sec. **??**.

To statistically characterize the inhomogeneity, we measured the PL spectra and TRPL decay traces of 30 QDs with the same nominal diameter $D = 29$ nm at 10 K. The PL spectrum of every QD consists of a dominant ZPB and several OP replicas with ~ 90 meV interval [**?**] (also see Fig. 6.9(a) for an example). However, the peak-energy E of the ZPB, the integrated PL intensity I, the FWHM ΔE of the ZPB, and the decay time τ vary among QDs. We plot their distributions in Fig. 6.6.

To verify the control over our QDs' structural parameters, we compare the variations in the QDs' optical properties with uncertainties in the structural parameters in the fabrication. On one hand, the statistical distributions of single-dot PL energy are obtained from the μ-PL of 30 individual QDs. As shown in Fig. **??**(a), the PL energy has a standard deviation of 34.5 meV. On the other hand, we can estimate the variation in the QDs' PL energy due to fluctuations in l, D, and x. The results are summarized in Table 6.1.

To evaluate the contribution of the fluctuation of $\Delta l = 2$ ML (1 ML$\sim$0.5 nm) we use a

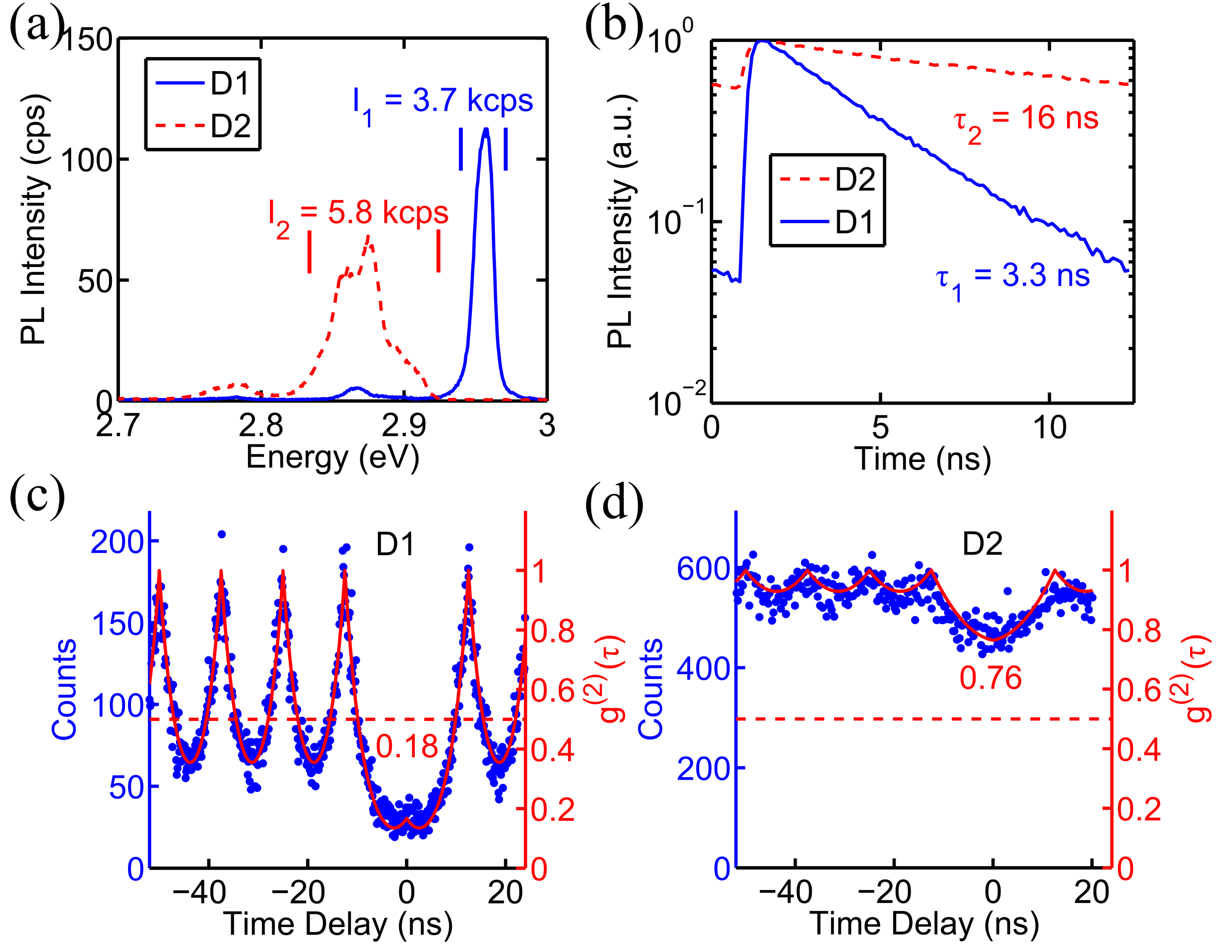

Figure 6.5: (a) The PL spectra of D1 and D2 with peak energies at 2.96 eV and 2.88 eV, integrated intensities of 3.7 kcps and 5.8 kcps, and ZPB FWHM of 15 meV and 35 meV, respectively. (b) The TRPL decay curves of D1 and D2 with decay times of 3.4 ns and 16.2 ns, respectively. (c) and (d) are the $g^{(2)}$ functions of D1 and D2 measured with the excitation intensity $P = 204$ W/cm^2 (0.4 photons per pulse) and $P = 76$ W/cm^2 (0.14 photons per pulse), respectively. The spectral filter window used in our second-order correlation measurements in this work are always adjusted to include the entire ZPB.

Table 6.1: The contributions of the thickness l, indium fraction x and diameter D fluctuations to the total PL energy E inhomogeneity ΔE for a circular $\text{In}_{x=0.15}\text{Ga}_{0.85}\text{N}$ nanodisk with $l = 3$ nm and $D = 29$ nm. ΔE is calculated from each contribution as $\Delta E = \sqrt{\Delta E_l^2 + \Delta E_x^2 + \Delta E_D^2}$.

Source	Fluctuation	Contribution to ΔE
Thickness	$\Delta l = 2$ ML	$\Delta E_l = 28$ meV
Diameter	$\Delta D = 1.7$ nm	$\Delta E_D = 6$ meV
Indium fraction	$\Delta x = 0.2\%$	$\Delta E_x = 8$ meV
	Total calculated	$\Delta E = 30$ meV
	Total observed	$\sigma_E = 34.5$ meV

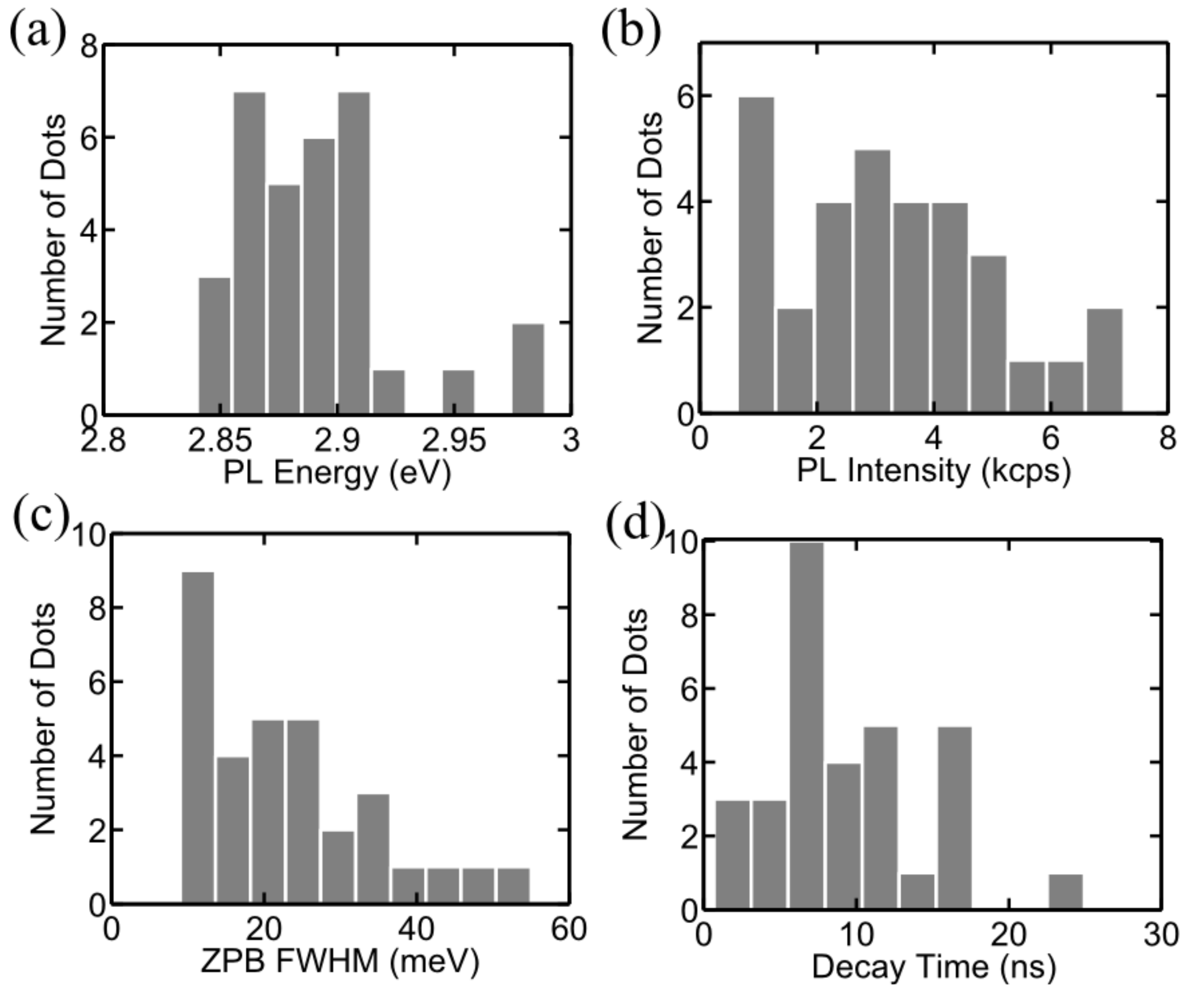

Figure 6.6: The statistical distributions of (a) the PL energy E, (b) the PL intensity I, (c) the FWHM ΔE of the ZPB and (d) the PL decay time τ of 30 QDs randomly chosen from the same array of diameter $D = 29$ nm. All data were taken at 10 K. The PL intensity unit kcps stands for kilo-count per second recorded by the end detector.

simple planar capacitor model in which the upper and lower InGaN/GaN interfaces are the two capacitor plates. We assume that a fixed amount of charge at the two plates leads to a fixed electric field strength F. Therefore, increasing l decreases E by $\Delta E = eF\Delta l$. The amount of E reduction from the intrinsic InGaN bandgap without any strain E_0 is $E_0 - E = eFl = 63$ meV which is extracted from the E vs. D relation of a QD.[172] Knowing $l = 3$ nm and $\Delta l = 2$ ML we get $\Delta E = eF\Delta l/l = 21$ meV. Increasing l also reduces carrier confinement in the vertical (growth) direction which further reduces the PL energy. This can be estimated by a simple 1D particle-in-a-box model, assuming the potential in the vertical direction acts as an infinite potential well, as $\Delta E = \Delta l \frac{\mathrm{d}}{\mathrm{d}l}\frac{(\hbar\pi/l)^2}{2m} = 18$ meV in which $\hbar$ is the reduced Planck constant and m is the effective mass of a GaN exciton, 1.6 times the free electron mass. Therefore, the total contribution due to Δl is roughly $\Delta E_l = \sqrt{21^2 + 18^2} = 28$ meV.

To study how the diameter influences the optical properties of our QDs, we measured the PL energy of nine dense arrays of QDs with different diameters. Each dense array has 100×100 QDs with the same nominal diameter. Fig. **??**(b) shows the PL energy E vs. QD diameter D data, which reflects mainly the relaxation of strain due to diameter reduction.[1] A linear fit of the data suggests that the PL energy changes with diameter at a rate $\frac{\Delta E}{\Delta D} = -3.5$ meV/nm. On the other hand, a statistics of QD diameter in the same array measured by SEM suggests that the diameter fluctuation is $\Delta D = 2$ nm as shown in Fig. **??**(c). Therefore, PL energy inhomogeneity ΔE caused by diameter fluctuation is only around $\Delta E_D = 6$ meV.

The indium-fraction inhomogeneity originates from the fundamental uncertainty in the number of indium atoms in each QD. Studies [173] have shown that InGaN is a random alloy in which indium atoms distribute randomly but uniformly, and that they do not form the so-called indium-rich islands of the nanometer-length scale especially when the indium fraction is as low as $x = 15\ \%$ as in our case. In a disk-shaped $In_{0.15}Ga_{0.85}N$ QD of 3 nm in thickness and 29 nm in diameter, there are around $N = 4,500$ indium atoms. Being a random alloy means that the number of indium atoms obeys the Poisson distribution whose standard deviation can be calculated as $\sigma_N = \sqrt{N} = 67$. Therefore, the minimum indium-fraction fluctuation is $\Delta x = x\frac{\sigma_N}{N} = 0.2\%$. This gives rise to a PL energy fluctuation of $\Delta E_x = (3.5\ \mathrm{eV} - 2.89\ \mathrm{eV})\frac{\Delta x}{x} = 8\ \mathrm{meV}$, in which 3.5 eV is GaN band gap and 2.89 eV is the average QD PL energy from Fig. **??**(a). Here we assumed that the band gap varies linearly with the indium fraction.

All three sources of inhomogeneities, as summarized in Table 6.1, add up to $\Delta E = \sqrt{\Delta E_l^2 + \Delta E_x^2 + \Delta E_D^2}$ 30 meV, which matches well with the observed total PL energy fluctuation of $\sigma_E = 34.5$ meV. From this analysis we also concluded that the QD thickness fluctuation is the dominant source of inhomogeneity.

The influence of l fluctuation on E can be understood using a simple capacitor model: $E = E_0 - eFl$ [174, 156], in which F is dominated by the strain-induced electrical field.

[1]Note that, with a reduction of the disk diameter, the PL energy may also increase due to lateral quantum confinement. However, this only leads to a change of < 10 meV varying the diameter from 30 nm to 20 nm.

Hence, based on Eqs. (4.11) and (5.2), δE can be described by the fluctuation in ϕ_B. According to Fig. 6.6(a), E varies by about 120 meV in the same $D = 29$ nm array, which allows us to estimate that ϕ_B varies from ~ 0 to 120 meV based on Eqs. (4.11) and (5.2). In the following we show that indeed, for a given D, the influence of structural parameter fluctuations on the optical properties can be modeled by varying only the potential barrier height ϕ_B.

6.3 Correlations among PL properties

Despite the seemingly random fluctuations in each PL property, we find that all measured PL properties are strongly correlated. Figure 6.7 shows the correlations among E, I, ΔE and τ. These correlations demonstrate that all QDs in the same array share the same radiative decay time $\tau_{\rm r}$ and that the observed PL inhomogeneities can all be modeled by the variation of ϕ_B, as shown below.

6.3.1 The Correlation between I and τ

The correlation between I and τ of individual QDs are linear as shown in Fig. 6.7(a). This suggests that $\tau_{\rm r}$ ($\propto \tau/I$) is insensitive to the mechanism that leads to the PL inhomogeneity among QDs of the same D. We have found earlier in Sec. 5.3.1 that $\tau_{\rm r}$ is also insensitive to D. Henceforth, we treat $\tau_{\rm r0}$ as a constant for all QDs of 22 nm $< D <$ 33 nm in our sample, whose value has already been obtained in Sec. 5.3.1 as $\tau_{\rm r0} = 17$ ns.

6.3.2 The Correlation between E and τ

The correlation between E and τ are shown in Figs. 6.7(b). As discussed in Sec. 6.2, the PL energy E fluctuation is mainly due to the thickness fluctuation δl, or equivalently $\delta\phi_B$. On the other hand, ϕ_B also determines τ through Equ. 5.4. Therefore, we can plot the theoretical correlation curve (Fig. 6.7(b) solid line) between E and τ by sweeping the ϕ_B value from 4 to 120 meV. For each ϕ_B value we obtain E using Equ. 4.11 and τ using Equ. 5.4. The understanding of the correlation is straightforward: In a QD with low E, the potential barrier height ϕ_B is large. Therefore, the exciton decay is dominated by the radiative decay with a decay time close to $\tau_{\rm r0} = 17$ ns, whereas the tunneling and thermal decay are suppressed. In a QD with high E, the ϕ_B is low. Therefore, the exciton undergoes tunneling and thermal nonradiative decay in addition to the radiative decay, leading to a short decay time.

6.3.3 The Correlation between ΔE and τ

The correlation between ΔE and τ in Fig. 6.7(c) can be understood as follows. The ZPB consists the contributions of multiple unresolved spectral lines, as manifested by the non-zero $g_0^{(2)}$ values from all our QDs (Fig. 6.8(a)). Therefore, ΔE is determined by the linewidth of

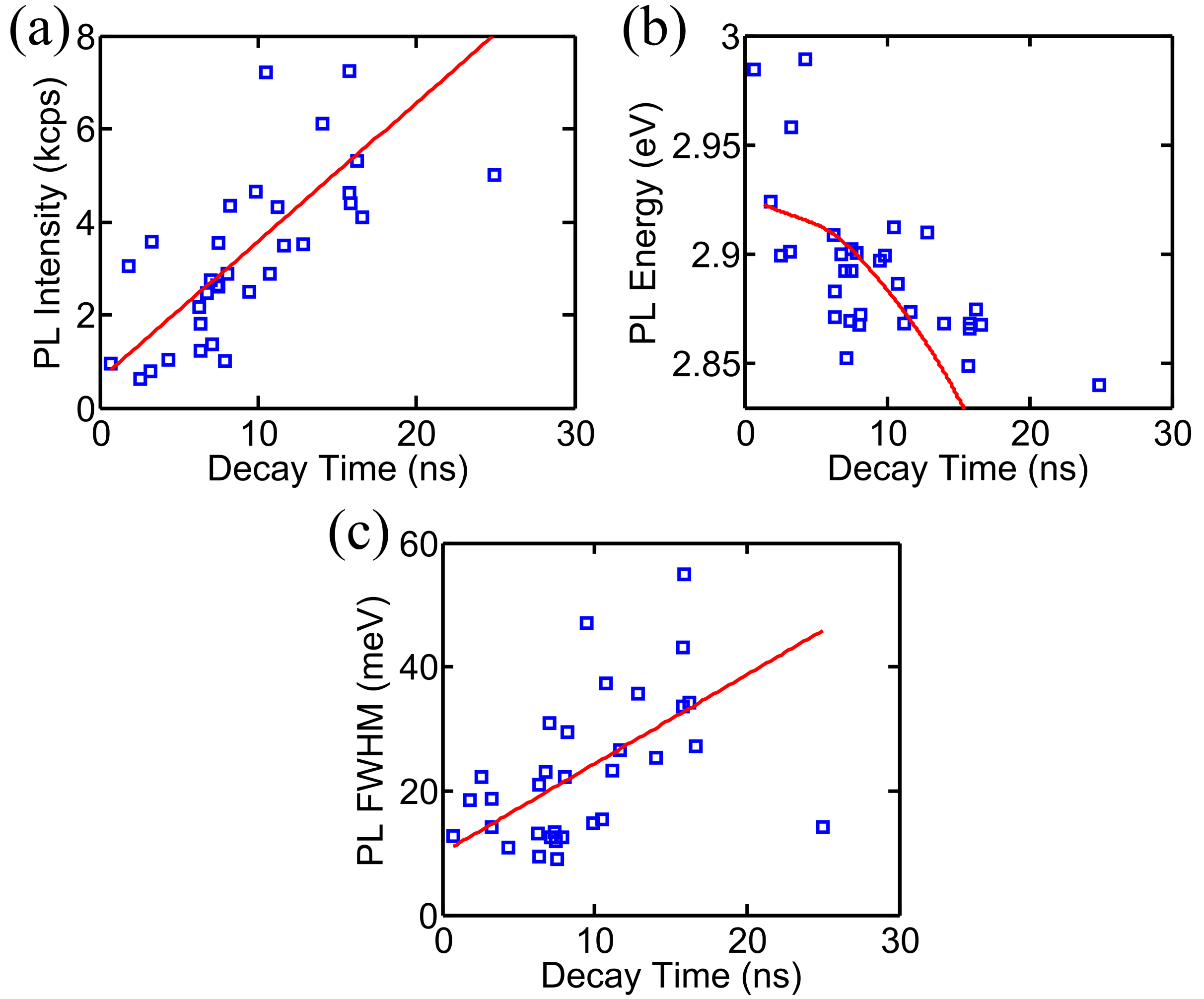

Figure 6.7: Statistical correlations among PL energy E, intensity I, decay time τ and the FWHM ΔE of the ZPB taken from 30 QDs randomly chosen from the same array of dot diameter $D = 29$ nm. All data are taken at 10 K. (a) The I-τ correlation. Each data point represents the data from one QD. The solid line is a linear fit showing an excellent linearity between I and τ. (b) The E-τ correlation. The solid line is the theoretical curve obtained by sweeping the ϕ_B value as described in Sec. 6.3.1. (c) The ΔE-τ correlation. The solid line is a fitting using Equ. 6.6.

each spectral line as well as the separation between lines. The impurity-scattering induces a broadening of $\Delta = 8.6$ meV in each spectral line as discussed in Sec. 5.3.1. The rest of the ΔE is due to the spectral diffusion that leads to further broadening in each spectral line and the exction-exciton interaction that leads to larger separation between lines. The spectral diffusion is caused by the interaction between the exciton's permanent dipole moment and the randomly appearing charges in the vicinity of the QD [175]. The permanent dipole moment is mainly due to the electron-hole separation by the strain-induced electric field. Hence, QDs with a greater thickness l, or equivalently ϕ_B, have stronger spectral diffusion. Thicker l (greater ϕ_B) also leads to greater separations between different multi-excitonic states due to stronger repulsive exciton-exciton Coulomb interaction, as will be discussed in Sec. 6.3.4. Meanwhile, a greater ϕ_B also leads to a longer τ as discussed earlier. Hence the positive correlation between ΔE and τ in Fig. 6.7(c) is explained. For simplicity, we approximate the positive correlation between ΔE and τ as a linear relation:

$$\Delta E = a + b\tau. \tag{6.6}$$

We obtain from Fig. 6.7(c) that $a = 10 \pm 3.5$ meV and $b = 1.4 \pm 0.4$ meV/ns.

6.3.4 The Correlation between $g_0^{(2)}$ and τ

In our QDs, as shown in Fig. 4.1(a), as well as in many other InGaN/GaN QDs [125, 126, 130, 131, 132], the biexciton emission typically has higher energy than the exciton emission, i.e. the biexciton has a negative binding energy $-B_{\mathrm{XX}}$. This is because our QDs are c-plane oriented, hence the electrons and holes are separated in the growth direction by polarization fields. Therefore, there are strong electron-electron and hole-hole repulsive interactions, while the electron-hole attractive interaction is weakened with increasing thickness [127, 176, 177]. Due to the large thickness of 3 nm of our dots, the biexciton binding energy becomes negative. Correspondingly, fluctuations in the InGaN thickness also lead to fluctuations in the B_{XX}.

The biexciton binding energy B_{XX} is positively correlated with the ZPB linewidth ΔE and decay time τ of the QD luminescence. This is because a QD with greater ϕ_B has a thicker InGaN layer, which leads to stronger repulsive electron-electron and hole-hole interactions and thus a greater B_{XX}. This, together with the stronger spectral-diffusion, leads to a larger overall ΔE in QDs whose $|\mathrm{X}\rangle$ and $|\mathrm{XX}\rangle$ lines are not resolved, as explained in Fig. 6.7(c). For simplicity, we assume that B_{XX} is proportional to the linewidth broadening $\Delta E - \Delta$, which in turn contains joint contributions from spectral diffusion and exciton-exciton interaction:

$$B_{\mathrm{XX}} = c_{\mathrm{XX}}(\Delta E - \Delta) = c_{\mathrm{XX}}(a + b\tau - \Delta). \tag{6.7}$$

The second equation is based on Equ. 6.6. Recall that Δ is the broadening caused by the impurity scattering as discussed in Sec. 5.3.1.

The B_{XX} also corresponds to the difference in the exciton and biexciton potential barrier

heights. This is because the strain-induced electrical field and, therefore, the repulsive electron-electron (hole-hole) interaction, is strongest at $r = 0$ and is negligible at $r = D/2$. As a result, the biexciton potential barrier height $\phi_{B,\mathrm{XX}}$ can be expressed as $\phi_{B,\mathrm{XX}} = \phi_B - B_{\mathrm{XX}}$, as illustrated in Fig. 5.1(b). Assuming that the potential profile scales with its height, we can describe the potential profile $\phi_{\mathrm{XX}}(r)$ for an EHP in the $|\mathrm{XX}\rangle$ state by modifying Equ. 5.1 as:

$$\phi_{\mathrm{XX}}(r) = \frac{\phi_{B,\mathrm{XX}}}{\phi_B}\phi(r). \tag{6.8}$$

The tunneling and thermal nonradiative decay rates of an EHP in the $|\mathrm{XX}\rangle$ state, $\gamma_{\mathrm{tnl,XX}}$ and $\gamma_{\mathrm{thm,XX}}$, are obtained by replacing $\phi(r)$ and ϕ_B with $\phi_{\mathrm{XX}}(r)$ and $\phi_{B,\mathrm{XX}}$ in the decay rate equations 5.7 and 5.8.

The radiative decay rate of an EHP in the $|\mathrm{XX}\rangle$ state $\gamma_{\mathrm{r,XX}}$ is assumed to be the same as that of the EHP in the $|\mathrm{X}\rangle$ state $\gamma_{\mathrm{r,X}}$. This is because the radiative decay rate is insensitive to the piezoelectric field and potential barrier height for 22 nm $< D <$ 33 nm, as shown in Fig. 5.4(a) and 6.7(a). Note that the decay rate of the $|\mathrm{XX}\rangle$ state is twice as fast as the decay rate of an EHP in the $|\mathrm{XX}\rangle$ state because there are two EHPs in $|\mathrm{XX}\rangle$.

The biexciton QE η_{XX} is determined by its radiative decay rate $\gamma_{\mathrm{r,XX}}$ and nonradiative decay rate $\gamma_{\mathrm{nr,XX}} = \gamma_{\mathrm{tnl,XX}} + \gamma_{\mathrm{thm,XX}}$ via $\eta_{\mathrm{XX}} = \gamma_{\mathrm{r,XX}}/(\gamma_{\mathrm{r,XX}} + \gamma_{\mathrm{nr,XX}})$. As we shall show next, the biexciton QE η_{XX} together with the exciton QE η_{X} determines the degree of antibunching of the QD emission.

We can apply the biexciton decay rates and the $g_0^{(2)}$ theory developed above to explain the correlation between $g_0^{(2)}$ and the total decay time τ of QD PL shown in Fig. 6.8(a), which is taken from 16 randomly chosen QDs of $D = 29$ nm at 10 K.

As discussed in Sec. 6.2, the variations in PL properties among these QDs can be accounted for by the variation of a single parameter ϕ_B from 0 to 120 meV. For a given ϕ_B value, we can calculate $\gamma_{\mathrm{tnl,X}}$ and $\gamma_{\mathrm{thm,X}}$ for excitons using Eqs. 5.7 and 5.8 with all other parameters obtained in Table 5.1. This gives us τ_{X} $(= \tau_{\mathrm{r,X}} + \gamma_{\mathrm{thm,X}} + \gamma_{\mathrm{tnl,X}})$ as well as η_{X} $(= \gamma_{\mathrm{r,X}}/\gamma_{\mathrm{X}})$. Due to the low excitation intensity P, the biexciton contributes little to the total decay time τ, therefore, τ_{X} can be treated as τ. Each τ value corresponds to a B_{XX} according to Equ. 6.7. Knowing B_{XX}, we can calculate the ϕ_{XX}, $\phi_{B,\mathrm{XX}}$ according to Equ. 6.8, from which we obtain the $\gamma_{\mathrm{tnl,XX}}$, $\gamma_{\mathrm{thm,XX}}$ and η_{XX}. Finally, $\eta_{\mathrm{XX}}/\eta_{\mathrm{X}}$ gives us $g_0^{(2)}$ (Equ. 6.5). The only unknown parameter is the c_{XX} in Equ. 6.7 used to obtain B_{XX}, which reflects the contribution of B_{XX} to the ZPB linewidth ΔE. The best match between the theory and experiment is obtained when $c_{\mathrm{XX}} = 0.9$, as shown by the solid line in Fig. 6.8(a), suggesting that B_{XX} contributes significantly to ΔE.

The ladle-shaped $g_0^{(2)}$-τ correlation in Fig. 6.8(a) results from the variation of the $\eta_{\mathrm{XX}}/\eta_{\mathrm{X}}$ ratio from dot to dot. The correlation curve reveals three regions I, II and III, as illustrated in Fig. 6.8(b), where different exciton and biexciton decay mechanisms dominate. In Region I, QDs have large τ, indicating high potential barriers ϕ_B, so that both the exciton and biexciton mainly decay radiatively and their QEs are both close to one, resulting in $g_0^{(2)}$ close to one. In

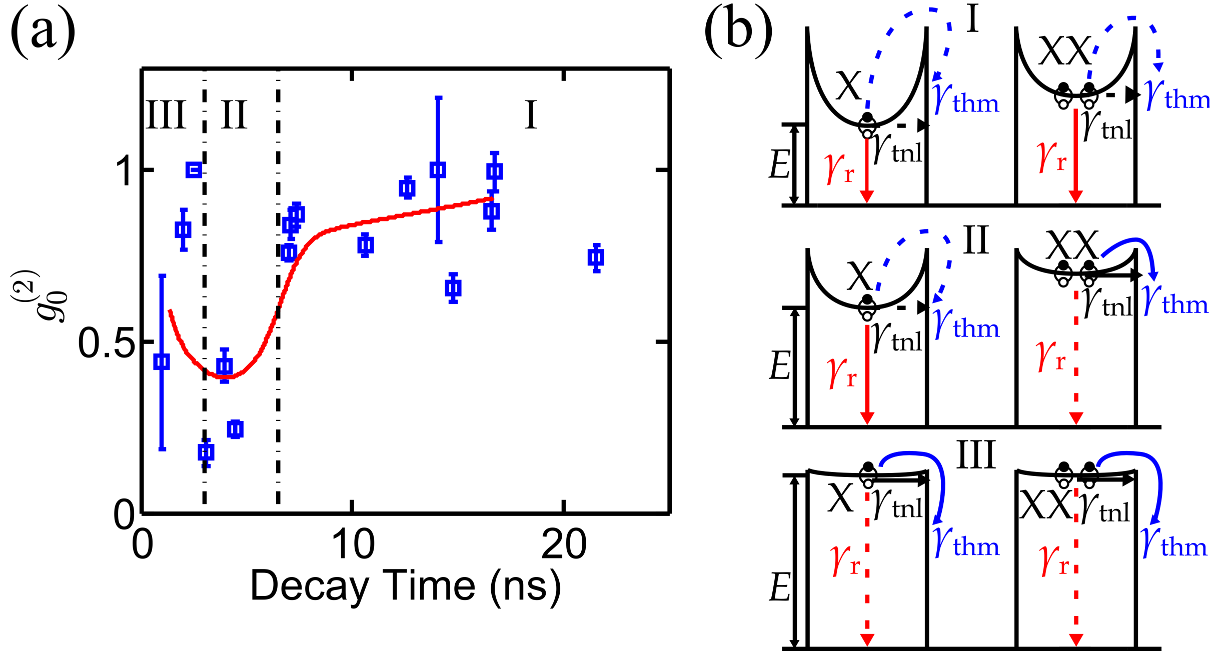

Figure 6.8: (a) The $g_0^{(2)}$ vs. decay time τ data of 16 randomly chosen QDs of diameter $D =$ 29 nm. The solid line is obtained by sweeping the value of ϕ_B as explained in Sec. 6.3.4. (b) An illustration of the different physics in the three regions described in Sec. 6.3.4. The solid arrows represent dominant decay channels, whereas the dashed arrows represent less dominant channels.

Region II, QDs have medium τ, suggesting relatively lower ϕ_B. In this region, excitons still experience high enough potential barriers so that they mainly decay radiatively with high η_{X}; whereas biexcitons' potential barriers are not high enough, due to the exciton-exciton Coulomb interaction, so that they mainly decay nonradiatively with low η_{XX}. This leads to low $\eta_{\mathrm{XX}}/\eta_{\mathrm{X}}$ and, consequently, strong anti-bunching in $g^{(2)}$. In Region III, QDs have very short τ, suggesting that the potential barriers ϕ_B for both excitons and biexcitons are very low. At the limit $\phi_B \to 0$, we have $\gamma_{\mathrm{X}} = \gamma_{\mathrm{XX}} \to c_1/D + c_2 v_B/D$ according to Eq. (5.3). $c_1/D + c_2 v_B/D$ is the maximum nonradiative decay rate allowed by surface recombination when there is no lateral potential barrier. On the other hand, $\gamma_{r,\mathrm{X}} = \gamma_{r,\mathrm{XX}}$. Therefore, we have $\eta_{\mathrm{XX}}/\eta_{\mathrm{X}} \to 1$. This explain why $g_0^{(2)}$ climbs back to unity as τ decreases in Region III.

6.4 Temperature Dependence of $g_0^{(2)}$

Single-photon emission was observed up to 90 K from a QD of diameter $D = 29$ nm as shown in Fig. 6.3(b). A systematic study on this QD shows a peculiar temperature dependence of $g_0^{(2)}$. As shown in Fig. 6.9, the $g_0^{(2)}$ value is the lowest when the temperature is around 80 K. This can be explained by the difference in exciton and biexciton's potential barrier heights in a QD.

Figure 6.9(a) shows the PL spectra of this QD. At a low temperature $T = 10$ K and a high excitation intensity $P = 100$ W/cm^2, the PL spectrum is composed of multiple overlapping peaks with an overall ZPB linewidth of 50 meV. Keeping the same temperature but lowering

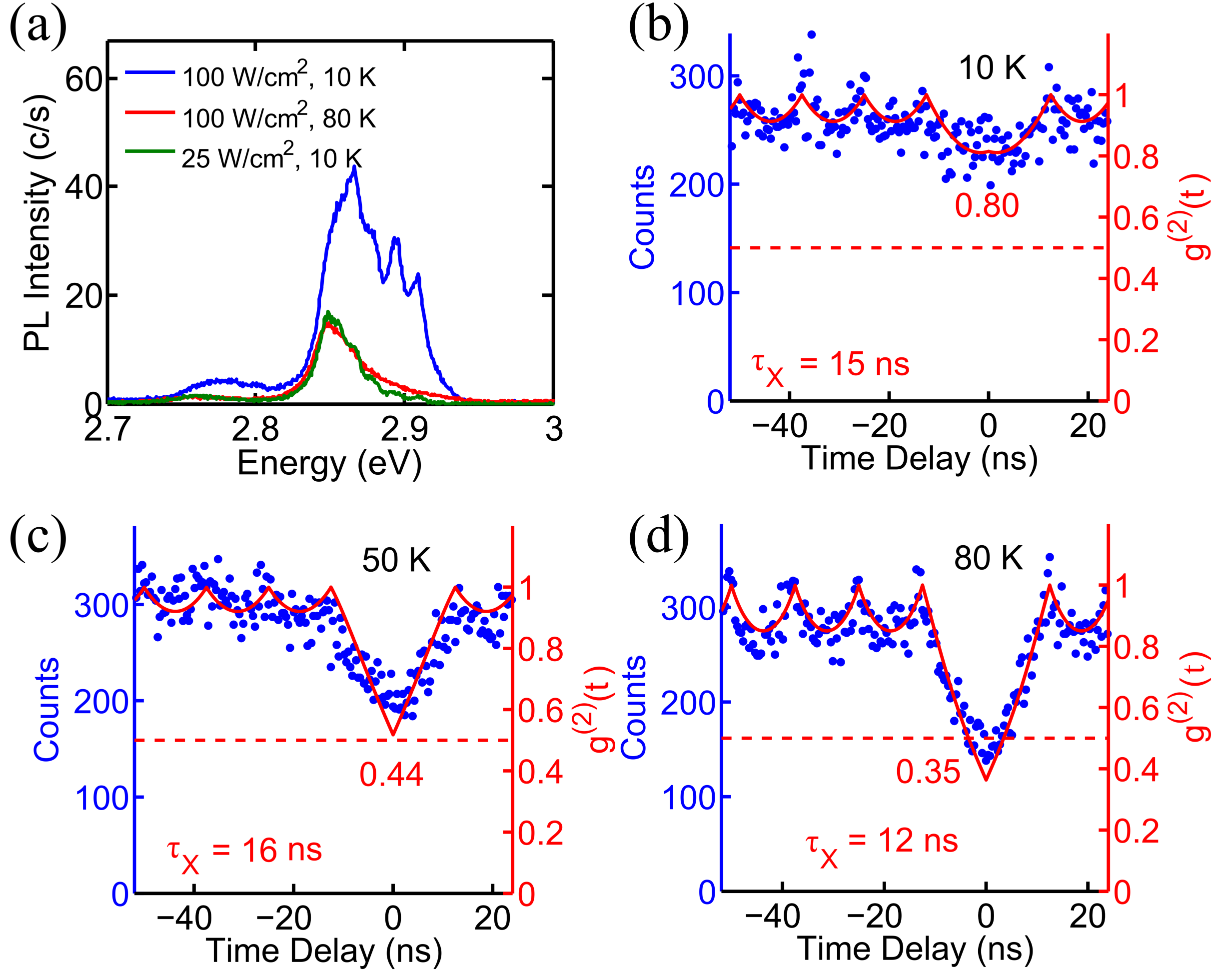

Figure 6.9: (a) The PL spectra of a QD of $D = 29$ nm at $P = 100$ W/cm^2, $T = 10$ K (blue); $P = 100$ W/cm^2, $T = 80$ K (red); and $P = 25$ W/cm^2, $T = 10$ K (green). (b-d) The scattered data points form the measured $g^{(2)}(t)$ of the QD at 10, 50 and 80 K, respectively, at $P = 100$ W/cm^2. All data are without background subtraction. The solid lines are the fitting curves obtained from the method developed in [**?**] (also briefly described in Sec. **??**). Each fitting returns the biexciton-to-exciton QE ratio $\eta_{\mathrm{XX}}/\eta_{\mathrm{X}}$, exciton total decay time τ_{X} and $g_0^{(2)}$. The fitted $g_0^{(2)}$ values are shown next to the central $g^{(2)}$ peaks (dips).

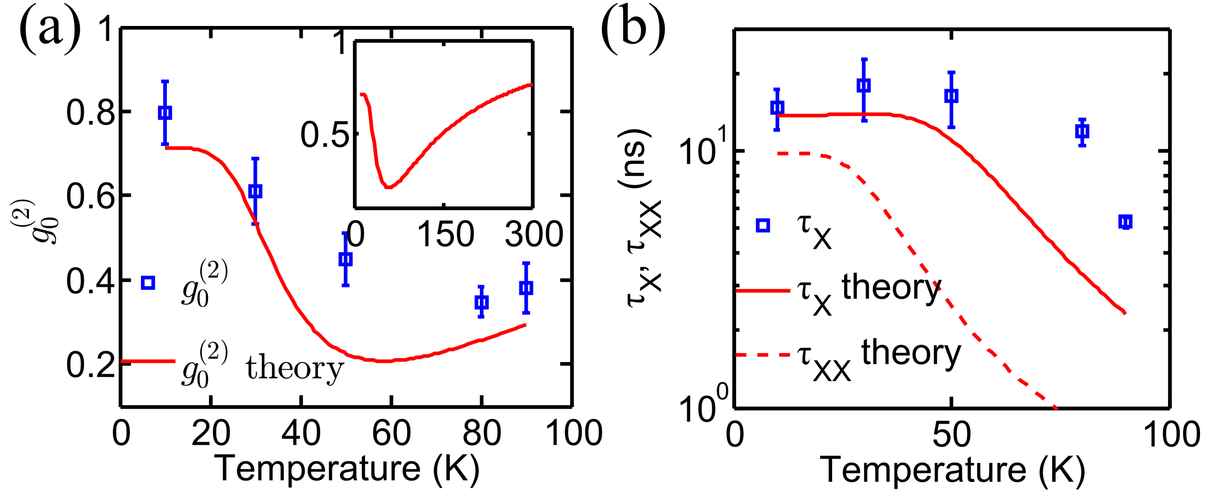

Figure 6.10: The blue squares in (a) and (b) are the $g_0^{(2)}$ and $\tau_{\rm X}$ extracted from the $g^{(2)}(t)$ data of the QD at 10, 30, 50, 80 and 90 K, three of which are shown in Fig. 6.9(b-d). The red lines are the theoretical curves based on the ϕ_B and $B_{\rm XX}$ values extracted from Fig. 6.9(a) as described in the text. The inset in (a) is an extension of the theoretical $g_0^{(2)}(T)$ curve to 300 K.

P weakens the higher energy peaks, suggesting that the higher energy peaks are due to multi-exciton emissions. Keeping the same P but increasing the temperature to 80 K weakens the higher energy peaks as well, suggesting that QEs of multi-excitons reduce faster with temperature than the QE of exciton does.

This mechanism is verified by the improvement of the antibunching in the $g^{(2)}(t)$ as the temperature increases from 10 to 80 K at a fixed laser excitation intensity P, as shown in Fig. 6.9(b-d). From each of the $g^{(2)}(t)$ data we obtain $g_0^{(2)}$ and the exciton decay time $\tau_{\rm X}$ using the method developed earlier. The resulting $g_0^{(2)}(T)$ and $\tau_{\rm X}(T)$ data are shown in Figs. 6.10(a) and (b), respectively. Both sets of data can be reproduced by the carrier dynamics model in Chap. 5 using parameters in Table 5.1 as follows: From the 10 K PL energy $E = 2.85$ eV and ZPB linewidth $\Delta E = 50$ meV (Fig. 6.9(a), $P = 100$ W/cm^2) we obtain $\phi_B = 80$ meV and $B_{\rm XX} = 37$ meV, according to Eqs. (4.11) and (6.7), respectively. Following the same steps as we used in Sec. 6.3.4, ϕ_B gives rise to $\gamma_{\rm X}(T)$ and $\eta_{\rm X}(T) = \gamma_{\rm r,X}(T)/\gamma_{\rm X}(T)$ through Equ. (5.3); whereas $B_{\rm XX}$ gives rise to $\phi_{B,\rm XX}$ based on Eq. (6.8), which leads to $\gamma_{\rm XX}(T)$ and $\eta_{\rm XX}(T) = \gamma_{\rm r,XX}(T)/\gamma_{\rm XX}(T)$ through Eq. (5.3) as well. Using Equ. (6.5) and recalling the assumption that $\gamma_{\rm r,X} = \gamma_{\rm r,XX}$ in Sec. **??**, the ratio $\eta_{\rm XX}(T)/\eta_{\rm X}(T) = \tau_{\rm XX}(T)/\tau_{\rm X}(T)$ gives rise to the theoretical $g_0^{(2)}(T)$ curve shown as the solid line in Fig. 6.10(a). For comparison, the theoretical $\tau_{\rm X}(T)$ and $\tau_{\rm XX}(T)$ are plotted in Fig. 6.10(b). From Fig. 6.10(b) it is evident that the improvement of the $g_0^{(2)}$ as temperature increases is due to the faster dropping of $\tau_{\rm XX}$ compared to τ_X, i.e. the biexciton's thermal decay rate increases faster than the exciton's. This is ultimately because, in the same QD, the biexciton has a lower potential barrier than the exciton as a result of the repulsive exciton-exciton Coulomb interaction.

However, $g_0^{(2)}$ does not always decrease with temperature. Instead, there is an optimal

temperature, at which $g_0^{(2)}$ reaches its minimal. In the inset of Fig. 6.10(a), $g_0^{(2)}$ increases as T increases above 80 K. This can be understood as following. At the limit $T \to \infty$, we have $\gamma_{\mathrm{X}} = \gamma_{\mathrm{XX}} \to c_2 v_B / D$. This leads to $g_0^{(2)} \to 1$, similar to what happened in the Region III of Fig. 6.8. The optimal temperature increases with ϕ_B, since a greater ϕ_B means higher QEs for both the exciton and biexciton, as well as a larger difference between them.

This anomalous temperature dependence of $g_0^{(2)}$ suggests that one way to improve the operating temperature of these QDs is to increase the ϕ_B value by, for instance, having a higher indium composition or a thicker InGaN layer.

6.5 Conclusion

We studied the carrier dynamics of site- and structure-controlled nanodisk-in-a-wire InGaN/GaN QDs. The minimized inhomogeneities in all key structural parameters–the QD diameter, thickness and indium composition–allowed a systematical mapping between the optical properties and structural parameters.

Our results revealed that the sidewalls in these etched QDs played a vital role in enhancing the radiative decay rate and enabling good antibunching, while it also ultimately limited the QE. The strain relaxation at the sidewall led to greatly enhanced radiative decay rates in QDs compared to QWs [157]. More importantly, it created potential barriers, which are different for the excitons and biexcitons and preferentially protected the excitons from surface recombination, leading to low $g_0^{(2)}$ values. This suggests that by engineering the potential barrier height, such as by varying the indium composition or nanodisk thickness, one could achieve purer single-photon emission and at higher temperatures with QDs fabricated by our method.

However, the QE was ultimately limited by the surface recombination at the sidewall, even at very low temperatures, due to tunneling of the carriers to the sidewall. Such surface dynamics has often been overlooked in dot-in-a-nanowire based optical devices, especially in low-temperature measurements.

Furthermore, the statistical correlations between various optical properties of numerous single QDs with markedly similar diameters enabled us to understand the impact of structural parameters on the optical properties. Together with the study on QD ensembles, we established a quantitative relation between the optical properties and the structural parameters. And we showed that variations in optical properties of QDs of the same diameter could be modeled by the variation of only one phenomenological parameter, the exciton potential barrier height.

These findings may be applicable to a wide range of strained III-N nanostructures with large surface-to-volume ratios, such as nanowires, nanospheres, and nanopillars. Hence the carrier dynamics we analyzed and quantitatively modeled in this work may have broad impacts on improving the performance of III-N based photonic devices.

CHAPTER 7

Electrically Driving and Controlling InGaN/GaN Quantum Dots

7.1 Electrically Driven Single-Photon Emitting Diodes

Single-photon sources (SPSs) are the key component of a range of important applications including quantum communication, quantum information processing and precision measurement. The practicality of these applications relies on the scalable fabrication of SPSs that can operate at non-cryogenic temperatures and can be integrated with other electrical and optical components. Quantum dots (QDs) based on III-N semiconductors are the most promising candidates for fulfilling these requirements. This is because high-temperature SPSs have only been demonstrated for QDs made of wide-bandgap semiconductors, such as II-V and III-N semiconductors and diamonds [36, 41, 34, 178, 35, 40], or non-semiconductor materials [32]. Among them, electrical-injection and site-control, two critical requirements for integration with other electrical and optical devices, have only been separately demonstrated for III-N QDs [1, 179, 40]. Here we demonstrate electrically driven SPSs based on site-controlled InGaN/GaN QDs.

Site-controlled III-N QDs have been fabricated in multiple ways, including those grown at apices of micro-pyramids [6], inversed micro-pyramids [180], nanowires [40], as well as our dot-in-nanowires (DINs) [1] made by plasma etching a planar single InGaN/GaN quantum well. Compared to all others, our DINs are particularly optimized for electrical-injection, since the current-pathway naturally overlaps with the QD active region, leading to the demonstration of electrically driven single-photon emission from site-controlled III-N QDs in this work.

7.1.1 Electroluminescence and Single-Photon Emission

The sample and measurement setup used in this section has been shown in Chap. 3. We first study the EL properties of a single DIN. Fig. 7.1(a) shows the EL intensity as a function of the applied voltage suggests a clear turn-on behavior at ∼4 V forward bias. This suggests that electrons and hole are both present in the InGaN region only at bias $V_{bias} > 4$ V. The EL spectra of the DIN at different forward voltages are shown in Fig. 7.1(b). Each of the spectra is composed of a dominant zero-phonon peak at 3.06 eV with a weak shoulder at ∼20 meV

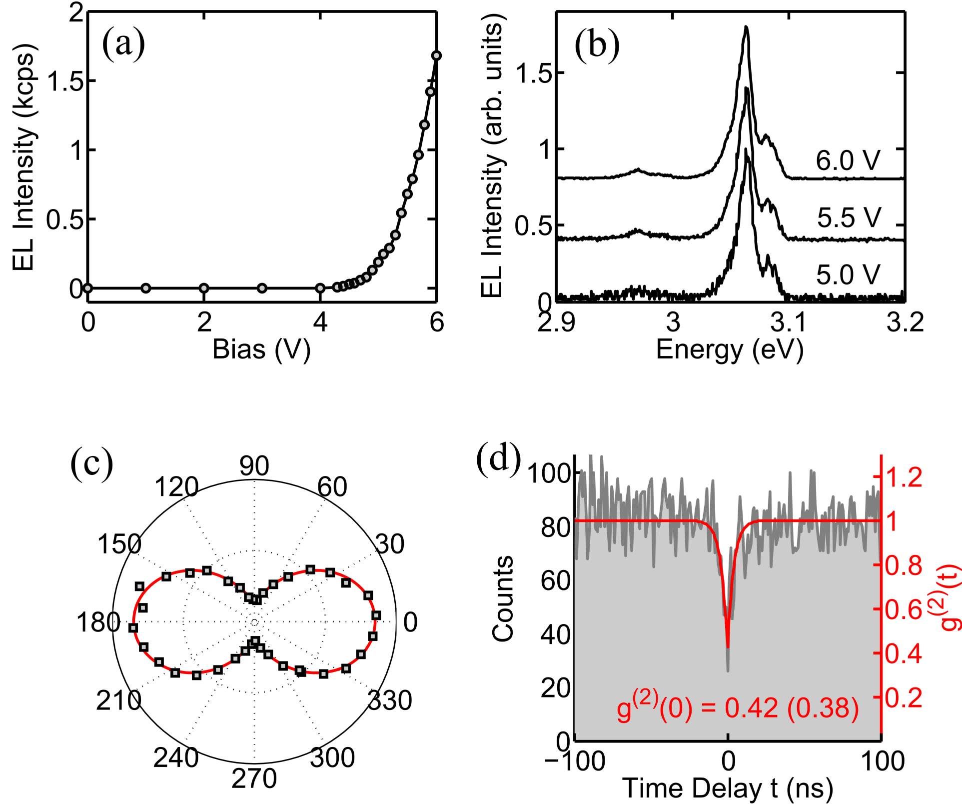

Figure 7.1: EL properties at 10 K. (a) The integrated EL intensities of the DIN vs. applied bias. (b) The EL spectra of the QD at various bias voltages. All spectra are normalized to their maximum intensity and shifted vertically for comparison. (c) The EL intensity vs. angle of the polarization selection at 5.7 V forward bias. The solid line is a fitting curve. (d) The $g^{(2)}(t)$ of the DIN EL at 5.7 V forward bias without background subtraction. The solid line is a fitting curve.

higher energy and an optical-phonon peak at 2.97 eV. The 90 meV optical-phonon energy is consistent with our previous results [1]. The zero-phonon peak and its higher energy shoulder are most likely due to emission from single exciton (X) and its many negatively charged states (X^{n-}, $n = 1, 2, ...$). This is because compared to the holes in the p-GaN region, electrons in the n-GaN region has higher concentration and higher mobility ($\sim$100 cm^{2}V^{-1}s^{-1} for electrons [181] and $\sim$10 cm^{2}V^{-1}s^{-1} for holes[182]). Therefore electrons arrive at the InGaN QD at bias $V_{bias} < 4$ V, before holes arrive. The broad linewidth of the zero-phonon peaks is due to the spectral diffusion as a result of local charge fluctuation caused by the current flow.

The EL is linearly polarized as shown in Fig. 7.1(c), which is taken by rotating a half-wave plate in front of a linear polarizer. The EL intensity vs. polarization angle (θ) data are fitted using the equation $\frac{I_1-I_2}{I_1+I_2}\cos^2(\theta+\theta_0)+\frac{I_2}{I_1+I_2}$, resulting in a degree of polarization of $\frac{I_1-I_2}{I_1+I_2} = 0.7 \pm 0.04$. The polarization angle θ_0 does not correspond to any crystal orientation and is random among DINs. Linearly polarized emission has been observed in many InGaN QDs including electrically driven ones [169, 7, 1, 92]. It has been attributed to the anisotropy in the InGaN lateral dimension. In our QDs, anisotropy can be caused by the RIE process which

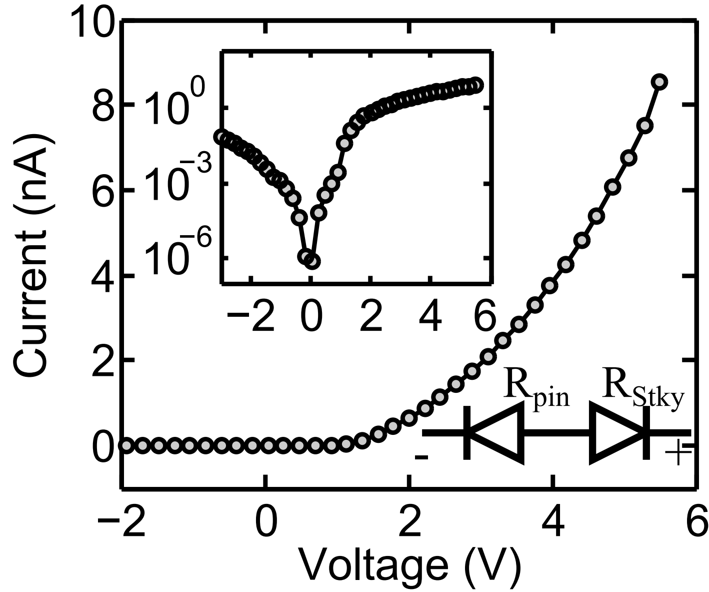

Figure 7.2: The current-voltage (I-V) characteristic of the DIN at 10 K. The upper-left inset is the semi-log of the I-V curve. The lower-right inset illustrates the effective circuit in which the pin-junction and the ITO/p-GaN Schottky contact are connected in series.

attacks the DIN sidewalls randomly. The anisotropic lateral shape leads to mixing between heavy and light hole states resulting in the linearly polarized emission [169].

To demonstrate the single-photon nature of the EL, we performed second-order correlation ($g^{(2)}$) measurement on the EL of the DIN, which exhibits a strong antibunching as shown in Fig. 7.1(d). The data can be fitted by a simple expression $g^{(2)}(t) = g^{(2)}(0) + (1 - g^{(2)}(0))(1 - exp(-|t|/\tau))$ yielding $g^{(2)}(0) = 0.42$ (or $g^{(2)}(0) = 0.38$ after adjusting for the APD dark counts [94]) and $\tau = 4$ ns. The non-zero $g^{(2)}(0)$ is due to higher order multi-exciton emission whose quantum efficiency is largely suppressed by the surface recombination in our DINs [1]. The parameter τ represents the decay time of the zero-phonon emission. The slow decay time is due to the strong polarization fields in the InGaN region which reduces the electron-hole wave-function overlapping [118].

7.1.2 Current-Voltage Characteristics

The current-voltage (I-V) characteristics of the DIN is shown in Fig. 7.2. Note that the current is the average of 8100 DINs connected in parallel. Comparing Fig. 7.1(a) and Fig. 7.2 we can see that the current that flows through the device at $V_{bias} < 4$ V is not converted into light emission. This confirms that electrons and holes start to arrive at the InGaN region at different biases. Due to the lower hole concentration and mobility in the p-GaN region, holes only start to arrive at the InGaN region at $V_{bias} > 4$ V. We note that hole injection can be improved by increasing the acceptor concentration in the p-GaN region.

At small forward bias of $V_{bias} < 2$ V, the current increases exponentially (inset of Fig. 7.2)

as the bias increases, which is expected from an ideal pin-junction. However, as V_{bias} ramps above 2 V the increase of the current becomes slow and nearly linear. This suggests that the diode is connected in series with another resistor, which is most likely the non-ohmic ITO/p-GaN contact [183]. Using the slope of the I-V curve at $V_{bias} > 2$ V and the diameter of the DIN we can estimate the ITO/p-GaN specific contact resistivity to be $\sim 10^{-2}$ Ωcm^2, consistent with the reported values ranging from 10^{-1} to 10^{-3} Ωcm^2 [101, 184, 185]. Therefore, the transportation behavior of our device can be modeled using a simple circuit composed of a pin-junction with resistance R_{pin} and a reverse Schottky junction with resistance R_{Stky} as shown in the lower inset of Fig. 7.2. At $V_{bias} < 2$ V, the total device resistance is dominated by the pin-junction, or $R_{pin} > R_{Stky}$. At $V_{bias} > 2$ V, the total device resistance is dominated by the ITO/p-GaN contact, or $R_{pin} < R_{Stky}$.

The above interpretation to the I-V curve is verified by the bias-dependent PL measurement of the DIN. The PL spectra of the DIN at a fixed laser excitation density of 100 W/cm^2 and varying voltages are shown in Fig. 7.3(a). Without applying any bias, the PL energy is at 3.09 eV, 30 meV higher than the EL energy in Fig. 7.1. As V_{bias} increases from 0 to 2 V the PL peak energy redshifts at a rate of ~ -10 meV/V. As V_{bias} goes above 2 V, the redshift stops at 3.06 eV. This trend is summarized in Fig. 7.3(b) with a finer bias increment.

The redshift at $V_{bias} < 2$ V is due to the decrease of the depletion width in the pin-junction as illustrated in Fig. 7.4. The PL energy is influenced by both the built-in polarization field E_{pol} and the external electric field E_{pin} due to the donor and acceptor depletion in the n-GaN and p-GaN regions, respectively. E_{pol} is determined by the spontaneous and piezoelectric polarizations in the InGaN region [186] and is independent of V_{bias}. E_{pin} is proportional to the depletion width in the n-GaN and p-GaN regions [162] and therefore decreases as the voltage drop V_{pin} on the pin-junction increases. At small bias of $V_{bias} < 2$ V, R_{pin} is greater than R_{Stky} and, hence, most of the voltage is applied on the pin-junction, i.e. $V_{bias} \approx V_{pin}$. As a result, the increase of V_{bias} quickly decreases the pin-junction depletion width, leading to a decrease in $|E_{pin}|$. Due to the quantum confined Stark effect [187, 188], a stronger total electric field $E_t = E_{pol} + E_{pin}$ leads to a lower PL energy. Since E_{pol} and E_{pin} have opposite directions, the redshift observed in Fig. 7.3 suggests that $|E_{pin}| < |E_{pol}|$.

The much slower redshift at $V_{bias} > 2$ V is due to the dominance of the R_{Stky} compared to R_{pin} as explained earlier. At large forward biases, R_{pin} becomes very small as expected from an ideal pin-junction. Hence, the voltage drop V_{pin} on the pin-junction reaches plateau. As a result, E_{pin} stops decreasing at bias > 2 V leading the near absence of further PL energy shift. The additional voltage drop $V_{Stky} = V_{bias} - V_{pin}$ is applied on the ITO/p-GaN contact, which only makes the p-GaN more depleted at the ITO/p-GaN interface.

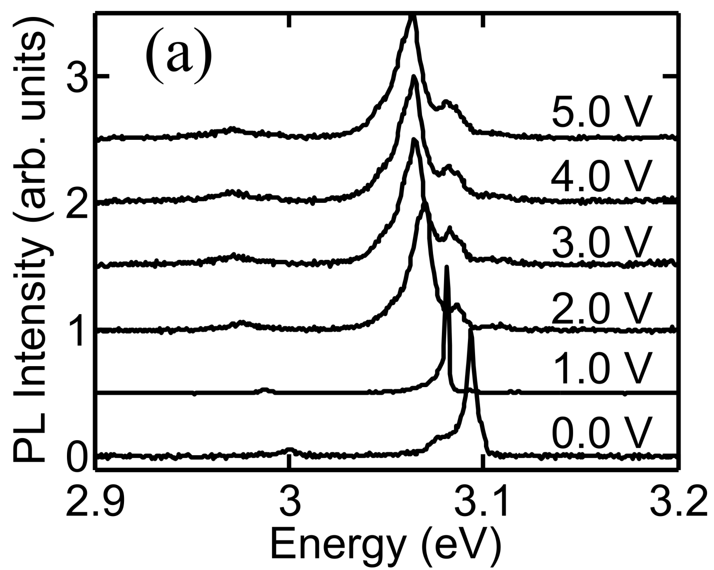

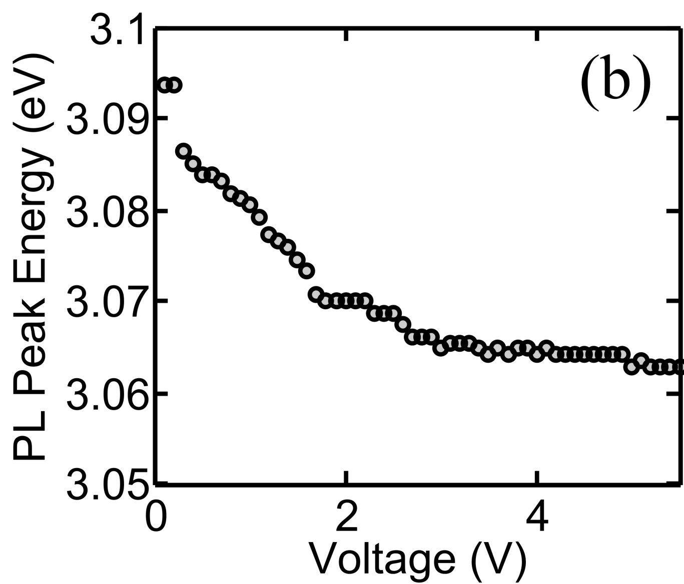

Figure 7.3: PL properties at 10 K. (a) The PL spectra of the DIN at several applied voltages. (b) The PL peak energy vs. the applied voltage.

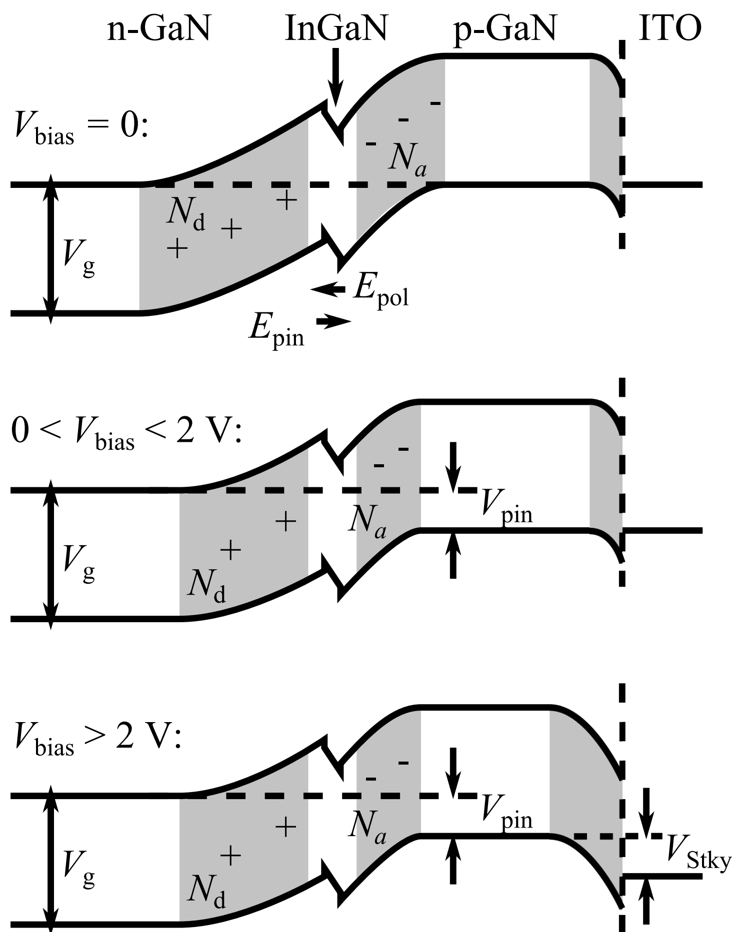

Figure 7.4: Schematic band diagrams of the DIN at $V_{bias} = 0$ V (upper panel), $0 < V_{bias} < 2$ V (middle panel) and $V_{bias} > 2$ V (lower panel).

7.2 Electrically Controlled Photoluminescence Properties

In contrast to the fast development in III-N single-photon devices, fundamental understanding of excitons, especially their charging and fine structures, in III-N QDs is lacking despite recent progresses [169, 189, 190, 191, 192]. This understanding, however, is important for building better single-photon sources and extending the application of III-N QDs to other fields such as single electron spin qubit [60, 61, 62] and entangled single-photon sources [16, 55].

The lack of understanding in exciton charging and fine structures in III-N QDs results from their complicated material properties compared to that of their III-As counterparts. First, many III-N QDs reported so far have linewidths of $\sim$1 meV [169, 190, 191, **?**], over an order of magnitude broader than that of III-As QDs, rendering it harder to resolve spectral features separated by less than 1 meV. This is due to the large exciton permanent dipole moment caused by the strong strain-induced electrical field and the higher defect densities in III-N materials, typically grown on lattice-mismatched substrate. Second, when linewidths are reduced, a single III-N QD often exhibits many spectral lines from both A- and B-excitons, their charged excitons and multi-excitons, all of which are separated by a few meV [169, 190, 191]. Indeed, in some cases, over five spectral lines are observed from the same QD [169] and their identification remains ambiguous. Third, the exciton fine structure splitting (FSS) is highly sensitive to the anisotropy and confinement in III-N QDs, which leads to FSS ranging from 100s μeV [191] to a few meV [190]. This further complicates the identification of spectral lines as one needs to also distinguishing between A-B splitting and FSS.

In this section, we unambiguously identify neutral and charged A- and B-excitons from single InGaN/GaN QDs and study their fine structures by inserting a QD in a GaN-nanowire p-i-n charge-tunneling diode. Similar diode structures have been widely used to study charged excitons and exciton fine structures in III-As QDs [193, 194, 195], but have not been used to study similar physics in III-N QDs. We show that our device is ideal for studying III-N QDs as it possesses the following advantages. First, the internal electrical field is significantly reduced due to the strain relaxation in GaN nanowire [117, 133, **?**] and the built-in potential of the p-i-n junction [162]. This strongly suppresses exciton permanent dipole moment, leading to much narrower spectral linewidths. Second, the charge-tunneling diode structure enables precise control of the number of charges tunnelling into the QD by tuning the bias voltage [193, 194], which separates neutral excitons from charged ones and greatly simplify the spectrum. Third, being able to study singly charged excitons, which do not have FSS [189], and neutral excitons separately allows clear differentiation between A-B exciton splitting and FSS.

7.2.1 Charge-Tunneling Diode

The sample used in this section is the same as the one in the previous section, except that here we look at low bias voltages. To understand the working principle of our charge-tunneling diodes, we first calculate the conduction and valence band profiles along the central vertical

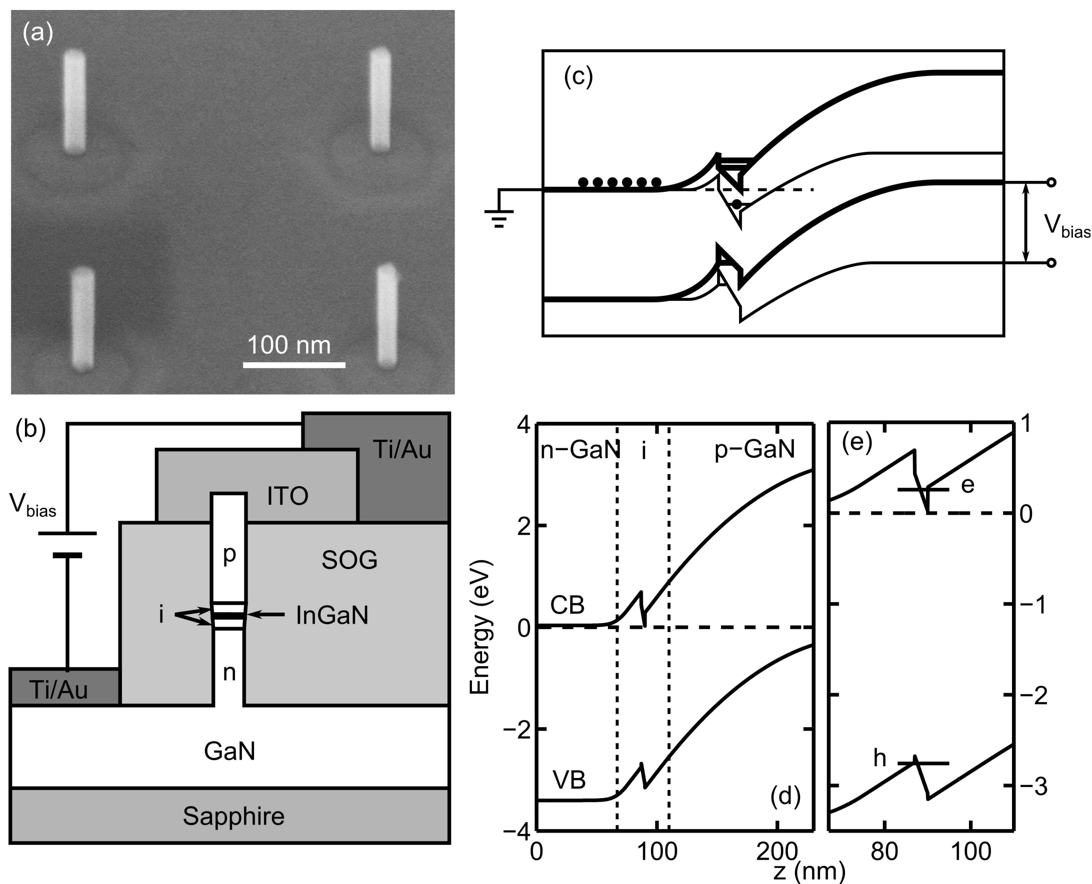

Figure 7.5: Sample structure and band profiles. (a) 45°-angle SEM image of four nanowire diodes without SOG and contacts. (b) Schematic cross-section view of a single InGaN/GaN DIN diode, including the ITO/Ti/Au p-contact, SOG insulating layer and Ti/Au n-contact. (c) Working principle of the charge-tunneling diode. (d) The conduction band (CB) and valence band (VB) profile along the growth direction (z). (e) The intrinsic (i) section of (d).

axis (z-axis) of a nanowire. We assume the p- and n-doping densities to be 1×10^{17} cm^{-3} and 1×10^{18} cm^{-3}, respectively. The calculation uses the commercial simulation package TiberCAD and solves three-dimensional (3D) strain distribution, k·p-method band structures, and classical carrier drift-diffusion equations self-consistently [196]. The resultant band profile at zero bias, $V_{\text{bias}} = 0$ V, is shown in Fig. 7.5(c). The electron and hole envelope functions and eigen-energies in the QD are then calculated by solving Schrodinger equations using the band profiles as shown in Fig. 7.5(d). The results exhibit the following features. First, due to the much higher doping density in the n-GaN region, the QD electron ground state is much closer to the Fermi level, which is aligned with the donor and acceptor levels, than the QD hole ground state. As a result, it requires much less forward bias to inject electrons into the QD than to inject holes. As illustrated in Fig. 7.5(d), when a forward bias is applied, $V_{\text{bias}} > 0$, the conduction band is lowered. When it is aligned with the n-GaN donor level, a single electron will tunnel from n-GaN into the QD, which forms Coulomb blockade preventing additional electrons from entering the QD. The QD will stay singly charged until V_{bias} increases further to overcome the Coulomb blockade. Second, the carrier diffusion in the p-i-n junction creates an electrical field of 0.3 MV/cm which reduces the internal field in the QD by 20%. This, combined with the effect of strain relaxation at the sidewall of the QD, results in a overall reduction of the internal field in a QD of 40 nm in diameter by $\sim 40\%$ compared to that in an un-etched InGaN/GaN quantum well. This is manifested as the small spectral linewidth of 2–6 meV from our QDs which is comparable to self-assembled InGaN QDs, especially when considering the close proximity of our QDs to the plasma etched sidewall surfaces. We expect even narrower linewidths if surface passivations are used.

We first measure the voltage-dependent PL of two QDs, QD1 and QD2, at a fixed excitation power density of $P = 100$ W/cm^2, as shown in Fig. 7.6. Note that, due to the photo-voltaic effect, all PL energy-voltage E-V_{bias} traces in Fig. 7.6(b)-(c) will be shifted towards left as the excitation laser power density increases. In another word, the excitation laser creates an effective positive bias. Therefore, all data presented here have their bias voltage corrected by the corresponding photo-voltage.

The energy E of spectral peaks red-shift as V_{bias} increases. This is due to the increment of the total electrical field intensity $|F_{\text{tot}}|$ in the QD region as a result of the decrement in the p-i-n junction built-in field intensity $|F_{\text{pin}}|$. Stronger $|F_{\text{tot}}|$ leads to lower exciton energy through the so-called quantum confined Stark effect. The red-shift ΔE of the PL energy is quadratic with V_{bias} due to the variation of the permanent dipole moment, or electron hole envelope function overlap, with the variation of F_{tot}. This can be expressed as $\Delta E \propto \beta F_{\text{tot}}^2$, where β is the polarizability. Using this equation we extract β values of -300–-800 meV/(MV/cm)^2 for all spectral speaks. The magnitude of β is, however, 3–8 times higher than a previous reported value from a self-assembled InGaN/GaN QD. We note that β sensitively depends on the indium composition, height, and diameter of a QD, none of which were specified in the previous work. For QD1, at $V_{\text{bias}} \sim -1$ V, $\Delta E/\Delta V_{\text{bias}}$ is nearly zero. This indicates that the

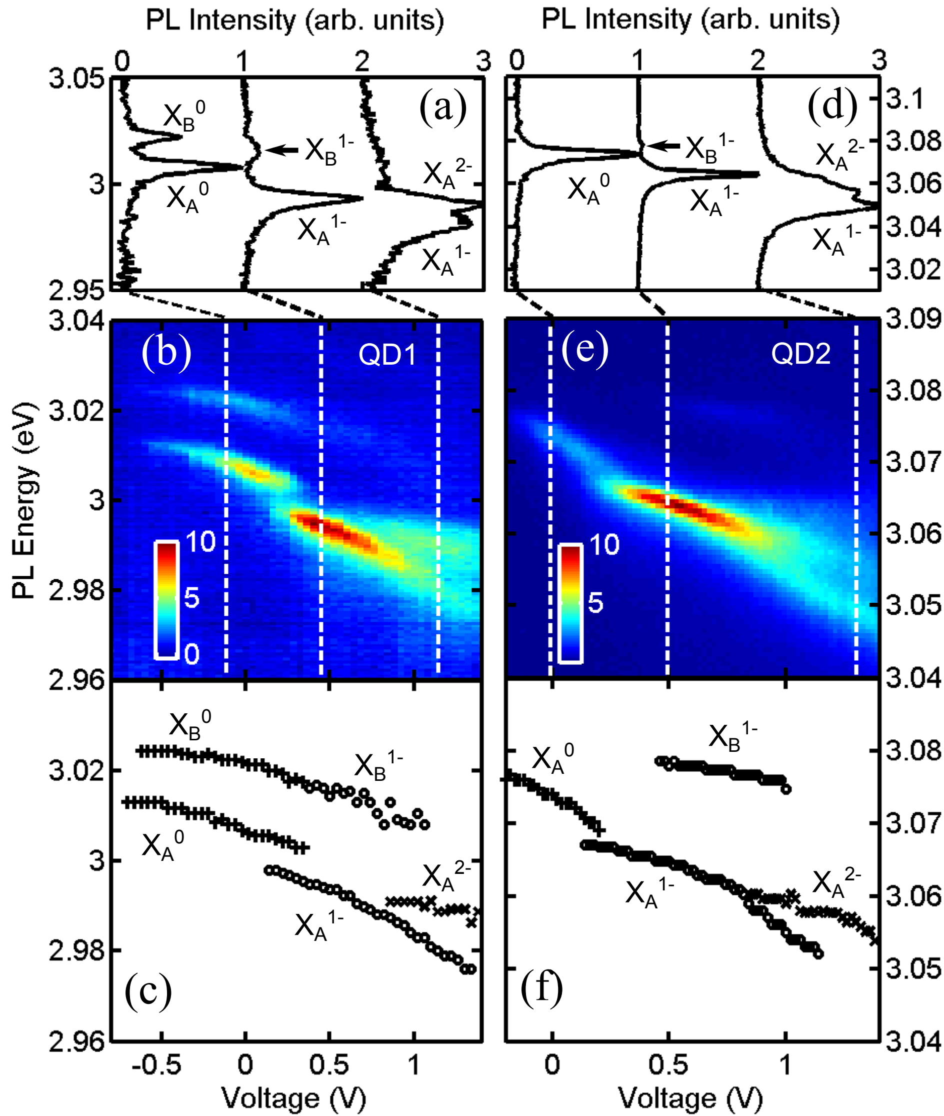

Figure 7.6: Voltage-dependent μ-PL spectra form two QDs, QD1 (a-c) and QD2 (d-f). (a) and (d) show spectra at voltages indicated by the dashed lines in (b) and (e), respectively. (c) and (f) shows the PL energy of various neutral and excitons as functions of voltage extracted from (b) and (e), respectively. Voltages are corrected from the laser induced photo-voltage.

F_{pin} being 400 kV/cm fully cancels F_{pol}, which is consistent with the simulated F_{pol} value in our partially strain-relaxed QDs.

The charge-tunneling effect is demonstrated by the discontinuity in E and $\Delta E/\Delta V_{\text{bias}}$ in the voltage-dependent PL energy shift as show in Fig. 7.6. Let us first consider the E-V_{bias} traces labeled X_{A}^{0}, X_{A}^{1-}, and X_{A}^{2-}. The first electron tunnels into the QDs at $V_1 \sim 0.25$ V, marked by the reduction in E and $|\Delta E/\Delta V_{\text{bias}}|$. Therefore, X_{A}^{0} and X_{A}^{1-} represents neutral and singly negatively charged excitons, respectively. The sudden reduction in E [clearer in Fig. 7.6(c)] at V_1 suggests that the attractive Coulomb interaction between two electrons and hole exceeds the repulsive Coulomb interaction between the two electrons. The sudden reduction in $|\Delta E/\Delta V_{\text{bias}}|$ [clearer in Fig. 7.6(f)] is due to the reduction in the permanent dipole moment as the additional electron in X_{A}^{1-} brings both electron and hole envelope functions closer to the center of the QD through Coulomb interaction. The second electron tunnels into the QDs at $V_2 \sim 0.8$ V, marked by the increment in E and reduction in $|\Delta E/\Delta V_{\text{bias}}|$. The increment in E is expected as an additional electron is added to an already-negative X_{A}^{1-}. The reduction in $|\Delta E/\Delta V_{\text{bias}}|$ is due to the same mechanism as that at V_1.

7.2.2 A- and B-Excitons

We show in the following that $X_{\text{A}}^{0,1-,2-}$ and $X_{\text{B}}^{0,1-,2-}$ are associated with A- and B-excitons, respectively. First, the integrated intensity of X_{A}^{0} and X_{B}^{0} at $V_{\text{bias}} = -0.04$ V are linearly dependent on the excitation power density P at $P < 150$ W/cm^2 [Fig. 7.7(a)], indicating they are both excitons as opposed to biexcitons. Again, we emphasize that the V_{bias} has already be corrected by the photo-voltage. For without such correction, the energy of X_{A}^{0} and X_{B}^{0} will red shift or even become X_{A}^{1-} and X_{B}^{1-} as P increases. This will lead to 'false' non-linear power dependence for both peaks. Second, both X_{A}^{0} and X_{B}^{0} are linearly polarized with high degree of polarizations of 80% and 60%, respectively, and polarization angles almost perpendicular (75°) to each other [Fig. 7.7(b)]. This further supports the X_{A}^{0} and X_{B}^{0} assignment, for if the two peaks are X_{A}^{0} and XX_{A}^{0} (or X_{B}^{0} and XX_{B}^{0}) they should have the same polarization. The orthogonal linear polarizations from X_{B}^{0} are due to the strain and geometrical anisotropies in the QD lateral plane. The X_{A}^{0}-X_{B}^{0} energy splitting being 13 meV is mainly due to the A- and B-valence band splitting Δ_2 caused by the spin-orbital interaction in the hole states [Fig. 7.8(a)].

7.2.3 Fine Structures of Neutral and Charged Excitons

The fine structure of X_{A}^{0} is studied in Fig. 7.8. The PL spectra of X_{A}^{0} ($V_{\text{bias}} = 0$ V) and X_{A}^{1-} ($V_{\text{bias}} = 0.5$ V) at two perpendicular polarization in Fig. 7.8(b) shows a discernible FSS in X_{A}^{0}. To quantify the FSS, polarization-dependent PL intensity I and E for X_{A}^{0} and X_{A}^{1-} are extracted in Fig. 7.8(c) and Fig. 7.8(d), respectively. The FSS in X_{A}^{0} is 370 ± 120 μeV, which originates from the electron-hole exchange interaction $\delta_{\text{x,y}}$. As X_{A}^{0} transits into X_{A}^{1-}, the FSS is no longer discernible [Fig. 7.8(d)]. This is expected, as both electron spin states are now

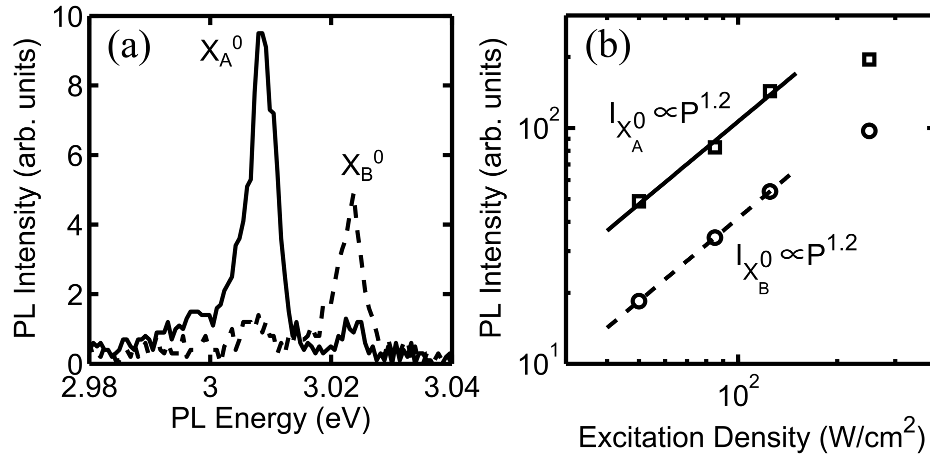

Figure 7.7: A-B exciton splitting in QD1. (a) PL spectra of -0.04 V corrected voltage at 90° (solid line) and 0°, respectively. (b) Intensity of X_{A}^0 and X_{B}^0 at -0.04 V corrected voltage and at various excitation densities.

occupied, leading to the the absence of FSS in X_{A}^{1-} as illustrated in Fig. 7.8(a).

We would like to mention that in majority of our QDs, we do not see X_{B}^0 or X_{B}^{1-}. When we do observe them, they are usually much weaker compared to X_{A}^0 or X_{A}^{1-} which always present. This is probably because B-holes lies at higher energies so that their lateral confinement potential is weaker, leading to more severe non-radiative decay for X_{B}^0 and X_{B}^{1-}. As such, further improvement in our device quality, especially the reduction of surface recombination is needed in order to have a better understanding of neutral and charged B-excitons.

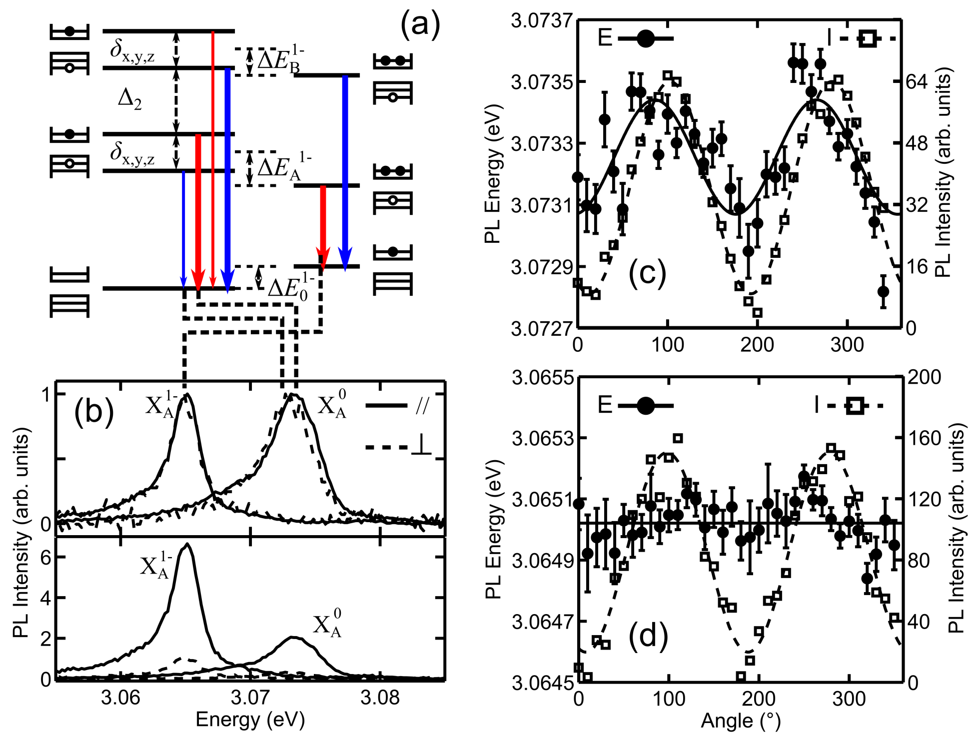

Figure 7.8: Fine-structures of X_A^0 and X_A^{1-} in QD2. (a) Illustration of the optical transitions of X_A^0, X_A^{1-}, X_B^0 and X_B^{1-} and their fine-structures. (b) X_A^0 (0 V) and X_A^{1-} (0.5 V) spectra at 90° (solid lines) and 0° (dashed lines). The inset contains the same spectra but normalized to their respective maximum in order to show the fine-structure splitting of X_A^0. (c) and (d) show the polarization-dependent emission energy (dot) and intensity (square) of X_A^{1-} and X_A^0, respectively.

CHAPTER 8

Conclusions and Future Work

8.1 Conclusions

We have shown in this thesis that top-down etched site-controlled InGaN/GaN QDs are suitable material platform for scalable quantum technologies including quantum communication and computation, which may one day revolutionize the landscape of the communication and computing industry. Our QDs are more efficient light emitters compared to the InGaN/GaN QW they are etched from. They possess atom-like discrete energy levels as demonstrated by both optically and electrically driven single-photon emission. Their controlled forming site enables us to scalably integrate QDs with electrical contacts at desired locations and shall also facilitate their integration with other solid-state components such as microcavities. In addition, they have the potential to operate at above cryogenic temperatures due to the adoption of III-N semiconductors and can be efficiently driven by electrical current, both merits further improve scalability and practicality. Finally, we have demonstrated the control of the number of charges in each QD and mapped out detailed energy levels in our QDs including A- and B-excitons and their fine structures, both are key to advanced quantum devices such as entangled-photon source and single-electron spin qubit. Specific achievements are summarized as following.

We have shown that despite being at close proximity of the etched sidewalls, excitons in our QDs can radiatively recombine efficiently. This is due to the following reasons. First, the strong strain relaxation in such as QD greatly reduces the internal polarization fields and, hence, improves the electron-hole-wavefunction overlap. This leads to an enhanced radiative recombination rate. Second, the non-uniform strain relaxation profile creates a lateral confinement potential barrier that hinders excitons from reaching the detrimental sidewall surface and, hence, suppress the non-radiative recombination rate.

The ability of controlling the site and structure of each QD also enabled comprehensive mapping between optical properties and QD structures, such as material composition, QD diameter, and thickness. This led to the discovery of several decay mechanisms in our QD in addition to the radiative recombination, including volume nonradiative recombination, tunneling-induced surface recombination and thermal-activation-induced surface recombination. All these decay channels can be quantitatively described by a simple analytical model. This model was

able to successfully explain several non-intuitive and potentially useful phenomena, including the enhanced photon antibunching with increasing temperature.

With a good understanding of the carrier dynamics and their dependence in QD structures, we were able to make useful devices based on our QDs. To date, we have demonstrated optically pumped single-photon sources that operate up to 90 K temperature and can be easily integrated with other photonic components due to their site-control and small foot-print. In addition, the geometry of our QDs is advantageous for current driven devices due to the naturally high overlap between the current pathway and QD active region. This allowed us to demonstrate the first electrical-driven site-controlled single-photon source based on III-N QDs, which marks another milestone towards practical single-photon sources that have both high scalability and high operating temperatures.

Finally, the capability of applying electrical bias to the QD also allowed us to demonstrate the first III-N charge-tunneling diode that can control the number of net charges in a III-N QD. This new apparatus opened up a new perspective to study the energy levels and fine structures in III-N QDs and led to the first unambiguous identification of neutral and charged A- and B-excitons and the unambiguous observation of fine structure splitting of neutral exciton in III-N QDs. Such device shall prove to be a powerful tool to understand exciton charging the fine-structure splitting in III-N QDs and shall enable more advance quantum technologies such as entanged-photon generation and single-electron qubit.

8.2 Future Work

8.2.1 Improve Quantum Dot Scalability

The work in this thesis represents an important step towards highly efficient and robust QDs that can be integrated with other solid-state components in large scale and operate in practical environments. However, most of the main issues of QDs that hinder the ultimate realization of this goal still remain, i.e., low operating temperature and insufficient scalability.

So far, the highest operating temperature of our QDs is 90 K, higher than all III-As QDs, as expected from III-N semiconductor, but still cryogenic and far from practical. This may be solved in two directions. First, improving the quantum efficiency of our QDs by developing surface passivation or material regrowth technique to reduce surface recombination. This shall also reduce the spectral broadening and enable the resolution of finer spectral features for studying fundamental QD physics. Second, using heterostructures that have greater bandgap offset between QD and barrier regions to prevent carriers from escaping the QD to the barrier.

Despite precise site-control, the structure of each QD is still not sufficiently controlled, as manifested by the significant inhomogeneity in optical properties from one QD to another. This hinders the scalable integration of our QDs with other on-chip components. The inhomogeneity is mainly caused by the fluctuation in QD thickness. Therefore, the first step towards solving

this problem is to improve the material growth technique to enable more uniform QW growth across the wafer.

8.2.2 Integrated Systems Based on Our Quantum Dots

This thesis has mostly focused on the fundamental physics and applications of single bare QD. The tremendous potential of integrating these site-controlled QDs with other photonic and electronic component has not been demonstrated. Because of the precise site-control and small foot-print on the chip, our QDs can be integrated in large scale with a wide range of solid-state photonic and electronic components.

The integration with other photonic components include microcavities, waveguides, and antennas. These components either change the local density of photon states that a QD couples to or modify the propagation direction of emitted photons. Integration with microcavities can enhance the radiative decay rate through Purcell effect and improve the collection efficiency of emitted photons. It may also lead to indistinguishable photon emission due to the enhanced radiative decay rate. Integration with waveguide will allow efficient routing of photons to desired places on the chip. Integration with antenna and alike will allow efficient coupling with out-of-chip components such as optical fiber.

However, we would like to point out that the fabrication of high quality III-N microcavities and waveguides remains challenging. This is partly due to the relatively low refractive indices of III-N materials and the difficulty in growing lattice-matched III-N alternating layers with high refractive index contrast, which are commonly used to grow distributed Bragg reflectors. It is also partly due to the chemical robustness of III-N which renders many common nanofabrication techniques in other semiconductor materials ineffective, such as the oxidation and wet-etching of sacrificial layers which are important in making photonic crystal membranes. Therefore, serious efforts are needed to develop novel growth and fabrication methods for III-N materials.

On the positive side, however, III-N semiconductors typically have much large oscillator strength compared to low bandgap semiconductors. This lowers the requirements to the photonic components in many applications enabled by coupling with optical modes, such as Purcell radiative enhancement and strongly-coupled QD-cavity systems. For instance, in III-As semiconductors, very high quality optical microcavities are required to achieve strong-coupling between excitons and photons in both QD and QW systems. In III-N systems, however, strong coupling have been achieved with very low quality microcavities and with very little amount of III-N active medium.

The integration with other electronic components has been demonstrated in this thesis. Due to the small foot-print and the ability to control the properties of each QD, multiple QDs with their own properties and electrical contacts can be densely packed and individually controlled and driven. This capability has never been demonstrated before and thus may enable many

novel technologies that requires the switching of multiple light emitters with different properties in a sub-micron space. For instance, we can pack four QDs in a sub-wavelength space each with its own linear polarization direction (0°, 45°, 90°, 135°) and electrical contacts, and then coupled them to a common single-mode fiber. This way, a very efficient light source for BB84 quantum communication protocol is realized. For another instance, we can place multiple QDs in a bio-chemical solution each with its own electrical contacts. We can then turn them on and off one-by-oe and observe the response of a probe molecule in the solution. This way, we can track the position and motion of the probe molecule using a principle similar to that of the globe-positioning system (GPS).

BIBLIOGRAPHY

[1] Zhang, L., Teng, C.-H., Hill, T. A., Lee, L.-K., Ku, P.-C., and Deng, H., "Single photon emission from site-controlled InGaN/GaN quantum dots," *Applied Physics Letters*, Vol. 103, No. 19, 2013, pp. 192114.

[2] Zhang, L., Lee, L.-K., Teng, C.-H., Hill, T. A., Ku, P.-C., and Deng, H., "How much better are InGaN/GaN nanodisks than quantum wellsOscillator strength enhancement and changes in optical properties," *Applied Physics Letters*, Vol. 104, No. 5, Feb. 2014, pp. 051116.

[3] Zhang, L., Hill, T. A., Teng, C.-H., Demory, B., Ku, P.-C., and Deng, H., "Carrier dynamics in site- and structure-controlled InGaN/GaN quantum dots," *Physical Review B*, Vol. 90, No. 24, Dec. 2014, pp. 245311.

[4] Schneider, C., Huggenberger, a., Sünner, T., Heindel, T., Strauss, M., Göpfert, S., Weinmann, P., Reitzenstein, S., Worschech, L., Kamp, M., Höfling, S., and Forchel, a., "Single site-controlled In(Ga)As/GaAs quantum dots: growth, properties and device integration." *Nanotechnology*, Vol. 20, No. 43, Oct. 2009, pp. 434012.

[5] Tachibana, K., Someya, T., Ishida, S., and Arakawa, Y., "Selective growth of InGaN quantum dot structures and their microphotoluminescence at room temperature," *Applied Physics Letters*, Vol. 76, No. 22, 2000, pp. 3212.

[6] Edwards, P. R., Martin, R. W., Watson, I. M., Liu, C., Taylor, R. A., Rice, J. H., Na, J. H., Robinson, J. W., and Smith, J. D., "Quantum dot emission from site-controlled InGaN-GaN micropyramid arrays," *Applied Physics Letters*, Vol. 85, No. 19, 2004, pp. 4281.

[7] Hsu, C.-W., Lundskog, A., Karlsson, K. F., Forsberg, U., Janzén, E., and Holtz, P. O., "Single excitons in InGaN quantum dots on GaN pyramid arrays." *Nano letters*, Vol. 11, No. 6, June 2011, pp. 2415–8.

[8] Choi, K., Arita, M., Kako, S., and Arakawa, Y., "Site-controlled growth of single GaN quantum dots in nanowires by MOCVD," *Journal of Crystal Growth*, Vol. 370, May 2013, pp. 328–331.

[9] Lee, L. K. and Ku, P.-C., "Fabrication of site-controlled InGaN quantum dots using reactive-ion etching," *Physica Status Solidi (C)*, Vol. 9, No. 3-4, Dec. 2011, pp. 609–612.

[10] Jain, S., Willander, M., Narayan, J., and Van Overstraeten, R., "IIInitrides: Growth, characterization, and properties," *Journal of Applied Physics*, Vol. 87, No. 3, 2000, pp. 965.

[11] Siegle, H., Kaczmarczyk, G., Filippidis, L., Litvinchuk, A. P., Hoffmann, A., and Thomsen, C., “Zone-boundary phonons in hexagonal and cubic GaN,” *Physical Review B*, Vol. 55, No. 11, March 1997, pp. 7000–7004.

[12] Vurgaftman, I. and Meyer, J. R., “Band parameters for nitrogen-containing semiconductors,” *Journal of Applied Physics*, Vol. 94, No. 6, 2003, pp. 3675.

[13] Reimer, M. E., Bulgarini, G., Akopian, N., Hocevar, M., Bavinck, M. B., Verheijen, M. a., Bakkers, E. P., Kouwenhoven, L. P., and Zwiller, V., “Bright single-photon sources in bottom-up tailored nanowires,” *Nature Communications*, Vol. 3, March 2012, pp. 737.

[14] Gazzano, O., Michaelis de Vasconcellos, S., Arnold, C., Nowak, a., Galopin, E., Sagnes, I., Lanco, L., Lemaître, a., and Senellart, P., “Bright solid-state sources of indistinguishable single photons.” *Nature communications*, Vol. 4, Feb. 2013, pp. 1425.

[15] Nowak, a. K., Portalupi, S. L., Giesz, V., Gazzano, O., Dal Savio, C., Braun, P.-F., Karrai, K., Arnold, C., Lanco, L., Sagnes, I., Lemaître, a., and Senellart, P., “Deterministic and electrically tunable bright single-photon source.” *Nature communications*, Vol. 5, Feb. 2014, pp. 3240.

[16] Stevenson, R. M., Young, R. J., Atkinson, P., Cooper, K., Ritchie, D. A., and Shields, A. J., “A semiconductor source of triggered entangled photon pairs.” *Nature*, Vol. 439, No. 7073, Jan. 2006, pp. 179–182.

[17] Dousse, A., Suffczyski, J., Beveratos, A., Krebs, O., Lemaître, A., Sagnes, I., Bloch, J., Voisin, P., and Senellart, P., “Ultrabright source of entangled photon pairs.” *Nature*, Vol. 466, No. 7303, July 2010, pp. 217–20.

[18] Juska, G. and Dimastrodonato, V., “Towards quantum-dot arrays of entangled photon emitters,” *Nature Photonics*, Vol. 7, No. July, 2013, pp. 527–531.

[19] Bonadeo, N. H., Erland, J., Gammon, D., Park, D., Katzer, D. S., and Steel, D. G., “Coherent Optical Control of the Quantum State of a Single Quantum Dot,” *Science*, Vol. 282, No. 5393, Nov. 1998, pp. 1473–1476.

[20] Pelton, M. and Yamamoto, Y., “Ultralow threshold laser using a single quantum dot and a microsphere cavity,” *Physical Review A*, Vol. 59, No. 3, March 1999, pp. 2418–2421.

[21] Nomura, M., Kumagai, N., Iwamoto, S., Ota, Y., and Arakawa, Y., “Laser oscillation in a strongly coupled single-quantum-dotnanocavity system,” *Nature Physics*, Vol. 6, No. 4, Feb. 2010, pp. 279–283.

[22] Yoshie, T., Scherer, A., Hendrickson, J., Khitrova, G., Gibbs, H. M., Rupper, G., Ell, C., Shchekin, O. B., and Deppe, D. G., “Vacuum Rabi splitting with a single quantum dot in a photonic crystal nanocavity,” *Nature*, Vol. 432, No. November, 2004, pp. 9–12.

[23] Hennessy, K., Badolato, a., Winger, M., Gerace, D., Atatüre, M., Gulde, S., Fält, S., Hu, E. L., and Imamolu, a., “Quantum nature of a strongly coupled single quantum dot-cavity system.” *Nature*, Vol. 445, No. 7130, Feb. 2007, pp. 896–899.

[24] Bennett, C. and Brassard, G., “Quantum cryptography: Public key distribution and coin tossing,” *International Conference on Computers, Systems & Signal Processing*, 1984.

[25] Pooley, M. A., Ellis, D. J. P., Patel, R. B., Bennett, A. J., Chan, K. H. A., Farrer, I., Ritchie, D. A., and Shields, A. J., “Controlled-NOT gate operating with single photons,” *Applied Physics Letters*, Vol. 100, No. 21, 2012, pp. 211103.

[26] O’Brien, J. L., Pryde, G. J., White, a. G., Ralph, T. C., and Branning, D., “Demonstration of an all-optical quantum controlled-NOT gate.” *Nature*, Vol. 426, No. 6964, Nov. 2003, pp. 264–7.

[27] Xiao, M., Wu, L., and Kimble, H., “Precision measurement beyond the shot-noise limit,” *Physical review letters*, Vol. 59, No. 3, 1987, pp. 278–281.

[28] Polzik, E., Carri, J., and Kimble, H., “Spectroscopy with squeezed light,” *Physical review letters*, Vol. 68, No. 20, 1992, pp. 3020–3023.

[29] Rarity, J., Owens, P., and Tapster, P., “Quantum Random-number Generation and Key Sharing,” *Journal of Modern Optics*, Vol. 41, No. 12, Dec. 1994, pp. 2435–2444.

[30] Nielsen, M. and Chuang, I., *Quantum computation and quantum information*, Cambridge University Press, 2010.

[31] Darquié, B., Jones, M. P. A., Dingjan, J., Beugnon, J., Bergamini, S., Sortais, Y., Messin, G., Browaeys, A., and Grangier, P., “Controlled single-photon emission from a single trapped two-level atom.” *Science (New York, N.Y.)*, Vol. 309, No. 5733, July 2005, pp. 454–6.

[32] Lounis, B. and Moerner, W. E., “Single photons on demand from a single molecule at room temperature.” *Nature*, Vol. 407, No. 6803, Sept. 2000, pp. 491–3.

[33] Kurtsiefer, C., Mayer, S., Zarda, P., and Weinfurter, H., “Stable solid-state source of single photons,” *Physical review letters*, Vol. 85, No. 2, July 2000, pp. 290–3.

[34] Morfa, A. J., Gibson, B. C., Karg, M., Karle, T. J., Greentree, A. D., Mulvaney, P., and Tomljenovic-Hanic, S., “Single-photon emission and quantum characterization of zinc oxide defects.” *Nano letters*, Vol. 12, No. 2, Feb. 2012, pp. 949–54.

[35] Castelletto, S., Johnson, B. C., Ivády, V., Stavrias, N., Umeda, T., Gali, A., and Ohshima, T., “A silicon carbide room-temperature single-photon source,” *Nature Materials*, Vol. 12, No. 11, 2013, pp. 1–6.

[36] Michler, P., Imamoglu, A., Mason, M. D., Carson, P. J., Strouse, G. F., and Buratto, S. K., “Quantum correlation among photons from a single quantum dot at room temperature,” *Nature*, Vol. 406, No. 6799, Aug. 2000, pp. 968–970.

[37] Santori, C., Pelton, M., Solomon, G., Dale, Y., and Yamamoto, Y., “Triggered Single Photons from a Quantum Dot,” *Physical Review Letters*, Vol. 86, No. 8, Feb. 2001, pp. 1502–1505.

[38] Dousse, A., Suffczyski, J., Beveratos, A., Krebs, O., Lemaître, A., Sagnes, I., Bloch, J., Voisin, P., and Senellart, P., “Ultrabright source of entangled photon pairs.” *Nature*, Vol. 466, No. 7303, July 2010, pp. 217–20.

[39] Kako, S., Santori, C., Hoshino, K., Götzinger, S., Yamamoto, Y., and Arakawa, Y., “A gallium nitride single-photon source operating at 200 K.” *Nature materials*, Vol. 5, No. 11, Nov. 2006, pp. 887–92.

[40] Holmes, M. J., Choi, K., Kako, S., Arita, M., and Arakawa, Y., “Room-Temperature Triggered Single Photon Emission from a III-Nitride Site-Controlled Nanowire Quantum Dot.” *Nano letters*, Vol. 14, No. 2, Jan. 2014, pp. 982–986.

[41] Bounouar, S., Elouneg-Jamroz, M., Den Hertog, M. I., Morchutt, C., Bellet-Amalric, E., André, R., Bougerol, C., Genuist, Y., Poizat, J.-P., Tatarenko, S., Kheng, K., and Hertog, M. D., “Ultrafast Room Temperature Single-Photon Source from Nanowire-Quantum Dots,” *Nano letters*, Vol. 12, No. 6, May 2012, pp. 2977–2981.

[42] Steffen, R., Koch, T., Oshinowo, J., Faller, F., and Forchel, a., “Photoluminescence study of deep etched InGaAs/GaAs quantum wires and dots defined by low-voltage electron beam lithography,” *Applied Physics Letters*, Vol. 68, No. 2, 1996, pp. 223.

[43] Verma, V. B., Stevens, M. J., Silverman, K. L., Dias, N. L., Garg, A., Coleman, J. J., and Mirin, R. P., “Photon antibunching from a single lithographically defined InGaAs/GaAs quantum dot.” *Optics express*, Vol. 19, No. 5, Feb. 2011, pp. 4182–7.

[44] Song, H. Z., Usuki, T., Ohshima, T., Sakuma, Y., Kawabe, M., Okada, Y., Takemoto, K., Miyazawa, T., Hirose, S., Nakata, Y., Takatsu, M., and Yokoyama, N., “Site-controlled quantum dots fabricated using an atomic-force microscope assisted technique,” *Nanoscale Research Letters*, Vol. 1, No. 2, Aug. 2006, pp. 160–166.

[45] Martín-Sánchez, J., Alonso-González, P., Herranz, J., González, Y., and González, L., “Site-controlled lateral arrangements of InAs quantum dots grown on GaAs (001) patterned substrates by atomic force microscopy local oxidation nanolithography,” *Nanotechnology*, Vol. 20, No. 12, March 2009, pp. 125302.

[46] Baier, M. H., Pelucchi, E., Kapon, E., Varoutsis, S., Gallart, M., Robert-Philip, I., and Abram, I., “Single photon emission from site-controlled pyramidal quantum dots,” *Applied Physics Letters*, Vol. 84, No. 5, 2004, pp. 648.

[47] Tran, T., Muller, A., Shih, C. K., Wong, P. S., Balakrishnan, G., Nuntawong, N., Tatebayashi, J., and Huffaker, D. L., “Single dot spectroscopy of site-controlled InAs quantum dots nucleated on GaAs nanopyramids,” *Applied Physics Letters*, Vol. 91, No. 13, 2007, pp. 133104.

[48] Schliwa, A., Winkelnkemper, M., Lochmann, A., Stock, E., and Bimberg, D., “In(Ga)As/GaAs quantum dots grown on a (111) surface as ideal sources of entangled photon pairs,” *Physical Review B*, Vol. 80, No. 16, Oct. 2009, pp. 161307.

[49] Mohan, A., Felici, M., Gallo, P., Dwir, B., Rudra, A., Faist, J., and Kapon, E., “Polarization-entangled photons produced with high-symmetry site-controlled quantum dots,” *Nature Photonics*, Vol. 4, No. 5, 2010, pp. 302–306.

[50] Strittmatter, A., Holzbecher, A., Schliwa, A., Schulze, J.-H., Quandt, D., Germann, T. D., Dreismann, A., Hitzemann, O., Stock, E., Ostapenko, I. a., Rodt, S., Unrau, W., Pohl, U. W., Hoffmann, A., Bimberg, D., and Haisler, V., “Site-controlled quantum dot growth on buried oxide stressor layers,” *Physica Status Solidi (a)*, Vol. 209, No. 12, Dec. 2012, pp. 2411–2420.

[51] Toujyou, T. and Tsukamoto, S., “Temperature-Dependent Site Control of InAs/GaAs (001) Quantum Dots Using a Scanning Tunneling Microscopy Tip During Growth.” *Nanoscale research letters*, Vol. 5, No. 12, Jan. 2010, pp. 1930–1934.

[52] Shih, Y. H. and Alley, C. O., "New Type of Einstean-Podolsky-Rosen-Bohm Experiment Using Pairs of Light Quanta Produced by Optical Parametric Down Conversion," *Physical Review Letters*, Vol. 61, No. 26, 1988, pp. 2921–2924.

[53] Fattal, D., Inoue, K., Vučković, J., Santori, C., Solomon, G., and Yamamoto, Y., "Entanglement Formation and Violation of Bells Inequality with a Semiconductor Single Photon Source," *Physical Review Letters*, Vol. 92, No. 3, Jan. 2004, pp. 037903.

[54] Ghali, M., Ohtani, K., Ohno, Y., and Ohno, H., "Generation and control of polarization-entangled photons from GaAs island quantum dots by an electric field." *Nature communications*, Vol. 3, Jan. 2012, pp. 661.

[55] Singh, R. and Bester, G., "Nanowire Quantum Dots as an Ideal Source of Entangled Photon Pairs," *Physical Review Letters*, Vol. 103, No. 6, Aug. 2009, pp. 063601.

[56] Loss, D. and DiVincenzo, D. P., "Quantum computation with quantum dots," *Physical Review A*, Vol. 57, No. 1, Jan. 1998, pp. 120–126.

[57] Chen, P., Piermarocchi, C., Sham, L., Gammon, D., and Steel, D., "Theory of quantum optical control of a single spin in a quantum dot," *Physical Review B*, Vol. 69, No. 7, Feb. 2004, pp. 1–8.

[58] Greilich, A., Shabaev, A., Yakovlev, D. R., Efros, A. L., Yugova, I. A., Reuter, D., Wieck, A. D., and Bayer, M., "Nuclei-induced frequency focusing of electron spin coherence," *Science*, Vol. 317, 2007, pp. 1896–1899.

[59] Xu, X., Yao, W., Sun, B., Steel, D. G., Bracker, A. S., Gammon, D., and Sham, L. J., "Optically controlled locking of the nuclear field via coherent dark-state spectroscopy." *Nature*, Vol. 459, No. 7250, June 2009, pp. 1105–9.

[60] Gerardot, B. D., Brunner, D., Dalgarno, P. A., Öhberg, P., Seidl, S., Kroner, M., Karrai, K., Stoltz, N. G., Petroff, P. M., and Warburton, R. J., "Optical pumping of a single hole spin in a quantum dot," *Nature*, Vol. 451, 2008, pp. 441–444.

[61] Atatüre, M., Dreiser, J., Badolato, A., Högele, A., Karrai, K., and Imamoglu, A., "Quantum-dot spin-state preparation with near-unity fidelity," *Science*, Vol. 312, No. 5773, 2006, pp. 551–553.

[62] Xu, X., Wu, Y., Sun, B., Huang, Q., Cheng, J., Steel, D. G., Bracker, a. S., Gammon, D., Emary, C., and Sham, L. J., "Fast Spin State Initialization in a Singly Charged InAs-GaAs Quantum Dot by Optical Cooling," *Physical Review Letters*, Vol. 99, No. 9, Aug. 2007, pp. 1–4.

[63] Koppens, F. H. L., Buizert, C., Tielrooij, K. J., Vink, I. T., Nowack, K. C., Meunier, T., Kouwenhoven, L. P., and Vandersypen, L. M. K., "Driven coherent oscillations of a single electron spin in a quantum dot." *Nature*, Vol. 442, No. 7104, Aug. 2006, pp. 766–71.

[64] Nowack, K. C., Koppens, F. H. L., Nazarov, Y. V., and Vandersypen, L. M. K., "Coherent control of a single electron spin with electric fields," *Science*, Vol. 318, No. 5855, 2007, pp. 1430–1433.

[65] Press, D., Ladd, T. D., Zhang, B., and Yamamoto, Y., "Complete quantum control of a single quantum dot spin using ultrafast optical pulses." *Nature*, Vol. 456, No. 7219, Nov. 2008, pp. 218–21.

[66] Atatüre, M., Dreiser, J., Badolato, A., and Imamoglu, A., "Observation of Faraday rotation from a single confined spin," *Nature Physics*, Vol. 3, 2007, pp. 101–105.

[67] Kim, D., Economou, S., Bdescu, t., Scheibner, M., Bracker, A., Bashkansky, M., Reinecke, T., and Gammon, D., "Optical Spin Initialization and Nondestructive Measurement in a Quantum Dot Molecule," *Physical Review Letters*, Vol. 101, No. 23, Dec. 2008, pp. 236804.

[68] Imamoglu, a., Awschalom, D. D., Burkard, G., DiVincenzo, D. P., Loss, D., Sherwin, M., and Small, a., "Quantum Information Processing Using Quantum Dot Spins and Cavity QED," *Physical Review Letters*, Vol. 83, No. 20, Nov. 1999, pp. 4204–4207.

[69] Yao, W., Liu, R.-B., and Sham, L., "Theory of Control of the Spin-Photon Interface for Quantum Networks," *Physical Review Letters*, Vol. 95, No. 3, July 2005, pp. 030504.

[70] Clark, S. M., Fu, K.-M. C., Ladd, T. D., and Yamamoto, Y., "Quantum Computers Based on Electron Spins Controlled by Ultrafast Off-Resonant Single Optical Pulses," *Physical Review Letters*, Vol. 99, No. 4, July 2007, pp. 2–5.

[71] Kim, D., Carter, S. G., Greilich, A., Bracker, A. S., and Gammon, D., "Ultrafast optical control of entanglement between two quantum-dot spins," *Nature Physics*, Vol. 7, No. 3, Dec. 2010, pp. 223–229.

[72] John D. Joannopoulos, S. G. J., Winn, J. N., and Meade, R. D., *Photonic Crystals: Molding the Flow of Light*, Princeton University Press, New Jersey, 2nd ed., 2008.

[73] Kittel, C., *Introduction to Solid State Physics*, John Wiley & Sons, 8th ed., 2005.

[74] Englund, D., Fattal, D., Waks, E., Solomon, G., Zhang, B., Nakaoka, T., Arakawa, Y., Yamamoto, Y., and Vučković, J., "Controlling the Spontaneous Emission Rate of Single Quantum Dots in a Two-Dimensional Photonic Crystal," *Physical Review Letters*, Vol. 95, No. 1, July 2005, pp. 2–5.

[75] Santori, C., Fattal, D., Vucković, J., Solomon, G. S., and Yamamoto, Y., "Indistinguishable photons from a single-photon device." *Nature*, Vol. 419, No. 6907, 2002, pp. 594–597.

[76] Knill, E., Laflamme, R., and Milburn, G. J., "A scheme for efficient quantum computation with linear optics." *Nature*, Vol. 409, No. 6816, Jan. 2001, pp. 46–52.

[77] Orszag, M., *Quantum Optics*, Springer, New York, 2nd ed., 2000.

[78] Birnbaum, K. M., Boca, A., Miller, R., Boozer, A. D., Northup, T. E., and Kimble, H. J., "Photon blockade in an optical cavity with one trapped atom." *Nature*, Vol. 436, No. 7047, July 2005, pp. 87–90.

[79] Englund, D., Faraon, A., Fushman, I., Stoltz, N., Petroff, P., and Vucković, J., "Controlling cavity reflectivity with a single quantum dot." *Nature*, Vol. 450, No. 7171, Dec. 2007, pp. 857–61.

[80] Fushman, I., Englund, D., Faraon, A., Stoltz, N., Petroff, P., and Vučković, J., "Controlled phase shifts with a single quantum dot," *Science*, Vol. 320, No. May, 2008, pp. 769–773.

[81] Bose, R., Sridharan, D., Kim, H., Solomon, G. S., and Waks, E., "Low-Photon-Number Optical Switching with a Single Quantum Dot Coupled to a Photonic Crystal Cavity," *Physical Review Letters*, Vol. 108, No. 22, May 2012, pp. 227402.

[82] Duan, L.-M. and Kimble, H., "Scalable Photonic Quantum Computation through Cavity-Assisted Interactions," *Physical Review Letters*, Vol. 92, No. 12, March 2004, pp. 127902.

[83] Nogues, G., Rauschenbeutel, A., Osnaghi, S., Brune, M., Raimond, J. M., and Haroche, S., "Seeing a single photon without destroying it," *Nature*, Vol. 400, 1999, pp. 239–242.

[84] Cirac, J., Zoller, P., Kimble, H., and Mabuchi, H., "Quantum State Transfer and Entanglement Distribution among Distant Nodes in a Quantum Network," *Physical Review Letters*, Vol. 78, No. 16, April 1997, pp. 3221–3224.

[85] Reithmaier, J. P., Sek, G., Löffler, A., Hofmann, C., Kuhn, S., Reitzenstein, S., Keldysh, L. V., Kulakovskii, V. D., Reinecke, T. L., and Forchel, A., "Strong coupling in a single quantum dot-semiconductor microcavity system." *Nature*, Vol. 432, No. 7014, Nov. 2004, pp. 197–200.

[86] Das, A., Heo, J., Jankowski, M., Guo, W., Zhang, L., Deng, H., and Bhattacharya, P., "Room Temperature Ultralow Threshold GaN Nanowire Polariton Laser," Aug. 2011.

[87] Bhattacharya, P., Frost, T., Deshpande, S., Baten, M. Z., Hazari, A., and Das, A., "Room Temperature Electrically Injected Polariton Laser," *Physical Review Letters*, Vol. 112, No. 23, June 2014, pp. 236802.

[88] Goldstein, L., Glas, F., Marzin, J. Y., Charasse, M. N., and Le Roux, G., "Growth by molecular beam epitaxy and characterization of InAs/GaAs strained-layer superlattices," *Applied Physics Letters*, Vol. 47, No. 10, 1985, pp. 1099.

[89] Leonard, D., Krishnamurthy, M., Reaves, C. M., Denbaars, S. P., and Petroff, P. M., "Direct formation of quantum-sized dots from uniform coherent islands of InGaAs on GaAs surfaces," *Applied Physics Letters*, Vol. 63, No. 23, 1993, pp. 3203.

[90] Leon, R., Petroff, P. M., Leonard, D., and Fafard, S., "Spatially Resolved Visible Luminescence of Self-Assembled Semiconductor Quantum Dots," *Science*, Vol. 267, No. 5206, 1995, pp. 1966–1968.

[91] Unrau, W., Quandt, D., Schulze, J.-H., Heindel, T., Germann, T. D., Hitzemann, O., Strittmatter, a., Reitzenstein, S., Pohl, U. W., and Bimberg, D., "Electrically driven single photon source based on a site-controlled quantum dot with self-aligned current injection," *Applied Physics Letters*, Vol. 101, No. 21, 2012, pp. 211119.

[92] Deshpande, S., Das, A., and Bhattacharya, P., "Blue single photon emission up to 200 K from an InGaN quantum dot in AlGaN nanowire," *Applied Physics Letters*, Vol. 102, No. 16, 2013, pp. 161114.

[93] Koehl, W. F., Buckley, B. B., Heremans, F. J., Calusine, G., and Awschalom, D. D., "Room temperature coherent control of defect spin qubits in silicon carbide." *Nature*, Vol. 479, No. 7371, Nov. 2011, pp. 84–7.

[94] Brouri, R., Beveratos, a., Poizat, J. P., and Grangier, P., "Photon antibunching in the fluorescence of individual color centers in diamond." *Optics letters*, Vol. 25, No. 17, Sept. 2000, pp. 1294–6.

[95] Robledo, L., Childress, L., Bernien, H., Hensen, B., Alkemade, P. F. a., and Hanson, R., "High-fidelity projective read-out of a solid-state spin quantum register." *Nature*, Vol. 477, No. 7366, Sept. 2011, pp. 574–8.

[96] Amano, H., Kito, M., Hiramatsu, K., and Akasaki, I., "P-Type Conduction in Mg-Doped GaN Treated with Low-Energy Electron Beam Irradiation (LEEBI)," *Janpanese Journal of Applied Physics*, Vol. 28, No. 12, 1989, pp. L 2112–L 2114.

[97] Nakamura, S., Mukai, T., Senoh, M., and Iwasa, N., "Thermal annealing effects on p-type Mg-doped GaN films," *Japanese Journal of Applied Physics*, Vol. 31, No. 2B, 1992, pp. L 139– L 142.

[98] Nakamura, S., Iwasa, N., Senoh, M., and Mukai, T., "Hole compensation mechanism of p-type GaN films," *Japanese Journal of Applied Physics*, Vol. 31, No. 5A, 1992, pp. 1258–1266.

[99] Ho, J.-K., Jong, C.-S., Chiu, C. C., Huang, C.-N., Shih, K.-K., Chen, L.-C., Chen, F.-R., and Kai, J.-J., "Low-resistance ohmic contacts to p-type GaN achieved by the oxidation of Ni/Au films," *Journal of Applied Physics*, Vol. 86, No. 8, 1999, pp. 4491.

[100] Lin, C., Hibbard, D., Au, A., and Lee, H., "Low Resistance Optically Transparent Contacts to ptype GaN Using Oxidized Ni/Au and ITO for LED Application," *Mat. Res. Soc. Symp.*, Vol. 639, 2000, pp. 2–7.

[101] Kim, D., Sung, Y., Park, J., and Yeom, G., "A study of transparent indium tin oxide (ITO) contact to p-GaN," *Thin Solid Films*, Vol. 398-399, Nov. 2001, pp. 87–92.

[102] Liu, Y.-J., Huang, C.-C., Chen, T.-Y., Hsu, C.-S., Liou, J.-K., Tsai, T.-Y., and Liu, W.-C., "Implementation of an indium-tin-oxide (ITO) direct-Ohmic contact structure on a GaN-based light emitting diode." *Optics express*, Vol. 19, No. 15, July 2011, pp. 14662–70.

[103] Yu, P. and Cardona, M., *Fundamentals of Semiconductors: Physics and Materials Properties*, Graduate Texts in Physics, Springer, 2010.

[104] Elliott, R. J., "Intensity of optical absorption by excitons," *Physical Review*, Vol. 108, No. 6, 1957, pp. 1384–1389.

[105] Hanamura, E., "Very large optical nonlinearity of semiconductor microcrystallites," *Physical Review B*, Vol. 37, No. 3, 1988, pp. 1237–1279.

[106] Matsuura, M. and Kamizato, T., "Oscillator Strength of Excitons in Quantum Wells," *Surface Science*, Vol. 174, 1986, pp. 183–187.

[107] Stobbe, S., Johansen, J., Kristensen, P., Hvam, J., and Lodahl, P., "Frequency dependence of the radiative decay rate of excitons in self-assembled quantum dots: Experiment and theory," *Physical Review B*, Vol. 80, No. 15, Oct. 2009, pp. 1–14.

[108] Siozade, L., Colard, S., Mihailovic, M., Leymarie, J., Vasson, A., Grandjean, N., Leroux, M., and Massies, J., "Temperature dependence of optical properties of h-GaN films studied by reflectivity and ellipsometry," *Japanese Journal of Applied Physics*, Vol. 39, No. 1, 2000, pp. 20–25.

[109] Monier, C., Freundlich, A., and Vilela, M. F., "Oscillator strength of excitons in (In, Ga)As/GaAs quantum wells in the presence of a large electric field," *Journal of Applied Physics*, Vol. 85, No. 5, 1999, pp. 2713.

[110] Belousov, M. V., Ledentsov, N. N., Maximov, M. V., Wang, P. D., Yasievich, I. N., Faleev, N. N., Kozin, I. A., Ustinov, V. M., Kop'ev, P. S., and Torres, C. M. S., "Energy levels and exciton oscillator strength in submonolayer InAs-GaAs heterostructures," *Physical Review B*, Vol. 51, No. 20, 1995, pp. 14346 – 14351.

[111] Mallet, E., Réveret, F., Disseix, P., Shubina, T. V., and Leymarie, J., "Influence of excitonic oscillator strengths on the optical properties of GaN and ZnO," *Physical Review B*, Vol. 90, No. 4, July 2014, pp. 045204.

[112] Chuang, S. and Chang, C., "KP Method for Strained Wurtzite Semiconductors," *Physical Review B*, Vol. 54, No. 4, July 1996, pp. 2491–2504.

[113] Gil, B., *Physics of Wurtzite Nitrides and Oxides: Passport to Devices*, Springer series in materials science, Springer, 2014.

[114] Stutzmann, M., Ambacher, O., Eickhoff, M., Karrer, U., Lima Pimenta, a., Neuberger, R., Schalwig, J., Dimitrov, R., Schuck, P., and Grober, R., "Playing with Polarity," *Physica Status Solidi (B)*, Vol. 228, No. 2, Nov. 2001, pp. 505–512.

[115] Li, Q., Westlake, K. R., Crawford, M. H., Lee, S. R., Koleske, D. D., Figiel, J. J., Cross, K. C., Fathololoumi, S., Mi, Z., and Wang, G. T., "Optical performance of top-down fabricated InGaN/GaN nanorod light emitting diode arrays." *Optics express*, Vol. 19, No. 25, Dec. 2011, pp. 25528–34.

[116] Brown, R. H. and Twiss, R. Q., "A test of a new type of stellar interferometer on Sirius," *Nature*, Vol. 178, 1956, pp. 1046–1048.

[117] Kawakami, Y., Suzuki, S., Kaneta, A., Funato, M., Kikuchi, A., and Kishino, K., "Origin of high oscillator strength in green-emitting InGaNGaN nanocolumns," *Applied Physics Letters*, Vol. 89, No. 16, 2006, pp. 163124.

[118] Jarjour, A., Oliver, R., Tahraoui, A., Kappers, M., Humphreys, C., and Taylor, R., "Control of the Oscillator Strength of the Exciton in a Single InGaN-GaN Quantum Dot," *Physical Review Letters*, Vol. 99, No. 19, Nov. 2007, pp. 1–4.

[119] Chen, D., Luo, Y., Wang, L., Li, H., Xi, G., Jiang, Y., Hao, Z., Sun, C., and Han, Y., "Enhancement of electron-longitudinal optical phonon coupling in highly strained InGaN/GaN quantum well structures," *Journal of Applied Physics*, Vol. 101, No. 5, 2007, pp. 053712.

[120] Renwick, P., Tang, H., Bai, J., and Wang, T., "Reduced longitudinal optical phonon-exciton interaction in InGaN/GaN nanorod structures," *Applied Physics Letters*, Vol. 100, No. 18, 2012, pp. 182105.

[121] Shockley, W. and Read, W. T., "Statistics of the recombinations of holes and electrons," *Physical Review*, Vol. 87, No. 5, 1952, pp. 835–842.

[122] Iveland, J., Martinelli, L., Peretti, J., Speck, J. S., and Weisbuch, C., "Direct Measurement of Auger Electrons Emitted from a Semiconductor Light-Emitting Diode under Electrical Injection: Identification of the Dominant Mechanism for Efficiency Droop," *Physical Review Letters*, Vol. 110, No. 17, April 2013, pp. 177406.

[123] Seguin, R., Rodt, S., Strittmatter, A., Reiß mann, L., Bartel, T., Hoffmann, A., Bimberg, D., Hahn, E., and Gerthsen, D., "Multi-excitonic complexes in single InGaN quantum dots," *Applied Physics Letters*, Vol. 84, No. 20, 2004, pp. 4023.

[124] Rice, J. H., Robinson, J. W., Na, J. H., Lee, K. H., Taylor, R. A., Williams, D. P., OReilly, E. P., Andreev, A. D., Arakawa, Y., and Yasin, S., "Biexciton and exciton dynamics in single InGaN quantum dots," *Nanotechnology*, Vol. 16, No. 9, Sept. 2005, pp. 1477–1481.

[125] Schömig, H., Halm, S., Forchel, A., Bacher, G., Off, J., and Scholz, F., "Probing Individual Localization Centers in an InGaN/GaN Quantum Well," *Physical Review Letters*, Vol. 92, No. 10, March 2004, pp. 106802.

[126] Martin, R. W., Edwards, P. R., Taylor, R. A., Rice, J. H., Na, J. H., Robinson, J. W., Smith, J. D., Liu, C., and Watson, I. M., "Luminescence properties of isolated InGaN/GaN quantum dots," *Physica Status Solidi (a)*, Vol. 202, No. 3, Feb. 2005, pp. 372–376.

[127] Simeonov, D., Dussaigne, A., Butté, R., and Grandjean, N., "Complex behavior of biexcitons in GaN quantum dots due to a giant built-in polarization field," *Physical Review B*, Vol. 77, No. 7, Feb. 2008, pp. 075306.

[128] Winkelnkemper, M., Seguin, R., Rodt, S., Schliwa, A., Reismann, L., Strittmatter, A., Hoffmann, A., and Bimberg, D., "Polarized emission lines from single InGaN/GaN quantum dots: Role of the valence-band structure of wurtzite Group-III nitrides," *Physica E: Low-dimensional Systems and Nanostructures*, Vol. 40, No. 6, April 2008, pp. 2217–2219.

[129] Bardoux, R., Kaneta, A., Funato, M., Kawakami, Y., Kikuchi, A., and Kishino, K., "Positive binding energy of a biexciton confined in a localization center formed in a single In_xGa_{1x}N/GaN quantum disk," *Physical Review B*, Vol. 79, No. 15, April 2009, pp. 155307.

[130] Sebald, K., Kalden, J., Lohmeyer, H., and Gutowski, J., "Optical properties of single InGaN quantum dots and their devices," *Physica Status Solidi (B)*, Vol. 248, No. 8, Aug. 2011, pp. 1777–1786.

[131] Amloy, S., Moskalenko, E. S., Eriksson, M., Karlsson, K. F., Chen, Y. T., Chen, K. H., Hsu, H. C., Hsiao, C. L., Chen, L. C., and Holtz, P. O., "Dynamic characteristics of the exciton and the biexciton in a single InGaN quantum dot," *Applied Physics Letters*, Vol. 101, No. 6, 2012, pp. 061910.

[132] Chen, Y.-T., Tsai, W.-C., Chen, W.-Y., Hsiao, C.-L., Hsu, H.-C., Chang, W.-H., Hsu, T.-M., Chen, K.-H., and Chen, L.-C., "Growth of sparse arrays of narrow GaN nanorods

hosting spectrally stable InGaN quantum disks," *Optics Express*, Vol. 20, No. 15, 2012, pp. 16166–16173.

[133] Holmes, M. J., Park, Y. S., Warner, J. H., and Taylor, R. A., "Quantum confined Stark effect and corresponding lifetime reduction in a single In_xGa_{1x}N quantum disk," *Applied Physics Letters*, Vol. 95, No. 18, 2009, pp. 181910.

[134] Hsueh, T. H., Huang, H. W., Lai, F. I., Sheu, J. K., Chang, Y. H., Kuo, H. C., and Wang, S. C., "Photoluminescence from In 0.3 Ga 0.7 N/GaN multiple-quantum-well nanorods," *Nanotechnology*, Vol. 16, No. 4, April 2005, pp. 448–450.

[135] Chen, H.-S., Yeh, D.-M., Lu, Y.-C., Chen, C.-Y., Huang, C.-F., Tang, T.-Y., Yang, C. C., Wu, C.-S., and Chen, C.-D., "Strain relaxation and quantum confinement in InGaN/GaN nanoposts," *Nanotechnology*, Vol. 17, No. 5, March 2006, pp. 1454–1458.

[136] Kawakami, Y., Kaneta, A., Su, L., Zhu, Y., Okamoto, K., Funato, M., Kikuchi, A., and Kishino, K., "Optical properties of InGaN/GaN nanopillars fabricated by postgrowth chemically assisted ion beam etching," *Journal of Applied Physics*, Vol. 107, No. 2, 2010, pp. 023522.

[137] Ramesh, V., Kikuchi, A., Kishino, K., Funato, M., and Kawakami, Y., "Strain relaxation effect by nanotexturing InGaN/GaN multiple quantum well," *Journal of Applied Physics*, Vol. 107, No. 11, 2010, pp. 114303.

[138] Songmuang, R., Kalita, D., Sinha, P., den Hertog, M., Andre, R., Ben, T., Gonzalez, D., Mariette, H., and Monroy, E., "Strong suppression of internal electric field in GaN/AlGaN multi-layer quantum dots in nanowires," *Applied Physics Letters*, Vol. 99, No. 14, 2011, pp. 141914.

[139] Takeuchi, T., Sota, S., Katsuragawa, M., Komori, M., Takeuchi, H., Amano, H., and Akasaki, I., "Quantum-confined Stark effect due to piezoelectric fields in GaInN strained quantum wells," *Japanese Journal of Applied Physics*, Vol. 36, 1997, pp. L382–L385.

[140] Böcklin, C., Veprek, R. G., and Witzigmann, B., "Computational study of an InGaN/GaN nanocolumn light-emitting diode," *Physical Review B*, Vol. 81, No. 15, April 2010, pp. 155306.

[141] Novotny, L. and Hecht, B., *Principles of nano-optics*, Principles of Nano-optics, Cambridge University Press, 2006.

[142] Lukosz, W. and Kunz, R., "Light emission by magnetic and electric dipoles close to a plane interface. I. Total radiated power," *Journal of the Optical Society of America*, Vol. 67, No. 12, 1977, pp. 1607–1615.

[143] Lukosz, W., "Light emission by magnetic and electric dipoles close to a plane dielectric interface. III. Radiation patterns of dipoles with arbitrary orientation," *Journal of the Optical Society of America*, Vol. 69, No. 11, 1979, pp. 1495–1503.

[144] Claudon, J., Bleuse, J., Malik, N., Bazin, M., Jaffrennou, P., Gregersen, N., Sauvan, C., Lalanne, P., and Gérard, J., "A highly efficient single-photon source based on a quantum dot in a photonic nanowire," *Nature Photonics*, Vol. 4, No. March, 2010, pp. 174–177.

[145] Taflove, A. and Hagness, S. C., *Computational Electrodynamics: The Finite-Difference Time-Domain Method*, The Artech House antenna and propagation library, Artech House, Incorporated, 3rd ed., 2005.

[146] Friedler, I., Sauvan, C., Hugonin, J. P., Lalanne, P., Claudon, J., and Gérard, J. M., "Solid-state single photon sources: the nanowire antenna." *Optics express*, Vol. 17, No. 4, Feb. 2009, pp. 2095–110.

[147] Bleuse, J., Claudon, J., Creasey, M., Malik, N. S., Gérard, J.-M., Maksymov, I., Hugonin, J.-P., and Lalanne, P., "Inhibition, Enhancement, and Control of Spontaneous Emission in Photonic Nanowires," *Physical Review Letters*, Vol. 106, No. 10, March 2011, pp. 103601.

[148] Dirac, P. A. M., "The Quantum Theory of the Emission and Absorption of Radiation," *Proceedings of the Royal Society A: Mathematical, Physical and Engineering Sciences*, Vol. 114, No. 767, March 1927, pp. 243–265.

[149] Siegman, A. E., *Lasers*, University Science Books, 1986.

[150] Murray, C., Kagan, C. R., and Bawendi, M. G., "Synthesis and characterization of monodisperse nanocrystals and close-packed nanocrystal assemblies," *Annual Review of Materials Science*, Vol. 30, 2000, pp. 545–610.

[151] Tatebayashi, J., Ota, Y., Ishida, S., Nishioka, M., Iwamoto, S., and Arakawa, Y., "Site-controlled formation of InAs/GaAs quantum-dot-in-nanowires for single photon emitters," *Applied Physics Letters*, Vol. 100, No. 26, 2012, pp. 263101.

[152] Holmes, M., Kako, S., Choi, K., Podemski, P., Arita, M., and Arakawa, Y., "Measurement of an Exciton Rabi Rotation in a Single GaN/Al_{x}Ga_{1-x}N Nanowire-Quantum Dot Using Photoluminescence Spectroscopy: Evidence for Coherent Control," *Physical Review Letters*, Vol. 111, No. 5, July 2013, pp. 057401.

[153] Schniepp, H. and Sandoghdar, V., "Spontaneous Emission of Europium Ions Embedded in Dielectric Nanospheres," *Physical Review Letters*, Vol. 89, No. 25, Dec. 2002, pp. 257403.

[154] Niquet, Y. M., Priester, C., and Mariette, H., "Influence of the inhomogeneous strain relaxation on the optical properties of etched quantum wires," *Physical Review B*, Vol. 55, No. 12, March 1997, pp. R7387–R7390.

[155] Niquet, Y., Priester, C., Gourgon, C., and Mariette, H., "Inhomogeneous strain relaxation in etched quantum dots and wires: From strain distributions to piezoelectric fields and band-edge profiles," *Physical Review B*, Vol. 57, No. 23, June 1998, pp. 14850–14859.

[156] Ristić, J., Rivera, C., Calleja, E., Fernández-Garrido, S., Povoloskyi, M., and Di Carlo, A., "Carrier-confinement effects in nanocolumnar GaNAlxGa1xN quantum disks grown by molecular-beam epitaxy," *Physical Review B*, Vol. 72, No. 8, Aug. 2005, pp. 085330.

[157] Zhang, L., Lee, L.-K., Teng, C.-H., Hill, T. A., Ku, P.-C., and Deng, H., "How much better are InGaN/GaN nanodisks than quantum wells-Oscillator strength enhancement and changes in optical properties," *Applied Physics Letters*, Vol. 104, No. 5, 2014, pp. 51116.

[158] Feldmann, J., Peter, G., Göbel, E., Dawson, P., Moore, K., and Foxon, C., "Linewidth dependence of radiative exciton lifetimes in quantum wells," *Physical review letters*, Vol. 59, No. 20, 1987, pp. 2337–2340.

[159] Andreani, L., Tassone, F., and Bassani, F., "Radiative lifetime of free excitons in quantum wells," *Solid state communications*, Vol. 77, No. 9, 1991, pp. 641–645.

[160] Hall, R. N., "Electron-hole recombination in germanium," *Physical Review*, Vol. 87, 1952, pp. 387.

[161] Klimov, V. I. V., Mikhailovsky, A. A. A., McBranch, D. W., Leatherdale, C. A., and Bawendi, M. G., "Quantization of Multiparticle Auger Rates in Semiconductor Quantum Dots," *Science*, Vol. 287, No. 5455, Feb. 2000, pp. 1011–1013.

[162] Sze, S. M. and Ng, K. K., *Physics of Semiconductor Devices*, John Wiley & Sons, 2006.

[163] Padovani, F. and Stratton, R., "Field and thermionic-field emission in Schottky barriers," *Solid-State Electronics*, Vol. 9, 1966, pp. 695–707.

[164] Simon, J., Pelekanos, N., Adelmann, C., Martinez-Guerrero, E., André, R., Daudin, B., Dang, L., and Mariette, H., "Direct comparison of recombination dynamics in cubic and hexagonal GaN/AlN quantum dots," *Physical Review B*, Vol. 68, No. 3, July 2003, pp. 035312.

[165] Moriwaki, O., Someya, T., Tachibana, K., Ishida, S., and Arakawa, Y., "Selective growth of InGaN quantum dot structures and their microphotoluminescence at room temperature," *Applied Physics Letters*, Vol. 76, No. 22, 2000, pp. 3212.

[166] Oliver, R. a., Briggs, G. A. D., Kappers, M. J., Humphreys, C. J., Yasin, S., Rice, J. H., Smith, J. D., and Taylor, R. a., "InGaN quantum dots grown by metalorganic vapor phase epitaxy employing a post-growth nitrogen anneal," *Applied Physics Letters*, Vol. 83, No. 4, 2003, pp. 755.

[167] Sebald, K., Lohmeyer, H., Gutowski, J., Yamaguchi, T., and Hommel, D., "Microphotoluminescence studies of InGaN/GaN quantum dots up to 150 K," *Physica Status Solidi (B)*, Vol. 243, No. 7, June 2006, pp. 1661–1664.

[168] Rice, J. H., Robinson, J. W., Jarjour, A., Taylor, R. A., Oliver, R. a., Briggs, G. A. D., Kappers, M. J., and Humphreys, C. J., "Temporal variation in photoluminescence from single InGaN quantum dots," *Applied Physics Letters*, Vol. 84, No. 20, 2004, pp. 4110.

[169] Winkelnkemper, M., Seguin, R., Rodt, S., Schliwa, A., Reiß mann, L., Strittmatter, A., Hoffmann, A., and Bimberg, D., "Polarized emission lines from A- and B-type excitonic complexes in single InGaN/GaN quantum dots," *Journal of Applied Physics*, Vol. 101, No. 11, 2007, pp. 113708.

[170] Nair, G., Zhao, J., and Bawendi, M. G., "Biexciton Quantum Yield of Single Semiconductor Nanocrystals from Photon Statistics," *Nano letters*, Vol. 11, 2011, pp. 1136–1140.

[171] Dekel, E., Regelman, D. V., Gershoni, D., Ehrenfreund, E., Schoenfeld, W. V., and Petroff, P. M., "Cascade evolution and radiative recombination of quantum dot multiexcitons studied by time-resolved spectroscopy," *Physical Review B*, Vol. 62, No. 16, 2000, pp. 11038–11045.

[172] Zhang, L. and Shi, J., "Quantum size effect on the luminous properties of excitonic states in a quasi-one-dimensional wurtzite GaN nanowire: Two-parameter variational approach," *Current Applied Physics*, March 2013, pp. 1–6.

[173] Humphreys, C. J., "Does In form In-rich clusters in InGaN quantum wells?" *Philosophical Magazine*, Vol. 87, No. 13, May 2007, pp. 1971–1982.

[174] Adelmann, C., Sarigiannidou, E., Jalabert, D., Hori, Y., Rouviere, J.-L., Daudin, B., Fanget, S., Bru-Chevallier, C., Shibata, T., and Tanaka, M., "Growth and optical properties of GaN/AlN quantum wells," *Applied Physics Letters*, Vol. 82, No. 23, 2003, pp. 4154.

[175] Ostapenko, I. a., Honig, G., Kindel, C., Rodt, S., Strittmatter, A., Hoffmann, A., and Bimberg, D., "Large internal dipole moment in InGaN/GaN quantum dots," *Applied Physics Letters*, Vol. 97, No. 6, 2010, pp. 063103.

[176] Amloy, S., Yu, K. H., Karlsson, K. F., Farivar, R., Andersson, T. G., and Holtz, P. O., "Size dependent biexciton binding energies in GaN quantum dots," *Applied Physics Letters*, Vol. 99, No. 25, 2011, pp. 251903.

[177] Choi, K., Kako, S., Holmes, M. J., Arita, M., and Arakawa, Y., "Strong exciton confinement in site-controlled GaN quantum dots embedded in nanowires," *Applied Physics Letters*, Vol. 103, No. 17, 2013, pp. 171907.

[178] Mizuochi, N., Makino, T., Kato, H., and Takeuchi, D., "Electrically driven single-photon source at room temperature in diamond," *Nature Photonics*, , No. April, 2012, pp. 1–5.

[179] Deshpande, S., Heo, J., Das, A., and Bhattacharya, P., "Electrically driven polarized single-photon emission from an InGaN quantum dot in a GaN nanowire," *Nature Communications*, Vol. 4, April 2013, pp. 1675.

[180] Baier, M. H., Constantin, C., Pelucchi, E., and Kapon, E., "Electroluminescence from a single pyramidal quantum dot in a light-emitting diode," *Applied Physics Letters*, Vol. 84, No. 11, 2004, pp. 1967.

[181] Gotz, W., Johnson, N. M., Chen, C., Liu, H., Kuo, C., and Imler, W., "Activation energies of Si donors in GaN," *Applied Physics Letters*, Vol. 68, No. 22, 1996, pp. 3144.

[182] Nakayama, H. and Hacke, P., "Electrical transport properties of p-GaN," ... *JOURNAL OF APPLIED ...*, 1996.

[183] Margalith, T., Buchinsky, O., Cohen, D. a., Abare, a. C., Hansen, M., DenBaars, S. P., and Coldren, L. a., "Indium tin oxide contacts to gallium nitride optoelectronic devices," *Applied Physics Letters*, Vol. 74, No. 26, 1999, pp. 3930.

[184] Ding, Y., Guo, W., Zhu, Y., Liu, J., and Yan, W., "Rapid thermal annealing effects on vacuum evaporated ITO for InGaN/GaN blue LEDs," *Journal of Semiconductors*, Vol. 33, No. 6, June 2012, pp. 066004.

[185] Choi, J.-H., Jang, S.-H., and Jang, J.-S., "Electrical, optical, and structural characteristics of ohmic contacts between p-GaN and ITO deposited by DC- and RF-magnetron sputtering," *Electronic Materials Letters*, Vol. 9, No. 4, July 2013, pp. 425–428.

[186] Bernardini, F. and Fiorentini, V., "Polarization fields in nitride nanostructures: 10 points to think about," *Applied Surface Science*, Vol. 166, No. 1-4, Oct. 2000, pp. 23–29.

[187] Miller, D. A. B., Chemla, D. S., Damen, T. C., Gossard, A. C., Wiegmann, W., Wood, T. H., and Burrus, C. A., "Band-edge electroabsorption in quantum well structures: the quantum-confined Stark effect," *Physical Review Letters*, Vol. 53, No. 22, 1984, pp. 2173–2176.

[188] Chichibu, S., a.C Abare, Mack, M., Minsky, M., Deguchi, T., Cohen, D., Kozodoy, P., Fleischer, S., Keller, S., Speck, J., Bowers, J., Hu, E., Mishra, U., Coldren, L., DenBaars, S., Wada, K., Sota, T., and Nakamura, S., "Optical properties of InGaN quantum wells," *Materials Science and Engineering: B*, Vol. 59, No. 1-3, May 1999, pp. 298–306.

[189] Bardoux, R., Guillet, T., Gil, B., Lefebvre, P., Bretagnon, T., Taliercio, T., Rousset, S., and Semond, F., "Polarized emission from GaN/AlN quantum dots: Single-dot spectroscopy and symmetry-based theory," *Physical Review B*, Vol. 77, No. 23, June 2008, pp. 235315.

[190] Kindel, C., Kako, S., Kawano, T., Oishi, H., Arakawa, Y., Hönig, G., Winkelnkemper, M., Schliwa, A., Hoffmann, A., and Bimberg, D., "Exciton fine-structure splitting in GaN/AlN quantum dots," *Physical Review B*, Vol. 81, No. 24, June 2010, pp. 241309.

[191] Amloy, S., Chen, Y. T., Karlsson, K. F., Chen, K. H., Hsu, H. C., Hsiao, C. L., Chen, L. C., and Holtz, P. O., "Polarization-resolved fine-structure splitting of zero-dimensional In_{x}Ga_{1-x}N excitons," *Physical Review B*, Vol. 83, No. 20, May 2011, pp. 201307.

[192] Hsu, C.-W., Moskalenko, E. S., Eriksson, M. O., Lundskog, A., Fredrik Karlsson, K., Forsberg, U., Janzen, E., and Olof Holtz, P., "The charged exciton in an InGaN quantum dot on a GaN pyramid," *Applied Physics Letters*, Vol. 103, 2013, pp. 013109.

[193] Warburton, R. J., Schäflein, C., Haft, D., Bickel, F., Lorke, A., Karrai, K., Garcia, J. M., Schoenfeld, W., and Petroff, P. M., "Optical emission from a charge-tunable quantum ring," *Nature*, Vol. 405, No. 6789, July 2000, pp. 926–9.

[194] Baier, M., Findeis, F., Zrenner, A., Bichler, M., and Abstreiter, G., "Optical spectroscopy of charged excitons in single quantum dot photodiodes," *Physical Review B*, Vol. 64, No. 19, Oct. 2001, pp. 195326.

[195] Ediger, M., Bester, G., Gerardot, B., Badolato, a., Petroff, P., Karrai, K., Zunger, a., and Warburton, R., "Fine Structure of Negatively and Positively Charged Excitons in Semiconductor Quantum Dots: Electron-Hole Asymmetry," *Physical Review Letters*, Vol. 98, No. 3, Jan. 2007, pp. 036808.

[196] Sacconi, F., Maur, M. A. D., and Carlo, A. D., "Optoelectronic Properties of Nanocolumn InGaN/GaN LEDs," *IEEE Transactions on Electron Devices*, Vol. 59, No. 11, 2012, pp. 2979–2987.